

ВІСНИК



Дніпропетровського університету

Науковий журнал

№ 2

ТОМ 21

2013

РЕДАКЦІЙНА РАДА:

акад. Академії наук ВО України, д-р фіз.-мат. наук, проф. **М.В. Поляков** (*голова редакційної ради*); ст. наук. співроб., проф. **В.І. Карплюк** (*заст. голови*); д-р фіз.-мат. наук, проф. **О.О. Кочубей**; д-р хім. наук, проф. **В.Ф. Варгалоук**; чл.-кор. НАПН України, д-р філос. наук, проф. **П.І. Гнатенко**; д-р фіз.-мат. наук, проф. **О.Г. Гоман**; д-р філол. наук, проф. **В.Д. Демченко**; д-р техн. наук, проф. **А.П. Дзюба**; д-р пед. наук, проф. **Л.І. Зеленська**; чл.-кор. НАН України, д-р фіз.-мат. наук, проф. **В.П. Моторний**; чл.-кор. НАПН України, д-р психол. наук, проф. **Е.Л. Носенко**; д-р філос. наук, проф. **В.О. Панфілов**; д-р біол. наук, проф. **О.Є. Пахомов**; д-р іст. наук, проф. **С.І. Світленко**; акад. Академії наук ВО України, д-р фіз.-мат. наук, проф. **В.В. Скалозуб**; д-р філол. наук, проф. **Т.С. Пристайко**; чл.-кор. НАН України, д-р біол. наук, проф. **А.П. Травлєєв**; д-р техн. наук, проф. **Ю.Д. Шептун**.

Серія: **ФІЗИКА.**
РАДІОЕЛЕКТРОНІКА
Випуск 20

Дніпропетровськ
"Ліра"

УДК 53.01(063)

Публікується за рішенням вченої ради Дніпропетровського національного університету імені Олеся Гончара згідно з планом видань на 2013 р.

Представлені результати досліджень з питань теоретичної фізики, фізики твердого тіла та радіофізики.

Обговорюються питання оцінки можливих сигналів абелевого Z' бозона, застосування $SU(2)$ ґраткової калібрувальної теорії поля, вдосконалення космологічних моделей, опису повністю іонізованої плазми та електромагнітного поля в середовищі з нерухомих дворівневих випромінювачів.

Розглядаються проблеми отримання та дослідження властивостей композитних матеріалів на основі синтетичних опалів, двооксиду ванадію, багатоконпонентних високоентропійних сплавів, магнітотвердих матеріалів у метастабільному стані. Також досліджуються структура та властивості твердих розчинів на основі монобориду заліза, процеси кристалізації в мікродротах і перезарядки в полікристалічних напівпровідниках. Представлено результати моделювання процесів кристалізації металів та розрахунку енергетичних і геометричних характеристик кремнієвих нанокластерів.

Досліджуються процеси у хвилеводно-діелектричній структурі у вигляді закритичного прямокутного хвилеводу з діелектричною вставкою.

Для наукових та інженерно-технічних працівників у галузі теорії поля, фізики твердого тіла, теоретичної та прикладної електродинаміки.

Редакційна колегія:

д-р фіз.-мат. наук **В.В. Скалозуб** (відп. редактор), ДНУ; д-р фіз.-мат. наук **В.М. Моїсєнко** (заст. відп. редактора), ДНУ; к-т фіз.-мат. наук **М.П. Дергачов** (відп. секретар), ДНУ; к-т фіз.-мат. наук **С.Ф. Лягушин** (відп. секретар), ДНУ; д-р фіз.-мат. наук **В.Ф. Башев**, ДНУ; д-р фіз.-мат. наук **М. Ф. Буланій**, ДНУ; д-р фіз.-мат. наук **В.Д. Гладуш**, ДНУ; д-р фіз.-мат. наук **В. С. Горелік**, Фізичний інститут імені П.М. Лебедева (Росія, Москва); д-р фіз.-мат. наук **О.О. Дробахін**, ДНУ; д-р техн. наук **В.М. Корчинський**, ДНУ; д-р фіз.-мат. наук **О.В. Коваленко**, ДНУ; д-р фіз.-мат. наук **О.Б. Лисенко**, Дніпродзержинський державний технічний університет; д-р фіз.-мат. наук **А. М. Овруцький**, ДНУ; д-р фіз.-мат. наук **О.А. Панков**, Гомельський державний технічний університет імені П. Сухого (Білорусь, Гомель); д-р фіз.-мат. наук **С.О. Погарський**, Харківський національний університет імені В.Н. Каразіна; д-р фіз.-мат. наук **О.А. Романова**, Саратовський державний університет (Росія, Саратов); д-р фіз.-мат. наук **Ю.М. Синюков**, Інститут теоретичної фізики імені М.М.Боголюбова НАН України; д-р фіз.-мат. наук **О.Й. Соколовський**, ДНУ; д-р фіз.-мат. наук **Є.Д. Солдатова**, ДНУ; д-р фіз.-мат. наук **М.П. Трубіцин**, ДНУ; д-р фіз.-мат. наук **В.С. Хандецький**, ДНУ; д-р фіз.-мат. наук **І.М. Черненко**, Український державний хіміко-технологічний університет.

Представлены результаты исследований по вопросам теоретической физики, физики твердого тела и радиофизики.

Обсуждаются вопросы оценки возможных сигналов абелевого Z' бозона, применения $SU(2)$ решеточной калибровочной теории поля, усовершенствования космологических моделей, описания полностью ионизированной плазмы и электромагнитного поля в среде, образованной неподвижными двухуровневыми излучателями.

Рассматриваются проблемы получения и исследования свойств композитных материалов на основе синтетических опалов, двуокиси ванадия, многокомпонентных высокоэнтропийных сплавов, магнитотвердых материалов в метастабильном состоянии. Также исследуются структура и свойства твердых растворов на основе моноборида железа, процессы кристаллизации в микропроводах и перезарядки в поликристаллических полупроводниках. Представлены результаты моделирования процессов кристаллизации металлов, а также расчета энергетических и геометрических характеристик кремниевых нанокластеров.

Исследуются процессы в волноводно-диэлектрической структуре в виде закритического прямоугольного волновода с диэлектрической вставкой.

Для научных и инженерно-технических работников в области теории поля, физики твердого тела, теоретической и прикладной электродинамики.

Редакционная коллегия:

д-р физ.-мат. наук **В.В. Скалозуб** (отв. редактор), ДНУ; д-р физ.-мат. наук **В.Н. Моисеенко** (зам. отв. редактора), ДНУ; к-т физ.-мат. наук **М.П. Дергачёв** (отв. секретарь), ДНУ; к-т физ.-мат. наук **С.Ф. Лягушин** (отв. секретарь), ДНУ; д-р физ.-мат. наук **В.Ф. Башев**, ДНУ; д-р физ.-мат. наук **М. Ф. Буланый**, ДНУ; д-р физ.-мат. наук **В.Д. Гладуш**, ДНУ; д-р физ.-мат. наук **В. С. Горелик**, Физический институт имени П.Н. Лебедева (Россия, Москва); д-р физ.-мат. наук **О.О. Дробахин**, ДНУ; д-р техн. наук **В.М. Корчинский**, ДНУ; д-р физ.-мат. наук **А.В. Коваленко**, ДНУ; д-р физ.-мат. наук **А.Б. Лысенко**, Днепродзержинский государственный технический университет; д-р физ.-мат. наук **А. М. Овруцкий**, ДНУ; д-р физ.-мат. наук **А.А. Панков**, Гомельский государственный технический университет имени П. Сухого (Беларусь, Гомель); д-р физ.-мат. наук **С.А. Погарский**, Харьковский национальный университет имени В.Н. Каразина; д-р физ.-мат. наук **Е.А. Романова**, Саратовский государственный университет (Россия, Саратов); д-р физ.-мат. наук **Ю.М. Синюков**, Институт теоретической физики имени Н.Н.Боголюбова НАН Украины; д-р физ.-мат. наук **А.И. Соколовский**, ДНУ; д-р физ.-мат. наук **Е. Д. Солдатова**, ДНУ; д-р физ.-мат. наук **М. П. Трубицын**, ДНУ; д-р физ.-мат. наук **В. С. Хандецкий**, ДНУ; д-р физ.-мат. наук **И. М. Черненко**, Украинский государственный химико-технологический университет.

UDC 53.01(063)

*Published by the decision of the Academic Council of the Oles Honchar
Dnipropetrovsk National University in accordance with the publishing plan for 2013*

The results of investigations in theoretical physics, solid state physics and radiophysics are presented.

The problems on estimating the Abelian Z' boson signals, applying the SU(2) lattice gauge field theory, modifying the cosmological models, and describing the completely ionized plasma and electromagnetic field in medium consisting of the motionless two-level emitters are discussed.

The problems on obtaining and investigating properties of composite materials based on synthetic opals, vanadium dioxide, multicomponent high-entropy alloys, and hard magnetic materials in a metastable state are considered. The structure and properties of solid solutions based on iron monoboride, the crystallization processes in microwires, and the recharging processes in polycrystalline semiconductors are also investigated. The results of the metal crystallization process simulation and calculations for the Si - nanocluster energy and geometrical parameters are presented.

The processes in a waveguide-dielectric structure in the form of cut-off rectangular waveguide with dielectric insertion are investigated.

For scientific researchers and engineers in field theory, solid state physics, theoretical and applied electrodynamics.

Editorial Board:

Doctor of Science **V. V. Skalozub** (Editor), DNU; Doctor of Science **V. N. Moiseyenko** (Vice - Editor), DNU; Philosophy Doctor **M. P. Dergachov** (Secretary), DNU; Philosophy Doctor **S. F. Lyagushyn** (Secretary), DNU; Doctor of Science **V. F. Bashev**, DNU; Doctor of Science **M. F. Bulany**, DNU; Doctor of Science **V. D. Gladush**, DNU; Doctor of Science **V. S. Gorelik**, P.N. Lebedev Physical Institute (Russia, Moscow); Doctor of Science **O. O. Drobakhin**, DNU; Doctor of Science **V. M. Korchynsky**, DNU; Doctor of Science **A.V. Kovalenko**, DNU; Doctor of Science **A. B. Lysenko**, Dniprodzerzhynsk State Technical University; Doctor of Science **A. M. Ovrutsky**, DNU; Doctor of Science **A. A. Pankov**, P. Sukhoy Gomel State Technical University (Belarus, Gomel); Doctor of Science **S. A. Pogarsky**, V.N. Karazin Kharkiv National University; Doctor of Science **E. A. Romanova**, Saratov State University (Russia, Saratov); Doctor of Science **Yu. M. Sinyukov**, Bogolyubov Institute for Theoretical Physics of NAS of Ukraine; Doctor of Science **A. I. Sokolovsky**, DNU; Doctor of Science **Ye. D. Soldatova**, DNU; Doctor of Science **M. P. Trubitsyn**, DNU; Doctor of Science **V. S. Khandetsky**, DNU; Doctor of Science **I. M. Chernenko**, Ukrainian State University for Chemistry and Technology.

© Oles Honchar Dnipropetrovsk National
University, 2013
© "Lira", 2013

PACS 12.60.Cn, 13.66.Hk, 14.70.Pw

A. V. Gulov, Ya. S. Moroz

Oles Honchar Dnipropetrovsk National University

AMPLIFICATION OF Z' SIGNAL IN $e^+e^- \rightarrow \mu^+\mu^-$ PROCESS

One-parameter observables with the best value-to-uncertainty ratio are proposed to estimate possible signals of the Abelian Z' boson in the $e^+e^- \rightarrow \mu^+\mu^-$ scattering process. The value-to-uncertainty ratio is chosen as a natural criterion allowing the statistical amplification of the signal in experiment. The model independent relations between the Abelian Z' couplings to leptons are used in order to reduce the number of unknown parameters of the particle. The observables are constructed by angular integration with proper weight functions. In order to perform numeric optimization a set of orthogonal polynomials is introduced taking into account the kinematics of the process. The optimal weight functions are found to be smooth step-like functions close to the hyperbolic tangent shape. The observables are applied to data on differential cross-sections obtained in the LEP experiments. The Z' couplings to axial-vector and vector lepton currents are fitted and compared to other estimates.

Keywords: high energy physics, Z' bosons, differential cross-section, integrated cross-section.

Однопараметрические наблюдаемые с наилучшим отношением величины к неопределенности предложены для оценки возможных сигналов абелевого Z' бозона в процессе рассеяния $e^+e^- \rightarrow \mu^+\mu^-$. Отношение величины к неопределенности выбрано в качестве естественного критерия, позволяющего статистически усилить сигнал в эксперименте. Для уменьшения количества неизвестных параметров нового бозона применяются модельно-независимые соотношения между константами связи абелевого Z' с лептонами. Наблюдаемые построены угловым интегрированием с подходящей весовой функцией. Численная оптимизация выполняется при помощи системы ортогональных полиномов, введенных с учетом кинематики процесса. Оптимальные весовые функции выглядят сглаженными ступенчатыми, похожими на гиперболический тангенс. Наблюдаемые применены к дифференциальным сечениям из экспериментов LEP. Фитированы значения констант связи Z' с векторными и аксиально-векторными токами лептонов и сопоставлены с другими оценками.

Ключевые слова: физика высоких энергий, Z' бозоны, дифференциальные сечения рассеяния, интегральные сечения рассеяния.

Однопараметричні спостережувані з найкращим відношенням величини до невизначеності запропоновані для оцінки можливих сигналів абелевого Z' бозона в процесі розсіяння $e^+e^- \rightarrow \mu^+\mu^-$. Відношення величини до невизначеності обрано в якості природного критерію, який дозволяє статистично посилити сигнал в експерименті. Для зменшення кількості невідомих параметрів нового бозона застосовуються модельно-незалежні співвідношення між константами зв'язку абелевого Z' з лептонами. Спостережувані побудовані кутовим інтегруванням з доцільною ваговою функцією. Чисельна оптимізація виконується за допомогою системи ортогональних поліномів, введених з урахуванням кінематики процесу. Оптимальні вагові функції виглядають згладженими ступеневими, схожими на гіперболічний тангенс. Спостережувані застосовані до диференціальних перерізів з експериментів LEP. Фітовані значення констант зв'язку Z' з векторними та аксіально-векторними струмами лептонів і порівняні з іншими оцінками.

Ключові слова: фізика високих енергій, Z' бозони, диференціальні перерізи розсіяння, інтегральні перерізи розсіяння.

Introduction

Electron-positron colliders provide possibility of precise measurements in high-energy physics. The history of LEP experiments showed that lepton processes can be sensitive to off-shell signals of physics beyond the standard model (SM). Unfortunately, the LEP statistics was not rich enough to detect clearly some signals of new heavy particles.

The special observables were designed to select probable signals of the Abelian Z' boson in various LEP processes [1, 2]. In particular, a one-parameter sign-definite observable was constructed as a generalized forward-backward cross-section of $e^+e^- \rightarrow \mu^+\mu^-$ process, and a hint of Z' boson was found at one standard deviation. However, the latest LHC experiments allow to conclude that the maximum likelihood values of Z' couplings from Ref. [1] seem to be overestimated. At the present time, the most powerful observables for Z' boson in $e^+e^- \rightarrow \mu^+\mu^-$ are found [3]. So, it is possible to revise the LEP data by means of the new approach.

Let us describe briefly main checkpoints of the present investigation. We use common phenomenological parameterization of Z' couplings with SM fermions as well as the model-independent relations between the Z' couplings [4]. The optimal one-parameter observables are constructed as the cross-sections integrated over the scattering angle with proper weight functions maximizing the value-to-uncertainty ratio for the observable. Then, we fit LEP data using the observables in order to estimate Z' coupling.

The low-energy phenomenology of the Abelian Z' boson

The Abelian Z' boson [5-7] is usually described by its couplings to vector and axial-vector currents. In general, there is also the mixing between Z and Z' bosons. The corresponding Lagrangian is

$$\begin{aligned} L_{\bar{f}fZ} &= \frac{1}{2} Z_{\mu} \bar{f} \gamma^{\mu} [(v_{fZ}^{SM} + \gamma^5 a_{fZ}^{SM}) \cos \theta_0 + (v_f + \gamma^5 a_f) \sin \theta_0] f, \\ L_{\bar{f}fZ'} &= \frac{1}{2} Z'_{\mu} \bar{f} \gamma^{\mu} [(v_f + \gamma^5 a_f) \cos \theta_0 - (v_{fZ}^{SM} + \gamma^5 a_{fZ}^{SM}) \sin \theta_0] f \end{aligned} \quad (1)$$

where we omit effective interactions inspired by loop corrections and next-to-leading order terms in inverse heavy mass scales.

Not all the coupling constants in (1) are independent, if we assume the Abelian Z' boson associated with an effective U(1) gauge symmetry at low energies. If we consider the single neutral vector boson with a mass of order TeVs, the following relations arise [4]

$$\begin{aligned} v_{f[T_3=1/2]} &= v_{f[T_3=-1/2]} = -2a, \quad a_{f[T_3=-1/2]} = -a_{f[T_3=1/2]} = a, \\ \theta_0 &= -a \frac{\sin(2\theta_w)}{\sqrt{4\pi\alpha_{em}}} \left(\frac{m_Z}{m_{Z'}} \right)^2 \end{aligned} \quad (2)$$

where T_3 is the third component of the weak isospin, and the fermions are taken from the same SM doublet. The relations can be motivated by general theoretical reasons (gauge symmetry, renormalizability at energies of the Z' decoupling) which are described in details in Ref. [4]. Let us note that the relations (3) cover a wide set of popular Z' models. In this regard, they can be called model-independent. Considering the cross-sections at energies below the Z' mass, it is convenient to use couplings

$$\bar{a}_f = \frac{m_Z}{\sqrt{4\pi m_{Z'}}} a_f, \quad \bar{v}_f = \frac{m_Z}{\sqrt{4\pi m_{Z'}}} v_f. \quad (3)$$

The virtual Z' boson state contributes to the differential cross-section of $e^+e^- \rightarrow \mu^+\mu^-$ process. In the lowest order in the inverse Z' mass the cross-section deviates from its SM value as

$$\begin{aligned} \frac{d\sigma}{dz} - \frac{d\sigma^{SM}}{dz} = & F_1(\sqrt{s}, z)\bar{a}^{-2} + F_2(\sqrt{s}, z)\bar{a}\bar{v}_e + \\ & + F_3(\sqrt{s}, z)\bar{a}\bar{v}_\mu + F_4(\sqrt{s}, z)\bar{v}_e\bar{v}_\mu + \dots \end{aligned} \quad (4)$$

where $z = \cos\theta_0$ is the cosine of the scattering angle and dots stand for higher corrections in the inverse Z' mass. Factors F_i arise from the interference between the SM scattering amplitude and the Z' exchange amplitude. They have to be computed numerically taking into account both the tree-level contribution and loop corrections.

Being measured in experiments, the cross-section (4) allows to estimate the Z' couplings \bar{a} , \bar{v}_e , and \bar{v}_μ . A non-zero value of some coupling mentioned can be called the Z' signal.

Minimal number of unknown parameters is preferable in fitting data. Therefore, one-parameter observable is the most prominent from the statistical point of view. Moreover, sign-definite observable is more informative, since it can also reject the hypothesis, whereas sign-indefinite one can only accept the signal. These properties are especially important in case of statistics which is not rich enough to detect clear signals at high confidence levels. Fortunately, the cross-section (4) contains one sign-definite term with \bar{a}^{-2} . If we could select this term in the cross-section, we would obtain a powerful observable to detect Z' signals in experiments. In case of lepton universality the term with $\bar{v}_e\bar{v}_\mu$ also becomes sign-definite.

It is also worth to note that factors $F_{2,3}$ are small with respect to $F_{1,4}$. Their contributions to the cross-section are about 1%, and their existence does not affect the key ideas of the present investigation. So, the Z' signal in $e^+e^- \rightarrow \mu^+\mu^-$ can be discussed as two-parametric.

The observables

The differential cross-section (4) contains two leading terms at \bar{a}^{-2} and $\bar{v}_e\bar{v}_\mu$. The corresponding factors $F_i(\sqrt{s}, z)$ are the functions of energy and scattering angle. We can use angular integration in order to suppress one factor comparing to another. Actually, this means that we will construct some integrated cross-section with specific properties.

In general, integrated cross-sections are well known in the literature. The most popular integration schemes are based on bin summation with equal weights but opposite signs. As examples, we can mention the total cross-section, the forward-backward cross-section, the center-edge cross-section, etc. However, the equal weight of bins is just a possible option. The most general integration scheme can be described by weight function $p(z)$:

$$\sigma = \int_{-1}^1 dz p(z) \left(\frac{d\sigma}{dz} - \frac{d\sigma^{SM}}{dz} \right). \quad (5)$$

In these notations, the popular mentioned cross-sections correspond to step-like weight functions. The observables used in previous analysis of LEP data are also based on step-like weight functions.

The statistical uncertainty of the observable (5) can be estimated taking into account that the actual number of events in bin is distributed under the Poisson distribution. This means the variance of events coincides with the average number of events. Then, the standard deviation of the observable is [3]

$$\delta\sigma \cong \sqrt{\frac{1}{L} \int_{-1}^1 dz p^2(z) \frac{d\sigma^{SM}}{dz}} \quad (6)$$

where L is the integrated luminosity of the experiment.

Let us consider the observable which amplifies the Z' signal as much as possible. This aim can be reached by maximizing the value-to-uncertainty (signal-to-uncertainty) ratio where the weight function is assumed to be varied in the optimization procedure. The general algorithm to find the optimal weight function is described in details in [3]. In the present paper we mention briefly just the main steps of the algorithm.

$$abs\left(\frac{\sigma}{\delta\sigma}\right) \propto abs\left(\frac{\int_{-1}^1 p(z) \left(\frac{d\sigma}{dz} - \frac{d\sigma^{SM}}{dz}\right) dz}{\sqrt{\int_{-1}^1 p^2(z) \frac{d\sigma}{dz} dz}}\right) \rightarrow \max \quad (7)$$

In fact, the optimization (7) has to be performed under additional constraints. First of all, the normalization of the weight function must be taken into account, since (7) is evidently invariant under the rescaling of the weight function. We choose the normalization

$$\int_{-1}^1 dz p^2(z) = 1. \quad (8)$$

Second, the weight function is chosen to suppress all the factors in the differential cross-section (4) except for either F_1 or F_4 . The most general scheme takes into account both the contributions of leading factors $F_{1,4}$ and small factors $F_{2,3}$ in the differential cross-section (4). In order to select the factor F_1 we can minimize the cumulative relative contribution of the factors $F_{2,3,4}$:

$$\frac{\sum_{i=2}^4 abs\left(\int_{-1}^1 dz p(z) F_i(\sqrt{s}, z)\right)}{\sum_{i=1}^4 abs\left(\int_{-1}^1 dz p(z) F_i(\sqrt{s}, z)\right)} \rightarrow \min \quad (9)$$

The factor F_4 is selected in a similar way using $F_{1,2,3}$ in the nominator. Eq. (9) does not specify a unique weight function, it defines a subspace in the Hilbert space of $p(z)$. It is clearly seen from the fact that Eq. (9) does not change when a function orthogonal to $F_{1,2,3,4}$ is added to $p(z)$.

The optimization (7) with the constraints (8) and (9) has to determine uniquely the weight function $p(z)$ for the most amplified Z' signal in the considered process. These calculations require choosing some basis in the Hilbert space of weight functions.

The most natural basis takes into account the kinematics of $e^+e^- \rightarrow \mu^+\mu^-$ process. Due to the absence of the flavor-changing neutral currents, there are no virtual bosons in the t-channel. Moreover, all the leptons can be considered as massless. This leads to the well-known two-polynomial structure of all the factors in the differential cross-sections:

$$F_i(\sqrt{s}, z) = a_i(\sqrt{s})p_1(z) + b_i(\sqrt{s})p_2(z) \quad (10)$$

where $p_1(z) \sim z$, $p_2(z) \sim (1+z^2)$. In this regard, it is convenient to use orthogonal polynomials as a basis in the Hilbert space of weight functions. We define orthogonal normalized polynomials in the standard way,

$$\int_{-1}^1 dz p_i(z) p_j(z) = \begin{cases} 1, & i = j \\ 0, & i \neq j \end{cases} \quad (11)$$

The full set of polynomials can be reconstructed starting from p_1 and p_2 and increasing the largest power of the polynomial [3]:

$$\begin{aligned} p_1 &= \sqrt{\frac{3}{2}}z, \quad p_2 = \frac{1}{2}\sqrt{\frac{15}{14}}(1+z^2), \\ p_3 &= \sqrt{\frac{6}{7}}\left(1 - \frac{5}{2}z^2\right), \quad p_4 = \frac{1}{2}\sqrt{\frac{7}{2}}(5z^3 - 3z). \end{aligned} \quad \dots(12)$$

Weight function $p(z)$ can be expanded by p_i :

$$p(z) = \sum_{i=1}^{\infty} c_i p_i(z). \quad (13)$$

Then, the normalization condition (8) becomes

$$\sum_{i=1}^{\infty} c_i^2 = 1. \quad (14)$$

Since the Z' contributions to the cross-section are described by two polynomials $p_{1,2}$, we use the fixed direction in the functional subspace based on $p_{1,2}$ in order to suppress either F_1 or F_4 factor:

$$k = c_2 / c_1. \quad (15)$$

This can be done by means of (9). The numerical analysis shows that the corresponding relative weight of F_1 or F_4 is 0.98. Thus, we can estimate the systematic error of the variable as 2 %.

There is also the normalization condition (14) allowing to determine one of the coefficients through the others. For instance,

$$c_1 = \sqrt{\frac{1 - c_3^2 - c_4^2 - \dots}{1 + k^2}} \quad (16)$$

Thus, two coefficients c_1 and c_2 are explicitly expressed by the other coefficients. As a result, c_3, c_4, \dots are to be varied to find the maximum (7).

In fact, the usage of orthogonal polynomials is just calculation tool to perform optimization (7) to find the most effective weight function. However, a convenient 'natural' basis helps us to obtain results in the most quick and simple way.

The signal-to-uncertainty ratio is maximized to find the coefficients at polynomial expansion (13). Increasing the number of polynomials in (13) we can observe asymptotic behavior of $p(z)$. We can estimate the relative accuracy of the result comparing the weight functions at the current and previous steps of the calculation:

$$\eta = \sqrt{\int_{-1}^1 dz (p_{\text{current}} - p_{\text{previous}})^2}. \quad (17)$$

Using eight polynomials from the basis, we find $\eta < 0.01$ at all the considered energies, which is below the systematic theoretical error (2%) of the observables. The results of optimization are shown in Tables 1, 2.

Table 1

The results of optimization of the weight function to select \bar{a}^{-2} for LEP energies. The parameter $k = c_2 / c_1$ is computed in accordance with (9), the coefficients c_i in (13) are found by (7)

\sqrt{s} , GeV	k	c_1	c_2	c_3	c_4	c_5	c_6	c_7	c_8
130	-0.567	0.770	-0.437	-0.416	0.193	-0.011	-0.050	-0.044	0.019
136	-0.524	0.802	-0.420	-0.392	0.141	0.025	-0.061	-0.040	0.014
161	-0.425	0.863	-0.367	-0.330	0.036	0.076	-0.056	-0.017	0.000
172	-0.402	0.876	-0.352	-0.314	0.014	0.083	-0.052	-0.011	-0.003
183	-0.385	0.885	-0.340	-0.302	-0.002	0.086	-0.048	-0.007	-0.004
189	-0.377	0.889	-0.335	-0.296	-0.009	0.088	-0.046	-0.006	-0.005
192	-0.374	0.891	-0.333	-0.294	-0.012	0.088	-0.045	-0.005	-0.005
196	-0.369	0.893	-0.330	-0.291	-0.016	0.089	-0.044	-0.004	-0.005
200	-0.365	0.894	-0.327	-0.288	-0.019	0.089	-0.043	-0.003	-0.006
202	-0.363	0.895	-0.325	-0.287	-0.020	0.089	-0.042	-0.003	-0.006
205	-0.361	0.897	-0.323	-0.285	-0.023	0.090	-0.041	-0.002	-0.006
207	-0.359	0.897	-0.322	-0.284	-0.024	0.090	-0.041	-0.002	-0.006

Table 2

The results of optimization of the weight function to select $\bar{\nu}_e \bar{\nu}_\mu$ for LEP energies. The parameter $k = c_2 / c_1$ is computed in accordance with (9), the coefficients c_i in (13) are found by (7)

\sqrt{s} , GeV	k	c_1	c_2	c_3	c_4	c_5	c_6	c_7	c_8
130	-1.258	-0.597	0.751	0.230	-0.150	0.009	0.039	0.034	-0.015
136	-1.362	-0.579	0.788	0.174	-0.102	-0.018	0.044	0.029	-0.010
161	-1.678	-0.510	0.856	0.052	-0.021	-0.045	0.033	0.010	0.000
172	-1.775	-0.490	0.870	0.025	-0.008	-0.046	0.029	0.006	0.002
183	-1.856	-0.474	0.879	0.006	0.001	-0.046	0.025	0.004	0.002
189	-1.894	-0.466	0.883	-0.003	0.005	-0.046	0.024	0.003	0.003
192	-1.912	-0.463	0.885	-0.006	0.006	-0.046	0.023	0.002	0.003
196	-1.934	-0.459	0.887	-0.011	0.008	-0.046	0.022	0.002	0.003
200	-1.955	-0.455	0.889	-0.015	0.010	-0.045	0.022	0.002	0.003
202	-1.965	-0.453	0.890	-0.017	0.010	-0.045	0.021	0.001	0.003
205	-1.980	-0.450	0.891	-0.020	0.011	-0.045	0.021	0.001	0.003
207	-1.989	-0.449	0.892	-0.022	0.012	-0.045	0.020	0.001	0.003

In Figs. 1, 2 we show how the optimal weight functions depend on the collision energy. As it is seen, the result is stable for different LEP energies.

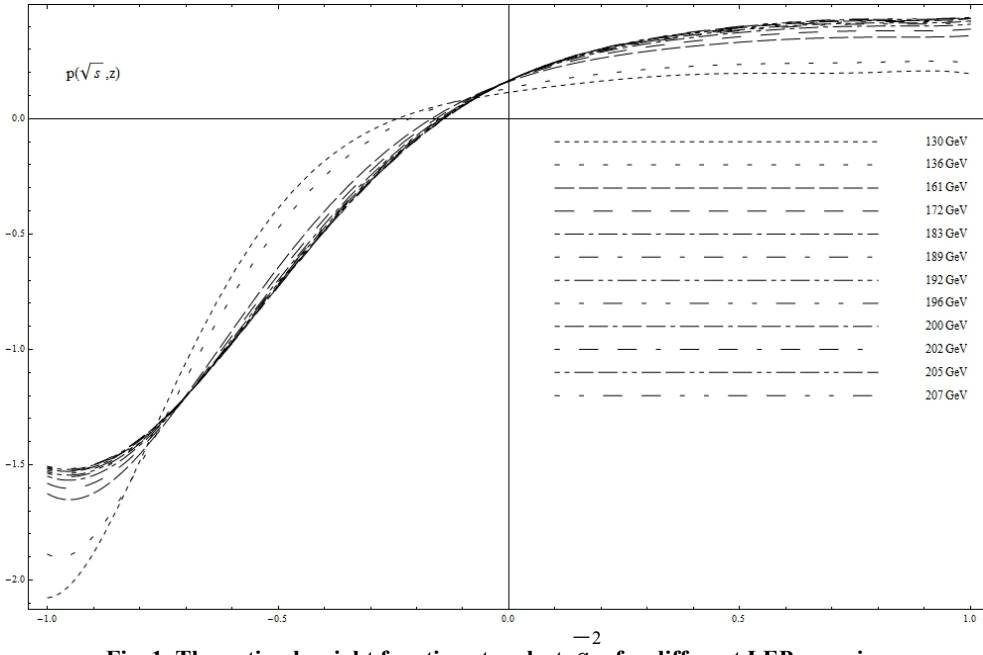


Fig. 1. The optimal weight functions to select a^{-2} for different LEP energies.

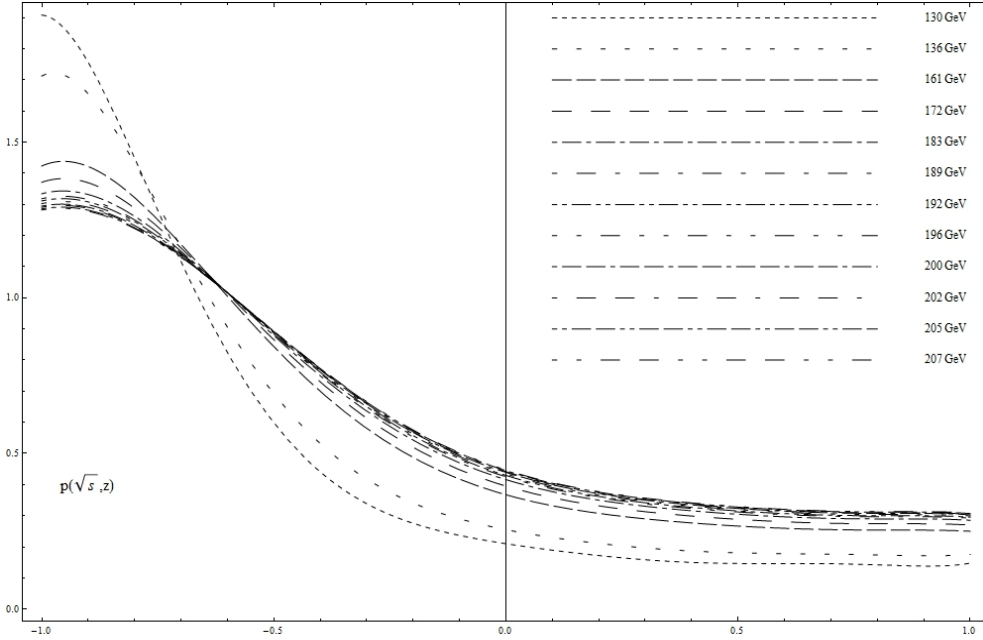


Fig. 2. The optimal weight functions to select $v_e v_\mu$ for different LEP energies.

Data fit

Data fit is performed in the standard way using chi-square function to combine different scattering energies together. First, we calculate both the mean values and the statistical uncertainties of our observables at different energies taking data on differential cross-sections published by the LEP Collaborations [8-10]. Dividing the values by a known numeric factor, we compute the experimental estimate of either a^{-2} or $v_e v_\mu$. In this way we obtain 21 data points for each type of observables. After that, we combine all

the data points altogether by means of the standard chi-square technique obtaining the mean values and the uncertainties of the Z' couplings:

$$\bar{a}^{-2} = (1.4369 \pm 4.8614) \times 10^{-5}, \quad \bar{v}_e \bar{v}_\mu = (-7.5890 \pm 6.0377) \times 10^{-5}$$

Conclusions

Let us discuss the obtained results. First of all, the uncertainty of \bar{a}^{-2} is close to the uncertainty within the indirect measurement of the axial-vector coupling by the total cross-sections and forward-backward asymmetries [1]. However, we use less data points, since the differential cross-sections were not published for some LEP energies depending on the collaboration. This reflects the fact that the new observables are more statistically powerful with respect to the observables used in [1].

Second, the mean value of \bar{a}^{-2} decreases comparing to the indirect estimates [1]. This is in accordance with the latest constraints from the LHC [11] showing that this coupling should be about 10^{-6} rather than 10^{-5} .

Finally, the mean value and the uncertainty of the vector coupling are quite large, so we cannot interpret them as some signal of the particle.

The new observables for searching for Z' signals in $e^+e^- \rightarrow \mu^+\mu^-$ process show they can be useful in data fitting. They have good perspectives in future experiments at lepton colliders such as the ILC.

References

1. **Gulov A. V.** Fitting of Z' parameters / A. V. Gulov and V. V. Skalozub // Int. J. Mod. Phys. A. – 2010. – 25. – P. 5787-5815.
2. **Gulov A. V.** Renormalizability and the model independent observables for Abelian Z' prime search / A.V. Gulov and V.V. Skalozub // Phys. Rev. D. – 2000. – 61. – 055007.
3. **Gulov A. V.** Optimal one-parameter observables for Z' searches in $e^+e^- \rightarrow \mu^+\mu^-$ process / A. V. Gulov // e-print arXiv:1308.4837v1 [hep-ph].
4. **Gulov A. V.** Renormalizability and model independent description of Z' signals at low energies / A.V. Gulov and V.V. Skalozub // Eur. Phys. J. C. – 2000. – 17. – P. 685-694.
5. **Leike A.** The phenomenology of extra neutral gauge bosons / A. Leike // Phys. Rep. – 1999. – 317. – P. 143-205.
6. **Langacker P.** The Physics of Heavy Z_0 Gauge Bosons / P. Langacker // Rev.Mod.Phys. – 2009. – 81. – P. 1199-1228.
7. **Rizzo T. G.** Z' phenomenology and the LHC / T. G. Rizzo // e-print arXiv:hep-ph/0610104. – 2006.
8. **Abbiendi G.** Tests of the standard model and constraints on new physics from measurements of fermion-pair production at 189–209 GeV at LEP / G. Abbiendi at al. (OPAL Collaboration) // Eur. Phys. J. C. – 2004. – 33. – P. 173-212.
9. **Abdallah J.** Measurement and interpretation of fermion-pair production at LEP energies above the Z resonance / J. Abdallah at al. (DELPHI Collaboration) // Eur. Phys. J. C. – 2006. – 45. – P. 589-632.
10. **Schael S.** Fermion pair production in e^+e^- collisions at 189–209 GeV and constraints on physics beyond the standard model / S. Schael at al. (ALEPH Collaboration) // Eur. Phys. J. C. – 2007. – 49. – P. 411-437.
11. **Gulov A. V.** Model-Independent Estimates for the Couplings of the Abelian Z' Boson in the Drell-Yan Process at the LHC / A. V. Gulov and A. Kozhushko // e-print arXiv:1307.2393v1 [hep-ph].

Received 13.07.2013.

V. I. Demchik, N. V. Kolomojets, V. V. Skalozub

Oles Honchar Dnipropetrovsk National University

SPATIAL STRUCTURE OF THE POLYAKOV LOOP IN EXTERNAL CHROMOMAGNETIC FIELD IN LATTICE SU(2) GLUODYNAMICS

Spatial distribution of Polyakov's loop in 3+1 dimensional SU(2) lattice gauge field theory is investigated in the presence of constant external Abelian chromomagnetic field H at finite temperature. The external field corresponds to the third group generator and is directed opposite X axis. Monte-Carlo simulations are performed on the 2×16^3 lattice at $\beta=3$, and various values of flux of the external field. The flux on the lattice is introduced through the so-called "twisted" boundary conditions. These conditions are the modification of the standard periodic boundary conditions and allow introducing an additional flux of the external field. The computations are performed with graphic processing units, the computer program is written in C++ language using OpenCL. It is discovered that in the presence of the external field the Polyakov loop has a non-trivial periodic spatial structure that is in contrast to a rather uniform distribution in the field absence.

Keywords: lattice gauge field theory, chromomagnetic field, "twisted" boundary conditions, Polyakov loop, SU(2) gluodynamics.

В 3+1 SU(2) решёточной калибровочной теории поля при конечной температуре изучается пространственное распределение петли Полякова в присутствии постоянного внешнего абелева хромомангнитного поля H , соответствующего третьему генератору группы и направленного против оси X . Монте-Карло моделирование проводилось на решётке 2×16^3 при $\beta=3$ и при разных значениях потока внешнего поля, который введен на решётку с помощью так называемых «подкрученных» граничных условий. Эти условия являются модификацией стандартных периодических граничных условий, позволяющей ввести на решётку дополнительный поток внешнего поля. Вычисления производились с использованием видеокарт, компьютерная программа написана на языке C++ с использованием OpenCL. Обнаружено, что при наличии внешнего поля распределение петли Полякова имеет нетривиальную периодическую пространственную структуру, в то время как в отсутствие внешнего поля её распределение скорее однородно.

Ключевые слова: решёточная калибровочная теория поля, хромомангнитное поле, «подкрученные» граничные условия, петля Полякова, SU(2)-глюодинамика.

В 3+1 SU(2) гратковій калібрувальній теорії поля при скінченній температурі вивчається просторовий розподіл петлі Полякова при наявності постійного зовнішнього абелевого хромомангнітного поля H , відповідного третьому генератору групи і спрямованого проти осі X . Монте-Карло моделювання проводилося на гратці 2×16^3 при $\beta=3$ і при різних значеннях потоку зовнішнього поля, який був введений за допомогою так званих «підкручених» граничних умов. Ці умови є модифікацією стандартних періодичних граничних умов, яка дозволяє ввести на гратку додатковий потік зовнішнього поля. Розрахунки проводилися за допомогою видеокарт, комп'ютерна програма написана мовою C++ з використанням OpenCL. Виявлено, що за наявності зовнішнього поля розподіл петлі Полякова має нетривіальну періодичну просторову структуру, в той час як за відсутності зовнішнього поля її розподіл скоріш однорідний.

Ключові слова: граткова калібрувальна теорія поля, хромомангнітне поле, «підкручені» граничні умови, петля Полякова, SU(2)-глюодинамика.

Introduction

Interest for studying of quantum phenomena in external magnetic fields is steadily growing. This is stimulated by increasing of experimental data obtained at modern colliders of particles and astrophysics observations (see [1, 2] and Refs therein). Modern experiments demonstrate the importance of accounting for effects related to magnetic fields in different phenomena of high-energy physics. In this regard, it is reasonable to reconsider known quantum effects with taking into account the presence of magnetic fields.

One of such phenomenon is a deconfinement phase transition. The Polyakov loop is the order parameter of it in the $SU(N)$ gauge theories. In continuum limit, it has zero value in confinement and is non-zero in deconfinement phases. The peak of Polyakov loop susceptibility considered as a function of temperature corresponds to the temperature of deconfinement phase transition [3]. The Polyakov loop is sensitive to breaking of $Z(N)$ center subgroup of $SU(N)$ gauge group [3, 4]. It allows for studying the quark-antiquark potential as well as other implicit parameters.

There are several basic approaches to investigate the deconfinement phenomenon. Nowadays, the most popular method is Monte-Carlo (MC) simulations on a lattice. It allows for getting numeric estimates of the quantities studied. In the present paper this method is applied. At zero external fields, the Polyakov loop properties are well investigated in the literature [3-5]. But this is not the case if the field is switched on. Even the influence of the field on the temperature of the phase transition is not settled finally [6].

As shown in literature, the value of the Polyakov loop in $SU(2)$ gauge theory decreases with increasing of the applied external field. This means the increasing of the temperature of deconfinement phase transition with increasing the value of the strength of external field [6]. The opposite behavior is detected in the $SU(3)$ gluodynamics.

The present paper is devoted to investigation of influence of the external Abelian chromomagnetic field on the Polyakov loop. We study the spatial distribution of the Polyakov loop for different values of field strengths at finite temperature. The values of the loop obtained from Monte Carlo simulations are averaged over the plane perpendicular to the external field direction. The distribution of this quantity along the field axis is the main object investigated.

Basic theory

Below, the standard lattice Wilson action for $SU(2)$ lattice gauge theory

$$S_W = \frac{\beta}{2} \sum_{n \in A} \sum_{\mu < \nu} \text{Re Tr} (I - U_{\mu\nu}(n)) \quad (1)$$

is used. Here, $U_{\mu\nu}(n) = U_\mu(n) U_\nu(n + \hat{\mu}) U_\mu^+(n + \hat{\nu}) U_\nu^+(n)$ is a plaquette variable, $\hat{\mu}$ is the unit vector along μ direction, $\mu = \{1, 2, 3, 4\}$, $\mu = 4$ corresponds to the Euclidian time direction, $\beta = 4/g^2$ is the inverse coupling constant, I is the 2×2 unit matrix and summation is performed over all sites of a lattice A and over all directions. Variable U_μ expresses the gauge field on the lattice,

$$U_\mu(x) = e^{i A_\mu(x) a}, \quad (2)$$

where $A_\mu(x)$ is a gauge field potential in continuum theory, a is a lattice spacing.

To introduce the external field, twisted boundary conditions are used [7]. They read

$$U_\mu(n_x, n_y, N_z, n_t) = \Omega U_\mu(n_x, n_y, 0, n_t) \quad (3)$$

$$\Omega = \begin{cases} \text{diag}(e^{i\varphi/2}, e^{-i\varphi/2}), \mu = 2; \\ I, \mu \neq 2, \end{cases} \quad (4)$$

N_z measures a number of lattice sites in z direction; φ is the flux of the external field. This means that the external constant chromomagnetic field is $\vec{H} = (-H, 0, 0)$. If $\varphi = 0$, then these boundary conditions restrict to the usual periodic ones. The connection between flux and field strength is the following

$$H = \frac{\varphi}{a^2}. \quad (5)$$

The relevant quantity, the Polyakov loop, is defined as usually [5]:

$$P(\vec{m}) = \text{Tr} \left[\prod_{j=0}^{N_t-1} U_4(\vec{m}, j) \right], \quad (6)$$

which is discretized version of its definition in continuous theory,

$$P(\vec{x}) = T \exp \left[ig \oint d\tau A_0(\vec{x}, \tau) \right], \quad (7)$$

T denotes time ordering. The equation (6) is a trace of the ordered products of all time-directed links corresponding to the space point \vec{m} . It gives a closed loop due to the periodic boundary conditions in the time direction.

Simulation results

In this investigation the standard MC lattice simulations are performed. To update a lattice the multi-hit heat-bath algorithm is used (the number of hits 10 is taken). Pseudorandom numbers are produced with RANLUX3 generator.

Production of pseudorandom numbers, updates of the lattice and measurements are performed with graphics processing unit (GPU). Averaging over a configuration is also performed with GPU. Averaging over run is performed with central processing unit (CPU). Computer program is written in C++; the GPU kernels are written in Open Computing Language (Open CL). The trivial parallelization is used: all the GPU procedures are performed in parallel, but there is not parallelization between GPUs.

All calculations are carried out with double precision. The simulations are performed with GPUs of HGPU cluster based on nVidia GeForce GTX 560 Ti, AMD Radeon HD 7970 (Tahiti), HD 6970 (Cypress) and HD 5870 (Cayman).

All the simulations are performed on the 2×16^3 lattice at $\beta = 3$ and flux φ up to 0.15. In this case lattice spacing equals to $a = 0.0940246$ fm. The relevant quantity is Polyakov loop for every x coordinate. After 300 thermalization sweeps the measured value is obtained as an average over 500 configurations. Nine bulk sweeps are performed to decorrelate configurations used in measurements. There are up to 18500 runs performed in the presence of chromomagnetic field and up to 46000 ones in the absence of it.

Within one sigma accuracy it is obtained that the Polyakov loop in the presence of non-zero chromomagnetic field has some periodic structure. It can be seen that the field brings a decrease of the variance of the loop. Also, we observed a non-monotonic behavior of the mean value of the loop as function of H .

To investigate the shape of the distribution of the measured quantity the standard χ^2 fit method is used. Every data set is fitted by a straight line corresponding to the mean of these data, by a single sine function and by combinations of two sine functions.

To avoid edge effects in fit, the data are periodically extrapolated from both sides. In fact, three periods along x axis were used in the fit. Fit results are presented in Table 1.

The data in columns are the values of minimal χ^2 corresponding to the four values of φ investigated and to the functions tried. In the gray cells the functions used are placed:

- $f_1(x) = M$, M is the mean value of the Polyakov loop over interval of x ;
- $f_2(x) = M + a \sin\left(2\pi \frac{x}{X} + x_0\right)$;
- $f_3(x) = M + a_1 \sin\left(2\pi \frac{x}{X_1} + x_1\right) + a_2 \sin\left(2\pi \frac{x}{X_2} + x_2\right)$;
- $f_4(x) = f_I(x)\theta(b_1 - x) + f_{II}(x)[1 - \theta(b_1 - x)]\theta(b_2 - x) + f_I(x)[1 - \theta(b_2 - x)]$,
 $f_I(x) = a_1 \sin\left(2\pi \frac{x}{X_1} + x_1\right)$, $f_{II}(x) = a_2 \sin\left(2\pi \frac{x}{X_2} + x_2\right)$,

where $\theta(x)$ is the Heaviside theta-function, $\theta(0) = 1$.

Table 1

The fit results; $\varphi_0 = 0.000591195$

Function	φ			
	0	φ_0	$16\varphi_0$	$256\varphi_0$
f_1	0.1364	11.83	20.31	13.7
f_2	0.08913	8.270	13.42	11.35
f_3	0.06628	5.836	11.13	9.729
f_4	0.07405	2.843	4.616	3.923

The last function means that the period of resulting function is divided by two intervals, and the data in each interval are described by different sine-function; b_1 and b_2 are the points of the connection of these curves. The minimal χ^2 values presented in the Table 1 correspond to the one period of data.

It can be seen from Table 1 that in the field presence the best fit function is the combination of two sine functions in different regions of data. The χ^2 corresponding to this function is in several times less than the one for the case of straight line, so such non-trivial distribution of the Polyakov loop is more preferred than the uniform one. If the external field is absent, the best fit function is superposition of the sine ones. However, for this case all fit functions give almost the same χ^2 because of a high variance, so all of them describe the data almost equally well. The data sets and the corresponding best fits are shown in Fig.1.

The space structure of the Polyakov loop may result in a chromoelectric field in the deconfinement phase. To our knowledge, this interesting phenomenon was not discussed in the literature. It requires further investigations which are out of the scope of the present paper.

Conclusions

In the present paper, a constant chromomagnetic Abelian field is introduced on the lattice through the twisted boundary conditions. The distribution of the Polyakov loop along the field direction is investigated for different values of field flux. It is observed

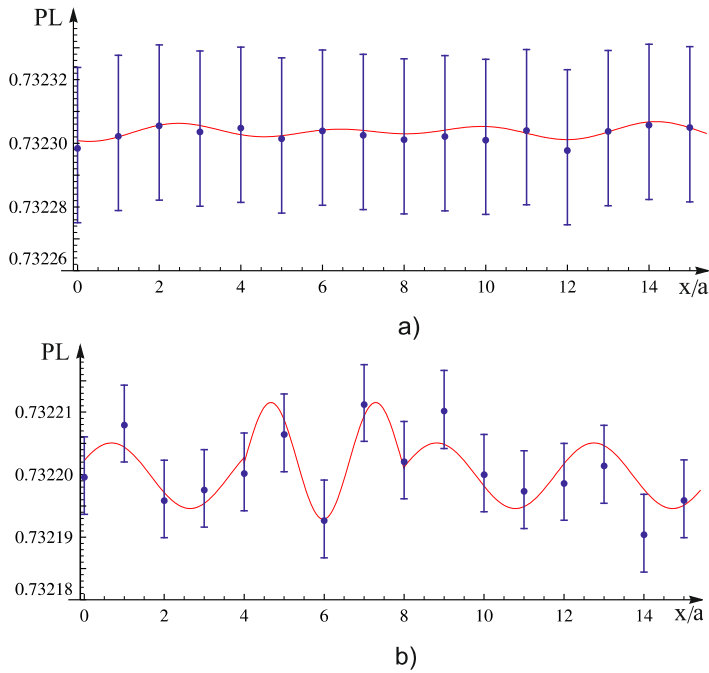


Fig. 1. Data sets for zero and non-zero fluxes and corresponding best fit curves:
 a) $\varphi = 0$ b) $\varphi = 256\varphi_0$. Error bars correspond to the 68% confidence intervals.

that in the field presence the Polyakov loop has a non-linear structure, within one sigma accuracy. If the external field is zero, such structure is not elucidated. The data fit shows that the distribution of the Polyakov loop is preferably described by a combination of two sine functions in two different intervals of data along the axis investigated. This observation is a signal of interesting new features of the deconfinement phase. These will be investigated separately.

References

1. **Fukushima K.** The Chiral Magnetic Effect / K. Fukushima, D. E. Kharzeev, H. J. Warringa // Physical Review D – 2008. – 78. – P. 074033–074046.
2. **Mizher A. J.** Phase diagram of hot QCD in an external magnetic field: possible splitting of deconfinement and chiral transitions / A. J. Mizher, M. N. Chernodub, E. S. Fraga // Phys. Rev. D – 2010. – 82. – P. 105016–105031.
3. **Fukugita M.** Finite size scaling study of the deconfining phase transition in pure SU(3) lattice gauge theory / M. Fukugita, M. Okawa, A. Ukawa // Nuclear Physics B – 1990. – 337. – P. 181–232.
4. **Fortunato S.** Polyakov loop percolation and deconfinement in SU(2) gauge theory / S. Fortunato, H. Satz // Phys. Lett. B – 2000. – 475. – P. 311–314.
5. **Gattringer C.** Quantum Chromodynamics on the Lattice. An Introductory Presentation / C.C. Gattringer, B. Lang // Quantum Chromodynamics on the Lattice. An Introductory Presentation: Berlin Heidelberg.: Springer, – 2010. – 343 p.
6. **Cea P.** Abelian chromomagnetic background field at finite temperature on the lattice/ P. Cea, L. Cosmai // arXiv: hep-lat/0101017v1, – 2001, P. 1–19.
7. **Demchik V.** The Spontaneous Generation of Magnetic Fields at High Temperature in SU(2)-gluodynamics on a Lattice / V. Demchik, V. Skalozub // arXiv: hep-lat/0601035v2, – 2006, P. 1–10.
8. **Meisinger P. N.** The Finite Temperature SU(2) Savvidy Model with a Non-trivial Polyakov Loop/ Meisinger P. N., Ogilvie M. C. // Physical Review D – 2002. – 66. – P. 105006–105036.

Received 13.07.2013.

S.S. Antropov

Oles Honchar Dnipropetrovsk National University

FITTING OF BINDER CUMULANTS IN SU(2) - GLUODYNAMICS

The Binder cumulants are calculated and analyzed in SU(2) lattice gluodynamics. The Binder cumulant is lattice observable quantity, which is constructed out of powers of the Polyakov loop. It describes different aspects of the lattice theories and equals to scaling function in case of SU(2) theory. Such computations become possible due to a technology of calculations on the graphics processing unit (GPU). GPU is used as a computing platform allowing a huge amount of statistical data to be treated over a short period of time. The statistics gathered allows the study of Binder cumulants for a great number of various lattices. Main features of cumulants fitting are described and discussed in detail. The cumulant fitting function is proposed which is based on analysis of obtained data. A few data points (10 up to 20) are sufficient for computation of this function. The important feature of the function constructed is ability to estimate quickly the critical value of the inverse coupling constant β_C on a lattice. The procedure of determination of the intersection point of Binder's cumulants, which should cross in one point, is considered. The updated fitting procedure is proposed for determination of such cumulants. The application of the results is discussed.

Keywords: SU(2) gluodynamics, lattice gauge theory, Monte-Carlo calculations, deconfinement phase transition.

В SU(2) глюодинамике на решетке вычисляются и анализируются кумулянты Биндера. Кумулянт Биндера является наблюдаемой на решетке величиной, которая строится из степеней петли Полякова. Он описывает различные аспекты решеточных теорий и в случае SU(2) теории совпадает с масштабной функцией. Такие расчеты стали возможными благодаря технологии вычислений на графических процессорах. Графических процессоры используются в качестве вычислительной платформы, что позволяет получать большое количество статистических данных за короткий промежуток времени. Собранный статистика делает возможным изучение кумулянтов Биндера на большом количестве различных решеток. Описаны и детально обсуждаются основные особенности фитирования кумулянтов. Опираясь на анализ полученных данных, предложена фитирующая функция для кумулянта. Для вычисления этой функции достаточно несколько точек (от 10 до 20). Важная особенность построенной функции заключается в возможности быстро оценить критические значения обратной константы связи β_C на решетке. Рассмотрена процедура нахождения точки пересечения тех кумулянтов Биндера, которые должны пересекаться в одной точке. Обсуждается применение полученных результатов.

Ключевые слова: SU(2) глюодинамика, калибровочная теория на решетке, Монте-Карло вычисления, фазовый переход к деконфайменту.

У SU(2) глюодинаміці на ґратці обчислюються та аналізуються кумулянти Біндера. Кумулянт Біндера є величиною, що спостерігається на ґратці та яка побудована із ступенів петлі Полякова. Він описує різноманітні аспекти ґраткових теорій та у випадку SU(2) теорії співпадає з масштабною функцією. Такі обчислення стали можливими завдяки технології розрахунків на графічних процесорах. Графічні процесори використовуються у якості обчислювальної платформи, що дозволяє отримувати велику кількість статистичних даних за короткі проміжки часу. Зібрана статистика робить можливим дослідження кумулянтів Біндера на великій кількості різноманітних ґраток. Описані та детально обговорюються основні особливості фітування кумулянтів. Спираючись на аналіз отриманих даних, пропонується фітуюча функція для кумулянтів. Для обчислення цієї функції достатньо декілька точок (від 10 до 20). Важлива особливість запропонованої функції полягає у можливості швидко оцінити критичне значення оберненої константи зв'язку β_C на ґратці. Розглянуто процедуру знаходження точки перетину тих кумулянтів Біндера, які повинні перетинатись у одній точці. Обговорюються застосування отриманих результатів.

Ключові слова: SU(2) глюодинаміка, калібрувальна теорія на ґратці, Монте-Карло розрахунки, фазовий перехід до деконфайменту.

Introduction

The Polyakov loop is quantity of interest in Monte-Carlo (MC) calculations in the lattice gluodynamics. In particular, it was used for calculation of critical indexes in SU(2)-theory [1]. The value of the Polyakov loop is an important order parameter of SU(N)-theories. It reads

$$P = \frac{1}{N_\sigma^3} \sum_{\vec{x}} \frac{1}{2} \text{Tr} \prod_{\tau=1}^{N_\tau} U_{\tau, \vec{x}} \quad (1)$$

where N_σ is the number of lattice sites in each spatial direction, N_τ is the number of lattice sites in the time direction, the summation is assumed over all the spatial coordinates of lattice sites \vec{x} . There are such quantities, which can be constructed out of powers of the Polyakov loop and describe different aspects of the theory. One of them is the Binder cumulant [2]

$$g_4 = \frac{\langle P^4 \rangle}{\langle P^2 \rangle^2} - 3 \quad (2)$$

where brackets $\langle \dots \rangle$ mean the averaging over MC configurations. The particular interest of studying (2) has arisen after ref. [2]. Such cumulant identically coincides with the scaling function of SU(2)-theory [2] and has been used for the critical temperature calculation [3, 4].

In present paper we analyze Binder cumulants. Such cumulants are calculated on various lattices to demonstrate features of fitting of the cumulants.

Lattice computations of the Binder cumulant

The Binder cumulants are investigated in SU(2)-gluodynamics on the lattice. Computer modeling is carried out using Monte-Carlo method. In the MC simulations, we use the hypercubic lattice $N_\tau \times N_\sigma^3$ with hypertorus geometry. The spatial part of the lattice is cubic. The main features of the chosen MC procedure are listed below. We chose the heat-bath as working algorithm in MC procedure. We use standard form of the Wilson action of the SU(2)-lattice gauge theory. We use the thermalization procedure to generate initial conditions for MC calculations. We chose common values for MC parameters: 200 thermalizing sweeps, then 1000 working MC iterations [5, 6]. We set up to 8 MC attempts for MC updating of each of lattice variables [5].

A few words should to say about our computing platform. We use the General Purpose computation on Graphics Processing Units (GPGPU) technology allowing studying large lattices on personal computers. The performance analysis indicates that the GPU-based MC simulation program shows better speed-up factors for big lattices in comparison with the CPU-based one. The GPU vs. CPU (single-thread CPU execution) speed-up factor is above 50 for the majority of lattice geometries and for some lattice sizes can overcome the factor 100 [7]. We use the video controller of the personal computer with GPU manufactured by ATI Company. The programming language is ATI CAL. Because of the features of this language and the GPU architecture we use lattices with even time part and the number of the sites in each of the spatial directions is always multiple of four. Calculations are carried out for lattices with the parameter N_τ , which is varied from 2 up to 16, and parameter N_σ has the values changing from 8 to 32. The number of the fitting points of the dependence of the Binder cumulant g_4 on β is varied for each lattice from 26 to 600.

The result of calculations of (2) is the set of the points. We put the accent on the functional dependence which describes the Binder cumulant both in critical region and beyond. To identify this relationship, it is necessary to apply a fitting procedure. For this procedure we use the step functions. Let us explain, the g_4 cumulant has two horizontal asymptotics, and in the critical area cumulant changes itself step-like. The next function (see Tab. 1) has the smallest parameter χ^2 and the best fits for the dependence $g_4(\beta)$ in the critical and beyond critical areas reads

$$g_4(\beta) = A_1 + \frac{A_2 - A_1}{1 + 10^{(\beta_0 - \beta) \times p}} \quad (3)$$

where A_1, A_2, β_0, p are the fitting parameters. The results of the fitting of the function (3) are given in the Fig. 1 and on the Tab. 2.

Table 1

Tested fitting curves	
Function	Parameters
$A_1 + \frac{A_2 - A_1}{1 + 10^{(\beta_0 - \beta) \times p}}$	A_1, A_2, β_0, p
$\frac{A_1 - A_2}{1 + \left(\frac{\beta}{\beta_0}\right)^p} + A_2$	A_1, A_2, β_0, p
$\frac{A_1 - A_2}{1 + e^{(\beta - \beta_0)/p}} + A_2$	A_1, A_2, β_0, p

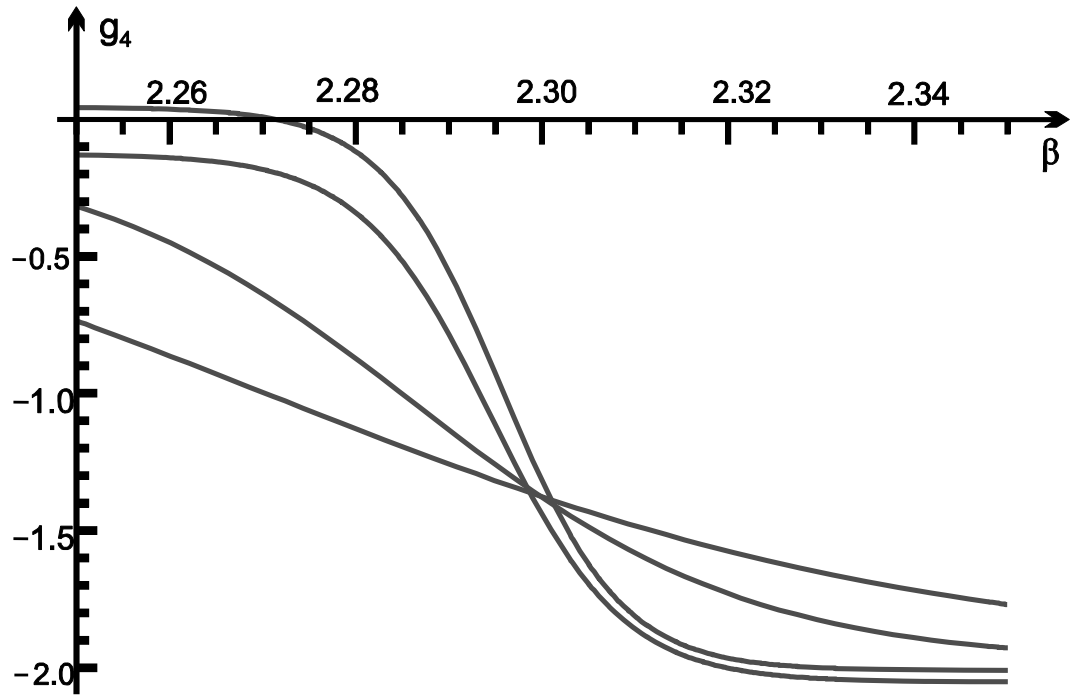


Figure 1. Binder cumulants. The cumulants are calculated on lattices with $N_\tau = 4$ and $N_\sigma = 8, 12, 24, 28$. The higher number of nodes in the lattice corresponds with the sharper step.

Table 2

Fitting of Binder cumulants by $A_1 + \frac{A_2 - A_1}{1 + 10^{(\beta_0 - \beta) \times p}}$

Lattice	Parameters					Number of points	Fitting range	
	χ^2	A_1	A_2	β_0	p		β_{\min}	β_{\max}
$N_\tau = 2, N_\sigma = 8$	0.006	-2	-0.13	1.86	-18	126	1.7	2.95
$N_\tau = 2, N_\sigma = 12$	0.013	-2	-0.08	1.86	-34	126	1.7	2.95
$N_\tau = 2, N_\sigma = 16$	0.013	-2	-0.16	1.87	-43	126	1.7	2.95
$N_\tau = 2, N_\sigma = 20$	0.015	-2	-0.11	1.87	-81	126	1.7	2.95
$N_\tau = 2, N_\sigma = 24$	0.015	-2	-0.28	1.87	-117	126	1.7	2.95
$N_\tau = 2, N_\sigma = 28$	0.008	-2	-0.03	1.87	-77	123	1.7	2.95
$N_\tau = 2, N_\sigma = 32$	0.006	-2	0.14	1.86	-63	124	1.7	2.95
$N_\tau = 4, N_\sigma = 8$	0.009	-1.953	-0.0523	2.2705	-12	126	1.7	2.95
$N_\tau = 4, N_\sigma = 8$	0.012	-1.957	-0.0507	2.2747	-11	26	1.7	2.95
$N_\tau = 4, N_\sigma = 12$	0.025	-1.98	-0.1	2.286	-24	253	1.7	2.95
$N_\tau = 4, N_\sigma = 12$	0.011	-2	-0.04	2.289	-16	26	1.7	2.95
$N_\tau = 4, N_\sigma = 16$	0.029	-2.01	-0.066	2.287	-30.1	236	1.7	2.95
$N_\tau = 4, N_\sigma = 16$	0.013	-1.99	-0.05	2.292	-30.9	26	1.7	2.95
$N_\tau = 4, N_\sigma = 20$	0.055	-2	-0.065	2.291	-48	246	1.7	2.95
$N_\tau = 4, N_\sigma = 24$	0.1	-2.0098	0.044	2.296	-68	126	1.7	2.95
$N_\tau = 4, N_\sigma = 24$	0.006	-2.001	0.061	2.291	-27	26	1.7	2.95
$N_\tau = 4, N_\sigma = 28$	0.089	-2.05	-0.13	2.29	-62	626	1.7	2.95
$N_\tau = 4, N_\sigma = 28$	0.012	-1.99	$-8 \cdot 10^{-5}$	2.28	-21	26	1.7	2.95
$N_\tau = 4, N_\sigma = 32$	0.12	-1.984	-0.2	2.3	-84	626	1.7	2.95
$N_\tau = 4, N_\sigma = 32$	0.01	-1.988	0.014	2.27	-28	26	1.7	2.95
$N_\tau = 4, N_\sigma = 36$	0.19	-2	-0.27	2.3	-105	600	2.28	2.31
$N_\tau = 6, N_\sigma = 8$	0.014	-1.65	-0.067	2.4	-10.5	127	1.7	2.95
$N_\tau = 6, N_\sigma = 12$	0.025	-1.9	0.05	2.4	-17	127	1.7	2.95
$N_\tau = 6, N_\sigma = 16$	0.032	-2	-0.04	2.4	-17	127	1.7	2.95
$N_\tau = 6, N_\sigma = 20$	0.092	-2	-0.02	2.4	-44	126	1.7	2.95
$N_\tau = 6, N_\sigma = 24$	0.14	-2	-0.04	2.4	-37	127	1.7	2.95
$N_\tau = 6, N_\sigma = 28$	0.2	-2	-0.1	2.4	-41	127	1.7	2.95
$N_\tau = 6, N_\sigma = 32$	0.04	-2	$7 \cdot 10^{-4}$	2.4	-200	26	1.7	2.95
$N_\tau = 8, N_\sigma = 12$	0.023	-1.8	-0.07	2.48	-11	126	1.7	2.95
$N_\tau = 8, N_\sigma = 16$	0.05	-1.9	0.005	2.49	-13	126	1.7	2.95
$N_\tau = 8, N_\sigma = 20$	0.06	-2	$5 \cdot 10^{-4}$	2.48	-13	126	1.7	2.95
$N_\tau = 8, N_\sigma = 24$	0.14	-2	-0.0014	2.5	-34	127	1.7	2.95
$N_\tau = 8, N_\sigma = 28$	0.022	-1.9	-0.06	2.49	-26	26	1.7	2.95
$N_\tau = 8, N_\sigma = 32$	0.0115	-2	-0.02	2.48	-15	26	1.7	2.95
$N_\tau = 16, N_\sigma = 20$	0.094	-1.17	-0.017	2.68	-7	126	1.7	2.95
$N_\tau = 16, N_\sigma = 24$	0.054	-1.7	0.04	2.75	-6	26	1.7	2.95
$N_\tau = 16, N_\sigma = 28$	0.021	-1.6	-0.017	2.67	-17	26	1.7	2.95
$N_\tau = 16, N_\sigma = 32$	0.021	-1.7	0.03	2.69	-23	126	1.7	2.95

If one knows the dependencies (3) for various lattices, it is easy to find the critical value of the inverse critical coupling constant β_C [3, 4]. If one fixes a number of lattice sites in the time direction N_τ and changes a number of sites in spatial directions N_σ , then the curves of the dependencies $g_4(\beta)$ will intersect each other in one point [8, 9]. The value of β in this point is a critical value for the lattice with $N_\tau = const$ and $N_\sigma \rightarrow \infty$. As shown above, the result of MC calculations of g_4 is the set of points; therefore one should fit data to find an intersection point of the cumulants. To locate this intersection point we use data from Tab. 3. The detailed procedure of the calculation of intersection point is described below. Values of the β_C received for various lattices are gathered in Tab. 4. For example, the following values of β_C was calculated in Ref. [3]: $1.8800(30)_{N_\tau=2}$, $2.2986(6)_{N_\tau=4}$, $2.4265(30)_{N_\tau=6}$, $2.5115(40)_{N_\tau=8}$; the next values was calculated in Ref. [4]: $1.87380(3)_{N_\tau=2}$, $2.29850(6)_{N_\tau=4}$, $2.51098(58)_{N_\tau=8}$. Listed values of β_C are in good agreement with our data (Tab. 4).

Let us consider the properties of the curve (3). First, as it seen from Tab. 2, the parameters of the curve based on the 600 data points, are merely the same as parameters of the curve based on the 25 data points. It leads to an important consequence: to estimate the parameters of a curve there is no need to perform the long MC calculation. Second, the parameter β_0 coincides (to within 2 up to 3 digits) with an inverse critical coupling constant β_C for a corresponding lattice. Using combination of both properties it is possible to estimate quickly a value of β_C on a lattice with any geometry $N_\tau \times N_\sigma^3$.

It is often necessary to construct and analyze a quantity which depends on Binder cumulants $g_4(\beta, N_\tau, N_\sigma)$ which is calculated using different N_τ and N_σ . Beta-function [10] is an example of such quantity. For lattices with identical values of N_τ the Binder cumulants should intersect in one point [8, 9] and beta-functions should self-intersect in a corresponding point. From Fig. 1, any three of curves do not cross in one point. Moreover, the position and the shape of curves are random variables which depend on a choice of a fitting interval, and also depend on the data amount. The interest causes studying of beta-function in the critical area. In this area the beta-function distorts mostly. This distortion appears due to many points of the cumulants intersections. In practice, applying fitting procedure to the sets of data from different lattices, one won't receive the set of cumulants, crossed in a point.

One needs to update the fitting procedure in such manner that required cumulants cross in one point. This is very similar to a problem of calculation of inverse critical coupling on a lattice. Considered problem is not trivial because of the condition, which is imposed on the curves during fitting.

It is possible to simplify fitting procedure of cumulants g_4 , making changes into initial objective: we will search only for a point of cumulants crossing. The easiest way to demonstrate the given approach is to fit data by straight lines. As it is known, Binder cumulants are linear near critical region [8, 9]. We compute such lines for the data from critical regions of different lattices. Fitting results are in Tab.3. From this, we calculate coordinates of all possible points of crossing of the straight lines and calculate mean deviations for such coordinates. Received coordinates are the random values of the fitting interval and lattice data. And next, we find a point of the intersection of the cumulants as weighted average of coordinates considered (Tab. 4).

Table 3

Fitting of Binder cumulants by straight lines $a\beta + b$

Lattice	Parameters			Number of points	Fitting range	
	χ^2	a	b		β_{\min}	β_{\max}
$N_\tau = 2, N_\sigma = 8$	0.007	-14	25	100	1.875	1.885
$N_\tau = 2, N_\sigma = 12$	0.013	-30	56	100	1.875	1.885
$N_\tau = 2, N_\sigma = 16$	0.016	-33	61	100	1.875	1.885
$N_\tau = 2, N_\sigma = 20$	0.018	-43	79	100	1.875	1.885
$N_\tau = 2, N_\sigma = 24$	0.019	-53	98	81	1.875	1.883
$N_\tau = 2, N_\sigma = 28$	0.014	-39	71	61	1.875	1.881
$N_\tau = 2, N_\sigma = 32$	0.012	-33	61	71	1.875	1.882
$N_\tau = 4, N_\sigma = 8$	0.0087	-13	29	100	2.295	2.305
$N_\tau = 4, N_\sigma = 12$	0.035	-21	47	207	2.295	2.35
$N_\tau = 4, N_\sigma = 16$	0.038	-25	55	191	2.295	2.33
$N_\tau = 4, N_\sigma = 20$	0.083	-32	71	191	2.295	2.32
$N_\tau = 4, N_\sigma = 24$	0.13	-72	165	100	2.295	2.305
$N_\tau = 4, N_\sigma = 28$	0.11	-48.7	110.6	541	2.295	2.314
$N_\tau = 4, N_\sigma = 32$	0.16	-49	111.3	541	2.2997	2.314
$N_\tau = 4, N_\sigma = 36$	0.2	-65	147	600	2.28	2.30995
$N_\tau = 6, N_\sigma = 8$	0.012	-4.1	8.7	101	2.422	2.432
$N_\tau = 6, N_\sigma = 12$	0.023	-4.05	8.4	101	2.422	2.432
$N_\tau = 6, N_\sigma = 16$	0.035	-15	35	101	2.422	2.432
$N_\tau = 6, N_\sigma = 20$	0.11	-47	113	101	2.422	2.432
$N_\tau = 6, N_\sigma = 24$	0.17	-48	116	101	2.422	2.432
$N_\tau = 6, N_\sigma = 28$	0.25	-44	106	101	2.422	2.432
$N_\tau = 8, N_\sigma = 12$	0.024	-6.5	15	100	2.507	2.5169
$N_\tau = 8, N_\sigma = 16$	0.061	-11	26	100	2.507	2.5169
$N_\tau = 8, N_\sigma = 20$	0.071	-20	48	100	2.507	2.5169
$N_\tau = 8, N_\sigma = 24$	0.16	-35	87	100	2.507	2.5169

Table 4

Critical values of the inverse coupling constant and values of Binder cumulant in the critical point

N_τ	2	4	6	8
β_C	1.875	2.301	2.422	2.508
$g_4(\beta_C)$	-1.54	-1.5	-1.23	-1.27

It is easy to change fitting procedure using Tab. 4, so that appropriate cumulants will cross in one point. We impose the condition on the Eq. (3) that this curve should pass through the point with fixed coordinates (Tab. 4). Thus, one parameter of the curve (3) is excluded. We choose to exclude A_2 , so the modified equation (3) for lattices with $N_\tau = 4$ looks:

$$g_4(\beta) = A_1 - \frac{(A_1 + 1.40864) \times (1 + 10^{(\beta_0 - 2.30086) \times p})}{1 + 10^{(\beta_0 - \beta) \times p}}. \quad (4)$$

The fitting procedure of data by the modified curves (3) leads to convergence yet not always. The convergence depends on the excluded parameter and on the software chosen for fitting. It can be complicated to adopt this software for any given relation. Therefore, it is more usual to exclude some another parameter of (3).

Conclusions

Our calculations became possible due to technology of GPU computations. It is necessary to notice that usage of GPU during lattice calculations makes possible to gather a huge amount of the statistical data that allows studying of the Binder cumulants for a great number of various lattices.

We have performed high-statistics calculations of the Binder cumulant in SU(2) lattice gluodynamics. It is important that the gathered statistics allow us to construct and analyze the Binder cumulants. Based on such analysis we propose the function for fitting of cumulants. A few points of data (10 up to 20) are sufficient for computation of this function. The remarkable feature of the function offered is ability to estimate quickly the critical value of the inverse coupling constant β_c . The values of β_c calculated are in good agreement with the values known in the literature [3, 4].

The procedure of determination of the intersection point of the Binder cumulants, which are computed on lattices with different numbers of spatial sites and equal numbers of time sites, is considered. The updated fitting procedure for determination of cumulants, which are crossed in one point, is proposed.

Acknowledgments

We would like to thank to our supervisor of this project, prof. V.V. Skalozub, for the valuable guidance and advice.

References

1. **Engels J.** Critical behavior of SU(2) lattice gauge theory: A Complete analysis with the χ^2 -method / J. Engels, S. Mashkevich, T. Scheideler, G. Zinovev // Phys. Lett. – 1996. – B 365. – P. 219. – [hep-lat/9509091].
2. **Binder K.** Critical Properties from Monte Carlo Coarse Graining and Renormalization / K. Binder // Phys. Rev. Lett. – 1981. – 47. – 693 p.
3. **Fingberg J.** Scaling and asymptotic scaling in the SU(2) gauge theory / J. Fingberg, U. M. Heller, F. Karsch // Nucl. Phys. – 1993. – B 392. – P. 493. – [hep-lat/9208012].
4. **Velytsky A.** Finite temperature SU(2) gauge theory: Critical coupling and universality class / A. Velytsky // Int. J. Mod. Phys. – 2008. – C 19. – 1079 p. – arXiv:0711.0748 [hep-lat].
5. **Creutz M.** Overrelaxation And Monte Carlo Simulation / M. Creutz // Phys. Rev. D – 1987. – V.36. – P. 515.
6. **Ilgenfritz E. M.** First Evidence for the Existence of Instantons in the Quantized SU(2) Lattice Vacuum / E. M. Ilgenfritz, M. L. Laursen, G. Schierholz, M. Muller-Preussker, H. Schiller // Nucl. Phys. – 1986. – B 268. – 693 p.
7. **Demchik V.** Monte Carlo simulations on Graphics Processing Units / V. Demchik, A. Strelchenko // arXiv:0903.3053 [hep-lat] – 2009.
8. **Binder K.** Finite size scaling analysis of Ising model block distribution functions / K. Binder // Z. Phys. – 1981. – B 43. – 119 p.
9. **Binder K.** Monte Carlo tests of renormalization group predictions for critical phenomena in Ising models / K. Binder, E. Luijten // Phys. Rept. – 2001. – 344. – 179 p.
10. **Antropov S. S.** Behavior of beta-function in the SU(2) lattice thermodynamics / S. S. Antropov, O. A. Mogilevsky, V. V. Skalozub // Phys. Atom. Nucl. – 2014. – V. 77. – *in print*.

Received 13.07.2013.

UDC 530.1

M. P. Korkina, O. O. Iegurnov

Oles Honchar Dnipropetrovsk National University

MATCHING OF STEPHANI AND DE SITTER SOLUTIONS ON THE HYPERSURFACE OF CONSTANT TIME

The spherically symmetric solution for perfect fluid with homogeneous energy density and inhomogeneous pressure is considered. This solution is known as Stephani solution. It is reobtained by a mass-function method. Also, the meaning of arbitrary functions which are present in the solution is discussed. The matching of this solution and the de Sitter is done on a hypersurface of constant time. The matching is done with the Lichnerowicz – Darmois conditions. The coordinates of the de Sitter solution are taken in a general form as arbitrary functions that depend on Stephani's time and the radial coordinate. The matching is done both for the special cases of the flat, open, and closed Universe and for the general case, which does not concretize the type of curvature. The equality of energy densities and the abrupt change of pressure are observed on the matching hypersurface. Also, restrictions for arbitrary functions (coordinates of de Sitter solution) are found.

Keywords: perfect fluid, Stephani solution, de Sitter solution, Lichnerowicz - Darmois conditions.

Рассматривается сферически симметричное решение для идеальной жидкости с однородной плотностью энергии и неоднородным давлением. Это решение – известное решение Стефани. Это решение получается повторно с помощью метода массовой функции. Обсуждается смысл произвольных функций, которые присутствуют в решении. Сшивка этого решения с решением де Ситтера выполняется по гиперповерхности постоянного времени. Сшивка производится с помощью условий Лихнеровича-Дармуа. Координаты решения де Ситтера выбираются в общем виде, как произвольные функции от координаты времени и пространственной радиальной координаты решения Стефани. Сшивка выполняется для частных случаев плоской, закрытой, открытой Вселенной и для общего случая, в котором не конкретизируется кривизна. На гиперповерхности сшивки наблюдаются равенство плотностей энергий и скачок давления. Устанавливаются ограничения на произвольные функции – координаты решения де Ситтера.

Ключевые слова: идеальная жидкость, решение Стефани, решение де Ситтера, условия Лихнеровича – Дармуа.

Розглядається сферично симетричний розв'язок для ідеальної рідини з однорідною густиною енергії та неоднорідним тиском. Цей розв'язок - відомий розв'язок Стефані. Цей розв'язок встановлюється повторно за допомогою метода масової функції. Обговорюється значення довільних функцій, які присутні у розв'язку. Зшивка цього розв'язку з розв'язком де Сіттера здійснюється на гіперповерхні постійного часу. Зшивка здійснюється за допомогою умов Ліхнеровича-Дармуа. Координати для розв'язку де Сіттера обираються у загальному вигляді, як довільні функції від координати часу та просторової радіальної координати розв'язку Стефані. Зшивка здійснюється для окремих випадків плоского, закритого і відкритого Всесвіту та для загального випадку, у якому не конкретизується кривизна. На гіперповерхні зшивки спостерігаються рівність густин енергій та стрибок тиску. Встановлюються обмеження на довільні функції – координати розв'язку де Сіттера.

Ключові слова: ідеальна рідина, розв'язок Стефані, розв'язок де Сіттера, умови Ліхнеровича – Дармуа.

Introduction

The most general class of non-static, perfect fluid solutions of Einstein's equations that are conformally flat is known as the "Stephani Universe" [1-5]. The spherically symmetric Stephani solution has been examined in numerous papers. A comprehensive review is presented in [5]. There are many papers devoted to applying this solution as star models, as generalization of the FLRW, and as a cosmological model [5-7]. In our opinion, this solution is attractive for the cosmological model for many reasons. Firstly, it is shear-free and inhomogeneous. The absence of a shear makes it simple for the cosmological purpose. The assumption of homogeneity is just a first approximation introduced to simplify Einstein's equations. So far this assumption has worked well, but future and modern observations can not be precise without taking into account inhomogeneity. And due to the fact, that modern and future observation data become more and more precise and that the smallest deviations from the standard model can be detected with high level of accuracy soon, makes inhomogeneous models actual. Secondly, Stephani solution has a general form in contrast to the FLRW solution where three solutions (flat, open, closed), non-transforming into each other, exist. Thirdly, the spatial curvature of this solution depends on time only via an arbitrary function, this fact is discussed in [3, 8].

The physical interpretation of the Stephani Universe is obscure. It is due to the many arbitrary functions and peculiar inhomogeneity – inhomogeneity is contained in pressure (depends on time and spatial coordinates), but density is homogeneous (depends on time only). It needs matching in order to determine some arbitrary functions. May be the main reason to use this solution in cosmological modeling is the fact that it is the generalization of the FLRW solution and, in our opinion, investigation of a more general solution is promising. The solution generalizes not only the FLRW but also the de Sitter solution [3]. In this connection, the idea to examine the Stephani solution on the de Sitter background looks reasonable.

In the first part of the article the solution for perfect fluid with inhomogeneous pressure (the Stephani solution) is reobtained with the mass-function method [9-12]. Some properties of it are discussed. In particular, we discuss a sense of the arbitrary functions and transformation to the FLRW and to the de Sitter solutions.

In the second part, the matching of de Sitter and Stephani solutions on the hypersurface of constant time is done. The Lichnerowicz – Darmois conditions were used. Some consequences of the matching are discussed.

Mass-function method

The mass-function method essentially simplifies the appearance of the Einstein equations in contrast to the standard one; it makes them easier for work. The mass-function was introduced in [9] and discussed in [10-12]. As shown in [9], the mass-function is invariant and in our consideration may be determined as full energy limited by some hypersurface of constant time and coordinates. For a spherically symmetric metric:

$$dS^2 = e^{\nu(R,t)} dt^2 - e^{\lambda(R,t)} dR^2 - r^2(R,t) d\sigma^2, \quad (1)$$

where $d\sigma^2 = d\theta^2 - \sin^2(\theta)d\phi^2$, the mass-function $m(R, t)$ is:

$$m(R, t) = r(R, t)(1 + e^\Phi - e^\Omega), \quad (2)$$

$$e^\Phi = e^{-\nu} \dot{r}^2(R, t), \quad e^\Omega = e^{-\lambda} r'^2(R, t), \quad (3)$$

where $\dot{r}(R, t) = \frac{\partial r(R, t)}{\partial t}$, $r'(R, t) = \frac{\partial r(R, t)}{\partial R}$.

Einstein's equations with the mass-function have the form:

$$\begin{cases} m' = r^2 r' T_0^0, \\ \dot{m} = r^2 \dot{r} T_1^1, \\ 2\dot{m}' = \dot{m}\Phi' + m'\dot{\Omega} + 4r\dot{r}r'T_2^2, \\ 2\dot{r}' = \dot{r}\Phi' + r'\dot{\Omega}. \end{cases} \quad (4)$$

Obtaining the Stephani solution

This solution was first found by Stephani [13] as a special example of a space-time embeddable in a flat five-dimensional space, and later reobtained by Krasinski [2]. We reobtained this solution with mass-function method.

The Stephani solution is an isotropic solution for perfect fluid with homogeneous density $\rho = \rho(t)$ and inhomogeneous pressure $p = p(R, t)$ (in spherically symmetric consideration). The stress-energy tensor for such perfect fluid is: $T_0^0 = \rho(t)$, $T_1^1 = T_2^2 = T_3^3 = -p(R, t)$. The Einstein field equations become

$$\begin{cases} m' = r^2 r' \rho, \\ \dot{m} = -r^2 \dot{r} p, \\ 2\dot{m}' = \dot{m}\Phi' + m'\dot{\Omega} - 4r\dot{r}r'p, \\ 2\dot{r}' = \dot{r}\Phi' + r'\dot{\Omega}. \end{cases} \quad (5)$$

Expressing the mass-function from the first equation of the set and substituting it into the third one gives

$$\frac{\dot{\rho}}{\rho} \left(\frac{1}{3} r \Phi' + \frac{4}{3} r' - 2r' \right) = 0, \quad (6)$$

from this equation the expression for Φ is obtained,

$$\Phi = \ln r^2 \psi^2, \quad (7)$$

where $\psi = \psi(t)$ is an arbitrary function of integration.

The fourth equation of the set (5) gives us the expression for Ω :

$$\Omega = \ln \frac{r'^2}{r^2 k'^2}, \quad (8)$$

where $k = k(R)$ - arbitrary function (prime is used for convenience).

From Eqs. (1) and (3) the metric is obtained,

$$dS^2 = \frac{\dot{r}^2}{r^2 \psi^2} dt^2 - r^2 (k'^2 dR^2 + d\sigma^2). \quad (9)$$

With the expressions (7) and (8) the mass-function is obtained:

$$m = r \left(1 + r^2 \psi^2 - \frac{r'^2}{r^2 k'^2} \right). \quad (10)$$

The expression (10) with the first equation of (1.5) gives us

$$\rho \frac{r^3}{3} = r + r^3 \psi^2 - \frac{r'^2}{r k'^2}. \quad (11)$$

It is integrated in elementary functions providing the expression for $r = r(R, t)$

$$r(R, t) = 2(e^{k(R)+\eta(t)} - \zeta(t)e^{-k(R)-\eta(t)})^{-1}, \quad (12)$$

$$\zeta(t) = \psi^2(t) - \frac{1}{3}\rho(t), \quad (13)$$

and $\eta(t)$ is an arbitrary function of integration.

Depending on the sign of $\zeta(t)$, the expression (12) gives

$$\begin{aligned} r^{-1} &= \sqrt{\zeta} \cdot \sinh(k + \alpha), \quad \zeta > 0, \\ r^{-1} &= \sqrt{|\zeta|} \cdot \cosh(k + \alpha), \quad \zeta < 0, \\ r^{-1} &= e^{k+\alpha}, \quad \zeta = 0, \end{aligned} \quad (14)$$

where $e^\alpha = \sqrt{|\zeta|} \cdot e^\alpha$.

In contrast to the FLRW solution where there are three non-transforming into each other solutions (flat, closed, open), there is the general solution here with flat, open, closed solutions as special cases. The existence of this solution shows that the distinction between the closed and open Universe is not required by Einstein's theory of gravitation as such, but is due to the very strong symmetry assumptions that are set into the models just from the beginning. From (5) it is also possible to obtain the equation that links density and pressure:

$$p(R, t) = -\rho(t) - \frac{\dot{\rho}}{3} \frac{r(R, t)}{\dot{r}(R, t)}. \quad (15)$$

The FLRW and de Sitter solutions as special cases of the Stephani solution

The Stephani solution, as mentioned above, is a generalization of the FLRW solution and the de Sitter one. When $\zeta(t) = 0$, the Stephani solution is transformed to the flat FLRW solution. If $\zeta(t) \neq 0$, the transformation occurs in such a way

$$\begin{aligned} \dot{\eta}(t) &= 0, \quad \psi(t) = \frac{\dot{a}(t)}{a(t)}, \\ \zeta(t) &= -\frac{1}{a^2(t)} : k(R) = \ln \cot \frac{R}{2}, \\ \zeta(t) &= \frac{1}{a^2(t)} : k(R) = \ln \coth \frac{R}{2}. \end{aligned} \quad (16)$$

The density in the de Sitter solution is $\rho = \frac{1}{a_\lambda^2} = const$. It can be obtained from Eqs. (13, 16):

$$\begin{aligned} \zeta(t) = 0 &: a(t) = e^{\frac{t}{a_\lambda}}, \\ \zeta(t) = -\frac{1}{a^2(t)} &: a(t) = a_\lambda \cosh \frac{t}{a_\lambda}, \\ \zeta(t) = \frac{1}{a^2(t)} &: a(t) = a_\lambda \sinh \frac{t}{a_\lambda}. \end{aligned} \quad (17)$$

Arbitrary functions and their meaning

The Stephani solution contains four arbitrary functions: $k(R)$, $\zeta(t)$, $\psi(t)$, $\eta(t)$. Also in our consideration, we do not set the equation of state, i.e. $\rho(t)$ is undefined. The determination of arbitrary functions may be proving to be elusive. It is true, but our analysis of the solution (9) shows that it is possible to understand their meaning.

The function $k(R)$ may be chosen arbitrary because it leads to a transition to another coordinate system, only. The part $\left(\frac{dk}{dR}\right)^2 dR^2 = dk^2$ in the expression (9) is just a transformation from R to k . The coordinate transformation may be chosen in such a way that the spatial part of the solution (9) is conformal to one of three homogeneous and isotropic spaces,

$$\begin{aligned} dk^2 + d\sigma^2 &= \frac{1}{\sinh^2(R_1)} (dR_1^2 + \sinh^2(R_1) d\sigma^2) = \\ &= \frac{1}{\sin^2(R_2)} (dR_2^2 + \sin^2(R_2) d\sigma^2) = \frac{1}{R_3^2} (dR_3^2 + R_3^2 d\sigma^2). \end{aligned} \quad (18)$$

Chosen $\eta(t)$ is also referring to the coordinate transformation. Thus Eq. (9) takes the form

$$dS^2 = \frac{r_\eta^2}{r^2 \psi^2} d\eta^2 - r^2 (k'^2 dR^2 + d\sigma^2) \quad (19)$$

where $r_\eta = \frac{\partial r}{\partial \eta}$.

The analysis of invariants of the spatial curvature tensor of the metric (9) shows that the invariants depend on the arbitrary function $\zeta(t)$, only. The scalar curvature tensor and the Kretschmann scalar, for example, are

$$\begin{aligned} R &= 6\zeta(t), \\ R_{\mu\nu\lambda\sigma} R^{\mu\nu\lambda\sigma} &= 12\zeta^2(t). \end{aligned} \quad (20)$$

Thereby spatial curvature depends on $\zeta(t)$ only. The type of space (flat, open, closed) is determined by the sign of $\zeta(t)$. So it is possible to assume that $\zeta(t)$ completely determines spatial curvature. This fact is also discussed in [3, 8].

Thus, $\psi(t)$ obtains the meaning of critical energy density. When spatial curvature is zero, then $\zeta(t) = 0$ and from Eq. (13) we have

$$\psi^2(t) = \frac{1}{3} \rho_c(t). \quad (21)$$

Lichnerowicz - Darmois conditions

The Lichnerowicz-Darmois matching conditions [14] are two metrics

$$\begin{aligned} dS_1^2 &= g_{\mu'\nu'} dx^{\mu'} dx^{\nu'}, \\ dS_2^2 &= g_{\mu\nu} dx^\mu dx^\nu, \end{aligned} \quad (22)$$

and are said to match across some hypersurface if first and second fundamental forms of this hypersurface are identical for the two metrics.

The first fundamental form is

$$dl_1^2 = a_{ik} du^i du^k \quad (i, k = 1, 2, 3), \quad (23)$$

where $a_{ik} = g_{\mu\nu} \xi_i^\mu \xi_k^\nu$, $\xi_i^\mu = \frac{\partial x^\mu}{\partial x^i}$.

The second fundamental form is

$$dl_2^2 = b_{ik} du^i du^k, \quad (24)$$

where $b_{ik} = \nu_{\mu;V} \xi_i^\mu \xi_k^\nu$, ξ_i^μ are tangent vectors to the hypersurface and ν^μ are normal vectors.

Matching Stephani and de Sitter solutions in general case

The matching has been done on the hypersurface of Stephani's constant time. Time and spatial coordinate of the de Sitter solution were chosen as arbitrary functions of the Stephani time and the radial coordinate. Both metrics have been taken in the general form without more precise definition of their curvature.

The Stephani metric, as mentioned above, is

$$dS_{st}^2 = \frac{\dot{r}^2}{r^2 \psi^2} d\tau^2 - r^2 (dk^2 + d\sigma^2), \quad (25)$$

where $r = r(k, \tau)$, $\psi = \psi(\tau)$, $\dot{r} = \frac{\partial r}{\partial \tau}$.

The matching is performed on the hypersurface $\tau = const.$ ξ_i^μ on this hypersurface is

$$\xi_i^\mu = \begin{pmatrix} 0 & 0 & 0 & 0 \\ 0 & 1 & 0 & 0 \\ 0 & 0 & 1 & 0 \\ 0 & 0 & 0 & 1 \end{pmatrix}. \quad (26)$$

Normal vectors are found from the equation

$$\begin{cases} \nu_\mu \nu^\mu = 1, \\ \nu_\mu \xi_i^\mu = 0. \end{cases} \quad (27)$$

The normal vector has only non-zero component

$$\nu_0 = \frac{\dot{r}}{r\psi}. \quad (28)$$

First and second fundamental forms for the Stephani solution are

$$dl_{st1}^2 = r^2 dk^2 + r^2 d\sigma^2, \quad (29)$$

$$dl_{st2}^2 = r^2 \psi dk^2 + r^2 \psi d\sigma^2. \quad (30)$$

The de Sitter metric is

$$dS_{ds}^2 = \left(1 - \frac{r_s^2}{a_\lambda^2}\right) dt^2 - \frac{1}{1 - \frac{r_s^2}{a_\lambda^2}} dr_s^2 - r_s^2 d\sigma^2, \quad (31)$$

$r_s = r_s(k, \tau)$, $t = t(k, \tau)$, $a_\lambda = \sqrt{\frac{3}{\Lambda}}$, and Λ is cosmological constant. We do the same manipulations with the de Sitter metric

$$\xi_i^\mu = \begin{pmatrix} 0 & t' & 0 & 0 \\ 0 & r_s' & 0 & 0 \\ 0 & 0 & 1 & 0 \\ 0 & 0 & 0 & 1 \end{pmatrix}. \quad (32)$$

According to Eq. (27) we have

$$v_0 = \frac{r_s'}{\sqrt{A^{-1}r_s'^2 - At'^2}}, \quad (33)$$

$$v_1 = \frac{t'}{\sqrt{A^{-1}r_s'^2 - At'^2}}. \quad (34)$$

where primes denote derivatives for k , $A = 1 - \frac{r_s^2}{a_\lambda^2}$.

The first and the second fundamental forms for the de Sitter solution are

$$dl_{ds1}^2 = (A^{-1}r_s'^2 - At'^2)dk^2 + r_s^2 d\sigma^2, \quad (35)$$

$$dl_{ds2}^2 = \frac{r_s t' (t'^2 A - 3r_s'^2 A^{-1})}{a_\lambda^2 \sqrt{A^{-1}r_s'^2 - At'^2}} dk^2 + \frac{r_s A t'}{\sqrt{A^{-1}r_s'^2 - At'^2}} d\sigma^2. \quad (36)$$

From the equality of the first and second fundamental forms the following equations can be obtained

$$r^2 = r_s^2, \quad (37)$$

$$r^2 = A^{-1}r_s'^2 - At'^2, \quad (38)$$

$$r^2 \psi = \frac{r_s t' (t'^2 A - 3r_s'^2 A^{-1})}{\sqrt{A^{-1}r_s'^2 - At'^2}}, \quad (39)$$

$$r^2 \psi = \frac{r_s A t'}{\sqrt{A^{-1}r_s'^2 - At'^2}}. \quad (40)$$

From these matching conditions the equality of energy densities on the hypersurface $\tau = \text{const}$ follow. From Eqs. (39) and (40) we have

$$r_s A t' = \frac{r_s}{a_\lambda^2} t' (t'^2 A - 3r_s'^2 A^{-1}), \quad (41)$$

and with Eq. (38)

$$A = \frac{1}{a_\lambda^2} (-r_s^2 - 2r_s'^2 A^{-1}),$$

$$r_s'^2 = \frac{r_s^2 - a_\lambda^2}{2},$$

with Eqs. (37) and (32) we obtain

$$\rho_{st} = \frac{1}{a_\lambda^2}. \quad (42)$$

But this is de Sitter's energy density. So, on the hypersurface $\tau = const$ the equality of energy densities holds

$$\rho_{st} = \rho_{ds}. \quad (43)$$

Matching Stephani and de Sitter solutions in the flat case

The de Sitter metric for the flat case has the form

$$dS_{ds}^2 = dt^2 - a_\lambda^2 e^{\frac{2t}{a_\lambda}} (dr_s^2 + r_s^2 d\sigma^2). \quad (44)$$

After transforming its spatial part to the convenient form, it takes the form

$$dS_{ds}^2 = dt^2 - a_\lambda^2 e^{\frac{2t}{a_\lambda} + 2X} (dX^2 + d\sigma^2). \quad (45)$$

The Stephani metric is

$$dS_{st}^2 = \frac{1}{\psi^2} d\tau^2 - 4e^{-2(R-\tau)} (dR^2 + d\sigma^2). \quad (46)$$

As mentioned, $t = t(\tau, R)$, $X = X(\tau, R)$. Below dots and primes mean derivatives with respect to the time and the radial coordinate, respectively. For the Stephani solution the normal vector has one non-zero component on the matching hypersurface $\tau = const$:

$$v_0 = \frac{1}{\psi}. \quad (47)$$

For the de Sitter solution the normal vector has two non-zero components

$$v_0 = \frac{X' a_\lambda^2 e^{\frac{t}{a_\lambda} + X}}{\sqrt{X'^2 a_\lambda^2 e^{2(\frac{t}{a_\lambda} + X)} - t'^2}}, \quad (48)$$

$$v_1 = -\frac{t' a_\lambda^2 e^{\frac{t}{a_\lambda} + X}}{\sqrt{X'^2 a_\lambda^2 e^{2(\frac{t}{a_\lambda} + X)} - t'^2}}, \quad (49)$$

From the equality of the first fundamental forms two matching conditions can be obtained

$$4e^{-2(R+\tau)} = X'^2 a_\lambda^2 e^{2(\frac{t}{a_\lambda} + X)} - t'^2, \quad (50)$$

$$4e^{-2(R+\tau)} = a_\lambda^2 e^{2(\frac{t}{a_\lambda} + X)} (X'^2 - 1). \quad (51)$$

Right-hand sides of these equations are equal; from this equality we obtain

$$t'^2 = a_\lambda^2 e^{2(\frac{t}{a_\lambda} + X)} (X'^2 - 1). \quad (52)$$

From the equality of the second fundamental forms such two matching conditions follow:

$$4\psi e^{-2(R+\tau)} = -\frac{a_\lambda e^{\frac{t}{a_\lambda}}}{\sqrt{X'^2 a_\lambda^2 e^{2(\frac{t}{a_\lambda})} - t'^2}} \left(a_\lambda X' e^{2(\frac{t}{a_\lambda})} + t' \right), \quad (53)$$

$$4\psi e^{-2(R+\tau)} = -\frac{e^{\frac{t}{a_\lambda}}}{\sqrt{X'^2 a_\lambda^2 e^{2(\frac{t}{a_\lambda})} - t'^2}} (-\dot{X}' a_\lambda t'^2 + X' a_\lambda \dot{t}' + X'^2 a_\lambda t'' -$$

$$-a_\lambda t' X' X'' + X'^3 a_\lambda^2 e^{2(\frac{t}{a_\lambda})} - X'^2 a_\lambda t' - 2t'^2 X'),$$

Equality of right-hand sides of Eqs. (53) and (54) together with Eq. (52) gives us

$$(X'^2 - 1)(1 - t' X' \dot{X}' - t' X'^3 + X') + e^{\frac{t}{a_\lambda}} (X'^2 - 1)^{\frac{3}{2}} (X' - X'^2 - iX') +$$

$$+ (-\dot{X}' t' - X' X'') = 0 \quad (55)$$

Two possibilities exist in this case
the first is

$$X'^2 = 1, \quad (56)$$

and the second one reads

$$\begin{cases} 1 - t' X' \dot{X}' - t' X'^3 + X' = 0, \\ X' - X'^2 - iX' = 0, \\ \dot{X}' t' + X' X'' = 0. \end{cases} \quad (57)$$

But Eq. (57) is an incompatible system. So, we conclude that $X = X(R) = R + const$, and from Eq. (52) $t = t(\tau)$.

Matching Stephani and de Sitter solutions in the open case

We take the de Sitter and Stephani metrics in the open case in the form

$$dS_{ds}^2 = dt^2 - \frac{a_\lambda^2 \sinh^2\left(\frac{t}{a_\lambda}\right)}{\sinh^2 X} (dX^2 + d\sigma^2), \quad (58)$$

$$dS_{st}^2 = \frac{\left(\frac{1}{2} \frac{\dot{\zeta}}{\zeta} + \coth(R + \tau)\right)^2}{\psi^2} d\tau^2 + \frac{1}{\zeta \sinh^2(R + \tau)} (dR^2 + d\sigma^2), \quad (59)$$

where $t = t(\tau, R)$, $X = X(\tau, R)$.

For the Stephani solution normal vector has the only non-zero component on the hypersurface $\tau = const$:

$$v_0 = \frac{\frac{1}{2} \frac{\dot{\zeta}}{\zeta} + \coth(R + \tau)}{\psi}. \quad (60)$$

The non-zero components of the normal vector for the de Sitter solution are

$$v_0 = \frac{X'a_\lambda \sinh \frac{t}{a_\lambda}}{\sqrt{X'^2 a_\lambda^2 \sinh^2 \frac{t}{a_\lambda} - t'^2 \sinh^2 X}}, \quad (61)$$

$$v_1 = -\frac{t'a_\lambda \sinh \frac{t}{a_\lambda}}{\sqrt{X'^2 a_\lambda^2 \sinh^2 \frac{t}{a_\lambda} - t'^2 \sinh^2 X}}. \quad (62)$$

From the equality of the first fundamental forms, the conditions follow:

$$\frac{1}{\zeta \sinh^2(R + \tau)} = X'^2 a_\lambda^2 \frac{\sinh^2 \frac{t}{a_\lambda}}{\sinh^2 X} - t'^2, \quad (63)$$

$$\frac{1}{\zeta \sinh^2(R + \tau)} = a_\lambda^2 \frac{\sinh^2 \frac{t}{a_\lambda}}{\sinh^2 X}. \quad (64)$$

From the equality of the right-hand sides of Eqs. (63) and (64) we have

$$t'^2 = a_\lambda^2 \frac{\sinh^2 \frac{t}{a_\lambda}}{\sinh^2 X} (X'^2 - 1). \quad (65)$$

From the equality of the second fundamental forms, the conditions follow:

$$\begin{aligned} \frac{\psi}{\zeta \sinh^2(R + \tau)} &= \frac{a_\lambda \sinh \frac{t}{a_\lambda}}{\sinh^2 X \sqrt{X'^2 a_\lambda^2 \sinh^2 \frac{t}{a_\lambda} - t'^2 \sinh^2 X}} \times \\ &\times (t' \cosh X \sinh X - aX' \sinh \frac{t}{a_\lambda} \cosh \frac{t}{a_\lambda}), \end{aligned} \quad (66)$$

$$\begin{aligned}
 \frac{\psi}{\zeta \sinh^2(R+\tau)} &= \frac{1}{\sqrt{X'^2 a_\lambda^2 \sinh^2 \frac{t}{a_\lambda} - t'^2 \sinh^2 X}} \left(a_\lambda \dot{X} t'^2 \sinh \frac{t}{a_\lambda} - \right. \\
 &- a_\lambda \dot{t}' X t' \sinh \frac{t}{a_\lambda} + X t'^2 \cosh \frac{t}{a_\lambda} - \frac{a_\lambda t' X'^2 \cosh X \sinh \frac{t}{a_\lambda}}{\sinh X} - \\
 &- a_\lambda X'^2 t'' \sinh \frac{t}{a_\lambda} + a_\lambda X'' t' X' \sinh \frac{t}{a_\lambda} - \frac{a_\lambda^2 X'^3 \cosh \frac{t}{a_\lambda} \sinh^2 \frac{t}{a_\lambda}}{\sinh^2 X} + \\
 &\left. + X t'^2 \cosh \frac{t}{a_\lambda} \right). \tag{67}
 \end{aligned}$$

The equality of the right-hand sides of Eqs. (66) and (67) gives

$$\begin{aligned}
 \cosh \frac{t}{a_\lambda} (X'^2 - 1)^{\frac{3}{2}} (X' - X'^2 - \dot{t} X') + \sinh X (-X'' X' - \dot{X} t') + \\
 + \cosh X (X'^2 - 1)(-1 - X'^2) + \cosh X (X'^2 - 1)^{\frac{3}{2}} (X'^3 + \dot{X} X t') = 0. \tag{68}
 \end{aligned}$$

Two possibilities exist for satisfying this equation:

$$1) \quad X'^2 = 1, \tag{69}$$

or

$$2) \quad \begin{cases} X' - X'^2 - \dot{t} X' = 0, \\ X'' X' + \dot{X} t' = 0, \\ 1 + X'^2 = 0, \\ X'^3 + \dot{X} X t' = 0. \end{cases} \tag{70}$$

The last set of equations is an incompatible system, so, we conclude from Eqs. (69), (65) that $X = X(R) = R + \text{const}$ and $t = t(\tau)$.

Matching Stephani and de Sitter solutions in the closed case

Now, we take the de Sitter and Stephani metrics in a more convenient for our purpose form

$$dS_{ds}^2 = dt^2 - a_\lambda^2 \frac{\cosh^2 \frac{t}{a_\lambda}}{\cosh^2 X} (dX^2 + d\sigma^2), \tag{71}$$

$$dS_{st}^2 = \frac{\left(\frac{1}{2} \frac{\dot{\zeta}}{\zeta} + \tanh(R+r) \right)^2}{\psi^2} dt^2 - \frac{1}{\zeta \cosh^2(R+h)} (dR^2 + d\sigma^2). \tag{72}$$

We match the functions $t = t(\tau, R)$, $X = X(\tau, R)$ on the hypersurface $\tau = \text{const}$. Dots and primes denote derivatives with respect to time and radial coordinate, respectively.

The non-zero component for the normal vector in the Stephani case on the matching hypersurface is

$$v_0 = \frac{\frac{1}{2} \dot{\zeta} + \tanh(R + \tau)}{\psi}. \quad (73)$$

And non-zero components for the de Sitter case are:

$$v_0 = \frac{X' a_\lambda \cosh \frac{t}{a_\lambda}}{\sqrt{X'^2 a_\lambda^2 \cosh^2 \frac{t}{a_\lambda} - t'^2 \cosh^2 X}}, \quad (74)$$

$$v_1 = -\frac{t' a_\lambda \cosh \frac{t}{a_\lambda}}{\sqrt{X'^2 a_\lambda^2 \cosh^2 \frac{t}{a_\lambda} - t'^2 \cosh^2 X}}. \quad (75)$$

From the equality of the first fundamental forms, the conditions follow

$$\frac{1}{\zeta \cosh^2(R + \tau)} = t'^2 - X'^2 a_\lambda^2 \frac{\cosh^2 \frac{t}{a_\lambda}}{\cosh^2 X}, \quad (76)$$

$$\frac{1}{\zeta \cosh^2(R + \tau)} = -\frac{a_\lambda^2 \cosh^2 \frac{t}{a_\lambda}}{\cosh^2 X}, \quad (77)$$

From the equality of the right-hand sides of Eqs. (76) and (77) we get

$$t'^2 = \frac{a_\lambda^2 \cosh^2 \frac{t}{a_\lambda}}{\cosh^2 X} (X'^2 - 1). \quad (78)$$

From the equality of the second fundamental forms, the conditions follow:

$$\frac{\psi}{\zeta \cosh^2(R + \tau)} = \frac{a_\lambda \cosh \frac{t}{a_\lambda}}{\cosh^2 X \sqrt{X'^2 a_\lambda^2 \cosh^2 \frac{t}{a_\lambda} - t'^2 \cosh^2 X}} \times$$

$$\times (a_\lambda X' \cosh \frac{t}{a_\lambda} \sinh \frac{t}{a_\lambda} - t' \sinh X \cosh X), \quad (79)$$

$$\frac{\psi}{\zeta \cosh^2(R + \tau)} = \frac{1}{\sqrt{X'^2 a_\lambda^2 \cosh^2 \frac{t}{a_\lambda} - t'^2 \cosh^2 X}} (a_\lambda t' \cosh \frac{t}{a_\lambda} \times$$

$$\times (t' X' - t \dot{X}') + a_\lambda X' \cosh \frac{t}{a_\lambda} (t'' X' - X'' t') + X' \sinh \frac{t}{a_\lambda} \frac{1}{\cosh^2 X} \times$$

$$\times (X'^2 a_\lambda^2 \cosh^2 \frac{t}{a_\lambda} - t'^2 \cosh^2 X) + t' X'^2 a_\lambda \cosh \frac{t}{a_\lambda} \tanh X -$$

$$- X t'^2 \sinh \frac{t}{a_\lambda}). \quad (80)$$

The equality of the right-hand sides of Eqs. (79) and (80) gives

$$\cosh X (t' \dot{X}' + X'' X') + \sinh X (X'^2 - 1) (1 + X'^2 - X'^3 - X' \dot{X} t') +$$

$$+ X' \sinh \frac{t}{a_\lambda} (X'^2 - 1)^{\frac{3}{2}} (t + X' - 1) = 0. \quad (81)$$

Two possibilities exist to satisfy this equation:

1)

$$X'^2 = 1, \quad (82)$$

or

2)

$$\begin{cases} t' \dot{X}' + X'' X' = 0, \\ 1 + X'^2 - X'^3 - X' \dot{X} t' = 0, \\ t + X' - 1 = 0. \end{cases} \quad (83)$$

This set of equations is incompatible, so, we conclude from Eqs. (82) and (78) that $X = X(R) = R + \text{const}$ and $t = t(\tau)$.

Conclusions

Matching conditions for the Stephani and the de Sitter solutions on hypersurface $\tau = \text{const}$ in the spherically symmetric case have been obtained (τ is a time coordinate of the Stephani solution). The coordinates of the de Sitter solution were taken in the general form as arbitrary functions depending on the Stephani's time and radial coordinate. Matching was done both for special cases (flat, open, closed) and for the

general case that does not concretize the type of curvature. From the matching conditions the equality of densities on the matching hypersurface has been obtained. From Eq. (15) we see that there is an abrupt change of pressure. Also it was obtained that de Sitter radial coordinate is different from the Stephani one on some shift and de Sitter time is an arbitrary function depending on Stephani's time.

References

1. **Kramer D.** Exact solutions of Einstein's field equations / Kramer D., Stephani H., MacCallum M.A.H., Herlt E. - Cambridge: Cambridge University Press, 1980. – p.462
2. **Krasinski A.** Space-Times with Spherically Symmetric Hypersurfaces / A. Krasinski // Gen. Relativity Gravitation – 1981. – Vol. 13 – No. 11 – P. 1021-1035.
3. **Krasinski A.** On the Global Geometry of the Stephani Universe / A. Krasinski // Gen. Relativity Gravitation – 1983. – Vol. 15 – No.7 – P. 673-689.
4. **Roberto A. Sussman** Towards a physical interpretation for the Stephani Universe / Roberto A. Sussman // Gen. Relativity Gravitation – 2000. – Vol. 32 – No. 8 – P. 1527-1557.
5. **Krasinski A.** Inhomogeneous Cosmological Models / A. Krasinski - Cambridge: Cambridge University Press, 1998. – P. 310.
6. **Henriksen R.N.** Space-times with constant vacuum energy density and a conformal Killing vector / R.N. Henriksen, A.G. Emslie, P.S. Wesson // Phys. Rev. D – 1983. – Vol. 27 – No.6 – P. 1219-1227.
7. **Wesson P.S.** Cosmological solution of Einstein's equations with uniform density and nonuniform pressure / P.S. Wesson, J. Ponce de Leon // Phys. Rev. D – 1989. – Vol. 39 – No. 2 – P. 420-422.
8. **Cook M.W.** On a Class of Exact Spherically Symmetric Solutions to the Einstein Gravitational Field Equations / M.W. Cook // Aust. J. Phys. – 1975. – Vol. 28 – P. 413-422.
9. **Hernandez C.W.**, Misner G.C. // Astrophys. J. – 1968. - Vol. 143 – P. 452.
10. **Cahill M.E.** Spherical Symmetry and Mass-Energy in General Relativity. I. General Theory / M.E. Cahill, G.C. McVittie // J. Math. Phys. – 1970. – Vol. 11 – No. 4 – P. 1382-1392.
11. **Glass E.N.** Shear-free gravitational collapse / E.N. Glass // J. Math. Phys. – 1979. – Vol. 20 – No. 7 – P. 1508-1514.
12. **Knutsen H.** Physical properties of an exact spherically symmetric solution with shear in general relativity / H. Knutsen // Gen. Relativity Gravitation – 1992. – Vol. 24 – No. 12 – P. 1297-1313.
13. **Stephani H.** Uber Losungen der Einsteinchen Feldgleichungen, dies sich in einen funfdimensionalen flachen Raum einbetten lassen / H. Stephani // Commun. math. Phys. – 1967. – Vol. 4 – P. 137-142.
14. **Bonnor W.B.** Junction Conditions in General Relativity / W.B. Bonnor, P.A. Vickers // Gen. Relativity Gravitation – 1981. – Vol. 13 – No. 1 – P. 29-36.

Received 13.07.2013.

UDC 533.9

V. N. Gorev, A.I. Sokolovsky

Oles Honchar Dnipropetrovsk National University

ONE-VELOCITY AND ONE-TEMPERATURE HYDRODYNAMICS OF PLASMA

The hydrodynamics of fully ionized plasma where the relaxation of the component temperatures and velocities is finished is investigated on the basis of the Landau kinetic equation. The reduced description parameters of the system are the component particle densities, the macroscopic velocity and the temperature of the system. The hydrodynamics is built starting from the Bogolyubov functional hypothesis. The consideration is based on a perturbation theory in small gradients of the reduced description parameters. The component distribution functions are found in the perturbation theory with accuracy up to the first order in the gradients. Hydrodynamic equations for the reduced description parameters are built taking into account dissipative processes. The obtained integral equations are solved by expansion in the Sonine polynomial series with the additional use of the electron-to-ion mass ratio smallness. The kinetic coefficients of the system are calculated taking into account smallness of the mass ratio. These results of the work are not only important themselves, but can be a basis for the investigation of relaxation phenomena at their final stage as a main approximation. The obtained hydrodynamic equations can be used for the hydrodynamic mode investigation.

Keywords: fully ionized electron-ion plasma, Landau kinetic equation, distribution functions, hydrodynamic equations, kinetic coefficients.

На основе кинетического уравнения Ландау изучается гидродинамика полностью ионизированной плазмы в случае завершённой релаксации скоростей и температур компонент. Параметрами сокращённого описания системы являются плотности числа частиц компонент, макроскопическая скорость и температура системы. Гидродинамика строится исходя из функциональной гипотезы Боголюбова. Рассмотрение базируется на теории возмущений по малым градиентам параметров сокращённого описания. Функции распределения компонент ищутся в теории возмущений с точностью до членов первого порядка по градиентам. Построены уравнения гидродинамики для параметров сокращённого описания с учётом диссипативных процессов. Полученные интегральные уравнения решаются разложением в ряд по полиномам Сонина с дополнительным учётом малости отношения масс электрона и иона. Кинетические коэффициенты системы вычислены с учётом малости отношения масс. Результаты работы не только важны сами по себе, но также могут быть основой для исследования релаксационных явлений вблизи завершения релаксации как главное приближение. Полученные уравнения гидродинамики могут быть использованы для изучения гидродинамических мод системы.

Ключевые слова: полностью ионизированная электрон-ионная плазма, кинетическое уравнение Ландау, функции распределения, уравнения гидродинамики, кинетические коэффициенты.

На основі кінетичного рівняння Ландау вивчається гідродинаміка повністю іонізованої плазми у випадку завершеної релаксації швидкостей та температур компонент. Параметрами скороченого опису системи є густини кількості частинок компонент, макроскопічна швидкість та температура системи. Гідродинаміка будується виходячи з функціональної гіпотези Боголюбова. Розгляд базується на теорії збурень за малими градієнтами параметрів скороченого опису. Функції розподілу компонент шукаються у теорії збурень з точністю до членів першого порядку по градієнтам. Побудовано рівняння гідродинаміки для параметрів скороченого опису з урахуванням дисипативних процесів. Отримані інтегральні рівняння розв'язуються розвиненням в ряд по поліномам Соніна з додатковим урахуванням малості відношення мас електрона та іона. Кінетичні коефіцієнти системи порашовано з урахуванням малості відношення мас. Результати роботи важливі не лише самі по собі, але також можуть бути використані для дослідження релаксаційних явищ поблизу завершення релаксації як головне наближення. Отримані рівняння гідродинаміки можуть бути використані для отримання гідродинамічних мод системи.

Ключові слова: повністю іонізована електрон-іонна плазма, кінетичне рівняння Ландау, функції розподілу, рівняння гідродинаміки, кінетичні коефіцієнти.

Introduction

In his famous work [1] Landau derived a kinetic equation for completely ionized gas with Coulomb interaction, which is widely used in the kinetic theory of plasma. On the basis of this equation he also studied the temperature relaxation in plasma. The problem of the relaxation times in the spatial uniform case was investigated by many authors (see, for example [2-4]). Present work is concerned with the non-homogenous case where the relaxation of the component temperatures and velocities is finished. The problem of the one-velocity and one-temperature hydrodynamics of two-component systems (a usual hydrodynamics) is not new [5-7], but it was usually investigated on the basis of the Boltzmann equation for uncharged particles.

The aim of the present work is to build usual hydrodynamics of plasma on the basis of the Landau kinetic equation and to obtain the component distribution functions and kinetic coefficients of the system. The mentioned results, besides being important themselves, obviously can be considered as the leading order approximation in the case of small differences of the component velocities and temperatures.

The article is organized as follows. First, the Landau kinetic equation is written. Then reduced description parameters of the system are introduced, and the component distribution functions are obtained in the homogenous case. Then hydrodynamic equations for the reduced description parameters are built, and the distribution functions in the non-homogenous case are calculated. Using these distributions, the kinetic coefficients of the system are found.

Basic equations of the theory

The well-known Landau kinetic equation for fully ionized electron-ion plasma is written

$$\frac{\partial f_{ap}(x,t)}{\partial t} = -\frac{p_{an}}{m_a} \frac{\partial f_{ap}(x,t)}{\partial x_n} + I_{ap}(f(x,t)),$$

$$I_{ap}(f) = -\sum_b \frac{\partial}{\partial p_n} \left[2\pi (e_a e_b)^2 L \int \left\{ f_{ap} \frac{\partial f_{bp'}}{\partial p'_l} - f_{bp'} \frac{\partial f_{ap}}{\partial p_l} \right\} D_{nl} \left(\frac{p}{m_a} - \frac{p'}{m_b} \right) d^3 p' \right] \quad (1)$$

where

$$D_{nl}(u) \equiv (|u|^2 \delta_{nl} - u_n u_l) / |u|^2 \quad (2)$$

Here $f_{ap}(x,t)$ is distribution function of the a -th component of the plasma ($a, b, c, \dots = e, i$). It is normalized by relation

$$\int f_{ap}(x,t) d^3 p = n_a(x,t) \quad (3)$$

where $n_a(x,t)$ is number of particle number density of the a -th component. The Landau equation is a model one but it adequately describes the role of the Coulomb interaction in the system at long distances. Therefore, it is widely used in the plasma theory.

As is known [5], the reduced description parameters in the one-velocity and one-temperature hydrodynamics are the particle number densities of the components $n_a(\vec{x},t)$, the temperature $T(x,t)$ and the velocity $v_n(x,t)$ of the system. By definition, these parameters are introduced as follows:

$$\pi_n = \sum_a \int f_{ap} p_n d^3 p = v_n \rho \quad (\rho \equiv n_e m_e + n_i m_i),$$

$$\varepsilon = \sum_a \int f_{ap} \varepsilon_{ap} d^3 p = \frac{3}{2} n T + \frac{1}{2} \rho v^2 \quad (n \equiv n_e + n_i) \quad (4)$$

where π_n and ε are the total momentum and the energy densities of the system, respectively ($\varepsilon_{ap} \equiv p^2 / 2m_a$).

The investigation is based on the functional hypothesis [5], which can be written as

$$f_{ap}(x, t) \xrightarrow{t \gg \tau_0} f_{ap}(x, \xi(t)) \quad (5)$$

where the reduced description parameters are denoted as ξ_μ : $\xi_0 = T$, $\xi_n = v_n$, $\xi_a = n_a$ ($\mu = 0, n, a$). In (5) τ_0 is a time which is much longer than the subsystem velocity and temperature relaxation times. The dependence of the reduced description parameters on the coordinates is supposed to be weak, so the gradients of the reduced description parameters are assumed to be small,

$$\frac{\partial^s \xi_\mu(\bar{x})}{\partial x_{n_1} \dots \partial x_{n_s}} \sim g^s \quad (g \ll 1). \quad (6)$$

Parameter g is estimated as $g = l_f / L$ where l_f is the mean free path, L is characteristic length of inhomogeneities in the system. In what follows, the contribution of the order g^s to a quantity A is denoted by $A^{(s)}$.

According to the functional hypothesis (5), hydrodynamic equations have the structure

$$\frac{\partial \xi_\mu(x, t)}{\partial t} \equiv L_\mu(x, f(\xi(t))) \quad (7)$$

where functional $L_\mu(x, f)$ can be found from the kinetic equation (1) and definitions (4). Then equation (1) is rewritten in view of (5) and (6) as the equation for the functional $f(x, \xi)$

$$\sum_\mu \int d^3 x' \frac{\delta f_{ap}(x, \xi)}{\delta \xi_\mu(x')} L_\mu(x', f(\xi)) = -\frac{p_n}{m_a} \frac{\partial f_{ap}(x, \xi)}{\partial x_n} + I_{ap}(f(x, \xi)). \quad (8)$$

This equation should be solved with additional conditions

$$\begin{aligned} \sum_a \int f_{ap}(x, \xi) p_n d^3 p &\equiv v_n(x) \sum_a m_a n_a(x), & \int f_{ap}(x, \xi) d^3 p &= n_a(x), \\ \sum_a \int f_{ap}(x, \xi) \varepsilon_{ap} d^3 p &= \frac{3}{2} T(x) \sum_a n_a(x) + \frac{1}{2} v(x)^2 \sum_a m_a n_a(x) \end{aligned} \quad (9)$$

that follow from definitions (3), (4).

In order to realize the reduced description method, one should calculate the functional $f(x, \xi)$ from equations (8) and (9). These equations are obviously solvable in a perturbation theory in the gradients of the reduced description parameters.

Hydrodynamic equations

Hydrodynamic equations (7) are obtained from conservation laws following from the kinetic equation (1) and the definitions (4)

$$\frac{\partial n_a}{\partial t} = -\frac{1}{m_a} \frac{\partial \pi_{al}}{\partial x_l}, \quad \frac{\partial \pi_n}{\partial t} = -\frac{\partial t_{nl}}{\partial x_l}, \quad \frac{\partial \varepsilon}{\partial t} = -\frac{\partial q_l}{\partial x_l}. \quad (10)$$

Here the total energy and momentum fluxes in the system q_l , t_{nl} , and momentum density of the a -th component π_{al}

$$q_l = \sum_a \int d^3 p \varepsilon_{ap} \frac{p_l}{m_a} f_{ap}, \quad t_{nl} = \sum_a \int d^3 p p_n \frac{p_l}{m_a} f_{ap}, \quad \pi_{al} = \int d^3 p p p_l f_{ap}. \quad (11)$$

are introduced ($\pi_n = \pi_{en} + \pi_{in}$).

To build hydrodynamic equations with taking into account dissipative processes the solution of equations (8), (9) should be found in the form of a series up to the first order in the gradients of the parameters $\xi_\mu(x)$ by using an iterative procedure

$$f_{ap}(x, \xi) = f_{ap}^{(0)} + f_{ap}^{(1)} + O(g^2). \quad (12)$$

Equation (8) shows that the distribution functions in the leading approximation coincide with the Maxwell ones

$$f_{ap}^{(0)} = w_{a,p-m_a v}, \quad w_{ap} \equiv \frac{n_a \beta^{3/2}}{(2\pi m_a)^{3/2}} \exp(-\beta \varepsilon_{ap}) \quad (\beta \equiv 1/T) \quad (13)$$

because for collision integral (1) the relation

$$I_{ap}(w) = 0 \quad (14)$$

is true.

The fluxes in the lab reference system are connected with ones in the accompanying reference system (ARS) by relations

$$q_n = q_n^o + t_{nl}^o v_l + (\varepsilon^o + \frac{1}{2} \rho v^2) v_n, \quad t_{nl} = t_{nl}^o + \rho v_n v_l, \quad \pi_{an} = \pi_{an}^o + m_a n_a v_n \quad (15)$$

where quantities taken in the ARS have superscript o. From (4), (11)-(13), (15) it can be obtained that the hydrodynamic equations with contributions up to the second order in gradients are given by relations

$$\begin{aligned} \frac{\partial n_a}{\partial t} &= -\frac{\partial n_a v_n}{\partial x_n} - \frac{1}{m_a} \frac{\partial \pi_{an}^{o(1)}}{\partial x_n}, & \frac{\partial v_n}{\partial t} &= -v_l \frac{\partial v_n}{\partial x_l} - \frac{1}{\rho} \frac{\partial n T}{\partial x_n} - \frac{1}{\rho} \frac{\partial t_{nl}^{o(1)}}{\partial x_l}, \\ \frac{\partial T}{\partial t} &= -v_n \frac{\partial T}{\partial x_n} - \frac{2}{3} T \frac{\partial v_n}{\partial x_n} - \frac{2}{3n} \frac{\partial q_n^{o(1)}}{\partial x_n} - \frac{2}{3n} t_{nl}^{o(1)} \frac{\partial v_n}{\partial x_l} + \frac{T}{n} \sum_a \left(\frac{1}{m_a} \frac{\partial \pi_{an}^{o(1)}}{\partial x_n} \right). \end{aligned} \quad (16)$$

Here we take into account that for the considered system

$$\varepsilon^o = \frac{3}{2} n T, \quad t_{nl}^{o(0)} = n T \delta_{nl}, \quad q_l^{o(0)} = 0, \quad \pi_{an}^{o(0)} = 0, \quad \pi_n^o = 0. \quad (17)$$

In equations (16) fluxes of mass $\pi_{an}^{o(1)}$, momentum $t_{nl}^{o(1)}$, energy $q_n^{o(1)}$ describe dissipative processes in the system.

According to the idea of the rotational invariance, the distribution functions of the first order in gradients in the ARS have the structure

$$\begin{aligned} f_{ap}^{(1)} &= w_{a,p-m_a v} \left[p_n \sum_b A_a^{N_b}(\beta \varepsilon_{ap}) \frac{\partial n_b}{\partial x_n} + p_n A_a^T(\beta \varepsilon_{ap}) \frac{\partial T}{\partial x_n} + \right. \\ &\quad \left. + (p_l p_n - \frac{1}{3} \delta_{nl} p^2) A_a^v(\beta \varepsilon_{ap}) \frac{\partial v_n}{\partial x_l} \right]_{p \rightarrow p-m_a v}. \end{aligned} \quad (18)$$

Scalar functions $A_a^{N_b}(\beta \varepsilon_p)$, $A_a^T(\beta \varepsilon_p)$, $A_a^v(\beta \varepsilon_p)$ can be found from integral equations

$$\begin{aligned} p_n \left\{ \frac{1}{n_a m_a} \delta_{ab} - \frac{1}{\rho} \right\} &= -\sum_b \int d^3 p' K_{ab}(p, p') p'_n A_b^{N_c}(\beta \varepsilon_{bp'}), \\ p_n \frac{\beta}{m_a} \left\{ \beta \varepsilon_{ap} - \frac{3}{2} - \frac{n}{\rho} m_a \right\} &= -\sum_b \int d^3 p' K_{ab}(p, p') p'_n A_b^T(\beta \varepsilon_{bp'}), \\ \frac{\beta}{m_a} \left\{ p_l p_n - \frac{1}{3} \delta_{nl} p^2 \right\} &= -\sum_b \int d^3 p' K_{ab}(p, p') (p'_l p'_n - \frac{1}{3} \delta_{ln} p'^2) A_b^v(\beta \varepsilon_{bp'}). \end{aligned} \quad (19)$$

Kernel $K(p, p')$ of these equations is defined through the collision integral (1) by the formulas

$$K_{ab}(p, p')w_{ap} = -M_{ab}(p, p')w_{bp'}, \quad M_{ab}(p, p') = \frac{\delta I_{ap}(f)}{\delta f_{bp'}} \Big|_{f_{cp'} \rightarrow w_{cp'}}. \quad (20)$$

Additional conditions (9) give the following restrictions on the solution of the integral equations (19)

$$\sum_a \int d^3 p w_{ap} p^2 A_a^T(\beta \varepsilon_{ap}) = 0, \quad \sum_a \int d^3 p w_{ap} p^2 A_a^{N_b}(\beta \varepsilon_{ap}) = 0, \quad (21)$$

which provide the uniqueness of the solution.

The solution of integral equations (19) will be found in the form of the expansions in the Sonine polynomials [8]

$$A_a^{N_b}(\beta \varepsilon_{ap}) = \sum_{s=0}^{\infty} g_{as}^{N_b} S_s^{3/2}(\beta \varepsilon_{ap}), \quad A_a^T(\beta \varepsilon_{ap}) = \sum_{s=0}^{\infty} g_{as}^T S_s^{3/2}(\beta \varepsilon_{ap}),$$

$$A_a^V(\beta \varepsilon_{ap}) = \sum_{s=0}^{\infty} g_{as}^V S_s^{5/2}(\beta \varepsilon_{ap}). \quad (22)$$

The Sonine polynomials $S_n^\alpha(x)$ are defined by the relation

$$S_n^\alpha(x) \equiv \frac{1}{n!} e^x x^{-\alpha} \frac{d^n}{dx^n} (e^{-x} x^{\alpha+n}), \quad (23)$$

and have the property of orthogonality

$$\int_0^\infty e^{-x} x^\alpha S_n^\alpha(x) S_{n'}^\alpha(x) dx = \frac{\Gamma(n+\alpha+1)}{n!} \delta_{nn'}. \quad (24)$$

The Sonine polynomials are useful in the next calculation because of the equality

$$\int d^3 p w_{ap} \varepsilon_p^{\alpha-1/2} S_s^\alpha(\beta \varepsilon_{ap}) S_{s'}^\alpha(\beta \varepsilon_{ap}) = \frac{2n_a T^{\alpha-1/2}}{\pi^{1/2}} \frac{\Gamma(n+\alpha+1)}{s!} \delta_{ss'},$$

which follows from (24).

Distribution function (18) allows calculating the first order in gradients contributions to fluxes (dissipative fluxes) in the ARS:

$$\pi_{an}^{o(1)} = \sum_b A_{ab} \frac{\partial n_b}{\partial x_n} + B_a \frac{\partial T}{\partial x_n}, \quad q_n^{o(1)} = \sum_a C_a \frac{\partial n_a}{\partial x_n} + D \frac{\partial T}{\partial x_n},$$

$$t_{nl}^{o(1)} = -\eta \left(\frac{\partial v_n}{\partial x_l} + \frac{\partial v_l}{\partial x_n} - \frac{2}{3} \frac{\partial v_m}{\partial x_m} \delta_{nl} \right), \quad (25)$$

where kinetic coefficients

$$A_{ab} = m_a n_a T g_{a0}^{N_b}, \quad B_a = m_a n_a T g_{a0}^T,$$

$$C_a = \frac{5}{2} T^2 \sum_b n_b (g_{b0}^{N_a} - g_{b1}^{N_a}), \quad D = \frac{5}{2} T^2 \sum_a n_a (g_{a0}^T - g_{a1}^T),$$

$$\eta = -T^2 \sum_a n_a m_a g_{a0}^V. \quad (26)$$

are introduced. Here η is shear viscosity but for other kinetic coefficients there are several standard notations (see, for example, [5 - 7]).

As seen, the usage of the Sonine polynomials is rather convenient, because the momentum density and the momentum flux are expressed in terms of only one polynomial, and the energy flux is expressed in terms of only two polynomials.

Calculation of the kinetic coefficients

Substituting expansions (22) in integral equations (19), multiplying by the Sonine polynomials and integrating over momentum give an infinite set of equations for coefficients $g_{as}^{N_b}$, g_{as}^T , g_{as}^V . For their approximate calculation we should artificially truncate the number of polynomials in (22) (see, for example [10]) to obtain a finite set equations for the coefficients $g_{as}^{N_b}$, g_{as}^T , g_{as}^V . From (26) it is evident that at least $A_a^{N_b}$ and A_a^T should be found in the two-polynomial approximation, and A_a^V – in the one-polynomial one.

From (19), (22) the following set of the truncated equations for the coefficients $g_{as}^{N_b}$ ($s=0,1$), g_{as}^T ($s=0,1$), g_{a0}^V is obtained

$$\begin{aligned} \sum_{s'=0,1} \sum_b G_{as,bs'} g_{bs'}^T &= -Y_{as}, & \sum_{s'=0,1} \sum_b G_{es,bs'} g_{bs'}^{N_e} &= -\frac{3n_i m_i T}{\rho} \delta_{s0}, \\ \sum_{s'=0,1} \sum_b G_{es,bs'} g_{bs'}^{N_i} &= \frac{3n_e m_e T}{\rho} \delta_{s0}, & \sum_{s'=0,1} \sum_b G_{is,bs'} g_{bs'}^{N_i} &= -\frac{3n_e m_e T}{\rho} \delta_{s0}, \\ \sum_{s'=0,1} \sum_b G_{is,bs'} g_{bs'}^{N_e} &= \frac{3n_i m_i T}{\rho} \delta_{s0}, & \sum_b g_{b0}^V H_{a0,b0} &= -10n_a m_a T \end{aligned} \quad (27)$$

where

$$Y_{e0} = -Y_{i0} = 3n_e n_i (m_i - m_e) / \rho, \quad Y_{a1} = -15n_a / 2. \quad (28)$$

Equations (27) contain the matrixes $G_{ak,bn}$, $H_{ak,bn}$ given by formulas

$$\begin{aligned} G_{as,bs'} &\equiv \left\{ p_n S_s^{3/2} (\beta \mathcal{E}_{ap}), p_n S_s^{3/2} (\beta \mathcal{E}_{bp}) \right\}_{ab}, \\ H_{as,bs'} &= \left\{ (p_l p_n - \delta_{nl} p^2 / 3) S_s^{5/2} (\beta \mathcal{E}_{ap}), (p_l p_n - \delta_{nl} p^2 / 3) S_s^{5/2} (\beta \mathcal{E}_{bp}) \right\}_{ab} \end{aligned} \quad (29)$$

which contain integral brackets defined by the relation

$$\{g, h\}_{ab} \equiv \int d^3 p d^3 p' g(p) w_{ap} K_{ab}(p, p') h(p'). \quad (30)$$

Using (22), relations (21) take the form

$$\sum_a m_a n_a g_{a0}^T = 0, \quad \sum_a m_a n_a g_{a0}^{N_b} = 0 \quad (31)$$

and must be used as additional conditions to equations (27).

In order to simplify the obtained results, we may take into account that the electron-ion mass ratio is small $\sigma \equiv \sqrt{m_e/m_i} \ll 1$. Using (1), (20), (29)-(31), we obtain the coefficients $g_{as}^{N_b}$ ($s=0,1$), g_{as}^T ($s=0,1$), g_{a0}^V in a perturbation theory in σ

$$\begin{aligned}
 g_{e0}^T &= -3 \frac{\sqrt{2}n_e + 7z^2n_i}{2^{5/2}z^2n_i(\sqrt{2}n_e + z^2n_i)} \lambda + O(\sigma), & g_{e1}^T &= \frac{3}{2^{1/2}(\sqrt{2}n_e + z^2n_i)} \lambda + O(\sigma), \\
 g_{i0}^T &= \frac{3n_e(\sqrt{2}n_e + 7z^2n_i)}{2^{5/2}z^2n_i^2(\sqrt{2}n_e + z^2n_i)} \lambda \sigma^2 + O(\sigma^3), \\
 g_{i1}^T &= \frac{3(5\sqrt{2}n_e + 5z^2n_i - 4z^2n_e)}{2^4z^4n_i(\sqrt{2}n_e + z^2n_i)} \lambda \sigma + O(\sigma^2), \\
 g_{e0}^{N_e} &= -\frac{3T(4\sqrt{2}n_e + 13z^2n_i)}{2^{9/2}z^2n_in_e(z^2n_i + \sqrt{2}n_e)} \lambda + O(\sigma), & g_{i0}^{N_e} &= g_{e0}^{N_e} = -\frac{n_e}{n_i} \sigma^2 g_{e0}^{N_e}, \\
 g_{e1}^{N_e} &= \frac{9T}{2^{7/2}n_e(z^2n_i + \sqrt{2}n_e)} \lambda + O(\sigma), & g_{e1}^{N_i} &= -\frac{n_e}{n_i} \sigma^2 g_{e1}^{N_e}, & g_{i0}^{N_i} &= -\frac{n_e}{n_i} \sigma^2 g_{i0}^{N_e}, \\
 g_{i1}^{N_e} &= -\frac{9T}{2^5z^2n_i(z^2n_i + \sqrt{2}n_e)} \lambda \sigma + O(\sigma^2), & g_{i1}^{N_i} &= -\frac{n_e}{n_i} \sigma^2 g_{i1}^{N_e}, \\
 g_{e0}^v &= -\frac{5}{2^3(n_e + \sqrt{2}n_iz^2)} \lambda + O(\sigma), & g_{i0}^v &= -\frac{5}{2^3z^4n_i} \lambda \sigma + O(\sigma^2) \tag{32}
 \end{aligned}$$

where the notation

$$\lambda = \frac{T^{1/2}}{e^4 L (\pi m_e)^{1/2}} \tag{33}$$

is introduced. As seen from (25), (26), the obtained expressions are important for calculation of the kinetic coefficients.

According to the standart definition of kinetic coefficients for the two-component systems [6, 7], we can introduce notations

$$\begin{aligned}
 t_{nl}^{o(1)} &= -\eta \left(\frac{\partial v_n}{\partial x_l} + \frac{\partial v_l}{\partial x_n} - \frac{2}{3} \delta_{nl} \frac{\partial v_m}{\partial x_m} \right) - \zeta \delta_{nl} \frac{\partial v_m}{\partial x_m}, \\
 \pi_{en}^{o(1)} &\equiv -D_e^T \frac{\partial \ln T}{\partial x_n} - \frac{n^2 m_e m_i}{\rho} D_{ei} d_n, & \pi_{in}^{o(1)} &\equiv -D_i^T \frac{\partial \ln T}{\partial x_n} - \frac{n^2 m_e m_i}{\rho} D_{ie} d_n, \\
 q_n^{o(1)} &= -\kappa \frac{\partial T}{\partial x_n} + T \left(\frac{\xi}{D_{ei}} + \frac{5}{2} \frac{1 - \sigma^2}{m_e} \right) \pi_{en}^{o(1)} \tag{34}
 \end{aligned}$$

where quantity d_n is defined by formula (with taking into account, that $\pi_{en}^{o(1)} + \pi_{in}^{o(1)} = 0$).

$$d_n = \frac{n_e n_i (m_i - m_e)}{\rho n} \frac{\partial \ln T}{\partial x_n} + \frac{n_e n_i m_i}{\rho n} \left(\frac{\partial \ln n_e}{\partial x_n} - \sigma^2 \frac{\partial \ln n_i}{\partial x_n} \right). \tag{35}$$

Here η , ζ are shear and bulk viscosity, D_a^T , D_{ab}^T are thermal diffusion and diffusion coefficients, κ is thermal conductivity, ξ is an additional kinetic coefficient.

Using definitions (34), (35) and formulas (25), (26), (32), we obtain the following expressions for the kinetic coefficients

$$\begin{aligned}
D_e^T = -D_i^T &= \frac{45n_e m_e T^2}{2^{9/2} (z^2 n_i + \sqrt{2} n_e)} \lambda + O(\sigma), \\
D_{ei} = -D_{ie} &= \frac{3T^2 (4\sqrt{2} n_e + 13z^2 n_i)}{2^{9/2} n z^4 (n_i + \sqrt{2} z^2 n_e)} \lambda + O(\sigma), \\
\kappa &= \frac{75n_e T^2}{2^{5/2} (4\sqrt{2} n_e + 13z^2 n_i)} \lambda + O(\sigma), \quad \eta = \frac{5m_e T^2}{2^3 z^4} \lambda \sigma^{-1} + O(\sigma^0), \quad \zeta = 0, \\
\xi &= \frac{45n_i n_e T^2}{2^{9/2} n_e m_e n (z^2 n_i + \sqrt{2} n_e)} \lambda + O(\sigma),
\end{aligned} \tag{36}$$

which define dissipative fluxes in the system.

Conclusions

The hydrodynamics of fully ionized two-component plasma with equal component temperatures and macroscopic component velocities has been investigated taking into account that the electron-to-ion mass ratio is small. The distribution functions of the plasma components are found up to the first order in gradients of hydrodynamic variables. The kinetic coefficients of the system have been calculated.

The considered hydrodynamic states are the states in which the relaxation of the component velocities and temperatures is finished. The obtained results are not only important themselves, but they are also very important for the relaxation processes investigation at the end of relaxation. In the last situation the results obtained in the present paper give the leading order approximation for the case of small differences of component temperatures and velocities. The developed here hydrodynamics will be used in another paper for investigation of the plasma modes taking into account the relaxation.

References

1. **Landau L.D.** Kinetic equation in the Coulomb interaction case / L.D. Landau // JETP. – 1937. - V. 7. – P. 203-209 (*in Russian*).
2. **Ishimaru S.** Basic Principles of Plasma Physics/ S. Ishimaru, London, Benjamin, 1973. – 324 p.
3. **Alexandrov A.F.** Fundamentals of plasma electrodynamics /A. F. Alexandrov, L. S. Bogdankevich, A.A. Rukhadze, Moscow, Vyshchaya Shkola, 1988, 424 p. (*in Russian*).
4. **Bobylev A.V.** Relaxation of two-temperature plasma /A. V. Bobylev, I. F. Potapenko, P.H. Sakanaka // Phys. Rev. E. – 1997. – V.56, No.2. – P. 2081-2093.
5. **Akhiezer A.I.** Methods of Statistical Physics/ A.I. Akhiezer, S. V. Peletminsky, Oxford, Pergamon Press, 1981. – 376 p.
6. **Silin V.P.** Introduction to the kinetic theory of gases / V.P. Silin, Moscow, 1998, 339 p. (*in Russian*).
7. **Ferziger J.H.** Mathematical theory of transport processes in gases / J.H. Ferziger, H.G Kaper, North Holland Publishing, Amsterdam, 1972. – 579 p.
8. **Lifshitz E.M.** Physical Kinetics/ E.M. Lifshitz, L. P. Pitaevsky, Oxford, Pergamon Press, 1981. – 452 p.

Received 13.07.2013

UDC 535.14:537.8

S. F. Lyagushyn, Yu. M. Salyuk, A. I. Sokolovsky

Oles Honchar Dnipropetrovsk National University

DYNAMICS OF ELECTROMAGNETIC FIELD AND ITS CORRELATIONS IN A MEDIUM CONSISTING OF TWO-LEVEL EMITTERS

Kinetics of electromagnetic field in a medium of motionless emitters is considered on the basis of reduced description method with using as its parameters the average value of the transversal electromagnetic field, its binary correlations, and energy density of the emitter subsystem. Material equations for such a medium are obtained. Electromagnetic waves existing in it are considered. Equilibrium correlations of the field and their connection with the material equations are investigated. The concept of binary correlation waves existing in a non-uniform case is developed. The description for waves of binary correlations with using the field mode correlations and compact designations are proposed. Four types of correlation modes in the equilibrium medium of emitters are found. Two of them correspond to a damped oscillation process and other two ones correspond to decaying waves. The connection between the energy density of the emitters and field correlations is shown. Modes of the non-equilibrium medium coupled to field correlation modes are investigated near the equilibrium. The phenomenon of creation of field correlations (correlation wave emission) in the process of emitter medium evolution is predicted.

Keywords: medium of emitters, transversal electromagnetic field, correlation modes, decaying waves of correlations, nonequilibrium medium, coupled oscillations.

Рассмотрена кинетика электромагнитного поля в среде, образованной неподвижными двухуровневыми излучателями, на основе методе сокращенного описания с использованием в качестве его параметров средних значений поперечного электромагнитного поля, его бинарных корреляций и плотности энергии подсистемы излучателей. Получены материальные уравнения для такой среды. Рассмотрены электромагнитные волны в ней. Исследованы равновесные корреляции поля и их связь с материальными уравнениями. Развита концепция волн бинарных корреляций, существующих в неоднородном случае. Предложены описание волн бинарных корреляций с помощью корреляций мод поля и компактная форма записи. Найдено четыре типа мод корреляций в равновесной среде из излучателей. Два из них отвечают затухающему колебательному процессу, еще два – затухающим волнам. Показана связь плотности энергии излучателей с корреляциями поля. Изучены моды связанных колебаний неравновесной среды и корреляций поля вблизи равновесия. Предсказано явление возникновения корреляций поля (излучения волн корреляций) при эволюции среды из излучателей.

Ключевые слова: среда из излучателей, поперечное электромагнитное поле, моды корреляций, затухающие волны корреляций, неравновесная среда, связанные колебания.

Розглянуто кінетику електромагнітного поля в середовищі, яке утворене нерухомими дворівневими випромінювачами, на основі методу скороченого опису з використанням у якості його параметрів середніх значень поперечного електромагнітного поля, його бінарних кореляцій і густини енергії підсистеми випромінювачів. Отримано матеріальні рівняння для такого середовища. Розглянуто електромагнітні хвилі в ньому. Досліджено рівноважні кореляції поля та їх зв'язок із матеріальними рівняннями. Розвинуто концепцію хвиль бінарних кореляцій, що існують у неоднорідному випадку. Запропоновано опис хвиль бінарних кореляцій за допомогою кореляцій мод поля та компактну форму запису. Знайдено чотири типи мод кореляцій у рівноважному середовищі з випромінювачів. Знайдено чотири типи мод кореляцій у рівноважному середовищі з випромінювачів. Два з них відповідають згасаючому коливальному процесу, а ще два типи мод кореляцій – згасаючим хвилям. Показано зв'язок густини енергії випромінювачів із кореляціями поля. Вивчено зв'язані коливання нерівноважного середовища та кореляцій поля поблизу від рівноваги. Передбачено явище виникнення кореляцій поля (випромінювання хвиль кореляцій) у процесі еволюції середовища з випромінювачів.

Ключові слова: середовище з випромінювачів, поперечне електромагнітне поле, моди кореляцій, згасаючі хвилі кореляцій, нерівноважне середовище, зв'язані коливання.

Introduction

The necessity of taking into account binary field correlations as additional independent variables together with the average field was pointed out for the first time in the paper [1]. This idea was put into life in the paper [2] where the field kinetics in the equilibrium entirely ionized plasma was investigated. In that paper the idea of field correlation waves existing was also expressed. In the paper [3] the kinetics of electromagnetic field in non-equilibrium plasma at the hydrodynamic stage of evolution was studied. In the approximation of a small correlation radius coupled oscillations of field correlations and hydrodynamic variables of plasma were investigated.

In our paper [4] the kinetics of electromagnetic field in a medium consisting of motionless two-level emitters distributed in the space with the density $n(x)$ was developed. The interaction between emitters and field was supposed to be weak (λ is its weakness parameter). The directions of dipole moments of emitters were considered to be equiprobable. Non-equilibrium field state was described by its average value $B_n(x,t) \equiv \xi_{1n}(x,t)$, $E_n(x,t) \equiv \xi_{2n}(x,t)$ and binary correlations $(\xi_{in}^x, \xi_{i'l}^{x'})_t$, defined for arbitrary local quantities $a(x)$, $b(x)$ by the general formula

$$(a^x, b^{x'})_t = \text{Sp } \rho(t) \{ \hat{a}(x), \hat{b}(x') \} / 2 - \text{Sp } \rho(t) \hat{a}(x) \text{Sp } \rho(t) \hat{b}(x') \quad (1)$$

($\hat{a}(x)$ and $\hat{b}(x)$ are the quantity operators, $\rho(t)$ - a statistical operator of the system). A state of the non-equilibrium system of emitters was described using their energy density $\varepsilon(x,t)$.

The aim of the present paper is to investigate the dynamics of such a system near the equilibrium in terms of the average field and its correlations. Preliminary results of the investigation were presented at the conference SPMTA-2012 [5].

The proposed research is relevant to the investigation of properties of emitted electromagnetic field in a superradiant state described by the Dicke type model. The quantum properties of the field are described by a binary and more complicated correlation functions. Our correlation functions (1) are one-to-one correspondent to ones discussed in quantum optics.

Hereafter the review of the theory developed in our paper [4] is given. The development of the theory of transversal modes of electromagnetic field started in the paper [6] is continued. On such a basis equilibrium correlations of electromagnetic field are calculated. Then the investigation of field correlation modes in the equilibrium medium of emitters is expounded. The last section is devoted to the discussion of coupled electromagnetic field correlations and non-equilibrium emitter medium. Presented here theory is the further development of our research in [6].

Basic equations of the theory

We restrict ourselves with considering transversal field dynamics. Average electromagnetic field obeys the usual Maxwell equations

$$\begin{aligned} \partial_t B_n(x,t) &= -c \text{rot}_n E(x,t), & \partial_t E_n(x,t) &= c \text{rot}_n B(x,t) - 4\pi J_n(x,t), \\ \text{div } B(x,t) &= 0, & \text{div } E(x,t) &= 4\pi \rho(x,t) \end{aligned} \quad (2)$$

where $J_n(x,t)$ and $\rho(x,t)$ are current and charge densities. The material equation connecting the current density and field with accuracy of order λ^2 takes the form

$$J_n(x,t) = \int d^3 x' \sigma(x-x', \varepsilon(x,t)) E_n(x',t) + c \int d^3 x' \chi(x-x', \varepsilon(x,t)) Z_n(x',t) \quad (3)$$

where $Z_n(x) \equiv \text{rot}_n B(x)$.

Fourier components $\sigma_k(\varepsilon)$, $\chi_k(\varepsilon)$ of the included kernels $\sigma(x, \varepsilon)$, $\chi(x, \varepsilon)$ (they are supposed to be known functions) are non-equilibrium generalization of the conductivity and magnetic susceptibility of the medium with taking into account spatial dispersion. In the developed theory the quantities $\sigma_k(\varepsilon)$, $\chi_k(\varepsilon)$ are of λ^2 order and do not depend linearly on the energy density ε . Equilibrium values of material coefficients are given by formulas $\sigma_k = \sigma_k(\varepsilon^{eq})$, $\chi_k = \chi_k(\varepsilon^{eq})/[1 - 4\pi\chi_k(\varepsilon^{eq})]$ since the definition $B_{nk} = \mu_k H_{nk}$, $\mu_k = 1 + 4\pi\chi_k$ (μ_k is magnetic permeability) is usually applied.

The Maxwell equations can be written more compactly in the form

$$\partial_t \xi_{in}^{\varepsilon}(x, t) = i \sum_{i'} \int dx' c_{in, i'l}(x - x') \xi_{i'l}^{\varepsilon}(x', t) - 4\pi J_{in}(x, t) \quad (4)$$

where we use the notations: $\hat{\xi}_{1n}^{\varepsilon}(x) \equiv \hat{B}_n(x)$, $\hat{\xi}_{2n}^{\varepsilon}(x) \equiv \hat{E}_n(x)$, $J_{1n}(x) \equiv 0$, $J_{2n}(x) \equiv J_n(x)$. Then the material equation (3) takes the form

$$J_{in}(x, t) = \sum_{i'} \int d^3 x' \sigma_{in, i'l}(x - x', \varepsilon(x)) \xi_{i'l}^{\varepsilon}(x', t). \quad (5)$$

Non-zero matrix components $c_{i'l}(x - x')$, $\sigma_{i'l}(x - x', \varepsilon)$, according to Eqs. (2) and (3), are given by formulas for their Fourier images

$$\begin{aligned} c_{1n, 2l}(k) &= -ik_m e_{nml}, & c_{2n, 1l}(k) &= ik_m e_{nml}; \\ \sigma_{2n, 2l}(k, \varepsilon) &= \sigma_k(\varepsilon), & \sigma_{2n, 1l}(k, \varepsilon) &= ice_{nml} k_m \chi_k(\varepsilon). \end{aligned} \quad (6)$$

The temporal equation for binary correlations (they are independent variables) has the form

$$\begin{aligned} \partial_t (\xi_{in}^{\varepsilon}, \xi_{i'l}^{\varepsilon})_t &= i \sum_{i''} \int d^3 x' c_{in, i''m}(x - x'') (\xi_{i''m}^{\varepsilon}, \xi_{i'l}^{\varepsilon})_t + i \sum_{i''} \int d^3 x' c_{i'l, i''m}(x - x'') (\xi_{in}^{\varepsilon}, \xi_{i''m}^{\varepsilon})_t - \\ &\quad - 4\pi (J_{in}^{\varepsilon}, \xi_{i'l}^{\varepsilon}) - 4\pi (\xi_{in}^{\varepsilon}, J_{i'l}^{\varepsilon}) \end{aligned} \quad (7)$$

The material equation for correlation current-field functions is given by the formula

$$(J_{in}^{\varepsilon}, \xi_{i'l}^{\varepsilon})_t = \sum_{i''} \int d^3 x'' \sigma_{in, i''m}(x - x'', \varepsilon(x)) (\xi_{i''m}^{\varepsilon}, \xi_{i'l}^{\varepsilon})_t + S_{in, i'l}(x - x', n(x)) \quad (8)$$

that matches the Onsager principle. The last term in (8) does not depend on time and is proportional to the emitter quantity density $n(x)$. Note that only the following its components differ from zero

$$S_{2n, 1l}(k, n) \equiv e_{nlm} k_m S_k(n), \quad S_{2n, 2l}(k, n) \equiv (\delta_{nl} - \hat{k}_n \hat{k}_l) T_k(n) \quad (9)$$

where $S_k(n)$, $T_k(n)$ are known functions of λ^2 order and $\hat{k}_l \equiv k_l / k$.

The temporal equation for the emitter energy density has the form

$$\partial_t \varepsilon(x, t) = (J_n^{\varepsilon}, E_n^{\varepsilon})_t + J_n(x, t) E_n(x, t) + R(n(x)) \quad (10)$$

where the last term correspond to the full dipole emission of the emitters under consideration

$$R(n) = -2\omega^4 n d^2 / 3\pi c^3. \quad (11)$$

Proposed in this section description of the electromagnetic field with using the relevant compact notation for the field, its correlations, and all material equations allows to conduct general investigation of the considered system.

Modes of transversal electromagnetic field in the equilibrium medium of emitters

According to Eqs. (2, 3), the transversal electromagnetic field, obey the equations

$$\partial_t B_{nk}^t = -ic[k, E_k^t]_n, \quad \partial_t E_{nk}^t = i \frac{c}{\mu_k} [k, B_k^t]_k - 4\pi \sigma_k E_{nk}^t. \quad (12)$$

The temporal equation for the electric field here has the form

$$\partial_t^2 E_{nk}^t + \partial_t E_{nk}^t 4\pi\sigma_k + E_{nk}^t \omega_k^2 / \mu_k = 0. \quad (13)$$

Its general solution is given by the formula

$$E_{nk}^t(t) = a_{nk}^t e^{z_{1k}^t t} + b_{nk}^t e^{z_{2k}^t t} \quad (14)$$

where a_{nk}^t and b_{nk}^t are vector fields independent of time, z_{1k} and z_{2k} are quantities defined by the formulas

$$z_{1k} = i\Omega_k - \gamma_k, \quad z_{2k} = -i\Omega_k - \gamma_k; \quad \Omega_k \equiv \sqrt{\omega_k^2 / \mu_k - (2\pi\sigma_k)^2}, \quad \gamma_k = 2\pi\sigma_k \quad (15)$$

($\omega_k \equiv ck$). According to Eqs. (12) and (14), the magnetic field is given by the expression

$$B_{nk}^t(t) = -\frac{ic}{z_{1k}} [k, a_k^t]_n e^{z_{1k}^t t} - \frac{ic}{z_{2k}} [k, b_k^t]_n e^{z_{2k}^t t}. \quad (16)$$

Expressions (14) and (16) can be regarded as a set of equations for the functions $a_{nk}^t e^{z_{1k}^t t}$ and $b_{nk}^t e^{z_{2k}^t t}$, thus obtaining

$$a_{nk}^t e^{z_{1k}^t t} = \frac{z_{1k}}{2i\Omega_k} E_{nk}^t(t) + \frac{c}{2i\Omega_k \mu_k} Z_{nk}^t(t), \quad b_{nk}^t e^{z_{2k}^t t} = -\frac{z_{2k}}{2i\Omega_k} E_{nk}^t(t) - \frac{c}{2i\Omega_k \mu_k} Z_{nk}^t(t). \quad (17)$$

Therefore right-hand sides of these relations are modes of the transversal electromagnetic field in the equilibrium medium. For our purposes the functions

$$\zeta_{ink}^t(t) \equiv E_{nk}^t(t) + \frac{c}{z_{ik} \mu_k} Z_{nk}^t(t), \quad \partial_t \zeta_{ink}^t(t) = z_{1k} \zeta_{ink}^t(t) \quad (18)$$

are convenient for using as modes (later only the transversal field and its correlations are considered, that is why the upper index t is omitted for simplicity). For further consideration it is convenient to introduce compact designations connecting the field modes with the field itself

$$\zeta_{ink} = \sum_{i'} R_{in,i'l}(k) \xi_{i'lk}, \quad \xi_{ink} = \sum_{i'} R_{in,i'l}^{-1}(k) \zeta_{i'lk}. \quad (19)$$

Appearing here matrixes have, according to (15), the following non-zero matrix elements

$$R_{in,1l}(k) = \frac{ic}{z_{ik} \mu_k} e_{nml} k_m, \quad R_{in,2l}(k) = \delta_{nl};$$

$$R_{1n,i'l}^{-1}(k) = (-1)^{i'} \frac{c}{2\Omega_k} e_{nml} k_m, \quad R_{2n,i'l}^{-1}(k) = (-1)^{i'} i \frac{z_{i'k}}{2\Omega_k} \delta_{nl}. \quad (20)$$

Now we substitute the formula (19) into Eq. (4) with the expression (5) for current and take into account the temporal equation for modes (18). Bearing in mind that field and its modes are arbitrary functions determined by the initial conditions, we come to the identity

$$\sum_{i''} a_{in,i''m}(k, \varepsilon^{eq}) R_{i''m,i'l}^{-1}(k) = R_{in,i'l}^{-1}(k) z_{i'l} \quad (21)$$

where the designation is used

$$a_{in,i'l}(k, \varepsilon) = ic_{in,i'l}(k) - 4\pi\sigma_{in,i'l}(k, \varepsilon). \quad (22)$$

From the relation (21) via a simple matrix multiplication we obtain the formula

$$\sum_{i''} R_{in,i''m}(k) a_{i''m,i'l}(k, \varepsilon^{eq}) = R_{in,i'l}(k) z_{i'l}. \quad (23)$$

These formula shows that $R_{in,i'l}(k)$ is a left eigenvector of the matrix $a_{in,i'l}(k, \varepsilon^{eq})$ determining the evolution of electromagnetic field in an equilibrium medium and

corresponds to an eigenvalue z_{ik} . Similarly, $R_{in,i'l}^{-1}(k)$ is a right eigenvector of this matrix and corresponds to the same eigenvalue $z_{i'k}$.

Equilibrium correlations of electromagnetic field

For simplicity let us consider equilibrium binary correlations of the transversal electromagnetic field restricting ourselves with the case of a uniform distribution of emitters in space. Since they do not depend on time, Eq. (7), with taking into account the material equation (8) and the definition (22), gives the relation

$$\begin{aligned} \sum_{i''} [a_{in,i''m}(k)(\xi_{i''m}^k, \xi_{i'l}^{k'})^{eq} + a_{i'l,i''m}(k)(\xi_{in}^k, \xi_{i''m}^{k'})^{eq}] = \\ = 4\pi V [S_{in,i'l}(k) + S_{i'l,in}(k')] \delta_{k',-k} \end{aligned} \quad (24)$$

(we use a periodical boundary conditions, V is a system volume). Now, taking into account the formulas (19) and (23), herefrom we find field mode correlations

$$\begin{aligned} (z_{ik} + z_{i'k'}) (\xi_{in}^k, \xi_{i'l}^{k'})^{eq} = \\ = 4\pi V \sum_{i_1 n_1 i_2 n_2} R_{in,i_1 n_1}(k) R_{i'l,i_2 n_2}(k') \{S_{i_1 n_1, i_2 n_2}(k) + S_{i_2 n_2, i_1 n_1}(k')\} \delta_{k',-k}. \end{aligned} \quad (25)$$

Actual expressions (9) and (20) for matrixes entering here give the following expressions for the binary correlation functions

$$\begin{aligned} (\xi_{in}^k, \xi_{i'l}^{k'})^{eq} = (\xi_{in}^k, \xi_{i'l}^{-k'})^{eq} \delta_{k',-k}, \\ (\xi_{in}^k, \xi_{i'l}^{-k'})^{eq} = V 4\pi (\delta_{nl} - \hat{k}_n \hat{k}_l) \left\{ \frac{2T_k(n)}{z_{ik} + z_{i'k}} + i \frac{\omega_k^2 S_k(n)}{c \mu_k z_{ik} z_{i'k}} \right\}. \end{aligned} \quad (26)$$

Here we make allowance that for the system under consideration [1] material coefficients $\sigma_k(\varepsilon)$, $\chi_k(\varepsilon)$ appearing in the material equation (3) and functions $S_k(n)$, $T_k(n)$ appearing in the material equation for correlations (8) are even functions of k_n

$$\sigma_{-k}(\varepsilon) = \sigma_k(\varepsilon), \quad \chi_{-k}(\varepsilon) = \chi_k(\varepsilon), \quad S_{-k}(n) = S_k(n), \quad T_{-k}(n) = T_k(n), \quad (27)$$

thus providing, in accordance with the formulas (15), the evenness of all the functions that are expressed through them

$$z_{i,-k} = z_{ik}, \quad \Omega_{-k} = \Omega_k, \quad \gamma_{-k} = \gamma_k, \quad \mu_{-k} = \mu_k \quad (28)$$

(see also (4) in the paragraph ahead). In fact, this result is connected with the rotational invariance of the considered quantities from which their dependence on $|k|$ follows.

Concept of binary correlation waves

In the spatially uniform case the nonequilibrium correlation function $(\xi_{in}^x, \xi_{i'l}^{x'})_t$ depends only on the difference of coordinates, therefore their Fourier components possess the property $(\xi_{in}^k, \xi_{i'l}^{k'})_t \sim \delta_{k',-k}$. Hence, the spatial non-uniformity of correlations is connected with the dependence of Fourier components $(\xi_{in}^{p+k/2}, \xi_{i'l}^{-p+k/2})_t$ on a vector k_l that can be regarded as a wave one and indexes i, n, i', l, p_l should be considered to be component numbers. Obviously, correlation functions of field modes $f_{in,i'l}^p(k, t) \equiv (\xi_{in}^{p+k/2}, \xi_{i'l}^{-p+k/2})_t$ can be used instead of correlation modes of field itself. Low-amplitude motions of electromagnetic field correlations can be described by deviations from their equilibrium values

$$\delta(\xi_{in}^k, \xi_{i'l}^{k'})_t = (\xi_{in}^k, \xi_{i'l}^{k'})_t - (\xi_{in}^k, \xi_{i'l}^{k'})^{eq}. \quad (29)$$

According to Eqs. (7) and (8) and the definition (22), in the equilibrium medium of emitters such quantities obey the evolution equation

$$\partial_t \delta(\xi_{in}^k, \xi_{i'l}^{k'})_t = \sum_{i''} [a_{in,i''m}(k, \varepsilon^{eq}) \delta(\xi_{i''m}^k, \xi_{i'l}^{k'})_t + a_{i'l,i''m}(k', \varepsilon^{eq}) \delta(\xi_{in}^k, \xi_{i''m}^{k'})_t]. \quad (30)$$

Applying (19) and (23), we find from here an evolution equation for field mode correlations

$$\partial_t \delta(\xi_{in}^k, \xi_{i'l}^{k'})_t = (z_{ik} + z_{i'l}^{k'}) \delta(\xi_{in}^k, \xi_{i'l}^{k'})_t, \quad (31)$$

i.e. they are also modes of correlations. The dispersion law for the modes of correlations in an equilibrium medium is evident from the relation

$$\partial_t \delta f_{in,i'l}^p(k, t) = (z_{i,p+k/2} + z_{i',-p+k/2}) \delta f_{in,i'l}^p(k, t) \quad (32)$$

$$\text{where } \delta f_p^{in,i'l}(k, t) \equiv \delta(\xi_{in}^{p+k/2}, \xi_{i'l}^{-p+k/2})_t. \quad (33)$$

At small wave vectors we have, according to the formulas (15) and (28):

mode	dispersion law
$\delta f_{1n,1l}^p(k, t)$	$i2\Omega_p - 2\gamma_p + O(k^2),$
$\delta f_{2n,2l}^p(k, t)$	$-i2\Omega_p - 2\gamma_p + O(k^2),$
$\delta f_{1n,2l}^p(k, t)$	$ic(p) \hat{p}_n k_n - 2\gamma_p + O(k^2),$
$\delta f_{2n,1l}^p(k, t)$	$-ic(p) \hat{p}_n k_n - 2\gamma_p + O(k^2)$

(34)

($c(p) \hat{p}_n \equiv \partial \Omega_p / \partial p_n$). Thus, in the limit of small wave vectors, the first two modes of correlations are damped oscillations and the next two modes describe decaying waves with the propagation velocity $\pm c(p) \hat{p}_n$ depending on the direction of the vector p_n .

Coupled oscillations of field correlations and a medium consisting of emitters

Let us consider coupled oscillations of field correlations and medium near the equilibrium. Coupled oscillations of an average field are absent according to (4) and (5) since in equilibrium the average field equals to zero $\xi_{in}^{eq} = 0$. To derive an equation for correlations we proceed from the relations (7), (8), (22), thus obtaining the generalization of Eq. (30)

$$\begin{aligned} \partial_t \delta(\xi_{in}^k, \xi_{i'l}^{k'})_t &= \sum_{i''} [a_{in,i''m}(k, \varepsilon^{eq}) \delta(\xi_{i''m}^k, \xi_{i'l}^{k'})_t + a_{i'l,i''m}(k', \varepsilon^{eq}) \delta(\xi_{in}^k, \xi_{i''m}^{k'})_t] + \\ &+ \frac{1}{\varepsilon^{eq} V} \sum_{i''} \delta \varepsilon_{k+k'} \sigma_{in,i''m}(-k', \varepsilon^{eq}) (\xi_{i''m}^{-k'}, \xi_{i'l}^{k'})^{eq} + \\ &+ \frac{1}{\varepsilon^{eq} V} \sum_{i''} \delta \varepsilon_{k+k'} \sigma_{i'l,i''m}(-k, \varepsilon^{eq}) (\xi_{in}^k, \xi_{i''m}^{-k})^{eq} \end{aligned} \quad (35)$$

where the proportionality of $\sigma_{in,i'l}(k, \varepsilon)$ to ε is taken into account. Eq. (10) for the density of emitter energy near the equilibrium $\delta \varepsilon(x, t) = \varepsilon(x, t) - \varepsilon^{eq}$ acquires the form taking into account Eq. (5)

$$\partial_t \delta \varepsilon_k = \frac{1}{\varepsilon^{eq} V^2} \delta \varepsilon_k \sum_{i'', k'} \sigma_{in,i'l}(k', \varepsilon^{eq}) (\xi_{i'l}^{k'}, \xi_{in}^{-k'})^{eq} + \frac{1}{V} \sum_{i'', k'} \sigma_{in,i'l}(k', \varepsilon^{eq}) \delta(\xi_{i'l}^{k'}, \xi_{in}^{-k'}). \quad (36)$$

In terms of mode correlations, these equations, according to the formulas (19) and (23), can be rewritten as follows

$$\begin{aligned}
 & \partial_t \delta(\zeta_{in}^k, \zeta_{i'l}^{k'})_t = (z_{ik} + z_{i'k'}) \delta(\zeta_{in}^k, \zeta_{i'l}^{k'})_t + \\
 & + \frac{1}{\varepsilon^{eq} V} \sum_{i_1 i_2 i'} \delta \varepsilon_{k+k'} R_{in, i_1 n_1}(k) \sigma_{i_1 n_1, i' m}(-k', \varepsilon^{eq}) R_{i' m, i_2 n_2}^{-1}(-k') (\zeta_{i_2 n_2}^{-k'}, \zeta_{i'l}^{k'})^{eq} + \\
 & + \frac{1}{\varepsilon^{eq} V} \sum_{i_1 i_2 i'} \delta \varepsilon_{k+k'} R_{i'l, i_1 n_1}(k') \sigma_{i_1 n_1, i' m}(-k, \varepsilon^{eq}) R_{i' m, i_2 n_2}^{-1}(-k) (\zeta_{in}^k, \zeta_{i_2 n_2}^{-k})^{eq}. \\
 \partial_t \delta \varepsilon_k & = \frac{1}{\varepsilon^{eq} V^2} \delta \varepsilon_k \sum_{i_1 i_2 i', k'} \sigma_{in, i'l}(k', \varepsilon^{eq}) R_{i'l, i_1 n_1}^{-1}(k') R_{in, i_2 n_2}^{-1}(-k') (\zeta_{i_1 n_1}^{k'}, \zeta_{i_2 n_2}^{-k'})^{eq} + \\
 & + \frac{1}{V} \sum_{i_1 i_2 i', k'} \sigma_{in, i'l}(k', \varepsilon^{eq}) R_{i'l, i_1 n_1}^{-1}(k') R_{in, i_2 n_2}^{-1}(k-k') \delta(\zeta_{i_1 n_1}^{k'}, \zeta_{i_2 n_2}^{k-k'}). \quad (35)
 \end{aligned}$$

Herefrom with taking into account the definition (33), we obtain the coupled set of equations for correlations of field modes $\delta f_{in, i'l}^p(k, t)$ and medium energy density $\delta \varepsilon_k(t)$

$$\partial_t \delta f_{in, i'l}^p(k, t) = \{z_{i, p+k/2} + z_{i', -p+k/2}\} \delta f_{in, i'l}^p(k, t) + M_{in, i'l}^p(k) \delta \varepsilon_k(t),$$

$$\partial_t \delta \varepsilon_k(t) = \sum_{i'l} \int d^3 p N_{in, i'l}^p(k) \delta f_{in, i'l}^p(k, t) + \nu \delta \varepsilon_k(t). \quad (36)$$

The equations include coefficients defined by the formulas

$$\begin{aligned}
 M_{in, i'l}^p(k) & = \frac{1}{\varepsilon^{eq} V} \sum_{i_1 i_2 i'} R_{in, i_1 n_1}(p + \frac{k}{2}) \sigma_{i_1 n_1, i' m}(p - \frac{k}{2}, \varepsilon^{eq}) R_{i' m, i_2 n_2}^{-1}(p - \frac{k}{2}) \times \\
 & \times (\zeta_{i_2 n_2}^{p-k/2}, \zeta_{i'l}^{-p+k/2})^{eq} + \\
 & + \frac{1}{\varepsilon^{eq} V} \sum_{i_1 i_2 i'} R_{i'l, i_1 n_1}(-p + \frac{k}{2}) \sigma_{i_1 n_1, i' m}(-p - \frac{k}{2}, \varepsilon^{eq}) R_{i' m, i_2 n_2}^{-1}(-p - \frac{k}{2}) \times \\
 & \times (\zeta_{in}^{p+k/2}, \zeta_{i_2 n_2}^{-p-k/2})^{eq}, \quad (37)
 \end{aligned}$$

$$\nu = \frac{1}{\varepsilon^{eq} V (2\pi)^3} \sum_{i_1 i_2 i'} \int d^3 k' \sigma_{in, i'l}(k', \varepsilon^{eq}) R_{in, i_1 n_1}^{-1}(-k') R_{i'l, i_2 n_2}^{-1}(k') (\zeta_{i_2 n_2}^{k'}, \zeta_{i_1 n_1}^{-k'})^{eq}, \quad (38)$$

$$N_{in, i'l}^p(k) = \frac{1}{(2\pi)^3} \sum_{i_1 i_2} \sigma_{i_1 n_1, i_2 n_2}(p + \frac{k}{2}, \varepsilon^{eq}) R_{i_2 n_2, in}^{-1}(p + \frac{k}{2}) R_{i_1 n_1, i'l}^{-1}(-p + \frac{k}{2}). \quad (39)$$

Notice that equilibrium correlation functions, according to the expressions (9) and (26), are proportional to the system volume and have the second order in interaction. Therefore in the set of equations (36) coefficients are of the following orders

$$M_{in,i'l}^p(k) \sim \lambda^4, \quad N_{in,i'l}^p(k) \sim \lambda^2, \quad \nu \sim \lambda^4. \quad (40)$$

and do not depend on volume in the thermodynamic limit. The solution of the set (36) can be searched for in the form $\delta f_{in,i'l}^p(k,t) = C_{in,i'l}^p(k)e^{z_t}$, $\delta \varepsilon_k(t) = C_k e^{z_t}$, it gives the following dispersion equation

$$z = \nu + \sum_{ii'} \int d^3 p \frac{M_{in,i'l}^p(k) N_{in,i'l}^p(k)}{z - z_{i,p+k/2} - z_{i',-p+k/2}}. \quad (41)$$

Its analysis can be based on the account of estimations (40) and on the detailed analysis for the case of small wave vectors; this will be done in another place.

Here we restrict ourselves to the analysis of (36) in the elementary perturbation theory in weak interaction. In order to simplify the formulas, we analyze a set of equations that are similar to the set (36)

$$\dot{x}_i = z_i x_i + a_i y, \quad \dot{y} = \sum_i b_i x_i + c y \quad (42)$$

where coefficients have the following order in λ : $a_i \sim \lambda^4$, $b_i \sim \lambda^2$, $c \sim \lambda^4$. We search for a solution in the form of series in powers of λ^2 . Quantities z_i in Eq. (42) are analogues to quantities $z_{i,p+k/2} + z_{i',-p+k/2}$ in the set (36), the last ones can also be expanded in λ according to the formulas (15). However, we shall not expand z_i in a series in λ while constructing perturbation theory for the set (42). It will allow avoiding partially time secular terms arising in the perturbation theory. Simple calculations give

$$x_i = x_{i0} e^{t z_i} + y_0 \frac{a_i}{z_i} (e^{t z_i} - 1) + O(\lambda^6), \quad y = y_0 + \sum_i \frac{x_{i0} b_i}{z_i} (e^{t z_i} - 1) + c y_0 t + O(\lambda^6) \quad (43)$$

where $x_{i0} \equiv x_i|_{t=0}$, $y_0 \equiv y|_{t=0}$. Secular term presence in the second expression is physically connected with the fact that really corrections to the frequencies z_i occur. Some interesting conclusions can be made from (43). If at the initial time moment the subsystem of field correlations is equilibrium and $x_{i0} = 0$, at the next time moments non-equilibrium correlations take place

$$x_{i0} = 0 \quad \Rightarrow \quad x_i = y_0 \frac{a_i}{z_i} (e^{t z_i} - 1) + O(\lambda^6), \quad y = y_0 + \sum_i c y_0 t + O(\lambda^6). \quad (44)$$

It means that the medium of two-level emitters radiates waves of correlations. Alternatively, if at the initial time moment the subsystem of emitters is equilibrium and $y_0 = 0$, it is excited under the impact of correlation waves

$$y_0 = 0 \quad \Rightarrow \quad x_i = x_{i0} e^{t z_i} + O(\lambda^6), \quad y = \sum_i \frac{x_{i0} b_i}{z_i} (e^{t z_i} - 1) + O(\lambda^6). \quad (45)$$

Obtained results show the non-trivial dynamics of the system of emitters and electromagnetic field. Near the equilibrium emitters do not interact with an average field, but interact with binary correlations of the field.

Conclusions

Modes of average transversal electromagnetic field and its correlations in a medium consisting of two-level emitters described by the Dicke type model have been investigated. Four types of correlation modes in the equilibrium medium of emitters have been found. Among them two types of correlation modes correspond to a damping oscillation process and two other correlation modes correspond to decaying waves. In this connection the concept of electromagnetic correlation waves has been proposed. In some sense these waves are close to secondary waves discussed in the condensed matter theory. Particularly, we mean the second sound in a superfluid liquid that can be considered as sound waves in the phonon subsystem (see, for example, [7]).

In the case of a nonequilibrium medium, its coupled oscillations with the oscillations of the field correlations have been studied. The phenomenon of field correlations arising (correlation waves radiation) in the process of emitter medium evolution has been predicted. On the other hand, waves of correlations can break equilibrium state of the emitter subsystem. The obtained dispersion equation (41) is similar to the one investigated in the mode-mode coupling theory. An approach developed in the last theory will be applied to our analysis of this equation in a subsequent paper.

References

1. **Peletminskii S.V.** Low-frequency asymptotics of electrodynamic Green functions / S.V. Peletminskii, V.I. Prikhod'ko, V.S. Shchokolov // Theoretical and Mathematical Physics. – 1975. – Vol. 25, No. 1. – P. 70-79 (in Russian).
2. **Sokolovsky A.I.** Kinetic theory of electromagnetic processes in equilibrium medium / A.I. Sokolovsky, A.A. Stupka // Visnyk of Dnipropetrovets'k University. Physics, Radio Electronics. – 2003. – №.10. – P. 63-70 (in Russian).
3. **Sokolovsky A.I.** Electromagnetic field correlations and sound waves / A.I. Sokolovsky, A.A. Stupka // Problems of Atomic Science and Technology. – 2007. – No. 3(2). – P. 335-339.
4. **Lyagushyn S.F.** Kinetics of system of emitters and nonequilibrium electromagnetic field / S.F. Lyagushyn, A.I. Sokolovsky // Physics of Particles and Nuclei. – 2010. – Vol. 41, No. 7. – P. 1035-1038.
5. **Lyagushyn S.F.** Waves of correlations of electromagnetic field in nonequilibrium emitter medium / S.F. Lyagushyn, Yu.M. Salyuk, A.I. Sokolovsky // 4th International Conference "Statistical Physics: Modern Trends and Applications" (Lviv, Ukraine, 3-6 July, 2012), Book of Abstracts. 2012. – P.140.
6. **Lyagushyn S.F.** Electromagnetic waves in medium consisting of two-level emitters / S.F. Lyagushyn, Yu.M. Salyuk, A.I. Sokolovsky // Proceedings of 2012 International Conference on Mathematical Methods in Electromagnetic Theory (Kharkiv, Ukraine, August 28-30, 2012), Proceedings CD-ROM, ISBN 978-1-4673-4479-1, NCE-5. – 2012. – P. 205-208.
7. **Khalatnikov I.M.** Theory of superfluidity / I.M. Khalatnikov, M.: Nauka, 1971, 320 p. (in Russian).

Received 13.07.2013.

V. V. Skalozub, E. V. Tsygankov

Oles Honchar Dnipropetrovsk National University

REAL-TIME FORMALISM FOR POLARIZATION OPERATOR OF A CHARGED SCALAR PARTICLE IN EXTERNAL ELECTROMAGNETIC FIELD

We extend the Keldysh real-time formalism to investigate the retarded polarization operator of a charged scalar particle in a statistical system that under the action of an external field deviates to any extent from the state of thermodynamic equilibrium. We consider the peculiarities of the interaction picture that exactly accounts for external field, the so-called Furry picture, and the perturbation theory of electrodynamics for nonequilibrium processes. The interaction Hamiltonian, S-matrix, and density matrix in the external electromagnetic field are constructed. We use these quantities to define the expectation values and Green's functions. The detailed analysis of the expansion of the casual Green function up to the e^2 terms is performed. We obtain the one-loop retarded polarization operator of charged scalar particles in the coordinate representation. The desired expression is presented as the sum of three terms given by means of integral equations. Some applications of the obtained results to the problem of the energy spectra of charged particles at external conditions and further prospects are discussed.

Keywords: scalar electrodynamics, polarization operator, Keldysh formalism, finite temperature, external electromagnetic field.

Мы расширяем формализм реального времени Келдыша для исследования поляризационного оператора заряженных скалярных частиц в статистической системе, которая под действием внешнего поля может сколь угодно сильно отклоняться от состояния термодинамического равновесия. Рассмотрены особенности построения представления взаимодействия, которое точно учитывает внешнее поле, так называемая картина Фарри, и теории возмущений скалярной электродинамики для неравновесных процессов. Построен гамильтониан взаимодействия, S-матрица и матрица плотности во внешнем электромагнитном поле. С помощью последних определено среднее значение операторов физических величин и функции Грина. Проведен детальный анализ членов разложения порядка e^2 причинной функции Грина, на основе чего была найдена форма однопетлевого запаздывающего поляризационного оператора в координатном представлении. Искомое выражение является суммой трех слагаемых, каждое из которых определяется интегральным соотношением. Обсуждаются дальнейшие перспективы и некоторые приложения полученных результатов к задаче поиска спектров заряженных частиц во внешних условиях.

Ключевые слова: скалярная электродинамика, поляризационный оператор, формализм Келдыша, конечная температура, внешнее электромагнитное поле.

Ми розширюємо формалізм реального часу Келдиша для дослідження поляризаційного оператора заряджених скалярних частинок у статистичній системі, яка під дією зовнішнього поля може як завгодно сильно відхилятися від стану термодинамічної рівноваги. Розглянуто особливості побудови представлення взаємодії, яке точно враховує зовнішнє поле, так звана картина Фаррі, та теорії збурень скалярної електродинаміки для нерівноважних процесів. Побудовано гамильтоніан взаємодії, S-матриця та матриця густини у присутності зовнішнього електромагнітного поля. Останні було використано для визначення середніх від операторів фізичних величин і функції Гріна. Проведено детальний аналіз членів розвинення порядку e^2 причинної функції Гріна, на основі чого було знайдено форму однопетельного поляризаційного оператора, що запізнюється, в координатному представленні. Шуканий вираз є сумою трьох доданків, кожен з яких визначено інтегральним співвідношенням. Обговорюються подальші перспективи та деякі застосування отриманих результатів до задачі пошуку спектрів енергії частинок у зовнішніх умовах.

Ключові слова: скалярна електродинаміка, поляризаційний оператор, формалізм Келдиша, скінченна температура, зовнішнє електромагнітне поле.

Introduction

Spectra of charged particles in external electromagnetic fields at finite temperature are important objects having various applications. They allow calculation and investigation of all thermodynamic functions of many-particle systems. Usually, to investigate a spectrum, the imaginary time formalism of finite temperature field theory is applied. However, in this formalism to perform an analytic continuation and derive spectrum by means of functional equations, an expression of interest has to contain a convenient integral representation (such as Fock-Schwinger proper time representation). Because of such difficulty, within this approach, the spectrum of gluons at finite temperature in the presence of chromomagnetic fields was calculated only for some special cases [1 - 3]. We are going here to apply an alternative approach developed already by Keldysh [4] and Schwinger [5] in studies on nonequilibrium quantum statistics. This method is out of technical difficulties related with the analytic continuation.

In reality, an environment considered is realized in heavy ion collision experiments at RHIC and LHC where very strong magnetic field are generated [6, 7]. The presence of magnetic field can be a source of properties of quark-gluon plasma discovered in modern experiments. So, the working out of formalism convenient in the described background is of interest.

In the present paper, to develop formalism, we investigate the case of scalar electrodynamics. At first, we consider the Keldysh formalism in the presence of external conditions. Further the perturbative analysis of exact two-point Green function is performed and the one-loop polarization operator of a charged scalar particle is calculated.

Scalar electrodynamics at external conditions

In the present section we develop the Keldysh formalism for scalar electrodynamics in an external field considering the one-loop polarization operator of a charged scalar particle as example.

The Lagrangian of a charged spinless particle in the external field reads

$$L = (\partial_\mu - ieA_\mu - ieA_\mu^{ext})^* \varphi^+(x) (\partial_\mu - ieA_\mu - ieA_\mu^{ext}) \varphi(x) - m^2 \varphi^+(x) \varphi(x) - \frac{1}{4} F_{\mu\nu} F^{\mu\nu}, \quad (1)$$

$$F_{\mu\nu} = \partial_\mu A_\nu - \partial_\nu A_\mu, \quad e = |e|, \quad g^{\mu\nu} = \text{diag}(1, -1, -1, -1)$$

where A_μ is potential of radiation field, A_μ^{ext} denotes potential of external electromagnetic field, satisfying the equation of motion $\partial_\mu F_{ext}^{\mu\nu} = 0$.

We present the Lagrangian as the sum of three terms

$$L = L_0^\gamma + L_0 + L_{int}.$$

They are as follows

$$L_0 = (\partial_\mu - ieA_\mu)^* \varphi^+(x) (\partial_\mu - ieA_\mu) \varphi(x) - m^2 \varphi^+(x) \varphi(x)$$

is the Lagrangian of scalar particle in the external field,

$$L_0^\gamma = -\frac{1}{4} F_{\mu\nu} F^{\mu\nu}$$

is the Lagrangian of free radiation field,

$$L_{int} = ie\varphi^+ D_\mu \varphi \cdot A^\mu - e^2 \varphi^+ \varphi A^2$$

is the interaction Lagrangian where

$$\varphi^+ D_\mu \varphi = -(\partial_\mu - ieA_\mu^{ext})^* \varphi^+ \varphi + \varphi^+ (\partial_\mu - ieA_\mu^{ext}) \varphi.$$

We define canonical momenta and introduce interaction Hamiltonian

$$H = \int d^3x (\pi\pi^+ + ieA_0^{ext} (\pi\varphi - \pi^+\varphi^+) + (\vec{\nabla} + ie\vec{A}_{ext})\varphi^+ (\vec{\nabla} - ie\vec{A}_{ext})\varphi - m^2\varphi^+\varphi + ieA_0(\pi\varphi - \pi^+\varphi^+) + ie\vec{A}\varphi^+ (\vec{\nabla} - ie\vec{A}^{ext})\varphi - ie(\vec{\nabla} + ie\vec{A}_{ext})\varphi^+ A_{ext}\varphi + e^2\varphi^+\varphi\vec{A}^2) + H_0^{\gamma} \quad (2)$$

Note the relation between interaction Lagrangian and Hamiltonian,

$$H_{int} = -L_{int} - e^2 A_0^2 \varphi^+ \varphi. \quad (3)$$

As we see, these functions differ by a non-covariant term, as is usual for time-dependent interactions [8].

Scalar electrodynamics in external fields at finite temperature

Following [4], we define the density matrix

$$i \frac{\partial \rho(t)}{\partial t} = H_{int}(t)\rho(t) - \rho(t)H_{int}(t) \quad (4)$$

with boundary conditions

$$\rho(-\infty) = \rho_0 = \exp \frac{\Omega_0 - H_0(-\infty) - H_0^{\gamma}(-\infty)}{kT}$$

where Hamiltonians are defined according to the previous section.

The complete set of wave functions in magnetic field is the solution of the equation

$$((\hat{p}_\mu + eA^{ext})^2 - m^2)\varphi_n(x) = 0, \\ A_\mu^{ext} = (0, 0, H \cdot x, 0).$$

We split the wave functions of stationary states φ_n with defined momenta p_y, p_z , and energy

$$\varepsilon_n^\pm = \pm \sqrt{p_z^2 + m^2 + |e|(2n+1)}, \\ \varphi_n = e^{-ie_n^\pm t + ip_y y + ip_z z} f_n(x)$$

in two sets. The first set contains wave functions with positive frequencies, the second one - with negative frequencies. We denote them as $\varphi_n^\pm(x)$. Field operators φ and φ^+ are of the form

$$\varphi_0(x) = \sum_n (\varphi_n^+(x)a_n^- + \varphi_n^-(x)b_n^+), \\ \varphi_0^+(x) = \sum_n (\varphi_n^{+*}(x)a_n^+ + \varphi_n^{-*}(x)b_n^-),$$

and a_n^\pm, b_n^\pm satisfy the commutation relations for Bose-operators. Field operators satisfy the equation

$$i \frac{\partial \varphi_0}{\partial t} = [\varphi_0, H_0].$$

These operators and operators of radiation field A_μ form the interaction picture of scalar electrodynamics in an external field (so-called Furry picture).

We solve the density matrix equation with S-matrix

$$S(t, -\infty) = T \exp(-i \int_{-\infty}^t H_{int}(t') dt').$$

Density matrix at time t is

$$\rho(t) = S(t, -\infty)\rho(t)S^+(t, \infty).$$

In what follows we consider the statistical averages of operator products taken at various time moments. So it is convenient to carry-over the time dependence of density matrix to operators, therefore we switch into the Heisenberg picture. We set density matrix at time $t = 0$ accounting for all changes from the moment of switching the interaction on:

$$\rho = \rho(0) = S(0, -\infty)\rho(t)S^+(0, \infty).$$

Now we use the operators which at $t = 0$ are equal to the free ones because the density matrix is defined as $\rho(0)$

$$\varphi(x) = S(0, x)\varphi_0(x)S(x, 0)$$

where, by definition,

$$S(t', t) = T \exp\left(-i \int_t^{t'} H_{int}(t'') dt''\right) = S(t', -\infty)S^+(t, -\infty).$$

Statistical average of the T -products of Heisenberg operators can be transformed into the form

$$Tr(\rho A(t)B(t')...) = Tr(\rho_0 T_c(A_0(t)B_0(t')...S_c)), \quad (5)$$

where T_c stands for ordering along the line which runs from $-\infty$, passes through the points $t, t' \dots$, runs to $+\infty$ and then returns back to $-\infty$.

The statistical averages of the T -products for operators of scalar and electromagnetic fields in the interaction picture

$$\begin{aligned} & Tr(\rho_0 T(\varphi(x_1)\varphi(x_2)\dots\varphi(x_n)\varphi^+(x_1)\varphi^+(x_2)\dots\varphi^+(x_n))) \\ & Tr(\rho_0 T(A_\mu(x_1)\dots A_\nu(x_{2n}))) \end{aligned}$$

can be reduced to sums of the products of pairs of these operators [9].

The Green functions of scalar field φ in the interaction picture are defined as follows

$$G_0^F(t_+\vec{r}, t'_+\vec{r}') = -iTr(\rho_0 T_c(\varphi_0(t_+\vec{r})\varphi_0^+(t'_+\vec{r}')) = -iTr(\rho_0 T(\varphi_0(t_+\vec{r})\varphi_0^+(t'_+\vec{r}'))),$$

$$G_0^{\tilde{F}}(t_-\vec{r}, t'_-\vec{r}') = -iTr(\rho_0 T_c(\varphi_0(t_-\vec{r})\varphi_0^+(t'_-\vec{r}')) = -iTr(\rho_0 \tilde{T}(\varphi_0(t_-\vec{r})\varphi_0^+(t'_-\vec{r}'))),$$

$$G_0^-(t_-\vec{r}, t'_+\vec{r}') = -iTr(\rho_0 T_c(\varphi_0(t_-\vec{r})\varphi_0^+(t'_+\vec{r}')) = -iTr(\rho_0 \varphi_0(t_-\vec{r})\varphi_0^+(t'_+\vec{r}'))),$$

$$G_0^+(t_+\vec{r}, t'_-\vec{r}') = -iTr(\rho_0 T_c(\varphi_0(t_+\vec{r})\varphi_0^+(t'_-\vec{r}')) = -iTr(\rho_0 \varphi_0^+(t'_-\vec{r}')\varphi_0(t_+\vec{r}'))$$

where t_+ stands for the point on the positive branch of integration line, t_- stands for the point on the negative one, and \tilde{T} denotes anti-time-ordering operator.

Exact Green's functions are defined as

$$G^F(t_+\vec{r}, t'_+\vec{r}') = -iTr(\rho_0 T_c(\phi_0(t_+\vec{r})\phi_0^+(t'_+\vec{r}')S_c)),$$

$$G^{\tilde{F}}(t_-\vec{r}, t'_-\vec{r}') = -iTr(\rho_0 T_c(\phi_0(t_-\vec{r})\phi_0^+(t'_-\vec{r}')S_c)) \quad (6)$$

$$G^\pm(t_\pm\vec{r}, t'_\mp\vec{r}') = -iTr(\rho_0 T_c(\phi_0(t_\pm\vec{r})\phi_0^+(t'_\mp\vec{r}')S_c)).$$

The results of this section are applied to calculate the one-loop polarization operator below.

Retarded polarization operator in order e^2

To obtain the particle energy spectrum, we investigate the poles of the full retarded Green function. One can derive it by solving the Schwinger-Dyson equation where the one-loop retarded polarization operator is taken into account. The similar method was applied to find the spectrum of QGP problem in Ref. [10].

The polarization operator and Green function are related by the Schwinger-Dyson equation

$$G(x, x') = G_0(x, x') + \int dy_1 dy_2 G_0(x, y_1) \Pi(y_1, y_2) G(y_2, x')$$

where

$$G = \begin{pmatrix} G^F & G^+ \\ G^- & G^{\tilde{F}} \end{pmatrix}, \quad G_0 = \begin{pmatrix} G_0^F & G_0^+ \\ G_0^- & G_0^{\tilde{F}} \end{pmatrix}, \quad \Pi = \begin{pmatrix} \Pi^F & \Pi^+ \\ \Pi^- & \Pi^{\tilde{F}} \end{pmatrix}.$$

Considering this equation in the order e^2 , we substitute $G(y_2, x')$ to $G_0(y_2, x')$ under the sign of integration.

$$\begin{aligned} G^{(2)}(x, x') = & \int dy_1 dy_2 (G^F(x, y_1) \Pi^F(y_1, y_2) G^F(y_2, x') + \\ & + G^+(x, y_1) \Pi^-(y_1, y_2) G^F(y_2, x') + G^F(x, y_1) \Pi^+(y_1, y_2) G^-(y_2, x') + \\ & + G^+(x, y_1) \Pi^{\tilde{F}}(y_1, y_2) G^-(y_2, x')). \end{aligned} \quad (7)$$

We consider $G^F(x, x')$ in order e^2 to obtain the components of the polarization operator.

$$\begin{aligned} G_0^F(t_+, \vec{r}, t'_+, \vec{r}') = & -i \text{Tr}(\rho_0 T_c(\varphi_0(t_+, \vec{r}) \varphi_0^+(t'_+, \vec{r}') S_c)), \\ S = T \exp & \left(i \int_{-\infty}^{\infty} L_{int}(t) \right), \quad \tilde{T} = \tilde{T} \exp \left(-i \int_{-\infty}^{\infty} L_{int}(t) \right), \\ G^{(2)}(x, x') = & -i \text{Tr}(\rho_0 \int dy_1 dy_2 (T(\varphi_0(x) \varphi_0^+(x') \frac{i^2}{2!} L_{int}^{(1)}(y_1) L_{int}^{(1)}(y_2)) + \\ & + \tilde{T}(\frac{(-i)^2}{2!} L_{int}^{(1)}(y_1) L_{int}^{(1)}(y_2)) T(\varphi_0(x) \varphi_0^+(x')) + \\ & + \tilde{T}(-i L_{int}^{(1)}(y_1)) T(\varphi_0(x) \varphi_0^+(x') i L_{int}^{(1)}(y_2))) + \\ & + \rho_0 \int dy_1 (T(\varphi_0(x) \varphi_0^+(x') i L_{int}^{(2)}(y_1)) + \tilde{T}(i L_{int}^{(2)}(y_1)) T(\varphi_0(x) \varphi_0^+(x'))) \end{aligned} \quad (8)$$

Let us turn to the first term of this expression

$$\begin{aligned} & -i \text{Tr} \rho_0 \int dy_1 dy_2 T(\varphi_0(x) \varphi_0^+(x') \frac{i^2}{2!} L_{int}^{(1)}(y_1) L_{int}^{(1)}(y_2)) = \\ & = -i \frac{i^2}{2} (ie)^2 \int dy_1 dy_2 (2D_0^{F\mu\nu}(y_1, y_2) \cdot G_0^F(x, y_1) D^\mu G_0^F(y_1, y_2) D^\nu G_0^F(y_2, x') + \\ & + G_0^F(x, y_1) D^\mu G_0^F(y_1, x') \cdot 2D_0^{F\mu\nu}(y_1, y_2) \cdot (-i \text{Tr}(\rho_0 T(\varphi_0(y_2) D^\nu \varphi_0^+(y_2)))) + \\ & + G_0^F(x, x') \frac{i^2}{2} \int dy_1 dy_2 \text{Tr}(\rho_0 (L_{int}^{(1)}(y_1) L_{int}^{(1)}(y_2))) \end{aligned} \quad (9)$$

The last expression can be presented as the sum of diagrams in Fig. 1.

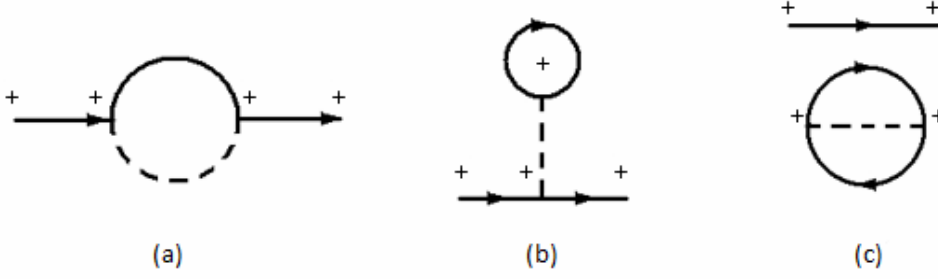


Fig.1 One-loop contributions in Π^F coming from $L_{int}^{(1)}$.

Solid and crossed lines correspond to Green's function of scalar particle and photon respectively.

Sign «+» denotes the vertex on the positive branch and «-» – on the negative one.

A type (b) diagram equals to zero in a constant homogeneous external field because the particle 4-momentum is conserved [11]. The disconnected diagrams cancel each other out. Hence, we obtain

$$\begin{aligned} \int dy_1 dy_2 G^F(x, y_1) \Pi_{(1)}^F(y_1, y_2) G^F(y_2, x') = \\ = ie^2 \int dy_1 dy_2 D_0^{F\mu\nu}(y_1, y_2) \cdot G_0^F(x, y_1) D^\mu G_0^F(y_1, y_2) D^\nu G_0^F(y_2, x') \end{aligned} \quad (10)$$

where $\Pi_{(1)}^F(y_1, y_2)$ in Eq. (7), is a contribution to $\Pi^F(y_1, y_2)$ coming from $L_{int}^{(1)}(y_1)$.

We denote $Tr(\rho_0 \dots) \equiv \langle \dots \rangle_0$ for convenience.

We rewrite the next term of (8) as follows

$$\begin{aligned} -i \int dy \langle T(\varphi_0(x) \varphi_0^+(x')) iL_{int}^{(2)}(y) \rangle_0 = \\ = -ie^2 \int dy G_0^F(x, y) G_0^F(y, x') \cdot g_{\mu\nu} D_0^{F\mu\nu}(y, y) + G_0^F(x, x') \int dy \langle T(L_{int}^{(2)}(y)) \rangle_0 = \\ = \int dy_1 dy_2 G^F(x, y_1) \Pi_{(2)}^F(y_1, y_2) G^F(y_2, x') + G_0^F(x, x') \int dy \langle T(L_{int}^{(2)}(y)) \rangle_0 \end{aligned} \quad (11)$$

where

$$\Pi_{(2)}^F(y_1, y_2) = -ie^2 \delta(y_1 - y_2) g_{\mu\nu} \cdot D_0^{F\mu\nu}(y_1, y_2) \quad (12)$$

is the second contribution to the polarization operator $\Pi^F(y_1, y_2)$.

Let us consider the last term of the expression (8)

$$\begin{aligned} -i \int dy_1 dy_2 \langle \tilde{T}(-iL_{int}^{(1)}(y_1)) T(\varphi_0(x) \varphi_0^+(x')) iL_{int}^{(1)}(y_2) \rangle = \\ = ie^2 \int dy_1 dy_2 D_0^{F\mu\nu}(y_1, y_2) (G_0^+(x, y_1) D_\mu G_0^-(y_1, x') \cdot (-i \langle T(\phi_0(y_2) D_\nu \phi_0^+(y_2)) \rangle_0 + \\ + G_0^F(x, y_2) D_\mu G_0^F(y_2, x') \cdot (-i \langle T(\varphi_0(y_1) D_\nu \varphi_0^+(y_1)) \rangle_0 + \\ + G_0^+(x, y_1) D_\mu G_0^-(y_1, y_2) D_\nu G_0^F(y_2, x') + \\ + G_0^F(x, y_2) D^\mu G_0^+(y_2, y_1) D^\nu G_0^-(y_1, x')) + \\ + G_0^F(x, x') \int dy_1 dy_2 \langle \tilde{T}(-iL_{int}^{(1)}(y_1)) T(iL_{int}^{(1)}(y_2)) \rangle_0. \end{aligned} \quad (13)$$

We represent the obtained sum as the sum of diagrams in Fig. 2 (except for the last term).

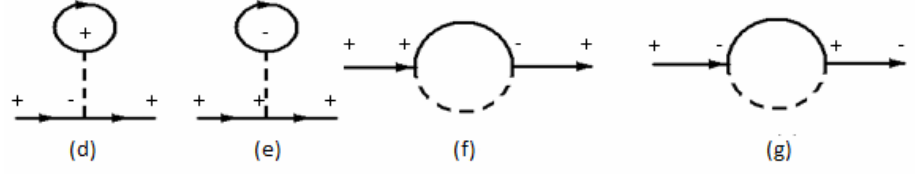


Fig. 2 One-loop contributions in Π^- and Π^+ .

Diagrams of type (d) and (e) equal zero the same way as the diagram of the type (b) does. Diagrams (f) and (g) contribute to Π^- and Π^+ , in accordance with Eq. (2).

Reducing the rest of terms in expression (8) by the Wick theorem

$$-i \int dy_1 dy_2 \langle \tilde{T} \left(\frac{(-i)^2}{2!} L_{int}^{(1)}(y_1) L_{int}^{(1)}(y_2) \right) T(\varphi_0(x) \varphi_0^+(x')) \rangle_0 -$$

$$-i \int dy \langle \tilde{T} (i L_{int}^{(2)}(y)) T(\varphi_0(x) \varphi_0^+(x')) \rangle_0, \quad (14)$$

we see that they do not contain the casual function G_0^F which depends on x or x' .

Therefore they have no effect on Π^F , Π^+ and Π^- but define $\Pi^{\tilde{F}}$. Their contribution containing vacuum diagrams is

$$G_0^F(x, x') (-i \int dy_1 dy_2 \langle \tilde{T} \left(\frac{(-i)^2}{2!} L_{int}^{(1)}(y_1) L_{int}^{(1)}(y_2) \right) \rangle_0 - i \int dy \langle \tilde{T} (i L_{int}^{(2)}(y)) \rangle_0).$$

The sum of all the vacuum loops in $G^{F(2)}(x, x')$, is a $\langle S^+ S \rangle_0$ in order e^2 , and obviously equals to zero.

The retarded Green function is defined by means of statistical average over the Heisenberg density matrix

$$G^R(x, x') = i \Theta(t' - t) \langle [\varphi(x), \varphi^+(x')] \rangle.$$

It is related with the above defined Green function by the equation

$$G^R = G^F - G^+ = -G^{\tilde{F}} + G^-$$

and satisfies the Schwinger-Dyson equation

$$G^R(x, x') = G_0^R(x, x') + \int dy_1 dy_2 G_0^R(x, y_1) \Pi^R(y_1, y_2) G^R(y_2, x')$$

where

$$\Pi^R = \Pi^F + \Pi^+ = -(\Pi^{\tilde{F}} + \Pi^-).$$

Finally, we obtain formula for Π^+ by using Eq. (13),

$$\int dy_1 dy_2 G_0^F(x, y_1) \Pi^+(y_1, y_2) G_0^-(y_2, x') =$$

$$= -ie^2 \int dy_1 dy_2 D_0^{-\nu\mu}(y_2, y_1) \cdot G_0^F(x, y_1) D^\mu G_0^+(y_1, y_2) D^\nu G_0^-(y_2, x'). \quad (15)$$

Summing up the carried out analysis of the expansion of the full Green function, Π^F is the sum of $\Pi_{(1)}^F + \Pi_{(2)}^F$, the retarded polarization operator looks as follows

$$\Pi^R = \Pi_{(1)}^F + \Pi_{(2)}^F + \Pi^+. \quad (16)$$

Its terms are defined by means of integral equations (10), (12) and (15). In this way the polarization operator of charged scalar particle in the electromagnetic field at finite temperature in the Keldysh formalism is constructed.

Conclusions

In this paper we have considered scalar electrodynamics at external conditions. We obtained the one-loop polarization operator of a charged scalar field at a finite temperature and in an external electromagnetic field.

Given by Eq.(16), the one-loop retarded polarization operator Π^R allows to investigate spectra of charged scalar particles in different environments. For this purpose we have to substitute it into the Schwinger-Dyson equation

$$G^R(x, x') = G_0^R(x, x') + \int dy_1 dy_2 G_0^R(x, y_1) \Pi^R(y_1, y_2) G^R(y_2, x'),$$

and study the singularity positions of the full Green function in momentum space. This problem will be considered separately.

References

1. **Skalozub V.V.** On the generation of Abelian magnetic fields in SU(3) gluodynamics at high temperature / V.V. Skalozub, A.V. Strelchenko // Eur. Phys. J. C. – 2006. – Vol. 45, N. 1. – P. 159-178.
2. **Bordag M.** Neutral gluon polarization tensor in a color magnetic background at finite temperature / M. Bordag V. Skalozub // Phys. Rev. D. – 2007. – V.75 Issue 12. – 32 p. [arXiv:hep-th/0611256].
3. **Bordag M.** Polarization tensor of charged gluons in color magnetic background field at finite temperature / M.Bordag V. Skalozub // Phys. Rev. D. – 2008. – V.77, Issue 10. –15 p. [arXiv:0801.2306 [hep-th]].
4. **Келдыш Л. В.** Диаграммная техника для неравновесных процессов / Л.В. Келдыш // ЖЭТФ. – 1964. – Т. 47. – С. 1515-1527.
5. **Schwinger J.** Brownian motion of a quantum oscillator / J. Schwinger // J. Math. Phys. – 1961. – V. 2. – P. 407-432.
6. **Sokolov V.** Estimate of the magnetic field strength in heavy-ion collisions/ V. Sokolov, A. Illarionov, V. Toneev // Int.J.Mod.Phys.A. – 2009. – V. 24. – P. 5925-5932
7. **Voskresenskii D.N.** /Properties of a pion condensate in a magnetic field/ D.N. Voskresenskii, N. Yu. Anisimov // JETP. – 1980. – Vol. 51, No. 1. – P. 13-22.
8. **Itzykson C.** Quantum Field Theory / C. Itzykson, J.B. Zuber. – McGraw-Hill, New-York, 1998. – 05 p.
9. **Le Bellac M.** Thermal field theory / M. Le Bellac. – CUP, 1996. – 256 p.
10. **Lebedev V.V.** Spectrum of quark-gluon plasma / V.V. Lebedev, A.V.Smilga // Ann. Phys. – 1990. – V. 202 (2). – P. 229-270.
11. **Байер В.Н.** Операторный подход к квантовой электродинамике во внешнем поле: массовый оператор /В.Н. Байер, В.М. Катков, В.М. Страховенко // ЖЭТФ. – 1974. – Т. 67. С.453-470.

Received 13.07.2013.

UDC 535.36

V. N. Moiseyenko¹, V. S. Gorelik², M. P. Dergachov¹, A. V. Yevchik¹,
T. V. Shvets¹, A. A. Beletsky¹

¹*Oles Honchar Dnipropetrovsk National University*

²*P.N. Lebedev Physical Institute of Russian Academy of Sciences*

OPTICAL PHENOMENA IN MATRIX NANOCOMPOSITES BASED ON SYNTHETIC OPALS

The matrix nanocomposites based on synthetic opals with pores filled with various active dielectrics ($\text{Bi}_{12}\text{SiO}_{20}$, $\text{Bi}_{12}\text{GeO}_{20}$, TeO_2 , KH_2PO_4 , $\text{Pb}_5\text{Ge}_3\text{O}_{11}$) are obtained. The fact of pores filling is proved by the changes in the reflection or transmission spectra. The crystalline state of embedded dielectrics is determined on the base of measured Raman spectra of the obtained nanocomposites. In all cases, Raman spectra of the nanocomposites undergo the changes (appearance of new bands, shift of the bands, spectral intensity redistribution) compared with the spectra of single crystals or polycrystalline powder of corresponding dielectrics. The modification of the photoluminescence spectrum of the opal- $\text{Bi}_{12}\text{SiO}_{20}$ system is connected with increasing the number of surface states under the restricted volume conditions. The appearance of intense emission in the opal- KH_2PO_4 spectrum under a 532 nm laser excitation is probably assigned to spontaneous parametric down-conversion which becomes observable due to enhancement of the pump field inside synthetic opal.

Keywords: photonic crystals, Raman scattering, luminescence, spontaneous parametric down-conversion.

Получены матричные нанокompозиты на основе синтетических опалов, поры которых заполняются различными активными диэлектриками ($\text{Bi}_{12}\text{SiO}_{20}$, $\text{Bi}_{12}\text{GeO}_{20}$, TeO_2 , KH_2PO_4 , $\text{Pb}_5\text{Ge}_3\text{O}_{11}$). Факт заполнения пор подтверждается изменениями в спектрах отражения или пропускания. На основании измеренных спектров комбинационного рассеяния света полученных нанокompозитов устанавливается кристаллическое состояние введенных диэлектриков. Во всех случаях спектры комбинационного рассеяния света нанокompозитов претерпевают изменения (появление новых полос, смещение полос, перераспределение спектральной интенсивности) по сравнению со спектрами монокристаллов или поликристаллических порошков соответствующих диэлектриков. Модификация спектра фотолюминесценции системы опал- $\text{Bi}_{12}\text{SiO}_{20}$ связывается с увеличением поверхностных состояний в условиях ограниченного объема. Появление интенсивного свечения в спектре опал- KH_2PO_4 при лазерном возбуждении на длине волны 532 нм связывается со спонтанным параметрическим рассеянием света, которое становится наблюдаемым вследствие усиления поля накачки внутри синтетического опала.

Ключевые слова: фотонные кристаллы, комбинационное рассеяние света, люминесценция, спонтанное параметрическое рассеяние света.

Отримані матричні нанокompозити на основі синтетичних опалів, пори яких заповнені різними активними діелектриками ($\text{Bi}_{12}\text{SiO}_{20}$, $\text{Bi}_{12}\text{GeO}_{20}$, TeO_2 , KH_2PO_4 , $\text{Pb}_5\text{Ge}_3\text{O}_{11}$). Факт заповнення пор підтверджується змінами у спектрах відбивання чи пропускання. На підставі вимірних спектрів комбінаційного розсіяння світла отриманих нанокompозитів встановлюється кристалічний стан введених діелектриків. У всіх випадках спектри комбінаційного розсіяння світла нанокompозитів зазнають змін (поява нових смуг, зсув смуг, перерозподіл спектральної інтенсивності) порівняно зі спектрами монокристалів або полікристалічних порошків відповідних діелектриків. Модифікація спектру фотолюмінесценції системи опал- $\text{Bi}_{12}\text{SiO}_{20}$ пов'язується із зростанням поверхневих енергетичних станів, що відповідають дефектам або домішкам, за умов обмеженого об'єму. Поява інтенсивного світіння у спектрі опал- KH_2PO_4 за лазерного збудження на довжині хвилі 532 нм пов'язується із спонтанним параметричним розсіянням світла, яке стає можливим спостерігати внаслідок посилення поля накачки усередині синтетичного опала.

Ключові слова: фотонні кристали, комбінаційне розсіяння світла, люмінесценція, спонтанне параметричне розсіяння світла.

Introduction

The creation and investigation of the matrix nanocomposites with active dielectrics attracts a great attention in physics of low-dimensional systems. Physical properties of nanocrystals of active dielectrics should be essentially different from those of bulk crystals because of the quantum-size effects in electronic and vibrational spectra [1]. On the other hand, in case of periodical arrangement of the nanocrystals, the effects attributed to the photonic crystals should be also expected. Thus, such structures have to enlarge our opportunities in the light flows controlling [2].

As a base matrix for obtaining these structures the synthetic opals are widely used. Regular arrangement of cavities and channels in initial synthetic opals allows for getting 3D periodical structures for a wide range of organic and inorganic compounds. A typical embedding procedure is a soaking of initial opal into the compound solution at temperatures close to room temperature or into the melt of compound with the following crystallization by cooling [3, 4]. In this case, a solid phase of embedded compound is formed under the other conditions than as usual. These special conditions are the high temperature, the limited volume of pores and the lack of atmosphere into interior pores.

The present work is devoted to the obtaining of matrix nanocomposites based on synthetic opals whose pores were filled with active dielectrics ($\text{Bi}_{12}\text{SiO}_{20}$, $\text{Bi}_{12}\text{GeO}_{20}$, TeO_2 , KH_2PO_4 , $\text{Pb}_5\text{Ge}_3\text{O}_{11}$), to their characterization with the use of reflection (or transmission) and Raman spectroscopy technique and to the study the secondary emission spectra of the obtained structures.

The obtaining and characterization of samples

Bulk opals were grown by slow crystallization of a colloidal solution of monodisperse SiO_2 globules synthesized by modified Stöber method [5]. After drying in air the obtained precipitate was annealed at 125°C for 1 h, then at 750°C for 2 h. The opal structure was a face-centered cubic lattice formed by hexagonal close-packed layers of monodisperse globules. To determine the structural parameters of opal matrix (globules diameter D and interplanar distance d) and, consequently, to estimate the geometrical sizes of pores the Bragg diffraction spectra in the reflected beams have been measured. According to the Bragg law, a spectral position λ_m of the reflection peak is connected with an interplanar distance d as follows

$$\lambda_m(\theta) = 2d\sqrt{\varepsilon_{eff} - \sin^2\theta} \quad (1)$$

where θ is an incident angle of light beam on system of the $\{111\}$ planes, ε_{eff} is an effective dielectric constant. The latter is determined by the dielectric constants ε_i of substances which form the composite and the volume part of substance f_i as follows

$$\varepsilon_{eff} = 0.74 \cdot \varepsilon_{\text{SiO}_2} + \sum_i f_i \cdot \varepsilon_i, \quad \sum_i f_i = 0.26 \quad (2)$$

The connection between D and d is determined by the geometry of globules arrangement and, in our case, is simply as $D = d\sqrt{3}/2$. For different opal samples in study the values of diameter D and interplanar distance d were varied between 250 – 270 nm and 204 – 220 nm, respectively. An average linear size of pores was about of 70 nm.

The filling of opal pores was carried out by melting-in a fine dispersive polycrystalline powder of corresponding dielectrics. (The exception was made in case of KH_2PO_4 (KDP), when the infiltration was performed by a multiple soaking of opals in supersaturated water – KDP solutions at room temperature.) For this purpose, a thin uniform layer of the substance powder was placed on the surface of synthetic opal (or

under the surface) and the whole system was held in the resistance furnace at temperatures above the substance melting temperature for 15 – 30 min. After this the samples were cooled down room temperature with the average cooling rate of 3 °C/min.

The filling of opal pores with active dielectrics resulted in shifting Bragg reflection peak to the longer wavelengths, if the refractive indexes of embedded dielectrics were higher than that of SiO₂ globules ($n_{\text{SiO}_2} = 1.47$). The reason for it is the increase of ε_{eff} by enlarging the value of the latest part of sum in expression (2). Some results corresponding to this case are presented in Fig. 1. In case of the close values of the refractive indexes of opal matrix and embedded substance, e.g. for opal-KDP system ($n_{\text{KDP}} = 1.49$), any significant shift was not observed, but the halfwidth of the Bragg reflection (or non-transmission) peak became smaller with an each next infiltration cycle (Fig. 2). It can be explained by diminishing the optical contrast in such system.

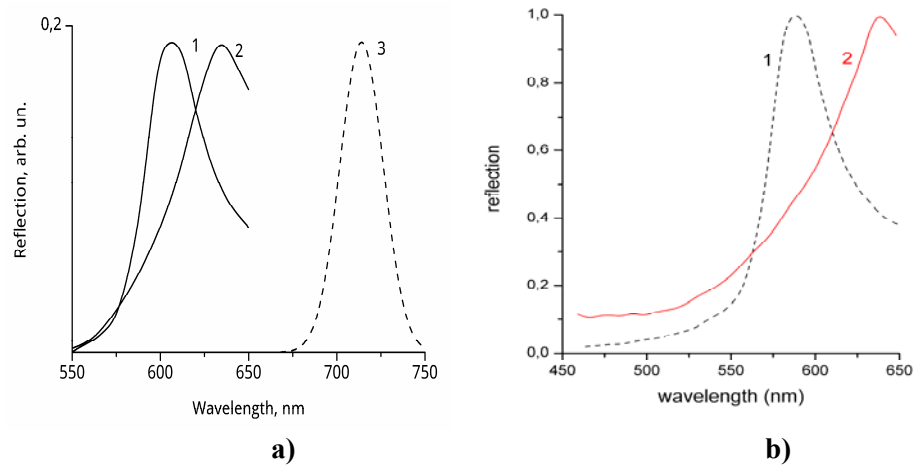


Fig. 1. The reflection spectra of initial opals (curves 1 in both parts) at $\theta = 7^\circ$ and the same opals after filling with Bi₁₂SiO₂₀ (curve 2 in the part a) and with TeO₂ (curve 2 in the part b) at $\theta = 60^\circ$ and 70° , respectively. The curve 3 is the calculated reflection spectrum of opal-Bi₁₂SiO₂₀ system at $\theta = 0^\circ$.

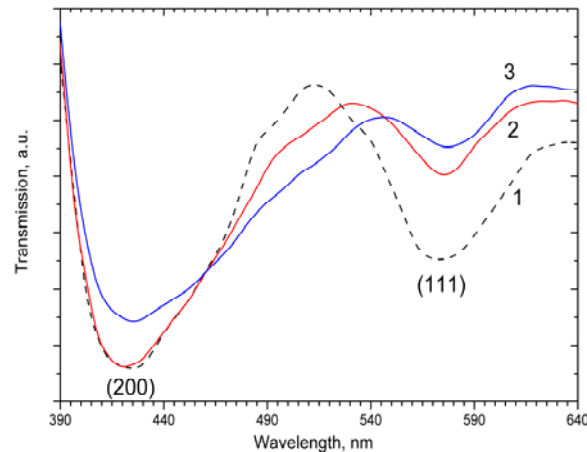


Fig. 2. The transmission spectra of initial opal (curves 1 in both parts) at $\theta = 7^\circ$ and the same opal filled with KH₂PO₄ after one (2) and two (3) soaking cycles.

Raman spectra of the obtained nanocomposites demonstrate clearly the crystalline state of embedded dielectrics in the opal pores (Fig. 3 - 5). According to results of our previous study, one can exclude an admixture of initial opal Raman spectrum from the further consideration. The reason for this is that the intensities of wide diffuse bands in its Raman spectrum are very small compared with those in the powder and nanocomposite spectra. We can also neglect the influence of photonic stop-band as it is situated far from the studied spectral region. The most features of Raman spectra of the obtained nanocomposites in comparison with the spectra of corresponding polycrystalline powder are the following: 1) an appearance of new bands; 2) a spectral redistribution mostly within a low- and medium-frequency range; 3) a total enhancement of Raman spectrum in case of nanocomposites.

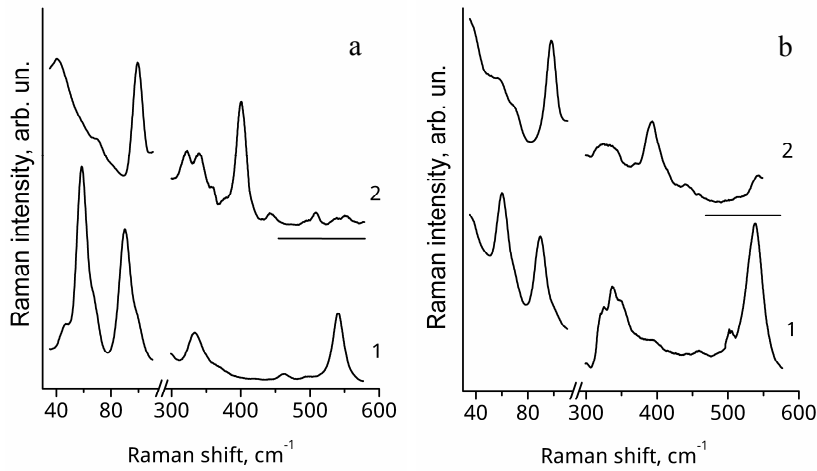


Fig. 3. Raman spectra of polycrystalline powders of $\text{Bi}_{12}\text{SiO}_{20}$ (1a), $\text{Bi}_{12}\text{GeO}_{20}$ (1b) and nanocrystals of $\text{Bi}_{12}\text{SiO}_{20}$ (2a), $\text{Bi}_{12}\text{GeO}_{20}$ (2b) in opal pores.

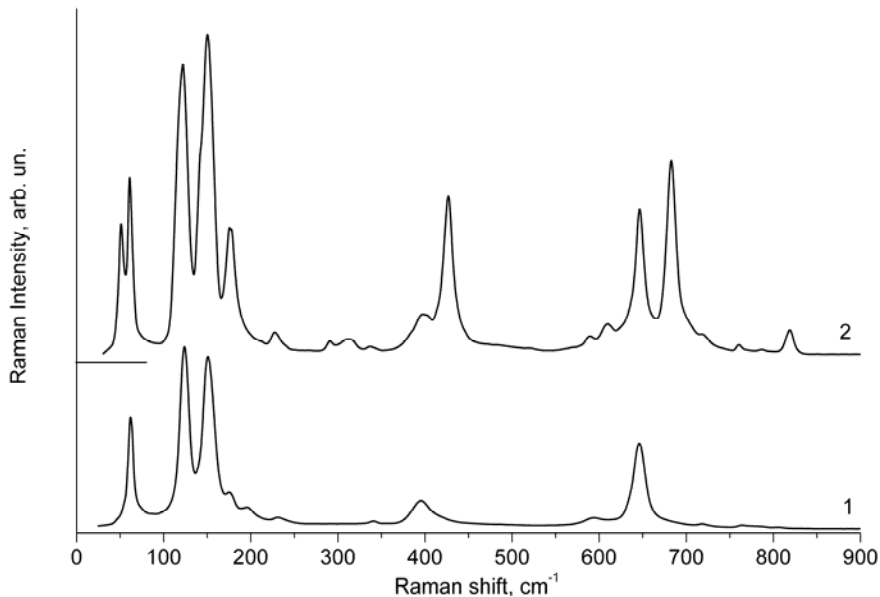


Fig. 4. Raman spectra of $\alpha\text{-TeO}_2$ polycrystalline powder (1) and TeO_2 crystals in opal pores (2). The spectra are correspondent to the same quantity of tellurium dioxide in the excitation volume.

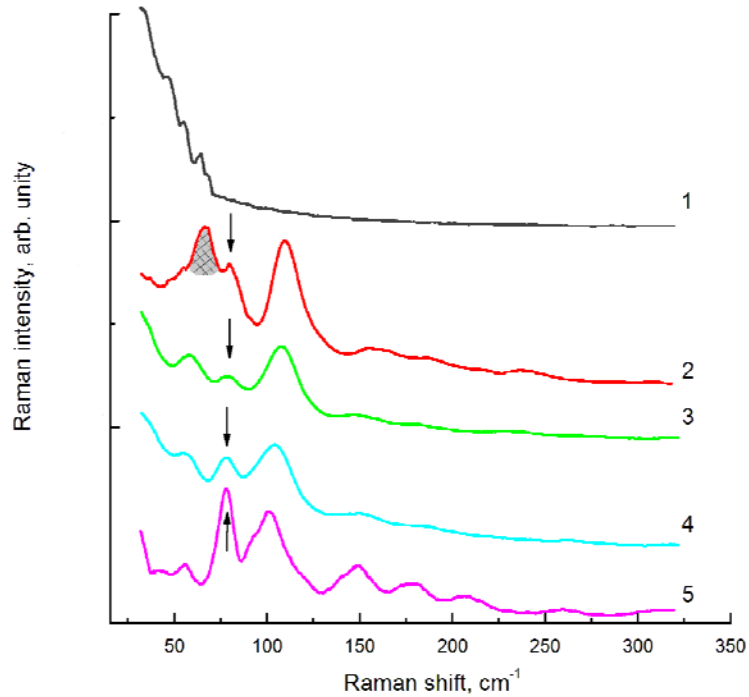


Fig. 5. Raman spectra of “opal - $\text{Pb}_5\text{Ge}_3\text{O}_{11}$ ” system from different volumes of sample (1 - 4) and single $\text{Pb}_5\text{Ge}_3\text{O}_{11}$ crystal (5).

Let us consider the reasons for these features by using the opal-tellurium dioxide Raman spectrum as an example. An appearance of new bands may testify the changes in crystalline structure. It is really, the frequencies of new bands appeared in opal-tellurium dioxide Raman spectrum (Fig. 4), except for a 51 cm^{-1} band, are well coincident with the majority of bands frequencies in the $\gamma\text{-TeO}_2$ spectrum [6]. Thus, one can conclude that both α -phase and γ -phase are formed in tellurium dioxide crystals grown into synthetic opal pores. As for a 51 cm^{-1} band, which is absent in the spectra of both crystalline phases, its appearance may be connected with the folding up of acoustic phonons branch by decreasing the Brillouin zone for TeO_2 nanocrystals in opal pores. The spectral redistribution within a $100 - 180\text{ cm}^{-1}$ range is probably due to the appearance of new $\gamma\text{-TeO}_2$ band at 142 cm^{-1} which enlarges the total intensity within a $140 - 180\text{ cm}^{-1}$ range.

The total enhancement in Raman spectra of the obtained nanocomposites can be explained by multiple reflections of exciting photon from disordered elements in synthetic opal structure which result in increasing a temporal interval of radiation-substance interaction.

Secondary emission spectra of the obtained nanocomposites

The obtained active matrix nanocomposites may be involved in the process of the optical radiation conversion due to their emission properties. The spectrum conversion into the volume of these nanocomposites occurs in processes of famous optical phenomena, such as photoluminescence and spontaneous parametric down-conversion.

In photoluminescence spectrum of the opal- $\text{Bi}_{12}\text{SiO}_{20}$ system a “red” shift of the luminescence band and an essential increase of integral intensity are observed in comparison with that spectrum of single $\text{Bi}_{12}\text{SiO}_{20}$ crystal (Fig. 6).

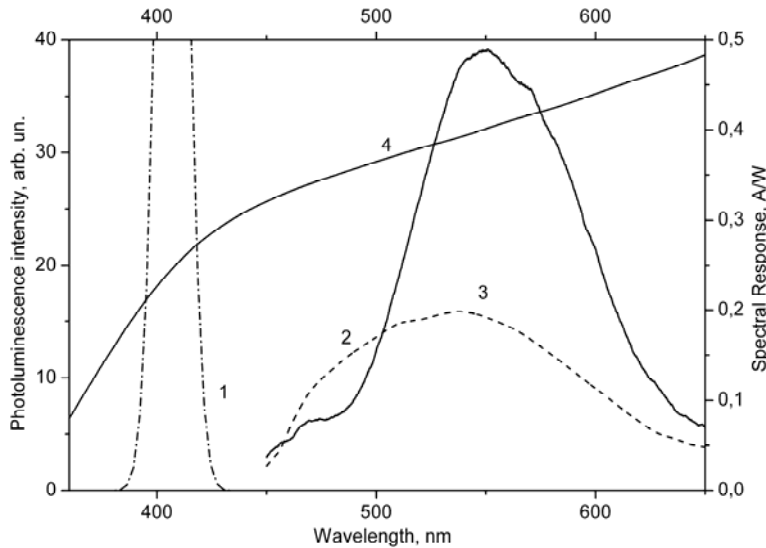


Fig. 6. Spectral shape of the 407 nm exciting line (1), photoluminescence spectra of single $\text{Bi}_{12}\text{SiO}_{20}$ crystal (2) and of opal- $\text{Bi}_{12}\text{SiO}_{20}$ system (3) with the spectral response of the typical Si solar cell (4). The photoluminescence spectra are correspondent to the same $\text{Bi}_{12}\text{SiO}_{20}$ quantity in the excited volume.

The reason of shift is most probably the rebuilding of the $\text{Bi}_{12}\text{SiO}_{20}$ energy spectrum under restricted volume conditions. The total intensity enhancement is caused both by the Bragg reflection of photons by system of the $\{111\}$ planes at the larger incident angles with the following output along the $[111]$ direction and by increasing a temporal interval of radiation-substance interaction due to the multiple scattering of light into nanocomposites volume.

The secondary emission spectra of the opal-KDP system under different excitation are presented in Fig. 7.

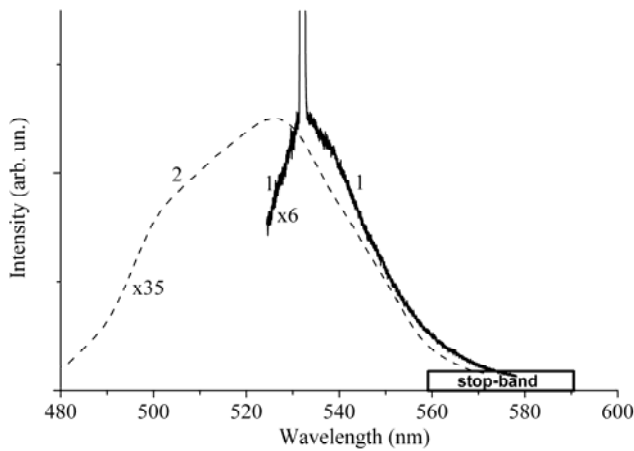


Fig. 7. The secondary emission spectral of the opal - KDP system under a 532 nm laser excitation (1) and a 400 nm LED excitation (2).

In both cases, we obtained a wide emission band within a 480 – 600 nm range. The emission intensity decreases within a stop-band region but it does not vanish completely because of the existence of point defects and structural disordering in photonic crystals. Basing on our previous study of nonlinear-optical photonic crystals [7], we assign this emission to the spontaneous parametric down-conversion.

Spontaneous parametric down-conversion is a process of spontaneous disintegration of pump photons ($\hbar\omega_p, \mathbf{k}_p$) into pairs of signal ($\hbar\omega_s, \mathbf{k}_s$) and idler ($\hbar\omega_i, \mathbf{k}_i$) photons. As this process is a second-order nonlinear process it occurs in media with no inversion symmetry. For spatially non-uniform media with regular structures (photonic crystals) a periodic modulation of linear and nonlinear susceptibilities should be considered in general case. By taking into account the $\chi^{(2)}$ periodic modulation the bi-photons spectrum should be determined by an additive sum of single harmonics of $\chi^{(2)}$ susceptibility. In contrast to parametric down-conversion spectrum of spatially uniform sample the bi-photon field spectrum of photonic crystal should be broadened, and the interference effects may appear in its spectral intensity distribution. Spontaneous parametric down-conversion intensity per a unit angle and spectral interval is determined by the value of quasi-synchronism Δ_m for the m -th order nonlinear diffraction. In case of 3D synthetic opal photonic crystals this magnitude is defined by the structure disordering degree, the nonlinear substance filling factor and by the existence of polydomain structure which forms additional superlattice. In our samples typical domain size was about of 70 nm. Then the phase quasi-synchronism condition becomes true for the greater number of directions and wavelengths.

Conclusions

The technology of embedding active dielectrics into opal pores has been worked out. Active dielectrics have been found to be in the nanocrystalline form. In some cases it is possible the formation of metastable phase. The essential shift of Bragg reflection band towards infrared spectral region has been obtained. In nanocomposites with nonlinear optical dielectrics the multiphoton processes are observed. The effect of enhancement of secondary emission in active matrix nanocomposites on the base of synthetic opals has been found.

Acknowledgments

This work is supported by the Ukrainian–Russian Project No. F53.2/030 “Creation and investigation of active matrix nanocomposites on the base of photonic glasses and crystals for solar cells”.

References

1. **Stroschio M.** Phonons in nanostructures/ M. Stroschio, M. Dutta // New York: Cambridge University Press, 2001. – 320 p.
2. **Joannopoulos, J.** Photonic crystals. Molding the flow of light / J. Joannopoulos, G. Johnson, J. Winn, R. Meade // Princeton and Oxford: Princeton University Press, Second Edition, 2008. – 632 p.
3. **Aliev A.** 2003. Thermal conductivity of opal filled with a LiIO₃ ionic conductor/ A. Aliev, N. Akhmedzhanova, V. Krivorotov, I. Kholmanov, A. Fridman //Phys. of the Solid State.– 2003.– V.45. – P.61-68.
4. **Gorelik V.** Optical and dielectric properties of nanostructured photonic crystals loaded by ferroelectrics and metals / V. Gorelik // Phys. of the Solid State. – 2009. – V.51. – P. 1321-1327.
5. **Stöber W.** Controlled growth of monodisperse silica spheres in the micron size range /W.Stöber, A.Fink, E.Bohn // J. Colloid and Interface Sci. – 1968. – V.26. – P.62-69.
6. **Champarnaud-Mesjard J.** Crystal structure, Raman spectrum and lattice dynamics of a new metastable form of tellurium dioxide: γ -TeO₂ / J. Champarnaud-Mesjard, S. Blanchandin, P. Thomas, A. Mirgorodsky, T. Merle-Mejean, B. Frit // J. Phys. and Chem. of Solids.– 2000.– V.61.– P. 1499–1507.
7. **Moiseyenko V.** Quantum Optics Phenomena in Synthetic Opal Photonic Crystals /V.Moiseyenko, M.Dergachov // Quantum Optics and Laser Experiments. Ed. By Sergiy Lyagushyn. - InTech-Open Access Publisher, Croatia, 2012. - P. 87 – 106, ISBN 978-953-307-937-0.

Received 13.07.2013.

UDC 535.36

A. V. Yevchik¹, V. N. Moiseyenko¹, V. S. Gorelik², M. P. Dergachov¹

¹*Oles Honchar Dnipropetrovsk National University*

²*P.N. Lebedev Physical Institute of Russian Academy of Sciences*

FABRICATION AND OPTICAL CHARACTERIZATION OF THIN SYNTHETIC OPAL FILMS FOR DESIGNING COATINGS OF SOLAR CELLS

A method for the fabrication of synthetic opal films with a thickness of 20 - 30 layers is given. Two methods for the characterization of synthetic opal thin films are described. The first method consists in studying the Bragg reflections spectra by using a special fiber-optic microprobe. In the measured spectra, together with the Bragg reflection peak, the presence of maxima due to thin film interference was observed. The film thickness of the samples is calculated by the position of the interference maxima. The second method is based on study of the laser diffraction on the structure of the synthetic opal film. The observed diffraction pattern consists of the six intense reflections, symmetrically located relative to the incident beam. The conditions for the observation of diffraction are described. The relation between structural parameters and the wavelength of radiation is installed. The peculiarity of the diffraction method is the ability to detect the defects related with the multidomain structure. The spectroscopic and diffraction techniques together provide a complete set of methods for the characterization of thin film opals.

Keywords: thin films of synthetic opals, Bragg diffraction spectra, laser diffraction, solar cells.

Приводится способ изготовления пленок синтетического опала с толщиной в 20 - 30 слоев. Описываются два метода характеристики тонких пленок синтетического опала. Первый метод заключается в исследовании спектров брэгговского отражения с использованием специального оптического волоконного микроскопа. В измеренных спектрах, наряду с пиком брэгговского отражения, наблюдаются максимумы, обусловленные интерференцией в тонкой пленке. По положению интерференционных максимумов вычисляются толщины пленок исследуемых образцов. Второй метод базируется на исследовании дифракции лазерного излучения на структуре пленки синтетического опала. Наблюдаемая картина дифракции состоит из шести интенсивных рефлексов, симметрично расположенных относительно падающего пучка. Описываются условия наблюдения дифракции. Устанавливается связь между структурными параметрами и длиной волны излучения. Особенность дифракционного метода заключается в возможности обнаружения дефектов, связанных с полидоменностью структуры. Спектроскопический и дифракционный методы вместе обеспечивают полноценный комплекс методов для характеристики тонких пленочных опалов.

Ключевые слова: тонкие пленки синтетических опалов, спектры брэгговской дифракции, дифракция лазерного излучения, солнечные элементы.

Наводиться спосіб виготовлення плівок синтетичного опала з товщиною в 20 - 30 шарів. Надається опис двох методів характеристики тонких плівок синтетичного опала. Перший метод полягає в дослідженні спектрів бреггівського відбиття з використанням спеціального оптичного волоконного мікроскопа. У вимірних спектрах, поряд з піком бреггівського відображення, спостерігаються максимуми, обумовлені інтерференцією у тонкій плівці. За положенням інтерференційних максимумів обчислюються товщини плівок досліджуваних зразків. Другий метод базується на дослідженні дифракції лазерного випромінювання на структурі плівки синтетичного опала. Спостережувана картина дифракції складатиметься з шести інтенсивних рефлексів, симетрично розташованих відносно падаючого пучка. Надається опис умов спостереження дифракції. Встановлюється зв'язок між структурними параметрами і довжиною хвилі випромінювання. Особливість дифракційного методу полягає в можливості виявлення дефектів, пов'язаних з полідоменністю структури. Спектроскопічний і дифракційний методи разом забезпечують повноцінний комплекс методів для характеристики тонких плівкових опалів.

Ключові слова: тонкі плівки синтетичних опалів, спектри бреггівської дифракції, дифракція лазерного випромінювання, сонячні елементи.

Introduction

A great interest in applying synthetic opals in designing solar cells is caused by the following reason. These materials have the ability to convert the solar radiation spectrum either by selection of a certain part of the spectrum or by conversion of radiation energy (in the composite with luminescent materials, nonlinear optical materials, etc.). Currently, most of the experimental works in the field of photonic crystal research are performed on bulk synthetic opals. However, the presence of significant structural disorder in the bulk samples obtained by sedimentation lays obstacles to the complete exploitation of the features of their optical properties caused by photonic band structure. It is known [1] that film opals have an improved structure. Moreover, the creation of large surfaces with film opals is easier to implement.

In view of the above mentioned it becomes necessary to fabricate synthetic opals with the small number of layers as well as to carry out their optical characterization.

Samples

The opal structure has a face-centered cubic (fcc) lattice formed by hexagonal closely packed layers of monodisperse SiO₂ globules. Synthesis of silicon dioxide globules was carried out by modified Stöber method [2]. Opal films were grown by vertical pulling of quartz or glass substrate from suspension of nanodisperse silica globules with middle size of about $D = 280$ nm. Speed of pulling was about of 100 nm/s.

In this case, under action of surface tension forces of particle suspension, globules were stacked in a uniform layer. Such method, as experience shows, is the most effective and occupies much less time than the method of film growing in a region of moving meniscus by liquid evaporation from suspension [1]. The obtained samples were dried up during a day at room temperature with the subsequent annealing at $T = 480$ °C.

Experiment and results

Characterization of samples means the determination of their structural parameters (diameter of globules and interplanar distance). For this purpose, the Bragg diffraction spectra in the reflected beams have been measured. According to the Bragg law, a spectral position λ_{max} of the reflection peak is connected with the interplanar distance d as follows

$$\lambda_{max}(\theta) = 2d \sqrt{\varepsilon_{eff} - \sin^2 \theta}$$

where θ is an incident angle of light beam on the system of the {111} planes, $\varepsilon_{eff} = 0.74 \cdot \varepsilon_{SiO_2} + 0.26 \cdot \varepsilon_{pore}$ is an effective dielectric constant; ε_{SiO_2} is a dielectric constant of SiO₂ globules, ε_{pore} is a dielectric constant of the substance into pores (for the composition of substances the dielectric constant also will be effective). The connection between the globule diameter D and the interplanar distance d along the [111] direction is given by the ratio $D = d \cdot f$ where $f = \sqrt{3}/2$ for fcc lattice.

To measure the Bragg diffraction spectra a special optical probe shown in Fig. 1, *a* was used. In the probe scheme the light was gathered to the optical concentrator 2 through the fiber bundle 1, and then light was incident on the sample 3 at angle θ . The reflected from the sample surface light was gathered to the fiber 4 at the same angle. The spectra were registered with using a modified spectrometer based on a double monochromator DFS-12.

One of these spectra is shown in Fig. 1, *b*. The spectrum has a characteristic peak at 630 nm, its position is determined by the above described Bragg law. Thus, the structural parameters of the opal sample can be determined from the spectral position of the peak. Along with the Bragg diffraction spectra the interference maxima marked in Fig. 1, *b* as *m* (maximum position coincides with the Bragg diffraction peak), and *m*+1, were able to register. The presence of these maxima is caused by the phenomenon of interference in thin films. The thickness of the film *t* is determined by the position of these maxima λ_m and λ_{m+1} in such a way

$$t = 1/2n_{eff}(1/\lambda_{m+1} - 1/\lambda_m)$$

where n_{eff} is an effective refractive index. For investigated samples the film thickness is in the range from 2 μm till 4 μm .

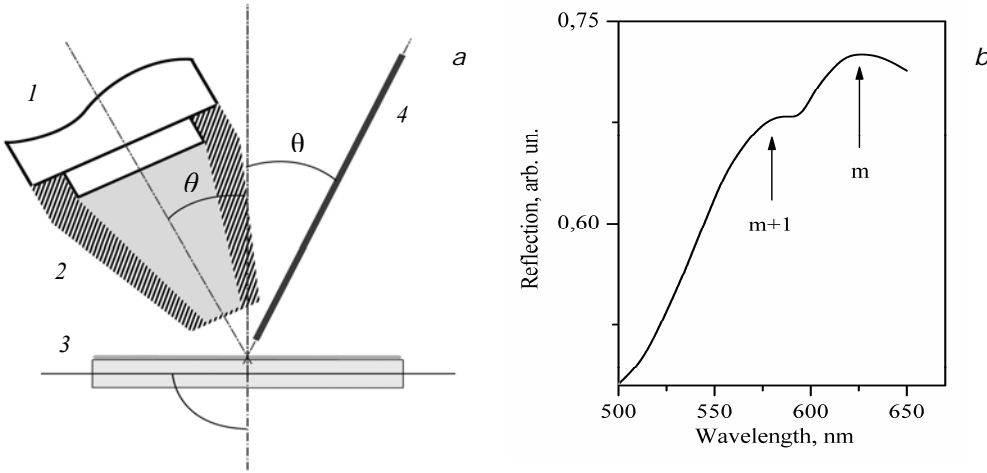


Fig. 1. Measurements of Bragg diffraction spectra. *a* – optical probe scheme; *b* – Bragg diffraction spectrum measured with the optical probe.

Investigation of the light diffraction in synthetic opals is also an important method for the characterization of opal films [3, 4]. To describe the laser radiation diffraction on the synthetic opal structure, the widely known approach developed by Laue [5] and used for describing the X-ray diffraction in ordinary crystals is applicable.

The observed diffraction pattern was characterized by symmetry C_6 and consisted of six intense reflections, symmetrically located relative to the incident beam (see Fig. 2, *a*). An optical scheme used to observe the diffraction is shown in Fig. 2, *b*. For this scheme, one DPSS and two semiconductor lasers with wavelengths of $\lambda_{green}=532$ nm, $\lambda_{blue}=407$ nm, and $\lambda_{red}=635$ nm, respectively, were used. The beam was oriented along the [111] direction, normal to the film surface.

As known in this geometry not for every wavelength and the incident beam orientation the diffraction can be observed. Condition for the occurrence of diffraction is

$$\vec{k} - \vec{k}_0 = \vec{G}$$

where \vec{k}_0 and \vec{k} are the wave vectors of incident and diffracted beams and \vec{G} is the reciprocal lattice vector. This condition is equivalent to the set of equations:

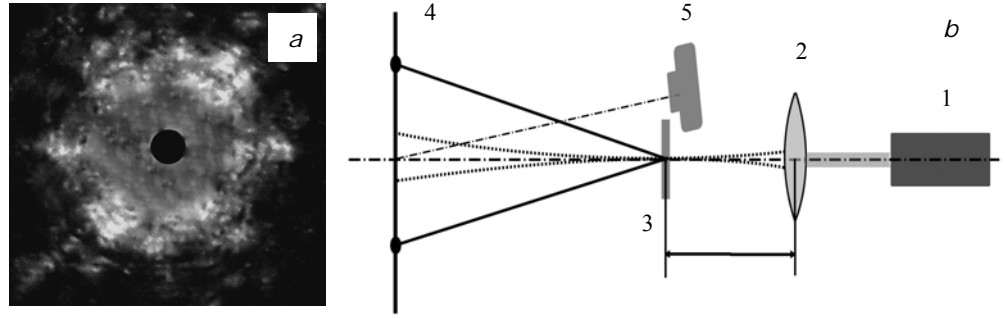


Fig. 2. Experiment on observation of diffraction. *a* – diffraction pattern; *b* – optical scheme of the experiment of the laser beam diffraction in the opal film.
1 - laser; 2 – lens; 3 – sample; 4 – screen; 5 – camera.

$$\begin{cases} d_1 n_{eff} = (\cos \alpha - \cos \alpha_0) = m_1 \lambda; \\ d_2 n_{eff} = (\cos \beta - \cos \beta_0) = m_2 \lambda; \\ d_3 n_{eff} = (\cos \gamma - \cos \gamma_0) = m_3 \lambda; \end{cases}$$

where d_1 , d_2 , and d_3 are periods of nodal lines forming a certain system of coordinates, in general, oblique. The beam incident to the origin of the coordinate system will form angles α_0 , β_0 , γ_0 with its axes, while the diffracted beam forms angles α , β , γ . For each wavelength, and orientation of the incident beam in respect to the sample, an own coordinate system for the implementation of diffraction will be determined. It is possible to find the relation between D and λ . Using also the geometric condition $\cos^2 \alpha + \cos^2 \beta + \cos^2 \gamma = 1$ and assuming $m_1 = m_2 = m_3 = 1$, we can obtain

$$D = \frac{\lambda}{2} \cdot \frac{1}{n_{eff}^2} \cdot \frac{(f_1^2 + f_2^2 + f_3^2)}{(f_1 \cos \alpha_0 + f_2 \cos \beta_0 + f_3 \cos \gamma_0)}, \quad f_i = \frac{D}{d_i}.$$

The table below gives the values of the angles and f_i for which the diffraction is possible in this experiment. The calculated values of D are also given.

Table

Values of angles and f_i for which the diffraction is possible, D - the calculated size of the globules

λ , nm	$\alpha_0, ^\circ$	$\beta_0, ^\circ$	$\gamma_0, ^\circ$	f_1	f_2	f_3	D , nm
407	90	90	30	$1/\sqrt{3}$	1	1	295
532	90	45	45	1	$1/\sqrt{2}$	$1/\sqrt{2}$	286
635	90	30	30	1	1	1	296

Characterization with using this method provides a great opportunity to analyze the quality of the sample. Defects and the overall disorder of the structure directly affect the diffraction pattern. The character of distribution and brightness of diffraction reflexes in the obtained diffraction patterns were various in some different sites of the sample. This fact testifies a polydomain structure of the film (Fig. 3).

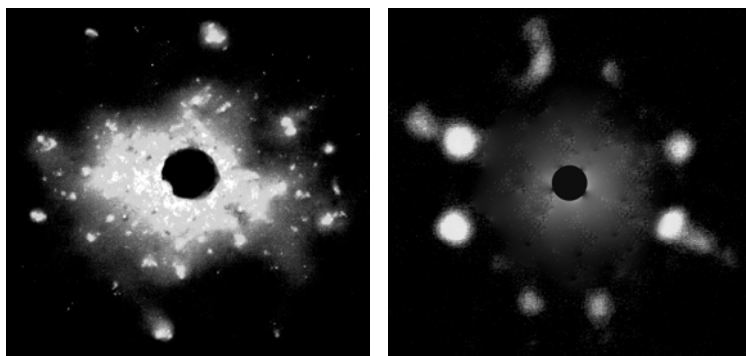


Fig. 3. The diffraction patterns obtained in sample sites, where the structure disruptions occur.

Conclusions

Two methods for the characterization of synthetic opals are described. The spectroscopic method has shown the presence of interference in a thin film along with Bragg diffraction. The conditions of the laser diffraction occurrence in performed experiments were identified. It is found that the diffraction method, as a method for characterization, gives also the information about the types of defects. Together, these methods provide an indispensable instrument for the characterization and analysis of thin coatings based on synthetic opals.

Acknowledgments

This work is supported by the Ukrainian–Russian Project No. F53.2/030 “Creation and investigation of active matrix nanocomposites on the base of photonic glasses and crystals for solar cells”.

References

1. **Plekhanov A. I.** Nanocrystallization of Single-Crystal Opal Films and Film Opal Heterostructures / A. I. Plekhanov, D. V. Kalinin, V. V. Serdobinceva // Russian Nanotechnology. – 2006. – V. 1, №. 1-2. P. 245-251. (in Russian).
2. **Stöber W.** Controlled growth of monodisperse silica spheres in micron size range / W. Stöber, A. Fink, E. Bohn // J. Coll. Interf. Sci. – 1968. - V. 26, №. 1. P. 62–69.
3. **Garcia-Santamaria F.** Optical diffraction and high-energy features in three-dimensional photonic crystals / F. Garcia-Santamaria, J. F. Galisteo-Lopez, P. V. Braun, C. Lopez // Phys. Rev. – 2005. - V. 71, №. 19. P. 195112-1-195112-5.
4. **Kosobukin V. A.** On the theory of diffraction of light in photonic crystals with allowance for interlayer disordering / V.A. Kosobukin // Phys. Solid State. – 2005. – V. 47, №. 11. P. 2035-2045.
5. **Kitaygorodskiy A. I.** X-ray diffraction analysis – M., 1950. – 650 p.

Received 13.07.2013.

UDC 532.696:621.92

O. V. Sukhova, K. V. Ustinova, Yu. V. Syrovatko

Oles Honchar Dnipropetrovsk National University

X-RAY MICROANALYSIS OF Fe(B,C)-BASED SOLID SOLUTIONS

The structure and properties of FeB-based solid solutions of Fe–B–C alloys cooled within the range of crystallization rates from 10 to 10^3 K/s are investigated. The solubility of Mn, Cr, V, Ti, Si, Al, Ni, Cu, Mo, or Nb in Fe(B,C) phase is estimated using X-ray microanalysis. The crystallization of this phase is established to proceed either from the liquid or under peritectic reaction depending on alloying element added. The existence of two polymorphic modifications of iron monoboride with transition temperature at about 1398 K is confirmed. The elements which additions allow increasing hardness and decreasing brittleness of Fe(B,C)-based solid solutions are determined. The change of the structure and properties of the phase caused by the increase in a cooling rate up to 10^3 K/s is described. The brittleness of Fe(B,C) crystals lowers with decreasing quantity of the electrons taking part in the electron exchange and weakening “boron-boron” and “metal-boron” bonds of the phase crystal lattice while the iron atoms are substituted by the atoms of alloying elements.

Keywords: iron monoboride, alloying elements, solid solutions, dendrite parameters, electron structure, microhardness, brittleness.

Исследуются структура и свойства твердых растворов на основе борида FeB в сплавах Fe–B–C, закристаллизованных в интервале скоростей охлаждения $10\text{--}10^3$ К/с. Растворимость Mn, Cr, V, Ti, Si, Al, Ni, Cu, Mo или Nb в фазе Fe(B,C) определяется с использованием рентгеноспектрального микроанализа. Установлено, что в зависимости от состава легирующих добавок кристаллизация этой фазы может протекать как непосредственно из жидкости, так и по перитектической реакции. Подтверждается существование двух полиморфных модификаций моноборида железа с температурой перехода 1398 К. Определяются элементы, введение которых позволяет увеличить твердость и уменьшить хрупкость твердых растворов на основе моноборида железа. Описывается изменение структуры и свойств фаз, вызванное увеличением скорости охлаждения до 10^3 К/с. Показано, что снижение хрупкости твердых растворов на основе Fe(B,C) при замещении атомов железа атомами легирующих элементов связано с уменьшением количества электронов, участвующих в электронном обмене, и ослаблением связей «бор–бор» и «металл–бор» в кристаллической решетке фазы.

Ключевые слова: моноборид железа, легирующие элементы, твердые растворы, дендритные параметры, электронное строение, микротвердость, хрупкость.

Досліджуються структура та властивості твердих розчинів на основі бориди FeB у сплавах Fe–B–C, закристалізованих в інтервалі швидкостей охолодження $10\text{--}10^3$ К/с. Розчинність Mn, Cr, V, Ti, Si, Al, Ni, Cu, Mo або Nb у фазі Fe(B,C) визначається із застосуванням методу рентгеноспектрального мікроаналізу. Встановлено, що залежно від складу легуючих домішок кристалізація цієї фази може відбуватися як безпосередньо з рідини, так і за перитектичною реакцією. Підтверджується існування двох поліморфних модифікацій моноборида заліза з температурою переходу 1398 К. Визначаються елементи, додавання яких дозволяє збільшити твердість і зменшити крихкість твердих розчинів на основі моноборида заліза. Надається опис зміни структури та властивостей фаз, спричинену збільшенням швидкості охолодження до 10^3 К/с. Показано, що зниження крихкості твердих розчинів на основі Fe(B,C) у разі заміщення атомів заліза атомами легуючих елементів пов'язане зі зменшенням кількості електронів, що беруть участь в електронному обміні, та послабленням зв'язків «бор–бор» і «метал–бор» у кристалічній ґратці фази.

Ключові слова: моноборид заліза, легуючі елементи, тверді розчини, дендритні параметри, електронна будова, микротвердість, крихкість.

Introduction

Fe–B–C alloys for industrial applications can be successfully utilized since the alloys have sufficient thermal stability to resist oxidation, corrosion, abrasive wear at elevated temperatures [1, 2]. Strengthening is accomplished through structure stabilization by Fe(B,C) crystals appearing in the high boron iron alloys. However, under impact loads these alloys become inadequate because of their low resistance to cracking. It results in the loss of the valuable properties and severely limits the high temperature characteristics of the alloys restricting their use in critical applications. Recent results have indicated that the alloying of the Fe(B,C) crystals not only influences their morphology, but also significantly reduces their brittleness [3–6]. To obtain a high-quality coatings based on Fe–B–C alloys with good comprehensive mechanical properties, it is important to be aware of their microstructure. X-ray microanalysis is one of the main methods of studying crystal structure. Since only a few studies have been carried out and are in some aspects contradictory, especially in the alloyed Fe–B–C system, experiments were initiated to determine the effect of alloying elements on the structure and the properties of Fe(B,C)-based solid solutions.

Experimental procedure and results

The chemical composition of Fe–B–C alloys, determined by chemical and spectral analyses, has been within the composition region 10–14 wt. pct. B, 0.1–1.2 wt. pct. C, 0–5 wt. pct. M (where M – one of the following elements: Mn, Cr, V, Ti, Si, Al, Ni, Cu, Mo, or Nb), Fe – remainder. The specimens have been prepared by melting the constituent elements of high purity in a resistance furnace and solidified by cooling in air. X-ray diffraction with CuK_α radiation and high resolution scanning electron microscopy (SEM) using a field emission gun Jeol-2010 F equipped with an energy dispersive X-ray link system, operating at 200 kV, have been employed to characterize the phases. Microhardness (H_μ) and critical stress intensity factor (K_{IC}) of Fe(B,C)-based solid solutions have been estimated by means of PMT-3 device from the following relationships

$$H_\mu = \frac{1854P}{d^2}, \quad (1)$$

$$K_{IC} = \frac{0,15k(2c/d)^{-3/2}}{F} H\sqrt{d/2}, F = 3, k = 3.2 \quad (2)$$

where d – diagonal length of hardness indentation, m; P – load, N; c – brittle fracture zone radius, m; H – Vickers hardness, MPa.

The structure and the properties of Fe(B,C)-based solid solutions have been investigated in the range of cooling rates from 10 to 10^3 K/s. The solid solution Fe(B,C) arises on the base of FeB iron boride and grows in the form of three-dimensional dendrites (Fig. 1,a). Under the quenching from the temperatures of 1653–1443 K in the Fe(B,C) dendrites the dark and the light twin bands are revealed after etching. Deformation by the twinning is a primary mechanism of plastic flow of metal with a close-packed lattice. Therefore it may be assumed that at the elevated temperatures the crystals of Fe(B,C) possess not the rhombic (α -modification) but more close-packed lattice (β -modification). The results of thermal analysis also show the possibility of polymorphic transformation $\beta\text{-Fe(B,C)} \rightarrow \alpha\text{-Fe(B,C)}$. The weak thermal effect registered may be related with heat production in consequence of polymorphic transformation.

The following changes have been observed after alloying the Fe(B,C) crystals with the elements specified above. X-ray microanalysis shows that within the investigated range of cooling rates Mn, V, or Cr dissolve in the phase in noticeable quantities, while the solubility of Ti, Si, Al, Mo, Nb, Ni or Cu is insignificant or practically absent (Fig. 1).

Manganese dissolves in the iron monoboride to the full (Fig. 1, b), critical stress intensity factor K_{IC} of the phase increasing (Table). This element slightly decreases dendrite parameters of alloyed Fe(B,C) crystals. Vanadium dissolved to the amount of 2–5 wt. pct. gives rise to the non-homogeneous structure of the Fe(B,C)-based solid solutions (Fig. 1, c).

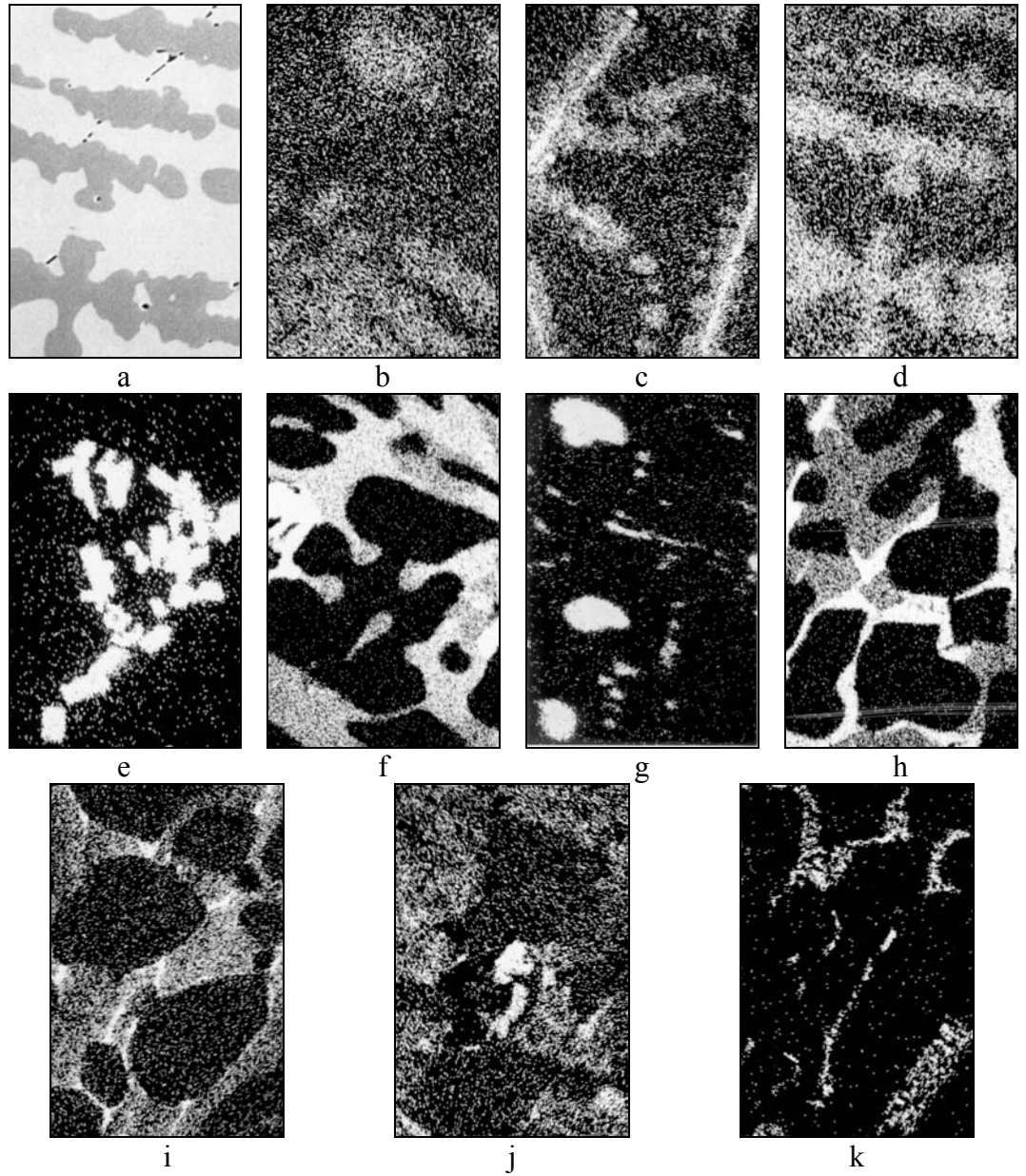


Fig.1. SEM images (x400) of Fe(B,C)-based solid solutions taken in: a – secondary electrons; b – MnK_{α} ; c – VK_{α} ; d – CrK_{α} ; e – TiK_{α} ; f – SiK_{α} ; g – AlK_{α} ; h – NiK_{α} ; i – CuK_{α} ; j – MoL_{α} ; k – NbL_{α}

A light needle-like phase is clearly seen in the dendrite interior. X-ray microanalysis data indicate this phase to be FeB_2 boride. It can be assumed that the first solid phase forming from the liquid has the composition FeB_2 . Then the peritectic reaction $\text{L} + \text{FeB}_2 \rightarrow \text{Fe(B,C)}$ takes place. Cooling through the peritectic temperature causes a type of nonequilibrium structure called surrounding. This nonequilibrium structure appears because there is not enough time for peritectic reaction to go to completion, and not all the liquid is consumed by reacting with FeB_2 to produce Fe(B,C) crystals. Instead, part of the liquid solidifies to produce a structure consisting of the phase of FeB_2 surrounded by a shell of Fe(B,C) .

Alloying with vanadium does not practically change dendrite parameters of Fe(B,C) phase but significantly enhances the critical stress intensity factor K_{IC} (Table). The dissolution of chromium in Fe(B,C) crystals is complete, as illustrated in Fig. 1, d. This element causes the largest increase in the plasticity of the phase slightly decreasing its dendrite parameters.

Titanium added to the iron monoboride dissolves in the dendrites insignificantly. Only traces of the element are revealed by X-ray microanalysis as small but noticeable background (Fig. 1, e). Consequently, at the boundaries of iron monoboride the numerous light crystals of TiC are seen in the SEM micrographs. For all that, the increase in microhardness H_{μ} and the decrease in critical stress intensity factor K_{IC} tend to be more marked while the dendrite parameters remain practically unchanged (Table).

The additions of silicon, aluminum, or nickel dissolve in the dendrites of Fe(B,C) in negligible quantities (Fig. 1, f–h). In the SEM micrographs Fe(B,C) crystals look dark. The studies indicate the presence of SiC , AlB_{12}C , or Ni_2B crystals, respectively, at the Fe(B,C) boundaries. Therefore, alloying with these elements does not essentially influence dendrite parameters (Table). Similarly, copper produces globular inclusions at the dendrite boundaries, as seen in Fig. 1, i.

Table

The influence of alloying elements on the dendrite parameters and the properties of Fe(B,C) -based solid solutions

Alloying element	Dendrite parameters, μm^*				H_{μ} , GPa**		K_{IC} , $\text{MPa}\cdot\text{m}^{1/2}$ ***	
	cooling rate, K/s				cooling rate, K/s		cooling rate, K/s	
	10	10^3	10	10^3	10	10^3	10	10^3
	d_0	l_0	d_0	l_0				
w/o	29.9	33.1	4.9	5.2	17.1	19.0	2.3	4.5
Mn	29.0	31.3	4.6	4.8	17.2	19.3	3.5	–
V	29.8	33.1	4.4	4.8	17.0	19.1	3.6	–
Cr	28.4	31.9	4.1	4.3	16.5	18.6	3.8	–
Ti	29.6	32.9	4.7	5.0	18.2	20.5	1.8	4.7
Si	29.1	31.1	4.6	4.9	17.9	20.0	2.2	5.1
Al	28.7	32.4	4.5	4.8	17.9	19.9	2.0	5.3
Ni	28.6	32.0	4.2	4.5	17.4	19.8	2.4	5.2
Cu	28.9	32.2	4.3	4.6	17.7	20.1	2.3	5.0
Mo	23.6	27.2	3.1	3.6	17.7	20.0	2.1	–
Nb	22.4	34.3	2.4	2.8	17.8	20.2	2.1	5.9

* d_0 – diameter of dendrite branches of II order; l_0 – spacing between the dendrite branches of II order, both accurate ± 2 pct.;

** – accurate up to 1–3 pct.;

*** – accurate up to 3–4 pct.; “–” indicates the impossibility to determine K_{IC} in case of no cracking

The dendrites of Fe(B,C) alloyed with molybdenum and niobium do not yield any significant changes in the structure. Only negligible content of these elements is revealed by X-ray microanalysis (Fig. 1,j,k). Correspondingly, the light crystals of Mo_2B , $\text{Mo}_2(\text{B,C})$, or NbB_2 are seen at the Fe(B,C) boundaries. Molybdenum and niobium cause substantial reduction in dendrite parameters, as shown in Table. In this case the microhardness and the critical stress intensity factor are not influenced.

The increase in a cooling rate up to 10^3 K/s brings about a significant increase in the microhardness and the critical stress intensity factor of Fe(B,C)-based solid solutions (Table). The results of alloying elements influence on dendrite parameters and micromechanical characteristics prove to be similar to those obtained for alloyed Fe(B,C) crystals cooled at the rate of 10 K/s. And what is more, not only manganese, chromium, or vanadium, but aluminum, molybdenum, or niobium as well reduce brittleness of Fe(B,C) phase, most likely because its crystals become smaller. Thus, the brittleness of Fe(B,C)-based solid solutions is dependent on alloying, with higher cooling rate giving rise to a higher K_{IC} .

The results obtained can be explained by the peculiarities in the structure formation of Fe(B,C)-based solid solutions. The stability of Fe(B,C) crystals depends on B–B and Fe–B bonds energy. The strength of these bonds is determined by the distraction of collectivized valence electrons of iron [7]. The ions of such elements as Mn, V, Cr, Mo, or Nb have p^6 -shells and form with boron the same valence bonds like the atoms of iron. As a result of substitution of iron atoms by the atoms of Mn, V, or Cr the fewer electrons take part in the electron exchange. The B–B and the Fe–B interactions weaken and therefore the microhardness and the brittleness of the solid solutions are found to decrease. The reverse is true for titanium. When alloying with this element, quantity of non-located electrons tends to increase. It causes strengthening above all the B–B bonds and, accordingly, gives rise to higher microhardness and brittleness of (Fe,Ti)(B,C) crystals.

Aluminum and silicon are sp -elements, whereas nickel or copper atomic configurations tend to the stable d^5 -states. It makes difficult the delivery of electrons and imposes restrictions on the electron exchange. Therefore the atoms of Al, Si, Ni, or Cu do not practically substitute for the iron atoms in the Fe(B,C) lattice. When dissolving, these elements are most likely able to form the metal–metal (M–M) bonds. In the electron exchange, some electrons of iron localized in the d^{10} -states pass over to the d^5 -states with the energy gain. It causes strengthening M–M bonds and weakening Fe–B bonds in the lattice of the crystals. Taking into account the negligible dissolution of these elements and small contribution of the above bonds in the bond energy balance their insignificant influence on micromechanical properties stands to reason.

The probability that molybdenum and niobium valence electrons are localized in the stable d^5 -configurations is high. That is why these elements are electron acceptors. Any redistribution of electrons in such system will result in the energetically non-advantageous destruction of the stable configurations. Therefore the solubility of molybdenum and niobium in Fe(B,C) crystals is negligible and they do not affect the micromechanical properties.

Conclusions

Alloying of Fe(B,C)-based solid solution with manganese, chromium, or vanadium can be recommended to lower the brittleness of the phase. As the results of X-ray microanalysis show, the effect can be achieved due to a high solubility of the above elements in Fe(B,C) crystals. Their atoms mainly substitute for the iron atoms in the Fe(B,C) lattice, this leads to weakening “metal–metal” and “boron–boron” bonds of the solid solutions.

The negligible dissolution of titanium, aluminum, silicon, nickel, copper, molybdenum, or niobium in Fe(B,C) crystals is responsible for the appearance of new phases based on these elements at the Fe(B,C) boundaries. The results can be explained by electron structure of the alloying elements that do not supply necessary electrons for the electron exchange and do not influence the properties of Fe(B,C)-based solid solutions.

References

1. **Petrow G.** Ternary Alloys. A Comprehensive Compendium of Evaluated Constitutional Data and Phase Diagrams / G. Petrow, G. Effenberg. – Weinheim: VCH Verlagsgesellschaft, 1991. – 944 p.
2. **Bennett L. H.** Alloy Phase Diagrams / L. H. Bennett, T. B. Massalski, B. C. Giessen – New York – Amsterdam – Oxford: North Holland, 1986. – 572 p.
3. **Callister Jr. W. D.** Materials Science and Engineering: An Introduction / Jr. W. D. Callister. – New York: John Wiley & Sons, Inc., 2003. – 867 p.
4. **Berns H.** Microstructure of Fe–Cr–C hardfacing alloys with additions of Nb, Ti, and B / H. Berns, A. Fischer // Metallography. – 1987. – V. 20. – P. 401–429.
5. **Villars P.** Handbook of Ternary Alloy Phase Diagrams / P. Villars, P. Prince, H. Okamoto. – New York: ASM International, 1995. – V. 5. – P. 5330–5333.
6. **Mukhopadhyay N. K.** Alloys Compounds / N. K. Mukhopadhyay, G. V. S. Murthy, B. S. Weatherly. – Singapore: World Scientific, 2002. – 206 p.
7. **Samsonov G.V.** Configurational Model of Substance / G. V. Samsonov, I. F. Pryadko, L. F. Pryadko. – Kyiv: Naukova Dumka, 1971. – 230 p.

Received 13.07.2013.

UDC 541.16:546.3

Z. A. Matysina, E. V. Elina, N. P. Botsva, M. Ye. Deviatkina

Oles Honchar Dnipropetrovsk National University

HYDROGEN ABSORPTION-DESORPTION ISOTHERMS IN MAGNESIUM INTERMETALLIC COMPOUNDS

A statistical theory of hydrogen absorption-desorption in the system $CeMgCo_4-H_2$ was developed. The values of free energies of the two phases formed by dissolving hydrogen in a crystal $CeMgCo_4$ both $CeMgCo_4H_4$ and $CeMgCo_4H_6$ were calculated. The calculation was carried out using simplifying assumptions: the crystal lattice was assumed geometrically ideal, the interatomic interaction only for the nearest atom pairs was taken into account, and the correlation in the substitution position of the lattice atoms was not taken into account. The thermodynamic equilibrium conditions of these phases were determined. The minimizing of the free energy, which determines the equations of thermodynamic equilibrium, allowed studying the hydrogen sorption of crystals at different temperatures. The possibility of occurrence of the hysteresis effect, which disappears with increasing temperature, was shown. The absorption-desorption isotherms close to the real ones were obtained, and the appearance of these curves at the phase transition temperatures was explained. The calculations show that the experimental study of the sorption isotherms of hydrogen in the crystals can allow their mind to reveal the presence or absence of phase transformations in the system, as well as a possible phase transition temperature, if any. Comparison of experimental and calculated isotherms showed their similar nature.

Keywords: hydrogen sorption, isotherms, intermetallic compounds.

Разработана статистическая теория процесса абсорбции-десорбции водорода в системе $CeMgCo_4-H_2$. Рассчитаны свободные энергии двух фаз $CeMgCo_4H_4$ и $CeMgCo_4H_6$, формирующихся при растворении водорода в кристалле $CeMgCo_4$. Расчет проводился с упрощающими предположениями: кристаллическая решетка принималась геометрически идеальной, межатомные взаимодействия учитывались только для ближайших атомных пар, корреляция в замещении позиций решетки атомами не учитывалась. Определены условия термодинамического равновесия фаз. Минимизация свободных энергий, определяющая уравнения термодинамического равновесия, позволила изучить водородную сорбционность кристаллов для разных температур. Установлена возможность появления гистерезисного эффекта, который исчезает с повышением температуры. Построены близкие к реальным изотермы, объяснено появление на них изгибов в точках фазового перехода. Выполненный расчет показывает, что экспериментальное исследование изотерм водородной сорбции в кристаллах позволяет по их виду выявить наличие или отсутствие в системе фазовых превращений, а также определить возможную температуру фазового перехода при его наличии. Сравнение экспериментальных и расчетных изотерм показало их сходный характер.

Ключевые слова: водородная сорбция, изотермы, интерметаллиды.

Розроблена статистична теорія процесу абсорбції-десорбції гідрогену в системі $CeMgCo_4-H_2$. Розраховані вільні енергії двох фаз $CeMgCo_4H_4$ і $CeMgCo_4H_6$, що формуються при розчиненні водню в кристалі $CeMgCo_4$. Розрахунок вільних енергій проводився з використанням таких спрощень: кристалічна решітка вважалась геометрично ідеальною, міжатомні взаємодії враховувались тільки для найближчих атомних пар, кореляція в заміщенні позицій решітки атомами не враховувалась. Визначено умови термодинамічної рівноваги фаз. Мінімізація вільних енергій, яка визначала рівняння термодинамічної рівноваги, дозволила вивчити сорбційність кристалів до водню при різних температурах. Показана можливість гистерезисного ефекту, який зникає з підвищенням температури. Побудовані близькі до реальних ізотерми і пояснена поява на них вигинів в точках фазового переходу. Виконаний розрахунок показав, що експериментальне дослідження ізотерм сорбції гідрогену в кристалах дозволяють за видом ізотерм виявити наявність або відсутність в системі фазових перетворень, а також визначити можливу температуру фазового переходу за його наявності. Порівняння результатів розрахунків та експериментальних ізотерм показало їх подібність.

Ключові слова: сорбція гідрогену, ізотерми, інтерметаліди.

Introduction

New perspective intermetallic hydride materials that proved to be attractive (because of their cheapness, non-toxicity, availability) for both the accumulation and storage of hydrogen and for practical use as battery electrodes supply [1] have been recently synthesized. Among the intermetallic compounds capable of absorbing hydrogen crystals are Mg_3MnNi_2 , Mg_3TiNi_2 , Mg_3AlNi_2 , $LaMgNi_4$, $CeMgCo_4$ and also other ones [2,3]. Their hydrogen sorption capacity makes up 5.4 - 7.6 % weight of hydrogen.

Investigation of the kinetics of hydrogen absorption-desorption in $CeMgCo_4$ compound showed that the system $CeMgCo_4-H_2$ demonstrates the formation of two hydrides (deuterides): with a relatively small amount of hydrogen more stable α phase of $CeMgCo_4H_4$ is formed while with a higher concentration of hydrogen β phase of $CeMgCo_4H_6$ is formed. In the process of absorption crystal lattice expands so that its increase in volume makes 20%. Experimental absorption-desorption isotherms show hysteresis effect (Fig. 1) [1]. Bends in the curves indicate the hysteresis loop for the implementation of the phase transition $\alpha \rightarrow \beta$.

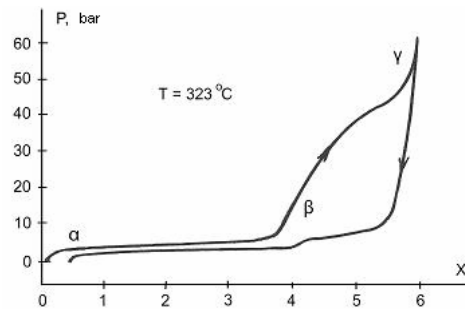


Fig.1. Experimental absorption-desorption isotherms for $CeMgCo_4-H_2$ system [1].

One may be interested in constructing the statistical theory for the hydrogen sorption processes in the $CeMgCo_4-H_2$ system, as well as ascertaining the conditions of thermodynamic equilibrium during phases formation process and describing isotherms of the process, identifying possible manifestations of the sorption hysteresis effect and the impact of $\alpha \rightarrow \beta$ phase transition.

Theory. The comparison with experiment

To achieve the objectives we have calculated free energies F_i of hydride phases $\alpha = CeMgCo_4H_4$ and $\beta = CeMgCo_4H_6$ using the known formula [4-8]

$$F_i = E_i - kT \ln W_i - kT N_H \ln \lambda_i \quad (1)$$

where $i = \alpha, \beta$; E_i – internal energy of the configuration for i -th phase, determined by the sum of the energy of interatomic interactions, W_i – thermodynamic probability of distribution of atoms in a crystal on their positions, calculated according to the rules of combinatorics, N_H – the number of hydrogen atoms in the crystal, λ_i – their activity, k – Boltzmann constant, T – absolute temperature.

The crystal structure of the intermetallic compound $CeMgCo_4$ is cubical. When forming the α and β phases hydrogen atoms first form octahedra around magnesium atoms, α phase occurs, and further with hydrogen concentration increasing hydrogen atoms begin to fill more lattice cavities, for example, centers of some of the planar surfaces of the unit cell, β phase occurs. The lattice parameter equals to $a = 7,501 \text{ \AA}$. Hydrogenation (deuteration) of $CeMgCo_4$ crystal does not change the crystal lattice type, but causes its expansion by 20%.

The calculation of free energies has been performed using simplifying assumptions: the crystal lattice was taken geometrically ideal, interatomic interactions were taken into account only for the nearest atom pairs, correlation in substitution of atom positions in the lattice was not taken into account, the dependence of the energy of interatomic interactions on the hydrogen concentration was taken quadratic, the known dependence of the activity of atomic hydrogen in the crystal on external pressure was applied

$$\lambda_i = G_i p^{1/2} \quad (2)$$

where p – pressure; $G_i = \text{const}$ for each phase.

For calculation of internal configuration energy E_i terms with the energies of pairs of metals interaction are included in the constant term E_{oi} of this energy. Energy E_i is determined by the formula

$$E_i = E_{oi} + N_{CH}u_{CH} + N_{MH}u_{MH} + N_{KH}u_{KH} + N_{HH}u_{HH}$$

where N_{CH} , N_{MH} , N_{KH} , N_{HH} – numbers of the nearest atomic pairs CeH , MgH , CoH , HH (or DD), a u_{CH} , u_{MH} , u_{KH} , u_{HH} – energy of their interaction.

Numbers of the nearest pairs of N_{CH} , N_{MH} , N_{KH} , N_{HH} can be found via considering the crystal lattice geometry. The unit cell of α phase contains four atoms of sodium and magnesium and 16 cobalt and hydrogen atoms. The connection between MgH atom pairs in octahedra is strong and short. CeH pairs exist at two distances r'_{CH} and r''_{CH} . Distances for the nearest atom pairs are $r'_{CH} = a / 2^{3/2} = 2,652$; $r''_{CH} = a \cdot 3^{1/2} / 4 = 3,248$; $r_{MH} = a / 4 = 1,875$; $r_{KH} = a \cdot 3^{1/2} / 8 = 1,624$; $r_{HH} = a / 2^{3/2} = 2,652$. Indicating the number of atoms' positions for metals Ce , Mg , Co as $6N$, we get the number of Ce , Mg , Co atoms as N , N , $4N$ respectively. The numbers of positions of hydrogen atoms in α and β phases are, respectively, $4N$ and $6N$. Some of these positions are vacant. Let assume c and c_v to be concentrations of hydrogen atoms and vacant positions.

Consider first α phase of $CeMgCo_4H_x$ ($0 \leq x \leq 4$). In this phase

$$c = N_H / 4N = x / 4, \quad c_v = 1 - c. \quad (3)$$

Calculating the numbers of the next atom pairs gives in result

$$\begin{aligned} N'_{CH} &= N_{CH}(r'_{CH}) = 8N \cdot c; & N''_{CH} &= N_{CH}(r''_{CH}) = 4N \cdot c; \\ N_{MH}(r_{MH}) &= 6N \cdot c; & N_{KH}(r_{KH}) &= 8N \cdot c; & N_{HH}(r_{HH}) &= 24N \cdot c^2. \end{aligned}$$

With taking into account these formulas, the configuration energy E_α

$$E_\alpha = E_{o\alpha} + 4N(2u'_{CH} + u''_{CH} + 3/2u_{MH} + 2u_{KH} + 6cu_{HH})c. \quad (4)$$

Thermodynamic probability W_α defined by the formula

$$W_\alpha = \frac{(4N)!}{N_H! (4N - N_H)!},$$

with using the Stirling formula $\ln(X!) = X(\ln(X) - 1)$, which is true for large numbers X , allows to obtain the natural logarithm

$$W_\alpha = 4N \ln(4N) - N_H \ln(N_H) - (4N - N_H) \ln(4N - N_H). \quad (5)$$

Substituting the expressions (4) and (5) in Eq. (1) with the formulas (3), we obtain the free energy of α phase

$$F_\alpha = E_{o\alpha} + 4N \{ U_\alpha(c) + kT [c \ln c + (1 - c) \ln(1 - c)] - kT c \lambda_\alpha \} \quad (6)$$

where $U_\alpha = U'_\alpha c + U''_\alpha c^2$, $U'_\alpha = 2u'_{CH} + u''_{CH} + 3/2u_{MH} + 2u_{KH}$, $U''_\alpha = 6u_{HH}$.

Energies U'_α and U''_α depend on the hydrogen concentration due to the significant expansion of the crystal lattice in the process of absorption. It increases the interatomic distances and interaction energies of atoms are reduced by the absolute value. Generally, this energy is determined by a fractional-rational function with polynomials of the fourth degree of concentration of hydrogen in the numerator and denominator of the works [4, 5, 8]. In our particular case, this dependence can be simplified and supposed to be quadratic. Thus, configuration energy E_α is of fourth degree of the hydrogen concentration.

The obtained formula (6) defines the dependence of the free energy of α phase on the temperature, pressure (taking into account (2)), the concentration of hydrogen atoms, their activity (G_α coefficient) and energy parameters of the interaction of atomic pairs.

The equilibrium concentration of hydrogen is defined by the minimal free energy

$$\partial F_\alpha / \partial c = 0. \quad (7)$$

Substitution free energy F_α (6) into the condition (7) with accepting the quadratic dependence of the energies U'_α , U''_α on hydrogen concentration results in a formula

$$\ln P = 2 \ln \frac{c}{G_\alpha(1-c)} + \frac{\Gamma_\alpha(c)}{kT} \quad (8)$$

where $\Gamma_\alpha(c) = \gamma_0 c^3 + \gamma' c^2 + \gamma'' c + \gamma^*$, and constants γ_0 , γ' , γ'' , γ^* are defined via u_{CH} , u_{MH} , u_{KH} , u_{HH} .

According to (8), one can calculate isotherms of hydrogen absorption-desorption in $CeMgCo_4H_x$ crystal with determining the dependence of P on the hydrogen concentration at different temperatures. Previously energy parameters γ_0 , γ' , γ'' , γ^* and G_α coefficient must be evaluated. This evaluation was performed using the experimental data for the process of hydrogenation-dehydrogenation in $CeMgCo_4H_x$ crystal at temperature equal 323 °C (Fig. 1). Evaluation showed that $G_\alpha = 1$ and the energy parameters are

$$\gamma_0 = 4,16 \text{ eV}, \quad \gamma' = -6,24 \text{ eV}, \quad \gamma'' = 2,08 \text{ eV}, \quad \gamma^* = 0,01 \text{ eV}. \quad (9)$$

Using the values calculated according to (8) the isotherms of hydrogen absorption - desorption in $CeMgCo_4H_x$ crystal were plotted for different temperatures (Fig. 2). As one can see, the graph has a certain degree of symmetry, so for $f = \ln P$ the following relation is true

$$f(c) = f(1 - c). \quad (10)$$

Moreover, we see the sorption hysteresis effect appearance. The hysteresis loop narrows with increasing temperature, shortens and disappears.

There is no mentioned symmetry on an experimental graph (Fig. 1). Possible explanation is following: at $x \geq 3$ ($c \geq 3/4$) the introduction of hydrogen atoms into the crystal is more intensive, hydrogen atoms begin to fill not only vertices of octahedra, but also other cavities of the crystal lattice, for example, the centers of the planar planes in the cell unit with coordinates $z = a/8, a/4, a/2, 3a/4, 7a/4$. It leads to the significant expansion of the crystal lattice and the implementation of the structural phase transition $\alpha \rightarrow \beta$.

The structure of β phase ($CeMgCo_4H_6$) is not yet clarified due to its instability. But it can be stated that the free energy of this phase will be similar to the F_α (6)

$$F_\beta = E_{\alpha\beta} + 6N \{ U_\beta(c) + kT [c \ln c + (1-c) \ln(1-c)] - kT c \lambda_\beta \}.$$

In β phase $c = N_H / 6N = x / 6$, $0 \leq c \leq 1$, $0 \leq x \leq 6$. The condition of thermodynamic equilibrium (7) also results in equation, similar to (8)

$$\ln P = 2 \ln \frac{c}{G_\beta(1-c)} + \frac{\Gamma_\beta(c)}{kT}.$$

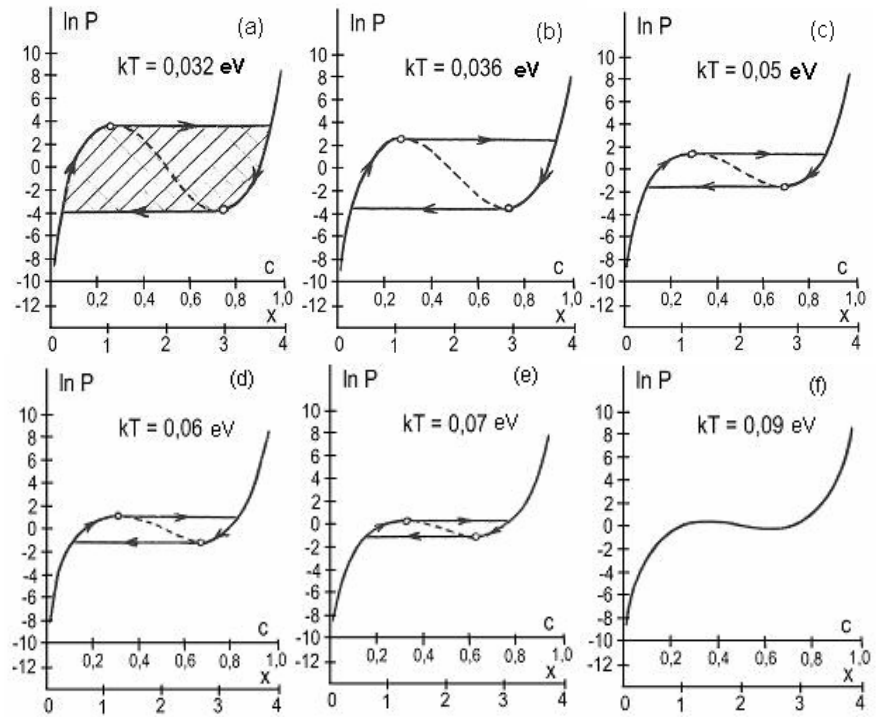


Fig.2. Estimated absorption-desorption isotherms of hydrogen in magnesium intermetallic compound $CeMgCo_4H_4$ according to (8) for the energy parameters (9) and for different temperatures equal to $kT = 0.032, 0.036, 0.05, 0.06, 0.07,$ and 0.09 eV (curves *a, b, c, d, e, f*). Dashed parts correspond to the unstable state of the system. Circles on the curves mark the extreme points. Shaded area shows the sorption hysteresis effect. Coordinates c, x define hydrogen concentration in the intermetallic compound: $0 \leq c \leq 1, 0 \leq x \leq 4$.

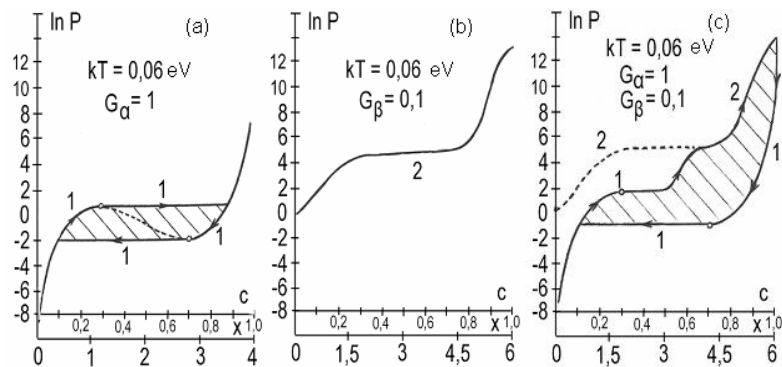


Fig.3. Estimated isotherms of hydrogen absorption-desorption: *a* – in $CeMgCo_4H_x$ crystal at $0 \leq x \leq 4, G_\alpha = 1, \Gamma_\alpha(c)$; *b* – in $CeMgCo_4H_x$ crystal at $0 \leq x \leq 6, G_\alpha = 0,1$ and $|\Gamma_\beta(c)| = 0,5 |\Gamma_\alpha(c)|$; *c* – in the system with $\alpha \rightarrow \beta$ phase transition at $x \approx 3$. Shaded area demonstrates the hysteresis effect.

Thus, due to the lattice expansion the absolute value of energy $\Gamma_\beta(c)$ is reduced in comparison with $\Gamma_\alpha(c)$ and activity of hydrogen atoms decreases (activity characterizes system energy changing simultaneously with changing number of hydrogen atoms entering the crystal)

$$|\Gamma_\alpha(c)| > |\Gamma_\beta(c)| \quad \text{and} \quad \lambda_\alpha > \lambda_\beta \quad (G_\alpha > G_\beta).$$

As an example, absorption-desorption isotherms were constructed in the α and β phases in the case of $G_\beta = 0,1G_\alpha$ and $|\Gamma_\beta(c)| = 0,5|\Gamma_\alpha(c)|$, which are shown in Fig. 3a, b.

According to Fig. 3b, the hysteresis effect in β phase at the selected temperature is absent. Fig. 3c is a superposition of graphs a and b taking implementation of the phase transition $\alpha \rightarrow \beta$ at $x \approx 3$ into account, when the curve 1 smoothly transforms into curve 2. Hydrogen atoms with increasing pressure (absorption) has been extensively introduced into the crystal while with decreasing pressure (desorption) intensively leave it. As a result of the phase transition $\alpha \rightarrow \beta$ hysteresis loop is distorted in comparison to that one in Fig. 3 in the absence of transformation. The comparison of the calculated and experimental isotherms in Fig. 3 and 1 indicates their similar nature.

Conclusions

A statistical theory of the hydrogen absorption-desorption in $CeMgCo_4$ crystal with forming hydrides (deuterides), i.e. α and β $CeMgCo_4H_4$ phases, makes it possible to explain and justify the behavior of the isotherms of the process, observed experimentally. The free energies of phases determining their dependency on temperature, pressure, hydrogen concentration, and activity of the hydrogen atoms and energy constants have been calculated. Minimization of the free energy, which determines the thermodynamic equilibrium equation, allowed studying the hydrogen sorptivity of crystals at different temperatures. The possibility of the hysteresis effect that disappears with increasing temperature has been shown. Consideration of the phase transformation $\alpha \rightarrow \beta$ allowed constructing the isotherms close to real ones and explaining the appearance of curves at the phase transition for them.

Performed calculations show that the experimental investigation of the hydrogen sorption isotherms in crystals can identify presence or absence of phase transformations in the system and also identify the possible phase transition temperature, if any. We should also note that the estimated energy parameters are not optimal. Summarizing results of independent experiments may allow using the above formulas to set the curves of absorption and desorption more clearly, as well as to estimate the temperature of phase transformations in the crystal.

References

1. Денис Р. В. Структура и водородсорбционные свойства новых соединений и сплавов на основе магния / Р.В. Денис, В.В. Березовец, И.В. Ковальчук и др. // Водородное материаловедение и химия углеродных наноматериалов. – К., 2009. – С.40-43.
2. Denys R. V. New Mg-M-Ni (M = Mn, Ti, Al) alloys as efficient hydrogen storage materials / R.V. Denys, I.Yu. Zavaliy et al. // Hydrogen materials science and chemistry of carbon nanomaterials. – 2007. – P. 332-335.
3. Chotard J. N. Hydrogen induced site depopulation in the LaMgNi₄ hydrogen system / J. N. Chotard, D. Sheptyakov, K. Yvon // Z. Kristallogr. – 2008. – V. 223. – P.690-696.
4. Матысина З. А. Атомный порядок и свойства сплавов. – Д., 1981. – 112 с.
5. Матысина З. А. Водород и твердофазные превращения в металлах, сплавах и фуллеритах / З. А. Матысина, Д. В. Щур. – Д., 2002. – 420 с.
6. Матысина З. А. Растворимость примесей в металлах, сплавах, интерметаллидах, фуллеритах / З. А. Матысина, С. Ю. Загинайченко, Д. В. Щур. – Д., 2006. – 514 с.
7. Смирнов А. А. Молекулярно-кинетическая теория металлов / А. А. Смирнов – М., 1966. – 488 с.
8. Смирнов А. А. Теория сплавов внедрения / А. А. Смирнов – М., 1979. – 368 с.

Received 13.07.2013.

O. I. Kushnerov, V. F. Bashev

Oles Honchar Dnipropetrovsk National University

MICROSTRUCTURE AND MECHANICAL PROPERTIES OF NEW MULTICOMPONENT HIGH-ENTROPY ALLOYS

The multicomponent high-entropy alloys CoCrCuFeNiSn_x ($x=0,5;1$) were investigated. Alloys were found to have two-phase (FCC + BCC) structure. No intermetallic phase formations were observed. The lattice constant of both the FCC and BCC phases increased with increasing content of the Sn atoms. Furthermore, increase of Sn content led to formation of BCC lattice-type phase B2 (ordered solid solution). Both of the alloys displayed a typical cast dendritic structure. Energy dispersive spectrometry revealed a segregation of Cu and Sn in the interdendritic space. Investigated alloys were found to exhibit high microhardness and excellent resistance to anneal softening. Their microhardness after annealing at 1000°C for 5 hours and cooling in the furnace remained almost the same. It was established that increasing of Sn content in the alloy has a positive effect on microhardness as by increasing the degree of elastic deformation of the crystal lattice, due to the large size of substituting Sn atoms, and by forming the ordered B2 phase.

Keywords: multicomponent high entropy alloy, structure, microhardness.

Впервые исследованы многокомпонентные высокоэнтروпийные сплавы CoCrCuFeNiSn_x ($x=0,5;1$). Установлено что сплавы имели двухфазную ОЦК+ГЦК структуру, интерметаллические фазы не обнаружены. Параметры решетки как в ОЦК так и в ГЦК фазах возросли с увеличением содержания Sn. Кроме того, увеличение содержания Sn приводило к формированию упорядоченного твердого раствора со структурным типом B2 на основе ОЦК фазы. Изученные сплавы демонстрировали типичную дендритную структуру. При помощи энергодисперсионного рентгеновского спектрометра обнаружена сегрегация атомов Cu и Sn в междендритное пространство. Исследованные сплавы демонстрировали высокие значения микротвердости и устойчивость к смягчению путем отжига. Значения микротвердости сплавов оставались практически неизменными после отжига в течении 5 часов при температуре 1000°C и последующего охлаждения в печи. Установлено, что увеличение содержания Sn в сплаве оказывало позитивное влияние на величину микротвердости как благодаря увеличению степени упругой деформации кристаллической решетки из за большого размера замещающих атомов Sn, так и благодаря формированию упорядоченной фазы B2.

Ключевые слова: высокоэнтропийный сплав, структура, микротвердость.

Вперше досліджені багатоконпонентні високоентропійні сплави CoCrCuFeNiSn_x ($x=0,5;1$). Встановлено що сплави мали двофазну ОЦК+ГЦК структуру, інтерметалічні фази не виявлені. Параметри решітки як в ОЦК так і в ГЦК фазах зростали зі збільшенням вмісту Sn. Крім того, збільшення вмісту Sn спричиняло формування впорядкованого твердого розчину зі структурним типом B2 на основі ОЦК фази. Досліджені сплави демонстрували типову дендритну структуру. За допомогою енергодисперсійного рентгенівського спектрометра виявлено сегрегацію атомів Cu та Sn у междендритний простір. Досліджені сплави демонстрували високі значення микротвердості та стійкість до пом'якшення шляхом відпалу. Значення микротвердості сплавів залишалися практично незмінними після відпалу впродовж 5 годин за температури 1000°C та наступного охолодження у пічці. Встановлено, що збільшення вмісту Sn у сплаві мало позитивний вплив на величину микротвердості як завдяки збільшенню ступеня пружної деформації кристалічної решітки спричиненого великими розмірами атомів заміщення Sn, так і завдяки формуванню впорядкованої фази B2.

Ключові слова: високоентропійний сплав, структура, микротвердість.

Introduction

Up to present time, the traditional strategy for developing alloys is to select one or two elements as principal components for primary properties and other minor elements incorporated for definite microstructure and properties. In the 1960-1990's many researchers have explored a wide range of bulk amorphous alloys based on at least three different components with significantly different atomic radii [1]. However, the design principles of the above alloys are still limited to the use of matrices containing a high concentration of one or two elements. The main reason for limiting the number of basic elements is the expected formation of a large number of brittle intermetallic compounds and complex microstructures in the structure of alloys. Recently some studies have developed a new thermodynamic approach to design alloys with multiprincipal metallic elements [2, 3] As a result, a new class of materials known in the literature as multicomponent high-entropy alloys (MHA) has been obtained. MHAs generally have at least five principal elements with the concentrations of each of them between 5 and 35 at.% (equiatomic or near-equiatomic concentrations being better). Alloys with multiprincipal elements tend to be thermodynamically stable because of their high entropy of mixing. Due to the high mixing entropy these equiatomic multicomponent alloys are observed to form solid solutions with simple crystal structures (FCC or BCC), without detectable intermetallic compounds or ordered phases. MHA's were first explored by Yeh et al., the results were published in 2004 [2]. For the past few years, a number of multicomponent alloys were obtained and studied. A unique structure and a complex of promising properties, such as hardness, wear resistance, oxidation resistance, corrosion resistance and high thermal stability [4-8] characterize these alloys. Improved mechanical characteristics are ensured by the strong distortion of the crystal lattice due to the differences in atomic radii of the elements. The higher the entropy of mixing, the more pronounced these characteristics of the alloy. This thermodynamic approach to the design of a multicomponent alloy allows to define a priori the number of elements and their relationship, and partly to evaluate the phase and structural state after crystallization. However, this approach cannot be a unique solution for the problem of choosing the specific alloying elements to obtain required characteristics. For this reason, basing on data like mixing entropy to assess MHA properties, it is need to specify the composition of the alloy empirically. Most of MHA's were designed with using such metals as Al, Ti, Cr, Fe, Co, Ni and Cu. In this paper effect of the value of mixing entropy and composition on the microhardness, phase composition and parameters of the fine structure of multicomponent alloys CoCrCuFeNiSn_x ($x=0,5;1$) in the as-cast (cooling rate of $\sim 10^3 \text{ K}\cdot\text{s}^{-1}$) state has been firstly investigated.

Materials and methods

Cast ingots of the alloys with multiprincipal metallic elements were polished and electrochemically etched for observation. The microstructures of the as-cast samples were studied using an optical microscope and scanning electron microscope (SEM) REMMA - 102-02. The chemical compositions of these cast alloys were analyzed by SEM energy dispersive spectrometry. X-ray diffraction (XRD) was carried out on a DRON -2.0 in monochromatic copper radiation. The microhardness was measured on a PMT-3 microhardness-meter at a load of 200 g. Selection of the components for investigated alloys was performed basing on the following considerations.

In accordance with the Gibbs equation

$$\Delta G_{mix} = \Delta H_{mix} - T \Delta S_{mix} . \quad (1)$$

Here ΔG_{mix} - the Gibbs potential, ΔH_{mix} - the enthalpy and ΔS_{mix} - entropy of mixing, which is determined from the equation

$$\Delta S_{mix} = -R \sum_{i=1}^n c_i \ln c_i, \quad (2)$$

c_i is an atomic fraction of the i -th component, R is an universal gas constant. Increasing of mixing entropy in accordance with Eq. (1) reduces the Gibbs free energy of the alloy and improves the stability of the solid solution. For the alloy where n is the number of components maximum mixing entropy is when they are mixed in equal atomic fractions. However, in practice, is not always possible to achieve the desired alloy properties by simply mixing the components in the equiatomic ratio. In this regard, additional criteria have been developed for carrying out selection of alloy elements [9,10]:

1. The value of the entropy of mixing should not be less than 12 J/(mol·K)).
 2. Enthalpy of mixing should be in the range from -15 kJ/mol to 5 kJ/mol. Too high enthalpy of mixing leads to the segregation of the individual components of the alloy, too low leads to the formation of complex structures and intermetallic compounds. The value of ΔH_{mix} is determined by the formula

$$\Delta H_{mix} = \sum_{i=1, i \neq j}^n \Omega_{ij} c_i c_j \quad (3)$$

where the regular melt-interaction parameter between i -th and j -th elements $\Omega_{ij} = 4\Delta H_{mix}^{AB}$, and ΔH_{mix}^{AB} - mixing enthalpy of binary liquid AB alloy.

3. Alloy components should not have large atomic-size difference. It is necessary for the formation of simple substitution solid solutions ($\delta \leq 4,6$, where δ - parameter characterizing the difference in atomic radii of the alloy components). For the ordered solid solutions, δ is required to be in the range of $4.6 \leq \delta \leq 6.5$.

$$\delta = 100 \sqrt{\sum_{i=1}^n c_i \left(1 - \frac{r_i}{\bar{r}}\right)^2} \quad (4)$$

where $\bar{r} = \sum_{i=1}^n c_i r_i$, r_i - the atomic radius of the i -th element.

Mixing enthalpies and atomic radii of charging elements and their concentration in the alloys investigated in this paper are shown respectively in Tab.1 and Tab. 2. Values of ΔH_{mix} , ΔS_{mix} and δ , calculated using the equations (2) – (4) for alloy CoCrCuFeNiSn_{0,5} are: $\Delta H_{mix} = 4.23$ kJ/mol, $\Delta S_{mix} = 14.69$ J/(mol·K), $\delta = 7.08$. For alloy CoCrCuFeNiSn₁: $\Delta H_{mix} = 4.89$ kJ/mol, $\Delta S_{mix} = 14.89$ J/(mol·K), $\delta = 8.95$. Thus, the parameter δ for the alloys exceeds the recommended limit, but, as pointed out in [12], this criterion appears to require some clarification.

The significantly larger atomic radius of tin should have a positive impact on the value of microstrains and mechanical characteristics of the materials (in particular, the microhardness H_μ). The value of microstrains is evaluated from the degree of distortion of the crystal lattice ($\Delta a/a$). In this paper, the level of microstrain and the value of the dislocation density were estimated from the broadening of the diffraction peaks.

Table 1

Atomic radii of elements and nominal chemical compositions of CoCrCuFeNiSn_x alloys

	Co	Cr	Cu	Fe	Ni	Sn
Atomic radii, nm.	0.125	0.129	0.128	0.126	0.125	0.158
Composition of CoCrCuFeNiSn _{0.5} , at. %	18.18	18.18	18.18	18.18	18.18	9.1
Composition of CoCrCuFeNiSn ₁ , at. %	16.67	16.67	16.67	16.67	16.67	16.67

Table 2

Values of ΔH_{mix} (kJ/mol), calculated by Miedema's model [12]

Element	Cr	Cu	Fe	Ni	Sn
Co	-4	6	-1	0	0
Cr		12	-1	-7	10
Cu			13	4	7
Fe				-2	11
Ni					-4

Results and discussion

The phase composition of the investigated CoCrCuFeNiSn_x alloys, crystal lattice parameters and the fine structure parameters (coherent scattering areas and microstrains) were determined from the XRD patterns. The dislocation density (ρ) was obtained from the profile of the first diffraction peak. XRD analysis allowed us to establish what CoCrCuFeNiSn_{0.5} and CoCrCuFeNiSn₁ alloys have two-phase (FCC + BCC) structure. With increase in Sn content increases the tendency to form a BCC lattice-type phase B2 (CsCl).

Results of XRD analysis are shown in Tab. 3, from which it is seen that increasing of Sn content in the alloy has a positive effect on microhardness as by increasing the degree of elastic deformation of the crystal lattice, due to the large size of substituting Sn atoms, and by forming the ordered B2 phase. The lattice constant of both the FCC and BCC phases increased with increasing content of the Sn atoms.

MHA were also found to exhibit excellent resistance to anneal softening. Tab. 3 shows that their microhardness after annealing, even at 1000°C for 5 hours and cooling in the furnace, remains almost the same.

Table 3

Phase composition, coherent scattering areas (L), the degree of distortion of the crystal lattice ($\Delta a/a$), microhardness (H_{μ}) and the dislocation density (ρ) of the investigated alloys

Alloy	Phase composition	L , nm	$\Delta a/a$	H_{μ} , MPa	H_{μ} , MPa (after heat treatment)	ρ , sm ⁻²
CoCrCuFeNiSn _{0.5}	FCC ($a=0.3586$ nm)+ BCC (CsCl-type, $a=0.2979$ nm)	$L_{\text{FCC}}=37\pm 2$ $L_{\text{BCC}}=27\pm 2$	$1.8 \cdot 10^{-3}$	3500 ± 200	3800 ± 200	$4.2 \cdot 10^{11}$
CoCrCuFeNiSn ₁	FCC ($a=0.3600$ nm)+ BCC (CsCl-type, $a=0.2981$ nm)	$L_{\text{FCC}}=19\pm 2$ $L_{\text{BCC}}=21\pm 2$	$2.3 \cdot 10^{-3}$	4000 ± 200	3900 ± 200	$1.6 \cdot 10^{12}$

Fig. 1 is a secondary electron image of the as-cast CoCrCuFeNiSn_{0.5} and CoCrCuFeNiSn₁ alloys subjected to electrochemical etching. Both of the alloys display a typical cast dendritic structure. Energy dispersive spectrometry revealed a segregation of Cu and Sn in the interdendritic space (Tab.4). The interdendritic space of CoCrCuFeNiSn₁ alloy can be divided into two phases of different composition.

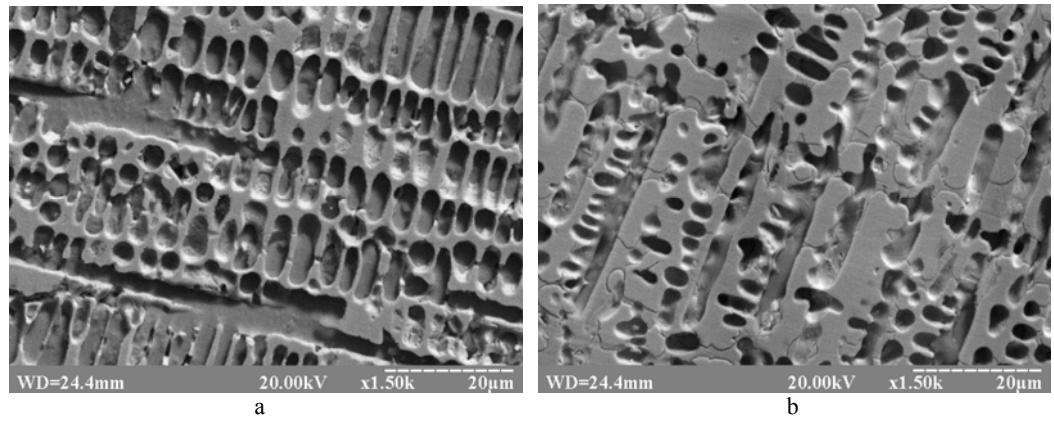


Fig.1. Microstructures of the CoCrCuFeNiSn_{0.5} (a) and CoCrCuFeNiSn₁ (b) alloys

Table 4

Chemical compositions of as-cast CoCrCuFeNiSn_x alloys

Alloy		Element, %					
		Co	Cr	Cu	Fe	Ni	Sn
CoCrCuFeNiSn _{0.5}	Dendrite	22.87	20.63	6.65	26.54	17.07	6.24
	Interdendrite	2.33	0.65	36.92	2.01	15.04	43.05
CoCrCuFeNiSn ₁	Dendrite	20.73	15.88	7.50	22.50	13.92	19.47
	Interdendrite	1.56	0.24	42.14	0.76	9.14	46.16
		4.91	1.28	10.63	2.48	18.97	61.73

Conclusions

The investigated multicomponent CoCrCuFeNiSn_x alloys reveal the presence of simple crystal structures, i.e. FCC solid-solution and BCC solid-solution phases. No intermetallic phase formation has been observed in these alloys.

In CoCrCuFeNiSn_x alloys revealed the presence of segregation microinhomogeneity within interdendrite space.

For the investigated alloys increase of Sn content leads to formation of ordered solid solution phase B2.

The alloy microhardness increase with Sn content increasing. Such a fact can be explained not only by the increased strengthen effect of lattice strain caused by the lattice sites occupation of Sn, but also by the ordering into the B2 phase. This conclusion is because the microhardness increased with increasing degree of ordering in the solid solution.

References

1. **Inoue A.** Glass-forming ability of alloys/ A. Inoue, T. Zhang, T. Masumoto// J. Non-Crystalline Solids. – 1993. – V. 156. –P. 473- 480.
2. **Yeh J.W.** Nanostructured high-entropy alloys with multiple principal elements: Novel alloy design concepts and outcomes/ J.W. Yeh, S.K. Chen, S.J. Lin, J.Y. Gan, T.S. Chin, T.T. Shun, C.H. Tsau, S.Y. Chang // Advanced Engineering Materials. –2004. –V.6. –P.299-303.
3. **Ranganathan S.** Alloyed pleasures: Multimetallic cocktails/ S. Ranganathan //Current Science. –2003. –V.85. –P.1404-1406.
4. **Tong C.J.** Mechanical performance of the Al_xCoCrCuFeNi high-entropy alloy system with multiprincipal elements/ C.J. Tong, M.R. Chen, S.K. Chen, J.W. Yeh, T.T. Shun, S.J. Lin, S.Y. Chang // Metallurgical and Materials Transactions A. –2005. –V.36A. –P.1263-1271.

5. **Wu J.M.** Adhesive wear behavior of Al_xCoCrCuFeNi high-entropy alloys as a function of aluminum content/ J.M. Wu, S.J. Lin, J.W. Yeh, S.K. Chen, Y.S. Huang // *Wear.*–2006. – V.261. – P.513-519.

6. **Chen Y.Y.** Microstructure and electrochemical properties of high entropy alloys - a comparison with type-304 stainless steel/ Y.Y. Chen, T. Duval, U.D. Hung, J.W. Yeh, H.C. Shih // *Corrosion Science.*–2005.–V.47. –P. 2257-2279.

7. **Li B.S.** Effects of Mn, Ti and V on the microstructure and properties of AlCrFeCoNiCu high entropy alloy/ B.S. Li, Y.P. Wang, M.X. Ren, C. Yang, H.Z. Fu // *Materials Science and Engineering A.*–2008. –V.498. –P.482–486.

8. **Chou H.P.** Microstructure, thermophysical and electrical properties in Al_xCoCrFeNi (0 ≤ x ≤ 2) high-entropy alloys/ H.P. Chou, Y.S. Chang, S.K. Chen, J.W. Yeh // *Materials Science and Engineering B.* –2009. –V.163. –P.184-189.

9. **Zhang Y.** Solid-Solution Phase Formation Rules for Multi-component Alloys/ Y. Zhang, Y.J. Zhou, J.P. Lin, G.L. Chen, P.C. Liaw // *Advanced Engineering Materials.*–2008. –V.10, Iss. 6. – P. 534–538.

10. **Zhang C.** Computational Thermodynamics Aided High-Entropy Alloy Design/ C. Zhang, F. Zhang, S. Chen, W. Cao // *JOM.* –2012. –V. 64, Iss. 7. –P. 839–845.

11. **Takeuchi A.** Classification of Bulk Metallic Glasses by Atomic Size Difference, Heat of Mixing and Period of Constituent Elements and Its Application to Characterization of the Main Alloying Element/ A. Takeuchi, A. Inoue // *Materials Transactions.*–2005. –V. 46, № 12. –P. 2817-2829.

12. **Sriharitha R.** Phase formation in mechanically alloyed Al_xCoCrCuFeNi (x = 0.45, 1, 2.5, 5) high entropy alloys/ R. Sriharitha, B. S. Murty, R. S. Kottada // *Intermetallics.* – 2013. – V.32. – P. 119-126.

Received 13.07.2013.

P. S. Gusevik, S. I. Ryabtsev, F. F. Dotsenko

Oles Honchar Dnipropetrovsk National University

STRUCTURE AND PROPERTIES OF PURE Mn, Bi AND MnBi FILMS IN METASTABLE STATE

The regularities of formation of Bi, Mn and MnBi metastable film structures obtained by modified three-electrode ion-plasma sputtering method (IPS) were researched. X-ray analysis shown that in the as-deposited Bi films a mixture of rhombohedral Bi phase ($L = 6.5$ nm) with traces of cubic Bi was formed. Heat treatment led to the enlargement of the grains and the complete disappearance of Bi with a cubic lattice. MnBi films were a mixture of rhombohedral Bi phase and β -Mn in the initial state. After heat treatment, traces of Bi_2Mn and MnO appeared besides those phases. The analysis of the temperature dependence of resistivity revealed that for pure Mn, Bi and MnBi the activation energies of the phase transitions were $E_A \sim 5000$ K, $E_A \sim 8500$ K and $E_A \sim 3500$ K respectively. After heating the Bi and MnBi films to the temperatures above 670 K and subsequently cooling them to a temperature of 490 K there was an abrupt change in resistance. The analysis of demagnetization curves showed that the hysteresis of magnetization was observed only in the films containing Bi because of the assumed manifestations of ferrimagnetic properties of Bi oxide in the non-equilibrium state.

Keywords: MnBi films, ion-plasma sputtering, hard magnetic materials, metastable state.

В работе исследованы закономерности формирования метастабильных структур пленок Bi, Mn и MnBi полученных модернизированным методом трехэлектродного ионно-плазменного распыления (ИПР). В результате рентгеноструктурного анализа установлено, что в свеженанесенных пленках чистого Bi образуется смесь фаз ромбоэдрического Bi ($L=6.5$ нм) и следов кубического Bi. Термообработка приводила к укрупнению зерен и полному исчезновению Bi с кубической решеткой. Пленки MnBi в исходном состоянии представляли смесь фаз ромбоэдрического Bi и β -Mn. После термообработки кроме указанных фаз появлялись следы Bi_2Mn и MnO. Анализ кривых температурной зависимости электросопротивления пленок позволил установить, что для чистых Mn, Bi и MnBi энергия активации фазовых переходов составляет $E_A \sim 5000$ К, $E_A \sim 8500$ К и $E_A \sim 3500$ К соответственно. При нагреве пленок чистого Bi и MnBi до температуры выше 670 К и последующем охлаждении до температуры 490 К происходило скачкообразное изменение сопротивления. Анализ кривых размагничивания пленок показал, что гистерезис намагничивания наблюдается только в пленках содержащих Bi, поскольку предполагается проявление ферримагнитных свойств оксида Bi в неравновесном состоянии.

Ключевые слова: пленки MnBi, ионно-плазменное распыление, магнитотвердые материалы, метастабильное состояние.

У роботі досліджені закономірності формування метастабільних структур плівок Bi, Mn, та MnBi отриманих модернізованим методом трьохелектродного іонно-плазмового розпилювання (ИПР). В результаті рентгеноструктурного аналізу встановлено, що в свіженанесених плівках чистого Bi утворюється суміш фаз ромбоэдричного Bi ($L=6.5$ нм) та слідів кубічного Bi. Термообробка приводила до збільшення зерен та повного зникнення Bi з кубічною решіткою. Плівки MnBi в початковому стані являли суміш фаз ромбоэдричного Bi та β -Mn. Після термообробки крім зазначених фаз з'являлись сліди Bi_2Mn та MnO. Аналіз кривих температурної залежності електроопору плівок дозволив встановити, що для чистих Mn, Bi та MnBi енергія активації фазових переходів складає $E_A \sim 5000$ К, $E_A \sim 8500$ К та $E_A \sim 3500$ К відповідно. При нагріві плівок чистого Bi та MnBi до температури більше 670 К та подальшому охолодженню до температури 490 К відбувалась стрибкоподібна зміна електроопору. Аналіз кривих розмагнічування плівок показав, що гістерезис намагнічування спостерігається тільки в плівках, які містять Bi, оскільки припускається наявність ферримагнітних властивостей оксиду Bi у нерівноважному стані.

Ключові слова: плівки MnBi, іонно-плазмове розпилювання, магнітотверді матеріали, метастабільний стан.

Introduction

Significant interest in studying of MnBi alloys is due to the manifestation of high coercivity and residual magnetization, which is typical for high magnetic materials [1]. The MnBi ferromagnetic phase presence allows using this material as magnetic elements for microelectronic devices and high-density information recording [2]. Recently research has been carried out to improve the magnetic properties of known magnetic materials by heat treatment and obtaining conditions influencing on the domain structure. It has also become topical the study of magnetic samples obtained under non-equilibrium conditions in the film form. Such films are amorphous or nanocrystalline compounds in which the important role played by the size effects. Such effects have a direct impact on the physical properties of samples. The paper investigates the structure, phase composition and physical properties of the Mn, Bi and MnBi films, as well as the influence of the deposition conditions and heat treatment on the original structure and properties.

Materials and methods

Investigations were carried out on pure Mn, Bi and MnBi thin films with compositions (atomic %): Mn₅₉Bi₄₁; Mn₅₆Bi₄₄; Mn₄₉Bi₅₁; Mn₄₂Bi₅₈. The films with thicknesses about $d \sim 150 - 400$ nm was obtained by a modernized three-electrode ion-plasma sputtering [3] under various deposition conditions (Table 1). The effective cooling rate for this method is theoretically estimated as $10^{12} - 10^{14}$ K/s [4] and associated with the relaxation of individual atoms on the substrate. Inert Ar was used as the working gas. The film thickness was determined by the gravimetric method through weighing the substrate before and after spraying.

Table 1

Conditions of thin film deposition

	Mn	Bi	Mn+41%Bi	Mn+44%Bi	Mn+51%Bi	Mn+58%Bi
d, nm	160	500	380	240	340	150
I _A , A	1	1	0.8	2	0.8	0.8
P _{Ar} , mPa	120	120	16	53	16	16
U, kV	-2	-2	-2	-2	-2	-2
φ, eV	20	20	200	100	200	200

where U - target voltage; I_A - anode current; P_{Ar} - working gas pressure (Ar); d - film thickness; φ - the kinetic energy of the deposited atoms.

The deposition of the films was carried out on NaCl single crystals and pyroceramics (sitall) substrates. The films deposited on NaCl substrates were used for studies of phase composition in the initial and heat-treated states. The phase composition investigation was carried out by X-ray analysis using the Debye camera with filtered Co-radiation and transmission electron microscopy (on the samples received under reduced thickness and deposition time). The lattice periods were estimated by the quadratic equations with an accuracy of ± 0.001 nm.

The physical properties and thermal stability were examined for the films deposited at pyroceramics substrates. The films surface resistivity was measured by four-probe method with continuous heating in a vacuum about ~ 10 mPa with controlled heating rates between 4 and 20 K/min. The activation energy calculation of phase transitions was

performed by the Kissinger method, i.e. by analyzing the phase transition temperature displacement with heating rate changing. The film coercive force H_c was investigated by the vibration magnetometer in the maximum magnetizing field about 0.5 T, with parallel and perpendicular orientation to the film surface.

Results and discussion

X-ray analysis results of the initial and heat-treated films are shown in Table 2. Investigations were performed on freshly deposited and heat-treated films with different thicknesses and obtained at different deposition conditions for studying the structure formation (for example, at reduced plasma gas pressure (from 120 to 16 mPa), which increases the energy of deposited atoms).

Table 2

Freshly deposited and heat-treated films phase composition

Composition (at.%)	Phase composition of films		
	The annealing temperature	In initial state	After heat treatment
Mn	770 K	β -Mn ($L=7.4$ nm) ($a=0.688$ nm)	β -Mn ($L=10.5$ nm) ($a=0.69$ nm) + MnO
Bi	650 K	rhomb Bi ($L=6.5$ nm) ($a=0.4552$ nm; $c=11.83$ nm) + cubic Bi + Bi_2O_3	rhomb Bi ($L=8$ nm) ($a=0.4515$ nm; $c=11.99$ nm) + Bi_2O_3
Mn+41%Bi	670 K	rhomb Bi ($L=7$ nm) ($a=0.4543$ nm; $c=11.84$ nm) + cubic Bi + β -Mn ($a=0.6985$ nm)	rhomb Bi ($L=9$ nm) ($a=0.4679$ nm; $c=11.37$ nm) + Bi_2Mn + β -Mn ($a=0.703$ nm) + MnO
Mn+44%Bi	660 K	rhomb Bi ($L=6.7$ nm) ($a=0.462$ nm; $c=11.8$ nm) + cubic Bi + β -Mn ($a=0.632$ nm)	rhomb Bi ($L=8$ nm) ($a=0.452$ nm; $c=11.22$ nm) + β -Mn ($a=0.697$ nm) + MnO
Mn+51%Bi	690 K	rhomb Bi ($L=6.5$ nm) ($a=0.4533$ nm; $c=12.08$ nm) + cubic Bi + β -Mn ($a=0.6292$ nm)	rhomb Bi ($L=13$ nm) ($a=0.4552$ nm; $c=11.85$ nm) + Bi_2Mn + β -Mn ($a=0.633$ nm) + MnO
Mn+58%Bi	670 K	rhomb Bi ($L=9.5$ nm) ($a=0.39$ nm; $c=11.91$ nm) + cubic Bi + β -Mn ($a=0.6249$ nm)	rhomb Bi ($L=11$ nm) ($a=0.4538$ nm; $c=12.05$ nm) + β -Mn ($a=0.6328$ nm) + MnO

where rhomb Bi - equilibrium rhombohedral Bi phase, cubic Bi - non-equilibrium cubic Bi phase, L - coherent scattering region size (CSR).

In the initial Mn films the nanocrystalline β -Mn phase (with CSR size $L \sim 7.4$ nm) was observed. After heat treatment in vacuum at a temperature of 770 K manganese is oxidized with the MnO oxide formation, and CSR size of β -Mn phase increases to 10.5 nm.

In the original Bi films there were the mixture of equilibrium rhombohedral Bi phase (with the CSR size $L \sim 6,5$ nm), nonequilibrium Bi with a cubic lattice, and traces of Bi_2O_3 oxide (Fig. 1c). The heat treatment of the films at a temperature of ~ 650 K leads to the decay of Bi cubic and its transition to the equilibrium state, and there is an increase of the CSR size of Bi rhombohedral to $L \sim 8$ nm. The structure of initial Bi film is shown in Fig. 1a.

In the MnBi films, as shown by electron diffraction and X-ray studies, in the initial state there were a mixture of the cubic and rhombohedral Bi phases as well as β -Mn traces. The CSR sizes of rhombohedral Bi phase for various compositions are shown in Table 2 and are in the range of $L \sim 6.5 - 9.5$ nm. After heat treatment at temperatures of 670 K there was a grain growth of rhombohedral Bi phase ($L \sim 8 - 13$ nm) and the change of the lattice to the values corresponding to the equilibrium state (Fig. 1d). As in the case of heat treatment of pure Mn and Bi, there were the decay of nonequilibrium Bi and β -Mn phase oxidation. Furthermore, in the $\text{Mn}_{59}\text{Bi}_{41}$ and $\text{Mn}_{49}\text{Bi}_{51}$ films obtained with the low

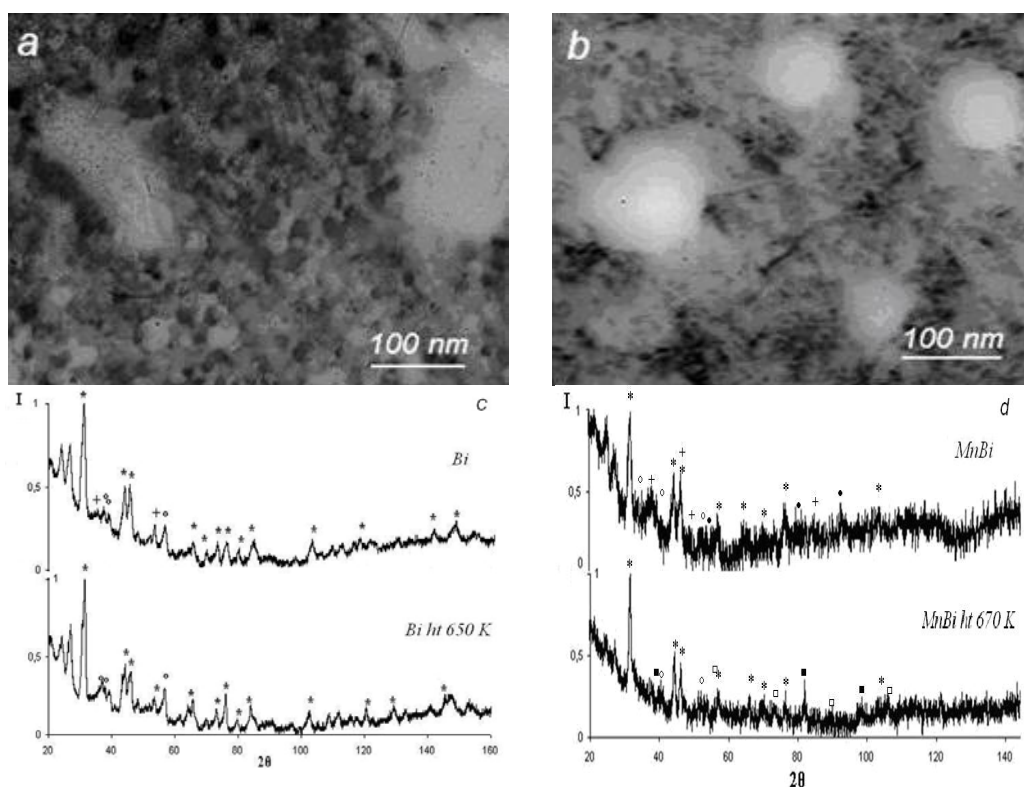


Fig. 1. X-ray diffraction patterns and microstructure of Bi and MnBi films: a) the structure of the original Bi film; b) the structure of the original $Mn_{49}Bi_{51}$ film; c) X-ray patterns of Bi film in initial and heat-treated states; d) X-ray patterns of $Mn_{49}Bi_{51}$ film where; * - Bi rhombohedral; + - Bi cubic; $^{\circ}$ - Bi_2O_3 ; \bullet - β -Mn; \blacksquare - Bi_2Mn ; \square - MnO.

pressure of working gas and the high energy of deposited atoms, after heat treatment there was intermediate Bi_2Mn phase formation. In the $Mn_{42}Bi_{58}$ film obtained under identical conditions the formation of the intermediate phase does not occur; this may be due to the relatively low film thickness (150 nm). The typical structure of MnBi film is illustrated in Fig. 1b. On the X-ray and electron diffraction there is broadening of the diffraction peaks, which may be associated with the occurrence of internal stresses during the formation of an intermediate phase.

The thermal stability of the films was investigated by recording the temperature dependence of the surface resistivity in a vacuum at a constant heating rate. The temperature dependence of the resistance curves are characterized by a number of characteristic sections.

In the pure Mn films the first section (from 295 K to 600 K) is characterized by a reversible change in resistance. This indicates that in this temperature range phase transitions does not occur and the sample structure remains stable. The second area is characterized by an irreversible decrease in the surface resistance in the temperature range from 620 K to 700 K, which indicates the phase transitions and changes in the film structure associated with recrystallization processes. At a temperature of ~ 800 K, the sample is subjected to strong oxidation. The third region is characterized by a reversible decrease in resistance during cooling from 770 K to 295 K.

In the MnBi films the first section is in the temperature range from 295 K to 570 K. The second section, showing a phase transition, is about from 570 K to 670 K, and the third temperature region is about from 700 K to the room temperature.

The Bi resistivity behavior during heating and cooling is different from the described above areas. At a temperature of 620 K there is a phase transition associated with the Bi melting, which is manifested in a relatively sharp decrease in resistance. The resulting melting point of Bi film is different from the data on the melting point of bulk samples by about 60 K. There is an instant increase in resistance (two fold) due to the Bi crystallization by lowering the sample temperature to ~ 480 K. The most typical temperature dependence of the surface resistance is shown in Fig. 2.

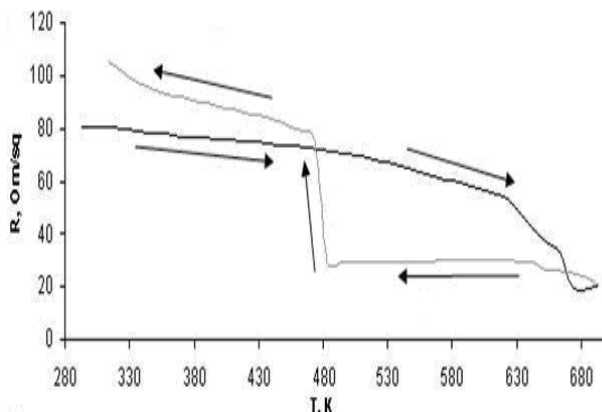


Fig. 2. The temperature dependence of the resistivity of Bi film.

As a result of the phase transition temperature displacement investigations with the increase in the heating rate there are the calculation of the activation energy of phase transformations (E_A) by the Kissinger method. In pure Mn and Bi films the activation energy is $E_A \sim 5 \times 10^3$ K and $E_A \sim 8.5 \times 10^3$ K. The MnBi films activation energy is in the range $E_A \sim 3 - 5 \times 10^3$ K, depending on the film thickness and phase composition.

The demagnetization curve analysis of the pure Mn films, as expected, did not show hysteresis characteristics in parallel and perpendicular fields. In Bi films the hysteresis properties are manifested due to the formation Bi_2O_3 oxide as a result, so the magnetic moment of the sample is uncompensated. MnBi films are characterized by anisotropy of magnetic properties. In the perpendicular magnetic field the films show the weak hysteresis properties. The coercivity does not exceed 2 kA/m in the initial state. Heat treatment at 720 K leads to an increase in coercivity up to 38 kA/m (Fig. 3). Heating above this temperature leads to the Mn oxidation, which leads to significant deterioration of magnetic properties. Thus, improvement of magnetic characteristics can be realized by choosing the exposure time at a predetermined temperature.

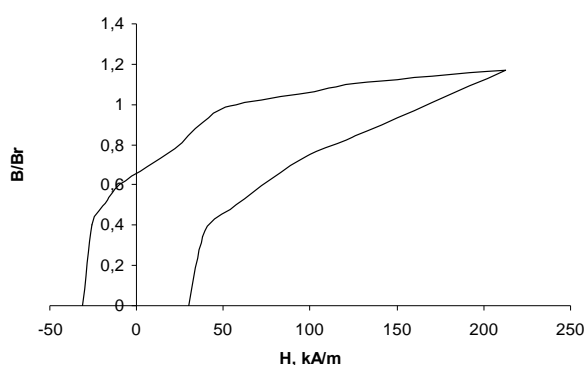


Fig. 3. Demagnetization curve of the $\text{Mn}_{49}\text{Bi}_{51}$ alloy after heat treatment

Conclusions

As a result, we can say that with the X-ray analysis and investigation of the magnetic properties of the Bi films was determined Bi_2O_3 oxide formation, which contributes to the manifestation of the hysteresis properties. The investigation of the deposition condition influence on the film structure has shown that the intermediate Bi_2Mn ferromagnetic phase is formed in the case of reduced pressure of the working gas and relatively high energy of the deposited atoms. The melting point of Bi films produced under non-equilibrium conditions is shifted by ~ 60 K compared to the bulk samples. Our investigation of the samples temperature stability has shown that the heating of the MnBi films to the temperature above 750 K leads to the active Mn oxidation that results in significant deterioration of the electrical and magnetic characteristics.

References

1. **Yang Y.B** Temperature dependences of structure and coercivity for melt-spun MnBi compound /Y.B. Yang, X.G. Chen, S. Guo, A.R. Yan // Journal of Magnetism and Magnetic Materials. – 2013. – V.330. – P. 106–110.
2. **Martin P.M.** Handbook of deposition technologies for films and coatings 3rd edition // Elsevier. – 2010, p. 912.
3. **Bashev V.F.** Structure and Electrical Properties of Ag–W Films in Metestable States. /V.F. Bashev, F.F. Dotshenko, I.S. Miroshnichenko, V.H. Pasalsky // Physics of Metals and Metallography. – 1992. – V. 73, No 2. – P. 152-156.
4. **Grant W.A.** Preparation of amorphous alloys by ion implantation /A. Ali, L.T. Chadderton, P.J. Grundy// London: Third international conference of rapidly quenched metals. – 1978.

Received 13.07.2013.

UDC 539.213 :539.26

N. A. Kutseva¹, V. F. Bashev¹, A. Y. Derun¹, V. S. Larin²

¹*Oles Honchar Dnipropetrovsk National University*

²*MicroFir Tehnologii Industriale, Kishinev, Moldova*

NANOCRYSTALLIZATION PROCESSES IN THE “FINEMET” TYPE MICROWIRES UNDER STRESS ANNEALING

Effect of thermal treatments such as conventional annealing and annealing under tensile stress on nanocrystallization behaviour of $\text{Fe}_{70.8}\text{Cu}_1\text{Nb}_{3.1}\text{Si}_{14.5}\text{B}_{10.6}$ glass-coated microwire was investigated. Initial microwire obtained by the Taylor-Ulitovski technique had an amorphous structure. It was found that conventional annealing within the temperature interval of 500 – 550 °C during 5 min led to the formation of primary α -Fe(Si) crystals in residual amorphous matrix. The mean grain size of the formed crystals was about of 16 nm and the crystallized volume fraction was 42%. The annealing under tensile stress resulted in changing mechanisms of crystallization, from primary to eutectic crystallization. The structure of microwire annealed within the mentioned temperature interval under stress was the mixture of α -Fe(Si) and Fe_3B crystalline phases. The mean grain size and crystallized volume fraction of the α -Fe(Si) crystals decreased up to 11 nm and 31 %, respectively. The optimal soft magnetic properties of microwires (coercivity was ~ 65 A/m) were achieved by annealing at 520 °C. It was connected with the formation of nanocrystalline structure of microwire.

Keywords: microwire, amorphous state, nanocrystalline structure, heat treatments.

В работе исследовалось влияние различных видов термообработки на процессы кристаллизации в микропроводе состава $\text{Fe}_{70.8}\text{Cu}_1\text{Nb}_{3.1}\text{Si}_{14.5}\text{B}_{10.6}$ в стеклянной изоляции. Исходный микропровод, полученный методом Улитовского-Тейлора, имел аморфную структуру. При традиционном отжиге в интервале температур 500 – 550 °C (5 мин.) происходило формирование первичных кристаллов α -Fe(Si) в оставшейся аморфной матрице. Средний размер кристаллов составлял ~ 16 нм и доля кристаллической фазы – 42 %. Отжиг при наличии одноосного растяжения приводил к смене механизма кристаллизации от первичной к эвтектической. Структура микропровода, отожженного в этом же температурном интервале при наличии нагрузки, представляла собой смесь фаз: α -Fe(Si) и Fe_3B . Средний размер и доля закристаллизовавшегося объема кристаллов α -Fe(Si) уменьшались до 11 нм и 31 %, соответственно. Оптимальные магнитные свойства микропровода (коэрцитивная сила ~ 65 А/м) получались отжигом при температуре 520 °C, что связывалось с образованием в нем нанокристаллической структуры.

Ключевые слова: микропровод, аморфное состояние, нанокристаллическая структура, термообработка.

У роботі досліджувався вплив різних видів термообробки на процеси кристалізації у мікродроті складу $\text{Fe}_{70.8}\text{Cu}_1\text{Nb}_{3.1}\text{Si}_{14.5}\text{B}_{10.6}$ в скляній ізоляції. Вихідний мікродріт, отриманий методом Улітовського-Тейлора, мав аморфну структуру. При відпалі в інтервалі температур 500 – 550 °C протягом 5 хв. спостерігалось утворення первинних кристалів α -Fe(Si) в аморфній матриці. Середній розмір кристалів складав 16 нм та частка кристалічної фази – 42 %. Відпал при прикладенні розтягнення приводив до зміни механізму кристалізації від первинної до евтектичної. Структура мікродроту, відпаленого під навантаженням в цьому температурному інтервалі, являла собою суміш фаз: α -Fe(Si) і Fe_3B . Середній розмір та частка кристалічної фази кристалів α -Fe(Si) зменшувались до 11 нм та 31 % відповідно. Оптимальні магнітні властивості мікродроту (коерцитивна сила ~ 65 А/м) були досягнуті відпалом за температури 520 °C, що було пов'язано із формуванням в ньому нанокристалічної структури.

Ключові слова: мікродріт, аморфний стан, нанокристалічна структура, термообробка.

Introduction

The soft ferromagnetic nanocrystalline alloys with trade mark “Finemet” are very promising for technological applications. The enhanced softness of these materials (coercivity less than 5 A/m, high initial permeability values) is usually achieved by the formation of nanocrystalline structure, which consists of an ultrafine α -Fe(Si) grains with typical size 10-15 nm embedded in a residual amorphous matrix. The most reported results are carried out on melt-spun nanocrystalline ribbons. On the other hand, the Taylor-Ulitovsky method allows to fabricate tiny metallic wires (the metallic nucleus diameter 1÷50 μm) covered by an insulating glass coating (the glass coating thickness 1÷20 μm). Nanocrystalline glass-coated microwires (MW) having the excellent combination of soft magnetic properties, stability of nanocrystalline state with small dimensions and their resistance to corrosion are very perspective as sensor elements in a large variety of electronic devices and sensors [1]. During the manufacturing process the large internal stresses ($\sim 1\text{GPa}$) arise as a result of difference between the thermal expansion coefficients of glass and alloy. The presence of such a residual stresses forms a complex domain structure of initial MW [2, 3]. It leads to increasing the coercivity and decreasing the initial permeability. The magnetoelastic anisotropy related to the internal stresses induced during the fabrication as well as the value and sign of the magnetostriction constant play a decisive role in the hysteretic magnetic properties of these thin wires. As well known, thermal treatments allow tailoring the magnetic properties of glass-coated MW [4, 5].

The aim of this work is to investigate the effect of thermal treatments such as conventional annealing and annealing under tensile stress on the structure and physical properties of MW.

Experimental details

Initial $\text{Fe}_{70.8}\text{Cu}_1\text{Nb}_{3.1}\text{Si}_{14.5}\text{B}_{10.6}$ MW with metallic nucleus diameter 16 μm and total diameter 26 μm have been obtained by the Taylor-Ulitovski technique. The microstructure of initial and heat-treated microwires has been characterized by X-ray diffraction (Mo K_α , Co K_α radiation). The annealing has been performed in conventional furnace at the temperature below crystallization temperature without applied stress (CA) and under applied tensile stress 10 g and 15 g on one microwire (SA). The temperature dependence of the electrical resistivity was used for studying crystallization processes occurring in MW. Thermal analysis for microwires was carried out using a Netzch 404 differential scanning calorimeter (DSC). Studied sample of a few mg weights placed in the alumina crucible and reference sample (empty crucible) were heated with identical thermal program (a heating rate was 20 K/min) while heat flow difference between sample and reference was recorded. Absorbed and released heat values were plotted as a function of temperature. Magnetic properties of microwires were measured by means of a conventional induction method at 50 Hz.

Results and discussion

The X-ray diffraction patterns showed that the initial microwires have amorphous structure (Fig.1). As can be seen, there are some broad diffusive halos, which are an inherent feature of disordered structures. Size of the coherently diffracting domains was approx. 2nm.

In order to study the structure changes and crystallization behaviour in microwires during isochronal heating a DSC test and measurements of electrical resistivity versus temperature were carried out, as shown in Figs. 2, 3.

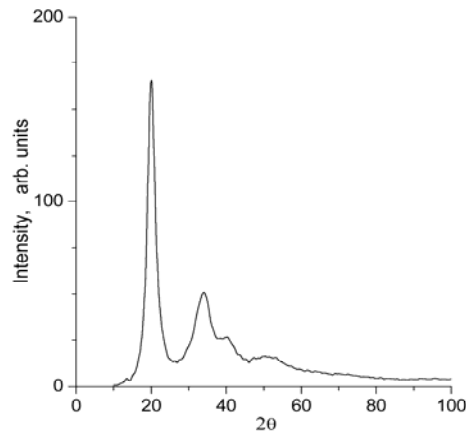


Fig. 1. Mo K_{α} X-ray diffraction pattern of initial microwire.

As can be seen from Fig. 3, the microwire resistivity increases slightly up to 300 °C and there is a sharp decrease of the resistivity from 300 °C to 500°C. The under stress annealing (SA) did not change the character of temperature dependency, but its values slightly increased.

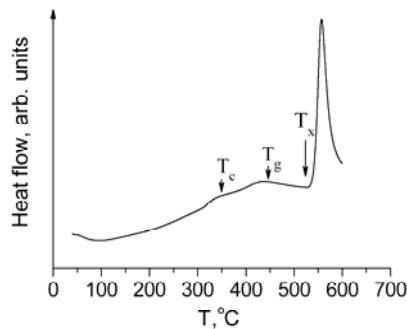


Fig. 2. The differential scanning calorimeter curve for microwires.

As X-ray results showed, with increasing the annealing temperature (CA) in the range from 500 °C to 550 °C it observed increase of main peak height and its sharpening. It can be explained the formation of the nanocrystalline structure (Fig. 4). As can be seen only a BCC α -Fe(Si) phase appears in residual amorphous matrix. The full width of the peak at half maximum and crystallized volume fraction (X_c) at the final stage of primary crystallization have been evaluated by deconvoluting the total profile of the amorphous halo and the (110) peak of α -Fe(Si) phase [6].

The mean grain size of the formed crystals is derived from the Scherrer equation. It is ~ 16 nm and $X_c \approx 42\%$. Thus, the conventional annealing in range of 500-550 °C leads to the formation nanocrystalline structure through primary crystallization. The other crystallization behavior we have in the case of SA at 110 MPa (Fig. 5).

The DSC curve shows exothermic effect in the temperature range from 200 °C up to the crystallisation temperature ($T_x = 520$ °C) and crystallization peak at the temperature 560 °C. The Curie temperature (T_c) was evaluated analysing the curve of magnetisation versus temperature. Its value was 317 °C. It corresponds to the change in the slope of DSC curve. The onset glass transition temperature T_g is 450 °C and the difference (ΔT) between T_x and T_g so called the width of the supercooled region that relates to the stability of amorphous phase, is 70 °C.

The results of the DSC curve correlates with the results of electrical resistance. As can

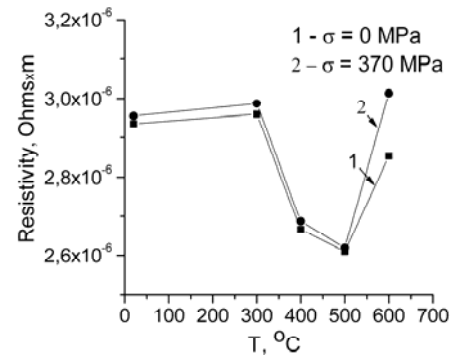


Fig. 3. The temperature dependence of the resistivity of microwires.

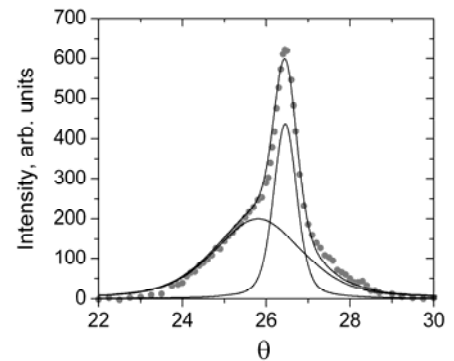


Fig. 4. Co K_{α} X-ray diffraction pattern of microwires treated at 550 °C (5 min).

One can see the width of the main peak does not decrease; moreover, it appears shoulders on the curve. After deconvoluting the total peak on the components it was found, that the structure of stress treated microwires consists of the mixture of α -Fe(Si) and (body tetragonal cubic) Fe_3B crystalline phases [7]. The mean grain size and crystallized volume fraction of α -Fe(Si) phase is 11 nm and 31 %, respectively. The lattice parameter of α -Fe(Si) phase is 0.284 nm and it differs from equilibrium one, likely it connects with the influence of metalloïd atoms according to data of phase diagram.

As well known amorphous structure is very often inhomogeneous and consists of the clusters with different short order. It is possible that stress annealing stimulates the processes of amorphous phase separation into two phases with different compositions and following formation of the mixture of α -Fe(Si) and Fe_3B crystalline phases through eutectic crystallization.

Magnetic characterization of initial and heat treated microwires was performed by conventional method. Coercivity of initial microwires was ~ 100 A/m. It was found that the coercivity values decreased to 62 A/m with increasing annealing temperature up to 520 °C. As X-ray analysis showed it was connected with formation of nanocrystalline structure.

Conclusions

Initial glass-coated $\text{Fe}_{70.8}\text{Cu}_1\text{Nb}_{3.1}\text{Si}_{14.5}\text{B}_{10.6}$ microwires have an amorphous structure. Size of the coherently diffracting domains is approx. 2nm. Conventional annealing in temperature range 500 – 550 °C leads to the formation of nanocrystalline structure consisting of α -Fe(Si) nanograins in residual matrix through primary crystallization.

Annealing under tensile stress in this temperature range leads to the formation of the mixture of α -Fe(Si) and Fe_3B crystalline phases through eutectic crystallization.

The optimal soft magnetic properties of microwires are achieved at the annealing at 520 °C (coercivity ~ 65 A/m).

References

1. **Zhukov, A.** Glass-coated magnetic microwires for technical applications/ A. Zhukov // J. Magn. and Magn. Materials. – 2002. – V. 242-245 – P. 216-223.
2. **Chiriac, H.** Amorphous glass-covered magnetic wires: preparation, properties, applications / H. Chiriac, A.Ovari // Progress in Materials Science. – 1996. – V. 40. – P. 333-407.
3. **Hernando, B.** Magnetic domain structure of amorphous $\text{Fe}_{73.5}\text{Si}_{13.5}\text{B}_9\text{Nb}_3\text{Cu}_1$ wires under torsional stress/ B. Hernando, M.L. Sanchez, V.M. Prida, J.D. Santos, J. Olivera, F.J. Belzunce, G. Badini, M. Vazquez // J.Appl.Phys. – 2008. – N 103. – 07E716.
4. **Miguel, C.** Coercivity and induced magnetic anisotropy by stress and/or field annealing in Fe- and Co- based (Finemet - type) amorphous alloys/ C. Miguel, A. Zhukov, J.J. del Val, J. Gonzalez // J. Magn. Magn. Mater. – 2005. – N 294. – P.245-251.
5. **Di, Y.** Magnetic and microwave properties of glass-coated amorphous ferromagnetic microwires/ Y. Di, J. Jiang, G. Du, B. Tian, S. Bie, H. He// J. Trans. Nonferrous Met. Soc. China. – 2007. – N 17. – P.1352-1357.
6. **Blazquez, J.** Microstructure and magnetic properties of $\text{Fe}_{78-x}\text{Co}_x\text{Nb}_6\text{B}_{15}\text{Cu}_1$ ($x=18, 39, 60$) alloys / J. Blazquez, V. Franco, C. Conde, A. Conde //J. Magn. Magn. Mater. - 2003. - N254-255. - P.460-462.
7. **Walter, J.L.** Crystallization of the amorphous alloys $\text{Fe}_{50}\text{Ni}_{30}\text{B}_{20}$ and $\text{Fe}_{80}\text{B}_{20}$ / J.L. Walter, S.F. Bartram, R.R. Russell // Met. Trans. – 1978. – V. 9A, N6 – P.803-814.

Received 13.07.2013.

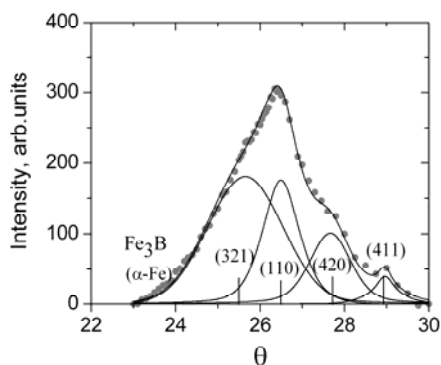


Fig. 5. Co K_{α} X-ray diffraction pattern of microwires treated at 550 °C (5 min) under stress 110 MPa.

V. S. Khandetsky, Yu. A. Tonkoshkur

Oles Honchar Dnipropetrovsk National University

INVESTIGATION OF RECHARGING PROCESSES FOR THE VOLUME LOCALIZED STATES IN POLYCRYSTALLINE SEMICONDUCTORS

The influence of recharging processes for the volume localized states in semiconductor component of polycrystalline structure on the kinetics of isothermal depolarization current is theoretically studied. The equation of continuity of electric induction on the borders of the insulator-semiconductor together with a first integral of the equations for the spatial charge is used as a model. Kinetic equations are recorded on the basis of the Shockley - Red - Hall statistics. The current density of depolarization, induced recharge of surface and volumetric local electronic states are determined as a result of the decision. The spectral characteristics of the current are obtained with using the Fourier transformation. In the spectra there are two clearly distinct maxima. The low-frequency maximum corresponds to the surface states, and the high-frequency one corresponds to the volume localized states. The values of parameters that are typical for the metal-oxide varistor ceramics based on ZnO are taken in the calculations. It is shown that the kinetic and spectral dependences of depolarization current at different temperatures can be used to evaluate the ionization energy and temperature dependences of the capture ratios of the electron states.

Keywords: polycrystalline semiconductor, isothermal depolarization current, localized electronic states, kinetics, spectrum, potential.

Теоретически исследуется влияние процессов перезарядки объемных локализованных состояний в полупроводниковой компоненте поликристаллической структуры на кинетику тока изотермической деполяризации. В качестве модели используется уравнения непрерывности электрической индукции на границах изолятор-полупроводник вместе с первым интегралом Пуассона для областей пространственного заряда. Кинетические уравнения записываются на основе статистики Шокли - Рида - Холла. В результате решения определяется плотность тока деполяризации, обусловленного перезарядкой поверхностных и объемных локальных электронных состояний. С использованием преобразования Фурье получаются спектральные характеристики тока. В спектрах явно выделяются два максимума: низкочастотный, соответствующий поверхностным и высокочастотный, соответствующий объемным локализованным состояниям. При расчетах принимаются значения параметров, характерные для металлооксидной варисторной керамики на основе ZnO. Показано, что кинетические и спектральные зависимости тока деполяризации при разных температурах можно использовать для оценки энергии ионизации и температурных зависимостей коэффициентов захвата электронных состояний.

Ключевые слова: поликристаллический полупроводник, ток изотермической деполяризации, локализованные электронные состояния, кинетика, спектр, потенциал.

Теоретично досліджується вплив процесів перезарядки об'ємних локалізованих станів в напівпровідниковій компоненті полікристалічної структури на кінетику струму ізотермічної деполяризації. В якості моделі використовується рівняння неперервності на межах ізолятор-напівпровідник сумісно з першим інтегралом Пуассона для областей просторового заряду. Кінетичні рівняння записуються на основі статистики Шоклі - Ріда - Холла. В результаті рішення визначається щільність струму деполяризації, обумовленого перезарядкою поверхневих і об'ємних локальних електронних станів. З використанням перетворення Фур'є одержуються спектральні характеристики струму. В спектрах явно виділяються два максимуми: низькочастотний, що відповідає поверхневим і високочастотний, що відповідає об'ємним локалізованим станам. При розрахунках приймаються значення параметрів, характерні для металоксидної варисторної кераміки на основі ZnO. Показано, що кінетичні і спектральні залежності струму деполяризації при різних температурах можна використовувати для оцінки енергії іонізації і температурних залежностей коефіцієнтів захвату електронних станів.

Ключові слова: полікристалічний напівпровідник, струм ізотермічної деполяризації, локалізовані електронні стани, кінетика, спектр, потенціал.

Introduction

Electron exchange processes for localized states in polycrystalline semiconductors with intercrystallite potential barriers can be studied by analyzing the isothermal depolarization (ID) current kinetics [1].

The known basic theoretical model of the ID current kinetics in polycrystalline semiconductors is based on the concept of recharging surface localized electronic states (LES) at the boundaries of the semiconductor crystallites and the matrix of the insulating phase [2]. The influence of volumetric LES in such structures has not been studied theoretically up to now.

At the same time, for several polycrystalline structures, in particular, metal oxide varistor ceramics, contribution of volumetric LES to the ID current can be considerable.

The presence of deep energy LES filled with electrons at the boundaries of semiconductor crystallites (e.g., ZnO) leads to the formation of surface charges and near-surface potential barriers (up to 1 eV or more) between the semiconductor crystallites [3]. The change of the filling of such LES by applying real (not admitting breakdown) polarizing voltage is usually insignificant, and needs more time for their discharge. Therefore, a significant contribution to the formation of the observed (fast) component of the ID current [1, 4] can be provided by volumetric LES of semiconductor crystallites.

In this paper a model of the kinetics of ID current, which takes into account the recharging processes for the volume LES in semiconductor crystallites is proposed. The effect on the value of its polarizing voltage and temperature is also studied; and the analysis of the information value of the model to obtain data on the characteristics of bulk LES is performed.

Element of the polycrystalline semiconductor structure

The element of the polycrystalline structure for the one-dimensional model is a layer of semiconductor material located in surface region. The region is isolated from both sides by dielectric thin films of intergranular phase.

Applying the polarizing voltage produces the additional filling and, accordingly, the devastation of surface and bulk LES that are energetically near the Fermi level and spatially located in the border areas of both the semiconductor layer.

After the decline of the applied voltage to zero, the sample depolarization starts. This process ends with relaxation to the initial filling of LES. The dependence of depolarization current versus time provides information on the nature of mentioned electrical transients [1, 4-6].

In order to concretize model, we consider a one-dimensional structure, characteristic for a metal-oxide varistor ceramics [3]. It includes a semiconductor layer ZnO with a thickness of $d_s \sim 10 \mu\text{m}$ located between two thin films of thickness $d_d \sim 20 \text{ \AA}$ of the dielectric intergranular phase. It is assumed that the charging occurs mainly for electron transitions between LES and the conduction band of ZnO.

It is necessary to solve two problems in the simulation. The first problem is to find the potential distribution and function of electron filling of surface and bulk LES in the crystallites in a steady state of polarization (for different values of voltage $V = V_{POL}$). The second one is to determine the dependence of these functions on time for the transition of the initially polarized object in equilibrium with its short-circuit ($V = 0$) using the kinetics of the ID current.

The model equations

The polarization state

Equations, that determine a steady-state polarization, are the equations of continuity of the electric charge displacement at the boundaries of a single insulator-semiconductor structure element (coordinates of the boundaries of the semiconductor layer $x = \mp d_s/2$, point $x = 0$ corresponds to the middle layer)

$$\varepsilon_0 \varepsilon_d \frac{V_d}{d_d} = \varepsilon_0 \varepsilon_s \frac{d}{dx} \Big|_{x=-d_s/2} + e N_S f_S \Big|_{x=-d_s/2} \quad (1)$$

$$\varepsilon_0 \varepsilon_s \frac{d}{dx} \Big|_{x=d_s/2} = \varepsilon_0 \varepsilon_d \frac{V_d}{d_d} + e N_S f_S \Big|_{x=d_s/2} \quad (2)$$

with the first integral of the Poisson equation for the space charge region of the form

$$\frac{d}{dx} = \frac{kT}{eL} F(Y) = \frac{kT}{eL} \text{sign}(-Y) \times \left\{ \int_0^Y \left[\frac{N_V}{n_{V0}} [(f_V(y) - f_V(0) + \exp(y) - 1)] - \frac{p_{V0}}{n_{V0}} [\exp(-y) - 1] \right] dy \right\}^{1/2}, \quad (3)$$

where N_q – surfactant concentration (index $q = S$) and bulk (index $q = V$) donor LES, composite index q is used in a similar manner, and then to describe the surface and volumetric parameters; f_q – the electron distribution function in the LES (at equilibrium Fermi function); $Y = e(\varphi - \varphi_0)/kT$, φ_0 – level of capacity in the semiconductor; n_{V0} and p_{V0} – the concentration of free electrons and holes in a semiconductor crystal; ε_d and ε_s – the relative dielectric permittivity of the dielectric intergranular phase and a semiconductor; ε_0 – electric constant; e – the absolute value of the electron charge; k – Boltzmann constant; T – temperature; $V_d = V - [(d_s/2) - (-d_s/2)]$; $V = V_{POL}$, V_{POL} – the value of the polarizing voltage applied to the unit cell of a polycrystalline structure; x – coordinate along the axis orthogonal to the layers of a single structural element.

The numerical solution of the set of nonlinear equations (1) – (3) provides the potential distribution $Y^{(POL)}(x)$ and the distribution functions of electrons on surface $f_S^{(POL)}(\pm d_s/2)$ and bulk $f_V^{(POL)}(x)$ LES for the polarized structure element of polycrystalline semiconductor.

Kinetics of depolarization

Kinetic equations describing the recharging LES during depolarization written on the basis of the Shockley-Read-Hall statistics [7] have the form

$$df_q(x, t)/dt = c_{nq} \left\{ [1 - f_q(x, t)] \cdot n(x, t) - f_q(x, t) n_{1q} \right\} \quad (4)$$

where $n_{1q} = N_C \exp(-\Delta E_q/kT)$ – the concentration of electrons in the conduction band, reduced to the level of E_q , ΔE_q – ionization energy, N_C – effective density of states in the conduction band of the semiconductor; $Y(x, t)$ and $n(x, t) = n_{V0} \exp[Y(x, t)]$ – potential

profile (band bending) and the concentration of free electrons in the space charge of the structural element of the semiconductor crystallites; c_{nq} - coefficient of electron capture LES ($c_{nq} = \sigma_{nq} \cdot \bar{v}_T / g$, σ_{nq} - the effective capture cross section, \bar{v}_T - average thermal velocity of the electrons, g - the degeneracy of LES).

The initial conditions for the surface and bulk LES are

$$\begin{aligned} f_S(\mp d_s / 2) &= f_S^{POL}(\mp d_s / 2), \\ f_V(x, 0) &= f_V^{POL}(x). \end{aligned} \quad (5)$$

The dependencies $Y(x, t)$ are found by the equation integrating $\frac{x}{L} = \int_{Y_{POL}(x)}^{Y(x,t)} dy / F[y(t)]$

where $Y_{POL}(x)$ is the solution of the set (1)–(2) with using the expression (3) for the first integral of the Poisson equation, L - Debye screening length of an intrinsic semiconductor. The depolarization current density caused by the recharging of the surface and bulk LES can be written as

$$\begin{aligned} j_{ID}(t) &= j_{ID}^{(S)}(t) + j_{ID}^{(V)}(t) = eN_S d[f_S(-d_s/2, t) - f_S(d_s/2, t)]/dt + \\ &+ eN_V \int_0^{L_{SC}^{(1)}} \{d[f_V(x, t)]/dt\} dx - eN_V \int_0^{L_{SC}^{(2)}} \{d[f_V(x, t)]/dt\} dx, \end{aligned} \quad (6)$$

where $L_{SC}^{(1)}$ и $L_{SC}^{(2)}$ are thicknesses of space charge regions located near the left and right edges of the semiconductor layer.

Overall analysis of the expression (6) is complicated and can be carried out only approximately with using numerical methods. However, given the idea that the near-surface space-charge region is formed deep ("slow") levels [3] (LES with the long relaxation times, which, in particular, also confirmed by the study of thermally stimulated depolarization currents [8]), can be considered as the potential distribution in the crystallites during depolarization $Y(x, t) \approx Y(x)$. This allows obtaining the analytical solution of the kinetic equation (4) and equation (6) for the surface and volume ID currents explicitly

$$j_{ID}(t) = j_{ID}^{(S)}(t) + j_{ID}^{(V)}(t) = j_0^{(S)} \cdot \exp(-t/\tau_S) + j_0^{(V)} \cdot \exp(-t/\tau_V) \quad (7)$$

where $\tau_S = [c_{nS}(n_{1S} + n_S)]^{-1}$; $\tau_V = [c_{nV}(n_{1V} + n_{V0})]^{-1}$;

$$j_0^{(S)} = -eN_S \tau_S^{-1} \cdot [f_S^{(POL)}(-d_s/2) - f_S^{(POL)}(d_s/2)];$$

$$j_0^{(V)} = -eN_V \tau_V^{-1} \cdot \int_0^{L_{SC}} [f_{V.1}^{(POL)}(x) - f_{V.2}^{(POL)}(x)] dx;$$

$$L_{SC} = \max(L_{SC}^{(1)}, L_{SC}^{(2)});$$

$L_{SC}^{(1)}$ and $L_{SC}^{(2)}$ are the thicknesses of the left and right areas of the space charge polarization in the semiconductor crystallite.

Functions $f_{V,1}^{(POL)}(x)$ и $f_{V,2}^{(POL)}(x)$ correspond to the LES charge on one side and their discharge on the other side of the semiconductor layer.

For the equation (7) it is accepted that the resulting volumetric component of the depolarization current $j_{ID}^{(V)}(t)$ can be approximately determined by its maximal component. This component is caused by LES. Its energy level is crossing the Fermi level [9]. It's supposed that $n_V(x) \approx n_{V1}$ and $\tau_V(x) \approx \tau_{VF}$.

The kinetic and spectral dependences of depolarizing current

Theoretical kinetic dependence of the isothermal depolarization current $j_{ID}(t)$ of the polycrystalline semiconductor element of structure obtained on the basis (7) is presented in Fig. 1. The corresponding spectral dependences $J_{ID}(\omega)$, as shown in this figure, are found using the direct sine-transform of Fourier:

$$J_{ID}(\omega) = \frac{2}{\pi} \int_0^{\infty} j_{ID}(t) \sin(\omega \cdot t) dt = J_{ID}^{(S)}(\omega) + J_{ID}^{(V)}(\omega) \quad (8)$$

where ω - cyclic frequency ($\omega \in [0, \infty]$), a $J_{ID}^{(q)}(\omega) = (2j_0^{(q)} / \pi) \times \omega / [\omega^2 + (1/\tau_q)^2]$.

The left (low-frequency) maximum of spectrum corresponds to the surface LES, and the right (high-frequency) one – to bulk LES. In the calculations, the values of the parameters are for metal oxide varistor ceramics based on ZnO: $\Delta E_V = 0.2$ eV; $N_V = 10^{17}$ sm⁻³; $c_{nV} = 10^{-12}$ sm³/s and $\Delta E_S = 0.5$ eV; $N_S = 10^{14}$ sm⁻²; $c_{nS} = 10^{-14}$ sm³/s; $n_{V0} = 10^{17}$ sm⁻³; $n_{V0} \gg p_{V0}$ [8]. As can be seen, there are two relaxation areas in the kinetics $j_{ID}(t)$. They are characterized by times τ_V and τ_S depending on the capture coefficients c_{nq} and ionization energies ΔE_q of LES. The first area (fast) is associated with the recharging of bulk LES, and the second (slow) one – with recharging surface LES, i.e. $\tau_V \ll \tau_S$. If $\tau_V \sim \tau_S$, then these areas are overlapped.

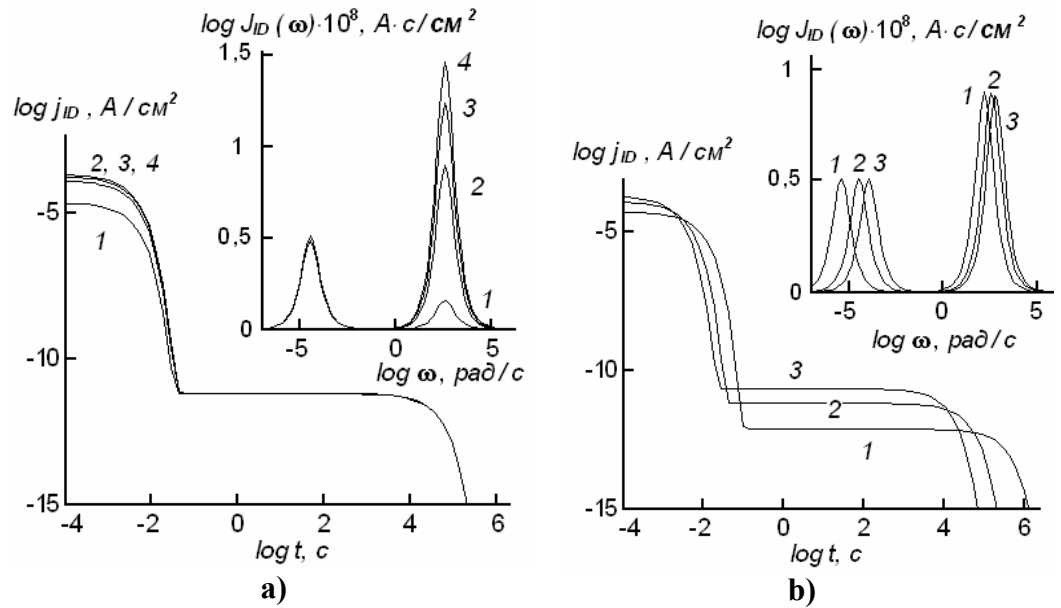


Fig. 1. Time $j_{ID}(t)$ and spectral $J_{ID}(\omega)$ dependences of isothermal depolarization current of structural element on V_{POL} , V: 1 – 0.5; 2 – 5; 3 – 10; 4 – 15 at $T=300$ K (a) and temperature T , K: 1 – 270; 2 – 300, 3 – 330 at $V_{POL} = 3$ V (b)

According to this in the spectra $J_{ID}(\omega)$ there are two dispersion areas: high-frequency region is associated with recharging volume LES and the low frequency one is due to the recharge of surface LES. For the frequencies of their maxima we have in accordance with (8)

$$\omega_{\max}^{(q)} = 1/\tau_q . \quad (9)$$

With increasing polarization voltage V_{POL} the dependences $j_{ID}^{(s)}(t)$ and $J_{ID}^{(s)}(\omega)$ are lifted up (current increases in absolute value) to a limiting value corresponding to full charge of surface LES on one side of the semiconductor layer and full discharge on the other. With increasing of polarization voltage V_{POL} the absolute value of the bulk component of the current density of depolarization $j_{ID}^{(v)}(t)$ and its maximum range $J_{ID}^{(v)}(\omega)$ increases. However, the saturation is not observed.

The growth temperature T increases the amount of ID current and speed depolarization. The temperature dependence of the frequency $\omega_{\max}(T)$ are straighten the coordinates $(\log(\omega_{\max}), 1/T)$. The activation energies conform to the calculation of ionization energies of the bulk and surface LES.

Parameters of localized states

The model gives the relationship between the parameters of bulk LES, relaxation times and ID current in a form similar to that in [2] for surface LES:

$$\ln \tau_q = -\ln c_{nq} N_C + \Delta E_q / (kT) . \quad (10)$$

The temperature dependences $\tau_q(T)$ or $\omega_{\max}^{(q)}(T)$ can be found from the spectral curves for the depolarizing current obtained at different temperatures. From Eq. (10) the formula follows for determining an ionization energy and capture coefficient of free electrons for the bulk (and surface) local electronic states:

$$\Delta E_q = \ln(10) \cdot k \cdot \Delta [\lg \tau_q(T) \times T^2] / \Delta(1/T) ; \quad (11)$$

$$c_{nq}(T) = [\tau_q(T) \cdot N_C(T)]^{-1} \cdot \exp[\Delta E_q / (kT)] . \quad (12)$$

Conclusions

In polycrystalline semiconductors with relatively high intercrystallite potential barriers isothermal depolarization currents depends on the recharging of both bulk and surface localized electronic states.

It is determined:

- the presence of two relaxation areas in the current spectrum and kinetics of isothermal depolarization due to charging volume and surface localized states, with the fast or, correspondingly, high frequency region is associated with charge of bulk LES, and slow or low-frequency region – with recharging surface LES;

- increasing the time and spectral dependencies to some "marginal" for the surface and the absence of "limit" for the volume dependencies of LES with increasing polarization voltage in the operating voltage range.

It is shown that the kinetic and spectral dependencies of the isothermal depolarization current obtained at different temperatures can be used to estimate the ionization energy and the temperature dependence of the capture coefficient of bulk (and surface) LES in semiconductor crystallites.

References

1. **Tonkoshkur A. S.** Isothermal Depolarization in Zinc Oxide Varistor Ceramics. /A.S. Tonkoshkur, I.V. Gomilko, A.Yu. Lyashkov // *Inorganic Materials*. - 1998. - Vol. 34, No. 9. - P. 939-943.
2. **Khandetskyi V. S.** Basic models of isothermal depolarization analysis for diagnostics of heterogeneous materials / V.S. Khandetskyi, Yu. A. Tonkoshkur // *Multidiscipline Modeling in Materials and Structures*. – 2012. – Vol. 8, № 1. – P. 105-119.
3. **Gupta T. K.** Application of Zinc Oxide Varistors / T.K Gupta // *J.Am.Ceram.*1990. - V. 73, №7. - P. 1817-1840.
4. **Philipp H. R.** Long Time Polarization Currents in Metal-Oxide Varistors / H.R. Philipp, L.M. Levinson // *J. Appl. Phys.* - 1976. - V. 47, №7. - P. 3177-3181.
5. **Kremer F.** Broadband Dielectric Spectroscopy. / F. Kremer // Berlin-Heidelberg -New York: Springer Verlag, 2003. - 729 p
6. **Bueno P. R.** Admittance and dielectric spectroscopy of polycrystalline semiconductors / P.R. Bueno, J.A. Varela, E. Longo // *J. European ceramic Society*. – 2007. – V. 27. P. 4313-4320.
7. **Zi S. M.** Physics of Semiconductor Devices – M.: Mir, 1984. - T. 1. - 456 p (in Russian).
8. **Tonkoshkur A. S.** Features thermo - depolarizing effects in zinc - oxide ceramics for varistor / A.S. Tonkoshkur, V.I. Klimenko, I.V. Gomilko // *GTF*. - 1997. - T. 67, №10. - S. 60-63.
9. **Yamasaki K.** Deep level transient spectroscopy of bulk traps and interface states in Si -MOS diodes / K. Yamasaki, M. Yoshida, T.Sugano // *Jpn. J. Appl. Phys.*- 1979.- V.18.- N 1.-P.113-122.

Received 13.07.2013.

UDC 538.956

E. V. Antonova, A. S. Tonkoshkur, V. A. Kolbunov

Oles Honchar Dnipropetrovsk National University

DIELECTRIC PROPERTIES OF POLYMER COMPOSITE MATERIAL BASED ON VANADIUM DIOXIDE

Results of investigation of the dielectric characteristics of “polyethylene-vanadium dioxide” composites with different volume fractions of filler within the radio frequencies range and the temperature range of 30-90 °C are presented. The two dispersion regions are found. The high-frequency region is due to the Maxwell charge separation on the boundaries of the polyethylene matrix - conductive filler of the crystallites VO₂. The low frequency region is associated with the presence of the transition layer at this boundary.

The semiconductor-metal phase transition is observed in the frequency dependence of the electrical conductivity of composite. This transition is realized in the filler particles of vanadium dioxide.

With increasing temperature, the relative permittivity of the composite has a tendency to the absolute value decrease. An increase of high-frequency electrical conductivity and a reduction of the dielectric relaxation time are observed.

Keywords: composite, polyethylene, filler, vanadium dioxide, permittivity.

Представлены результаты исследования диэлектрических характеристик композитов полиэтилен-диоксид ванадия с различными объемными долями наполнителя в диапазоне радиочастот и температурном диапазоне 30 – 90°C. Обнаруживаются две дисперсные области. Высокочастотная область обусловлена максвелловским разделением заряда на границе полиэтиленовая матрица – проводящий наполнитель (кристаллиты VO₂). Низкочастотная область связывается с наличием переходного слоя на этой границе.

В частотной зависимости электропроводности композитов проявляется фазовый переход металл-полупроводник (ФПП) в наполнителе.

Относительная диэлектрическая проницаемость композита имеет тенденцию к снижению по абсолютной величине с ростом температуры. Высокочастотная электрическая проводимость увеличивается, а времени релаксации диэлектрика сокращается.

Ключевые слова: композит, полиэтилен, наполнитель, диоксид ванадия, диэлектрическая проницаемость.

Представлені результати дослідження діелектричних характеристик композитів поліетилен - двооксид ванадію з різними об'ємними частками наповнювача в діапазоні радіочастот та температурному діапазоні 30 – 90°C. Виявлено дві дисперсні області. Високочастотна область обумовлена максвелловським розділенням заряду на границі поліетиленова матриця – провідний наповнювач (кристаліти VO₂). Низькочастотна область пов'язується з наявністю переходного шару на цій границі.

У частотній залежності електропровідності композитів проявляється фазовий перехід метал-напівпровідник (ФПМН) в наповнювачі.

Відносна діелектрична проникність композиту має тенденцію до зниження за абсолютною величиною з ростом температури. Високочастотна електрична провідність збільшується, а час релаксації діелектрика скорочується.

Ключові слова: композит, поліетилен, наповнювач, двооксид ванадію, діелектрична проникність.

Introduction

Recently, polymer composites with conductive fillers, in particular carbon-based system in a polyethylene matrix, have found application as self restoring fuses and resistors [1, 2]. Use as a filler material with a phase transition of the semiconductor-metal could eventually allow the development of electronic elements, which apart protect against current overloads and high temperatures also implement other functions including shutdown at low temperatures.

In order to develop the optimum technology for producing such composites one need information about their electrical properties at alternating current and physical processes responsible for them.

This paper presents the results of investigations of the dielectric characteristics of polyethylene-vanadium dioxide composites with different volume fraction of filler in the radio frequency and ranges of temperatures 30-90 °C.

Samples and methods of investigation

The initial components of the composite were fine crystalline vanadium dioxide (VO_2), obtained by reduction of vanadium pentoxide (V_2O_5) with carbon [3], and high-density polyethylene LDPE (15803-020).

The process of synthesis of polyethylene - VO_2 composites was performed using the technological scheme, similar to the technology of making self recovering fuses of the PolySwitch type [1].

The volume fraction of filler p_V was varied from 25 to 60 volume per cents. The samples had a cylindrical shape with the base diameter of 10 mm and the height of about 1 mm.

The dielectric characteristics were performed with a Q meter BM-560 in the radio frequency range (50 kHz to 10 MHz). Studies have shown the near-electrode phenomena that the measured electrical values are determined by the bulk properties of the samples.

The sample was placed into thermostat for studying the temperature dependences. Data registration was carried out after the establishment of the thermodynamic equilibrium of the sample with the environment.

Experimental results and discussion

Fig. 1 shows a typical frequency dependence of permittivity $\epsilon'(f)$ and electrical conductivity $\sigma(f)$ of composites with different percentages of vanadium dioxide. As seen, dielectric dispersion takes place in the test frequency range.

A decrease of dielectric permittivity ϵ' and the increasing of electrical conductivity σ with increasing frequency f at a constant temperature at low volume fractions VO_2 ($p_V < 50\%$) were observed. Conductivity values depend weakly on the frequency f (see Fig. 1b, curves 4 and 5) with a higher filler content p_V . The resulting regularities are also observed at other temperatures of the investigated range.

Dependences of ϵ' and σ on the volume fraction of filler are shown in Fig. 2. As can be seen, relative permittivity and specific conductivity increase with increasing volume fraction of filler p_V .

The values of rapprochement σ , measured at different frequencies and the same temperature at high frequencies with increasing p_V is observed. It should be noted that the change in electrical conductivity of composite samples at the transition through temperature of VO_2 PTMS (68 °C) is not very high (less than one order) [4].

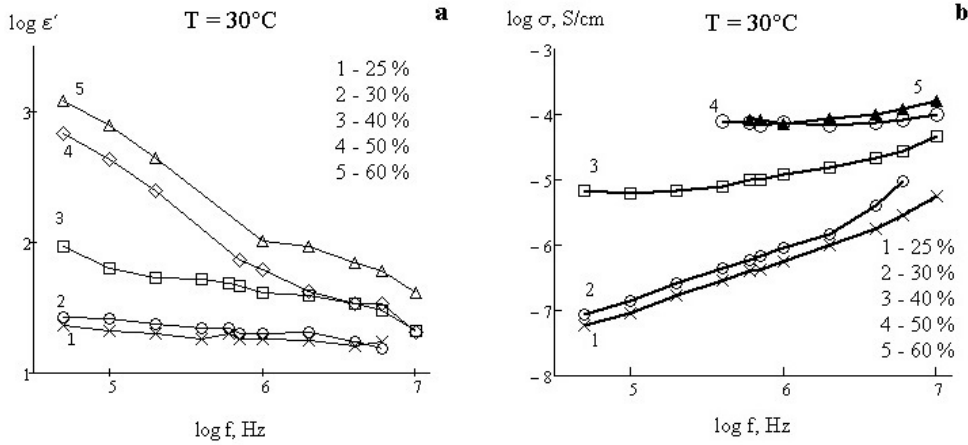


Fig. 1. The frequency dependence of the relative dielectric permittivity and conductivity of samples of composites based on polyethylene with different volume fractions of filler – vanadium dioxide (temperature 30°C)

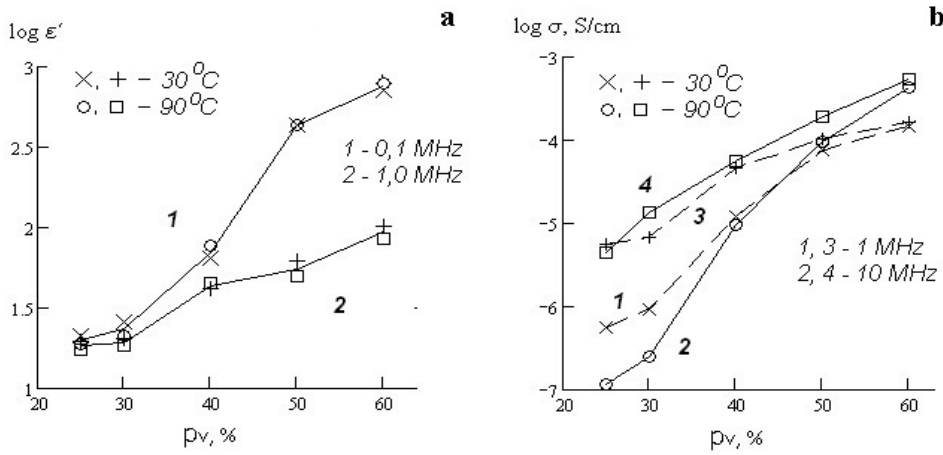


Fig. 2. The dependence of the relative dielectric permittivity (a) and conductivity (b) of composites based on polyethylene on the volume fraction of filler – vanadium dioxide at 30°C and 90°C

The effect of temperature on the dielectric spectra of the investigated composites is shown in Fig. 3.

It should be noted that the appearance of a minimum in the frequency dependence of the dielectric loss ϵ'' (Fig. 3b) was previously observed in other studies [5]. The presence of the minimum indicates the manifestation of two relaxation processes in the frequency range under consideration.

Decrease in values of ϵ' to those of the order of several units (Fig. 3a) indicates the Maxwell-Wagnerian nature [6] of high-frequency dispersion region.

The most likely reason of the low-frequency region dispersion is the presence of transition layers in the studied composite and polarization processes associated with them, as investigated and observed in other similar composites with conductive fillers [2, 7]. This assumption proves to be true because of anomalously high values of the low-frequency relative permittivity of the investigated structures.

The absolute value of the low frequency $\varepsilon'(f)$ is much higher than the values given by the two-component theory of dielectrics with conductive inclusions. So our calculations were performed with the use of the most correct well-known Bruggeman-Hanai formula $\varepsilon'_{th} = \varepsilon_{PE} / (1 - p'_V)^3$ [4] where ε_{PE} is a relative permittivity of polyethylene matrix $\varepsilon_{PE} \approx 2$ [2], and \tilde{p}_V is the volume fraction of filler VO₂ ($\tilde{p}_V = p_V / 100 = 0.3$ for the data in Fig. 2, 3). They result in the value $\varepsilon'_{th} \approx 6$ that is significantly less than obtained in the experiment.

With temperature increasing to the temperatures in the range of the phase transition VO₂ (<68°C) the observed decrease in the absolute value of the relative permittivity of the samples corresponds to the thermal expansion of the polyethylene matrix [2].

Dispersion curves of $\varepsilon'(f)$ and $\varepsilon''(f)$ before PTMS (curves 1, 2, and 3 in Fig. 3) have fuzzy character that corresponds to a relaxation process with a wider scatter of relaxation times. Thus PTMS leads to increased homogeneity of the filler particles VO₂ at the electrical properties (conductivity).

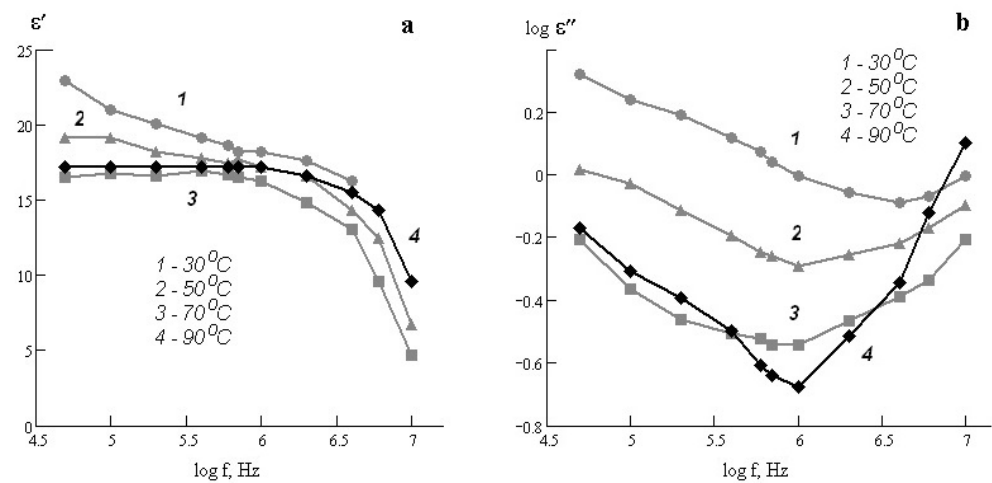


Fig. 3. The frequency dependence of the relative dielectric permittivity (a) and of the dielectric loss factor (b) of the composite sample based on polyethylene with a volume fraction of 30% of the vanadium dioxide at a temperature, °C: 1 – 30; 2 – 50; 3 – 70; 4 – 90.

Conclusions

Dielectric characteristics of “polyethylene - vanadium dioxide” composites with the volume fraction of filler from 25 to 60% show two dispersion area at radio frequency and temperature range from 30-90°C. The first one is the high-frequency region to be explained by the Maxwell charge separation at the boundaries of the polyethylene matrix-conductive filler of the crystallites VO₂. The second one is the low-frequency region associated with the presence of the transition layer at this interface.

In the frequency dependence of the electrical conductivity of the composites a phase transition semiconductor-metal occurring in the filler particles of vanadium dioxide is manifested. There is an increase of high-frequency electrical conductivity and reduced the set of the dielectric relaxation time.

References

1. **Wartenberg Mark F.** Patent US5747147 MKИ B32B9/00 Conductive polymer composition and device: Wartenberg Mark F (US); Lahlouh John G (US); Toth James (US); Raychem Corp (US) – № 19970130; Publ. 05.05.98.
2. **Degtyar'ov A. V.** Electrical Properties of Posistor Composite Materials Based on Polyethylene-Graphite // A. V. Degtyar'ov, A. S. Tonkoshkur, A. Yu. Lyashkov // Multidiscipline Modeling in Materials and Structures. VSP. – 2006. –V. 2, N 4. – P. 435-441.
3. **Ivon A. I.** Preparation of the crystalline vanadium dioxide (IV) reduction of vanadium oxide (V) with carbon // A. I. Ivon, V. R. Kolbunov, I. M. Chernenko // Questions of chemistry and chemical technology. – 2004. – № 2. – P. 68-72.
4. **Antonova K. V.** Conductivity of "polyethylene vanadium dioxide" composite // K. V. Antonova, V. R. Kolbunov, A. S. Tonkoshkur, A. Yu. Lyashkov // Technology and designing in electronic equipment – 2013 – №4 – P. 44 – 48.
5. **Shin S-G.** Effect of temperature on the dielectric properties of carbon black-filled polyethylene matrix composites below the percolation threshold // S-G. Shin, I-K. Kwon // Electronic Materials Letters – 2011. – V. 7, Issue 3. – P. 249–254.
6. **Dukhin S. S.** Dielectric phenomena and the double layer in disperse systems and polielektrolits. // S. S. Dukhin, V. N. Shilov – K.: Scientific Thought, 1972. – 226 p. (in Russian).
7. **Lipatov Yu. S.** Physical-chemistry of filled polymers // Yu. S. Lipatov – K.: Naukova Dumka, 1967. – 304 p. (in Russian).

Received 13.07.2013.

UDC 532.8

A. B. Lysenko, O. L. Kosynska, G. V. Borisova, A. A. Kazantseva

Dniprodzerzhynsk State Technical University

CRYSTALLIZATION KINETICS UNDER CONDITIONS OF THE QUENCHING FROM A LIQUID STATE

The model of bulk crystallization of the flat melt layers is presented. The model is based on the approach, according to which the processes of nucleation and crystal growth are carried out with effective rates proportional to the volume fraction of the parent phase. Contributions to the transformed volume fraction of x crystals nucleated at considerable distances from the surface of the film, and holding out initial spherical shape during the whole period of consolidation and also the crystals, arising on the near-surface critical areas that undergo the blocking effect of the surfaces and acquires the shape of truncated sphere are estimated in this model. The calculation analysis of crystallization kinetics of the $Fe_{80}B_{20}$ melt layers with thickness $l_o = 70 \mu m$, cooling on a massive copper heat receiver, is made with using the proposed model. It is shown that an increase in the critical areas of l_k relative volume occupied by truncated crystals increases, and at $l_k/l_o > 0,285$ their contribution to the overall share of the transformed volume becomes dominant.

Keywords: thin layers of melt, mass crystallization, the blocking effect of surfaces, spherical crystals, truncated crystals, contributions to the transformed volume fraction.

Представлена модель масової кристалізації плоских шарів розплаву малої товщини. Модель базується на приближенні, согласно которому процессы зарождения и роста кристаллов осуществляются с эффективными скоростями, пропорциональными объемной доле материнской фазы. В модели оцениваются вклады в долю превращенного объема x кристаллов, зарождающихся на значительных удалениях от поверхностей пленки и сохраняющих в течение всего периода затвердевания исходную сферическую форму, а также кристаллов, образующихся в приповерхностных критических зонах, которые испытывают блокирующее действие поверхностей и приобретают форму усеченной сферы. С использованием предложенной модели выполняется расчетный анализ кинетики кристаллизации слоев расплава $Fe_{80}B_{20}$ толщиной $l_o = 70 \mu m$, охлаждающихся на массивном медном теплоприемнике. Показано, что с ростом толщины критических зон l_k относительный объем, занятый усеченными кристаллами, возрастает и при $l_k/l_o > 0,285$ их вклад в общую долю превращенного объема становится доминирующим.

Ключевые слова: тонкие слои расплава, массовая кристаллизация, блокирующее действие поверхностей, сферические кристаллы, усеченные кристаллы, вклады в долю превращенного объема.

Наводиться модель масової кристалізації плоских шарів розплаву малої товщини, яка ґрунтується на наближенні, згідно з яким процеси зародження і росту кристалів здійснюються з ефективними швидкостями, пропорційними об'ємній частці материнської фази. У моделі оцінюються внески в частку перетвореного об'єму x кристалів, що зароджуються на значній відстані від поверхонь плівки і зберігають протягом усього періоду твердіння вихідну сферичну форму, а також кристалів, що утворюються у приповерхневих критичних зонах, які зазнають блокування поверхонь та набувають форми усеченої сфери. З використанням представлені моделі виконується розрахунковий аналіз кінетики кристалізації шарів розплаву $Fe_{80}B_{20}$ товщиною $l_o = 70 \mu m$, які охолоджуються на масивному мідному теплоприймачі. Показано, що з ростом товщини критичних зон l_k відносний об'єм, зайнятий усеченими кристаллами, зростає і при $l_k/l_o > 0.285$ їх внесок у загальну частку перетвореного об'єму стає доміантним.

Ключові слова: тонкі шари розплаву, масова кристалізація, блокуюча дія поверхонь, сферичні кристали, усечені кристали, внески в частку перетвореного об'єму.

© A. B. Lysenko, O. L. Kosynska, G. V. Borisova, A. A. Kazantseva, 2013

Introduction

The classical theory of mass crystallization is based on the kinetic equation of Kolmogorov [1] obtained under the assumption that the linear dimensions of individual crystals is incomparably smaller than the characteristic size of crystallized volume. This assumption is valid for the traditional metallurgical production processes of metal ingots and castings of large cross-sections. However, it does not hold under the conditions of quenching from the liquid state when the melt takes the form of a flat layer, the thickness of which is comparable with the size of the formed crystals. It is obvious that in this case the analysis of the crystal growth processes one should be taken into account not only the retarding action of neighboring particles, which is provided both by the classical model [1] and by the model based on the approximation of effective rates of crystal nucleation and growth [2–4], but also the possibility of the limiting size of those crystals that during the consolidation reach the layer surface has to be analyzed.

To solve the specified problem with developing the model [2], an improved model of crystallization of thin layers of melt is presented in the present paper, which allows evaluating the contributions to the transformed volume fraction of the two types of crystals forming in the central and near-surface areas of the layer. The calculation analysis of the mass crystallization kinetics of the $\text{Fe}_{80}\text{B}_{20}$ melt layers of $70\ \mu\text{m}$ thickness cooled by a massive copper substrate is made with the proposed model use.

Statement of the problem

Let us consider a liquid metal film of volume V_o and thickness l_o , which is cooled rapidly by the heat removing to the substrate (Fig. 1). Let us assume that by the time t_m the melt achieves the melting temperature T_m , the regular cooling mode is set in the film [5], and the whole volume simultaneously goes into the supercooled state.

At temperatures $T < T_m$ the film starts crystallizing by homogeneous nucleation and the further isotropic growth of the formed crystals. In the simplest version of the model we shall assume that the points lying within the melt volume and its surface are equivalent in their crystal-nucleating ability, i.e. at all points including surface ones a single mechanism of spontaneous nucleation operates.

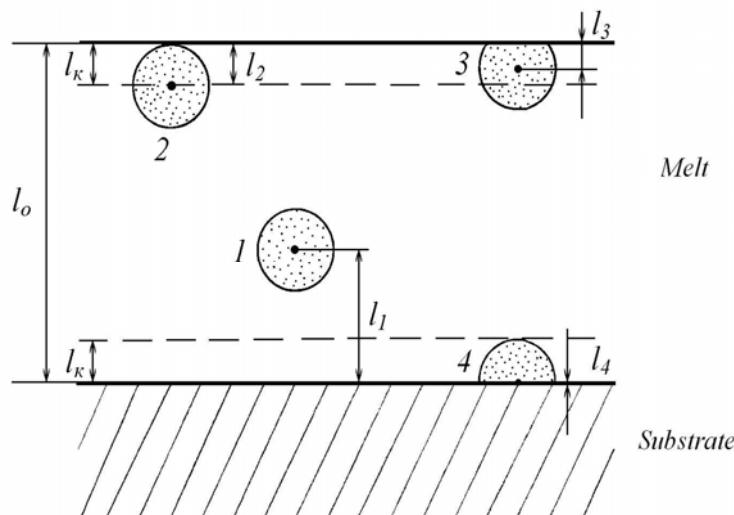


Fig. 1. Derivation of the kinetic crystallization equation of a thin melt layer that is cooled on the heat conductive substrate: 1 - 4 – hypothetical spherical crystals nucleated at a moment $t_m < t' < t_e$ at different distances l_i from the surfaces of the film; l_k – width of the critical near-surface zones.

Under such conditions of rapid quenching the transformation occurs in the temperature range from T_m to a final value T_e when the crystallized mass growth stops because of the complete exhaustion of the liquid phase or due to the material transition into the solid amorphous state. In the latter case the temperature T_e takes the sense of the glass transition temperature T_g . In the time scale the crystallization process takes a range of $t_m - t_e$.

Let us assume that the nuclei have a spherical shape inherited by crystals in their free growth at an effective rate:

$$u_{eff} = (1 - x)u \quad (1)$$

where x is the volume fraction which has undergone transformation; u is the real rate of crystal growth.

As shown in [2] by means of the approximation (1), the processes of the crystallization retarding through mutual collisions of neighboring crystals can be modeled.

The other factor limiting the free growth of crystals in a restricted volume is their interaction with the film surfaces. The blocking effect of the surfaces is experienced only by the fraction of crystals increasing with the growth ratio of the total surface area to film volume. Indeed, as schematically shown in the Fig. 1, the crystals nucleated at $t = t'$ at large enough distances from the surfaces $l_i \geq l_K$ (crystals 1, 2 in Fig. 1) hold the shape of spherical particles at any specified time $t' \leq t \leq t_e$. Therefore, the contribution of each crystal $V_1(t', t)$ to the total volume subjected to the conversion may be determined according to the formula for the volume of a sphere:

$$V_1(t', t) = \frac{4}{3}\pi R^3(t', t) \quad (2)$$

where $R(t', t)$ is a radius for a crystal nucleated at the moment t' and growing till the moment t with the effective rate u_{eff} .

It is obvious, that

$$R(t', t) = R_K(t') + \int_{t'}^t (1 - x(t''))u(t'')dt'' \quad (3)$$

where R_K is a radius of critical nucleus; $t' \leq t'' \leq t$.

On the other part, if crystals arise in near-surface critical zones (crystals 3, 4 in Fig. 1), at some time moments $t' \leq t_i \leq t$ they grow up to the nearest surface of the film that prevents their further growth in this zone. Quantitatively, this effect can be evaluated through setting to the considered crystals a truncated sphere form corresponding to the shape of the smaller final volume V_2

$$V_2(t', t) = \frac{\pi}{3}(2R^3(t', t) + 3R^2(t', t) \cdot l_i(t', t) - l_i^3(t', t)) \quad (4)$$

where $l_i(t', t)$ is a distance from the centre of a crystal forming in the critical zones to the blocking film surface.

The width of the critical zones can be found from the condition that it is equal to the radius R_e of crystals nucleated at a moment t' on their boundaries (crystal 2 in Fig. 1) and then growing isotropically in interval $t' - t$ according to Eq. (3), i.e.

$$l_K(t', t) = R(t', t). \quad (5)$$

Derivation of kinetic equation

On the basis of the above considered principles of modeling, we can derive the kinetic equation taking into account the specifics of crystallization processes in thin layers.

Let us suppose that at time $t_m \leq t' \leq t_e$ a crystallized volume fraction is $x(t')$ and determine the number of critical size nuclei $R_K(t')$ arising in the areas of location of the parent phase for a small period of time between t' and $t'+dt'$

$$dN(t') = V_0(1 - x(t'))I(t')dt' \quad (6)$$

where $I(t')$ is a frequency of nucleation per volume unit in the parent phase.

This total amount includes both nuclei arising away from the surface (dN_1) and ones with nucleation centers in the critical near-surface zones (dN_2). So far as by hypothesis the nucleation processes are equiprobable at all points of the melt layer, the quantities (dN_1) and (dN_2) will be proportional to the relative volume of the considered parts of the film, i.e.

$$dN_1(t', t) = \left(1 - \frac{2l_K(t', t)}{l_0}\right) dN(t'), \quad (7)$$

$$dN_2(t', t) = \frac{2l_K(t', t)}{l_0} dN(t'). \quad (8)$$

Further we define the value of the crystallizing volume increment provided by crystals nucleated within a specified short time interval in two zones of the film:

$$dV_1(t', t) = V_1(t', t)dN_1(t', t), \quad (9)$$

$$dV_2(t', t) = V_2(t', t)dN_2(t', t). \quad (10)$$

As follows from Fig. 1, the parameter $l_i(t', t)$ involved to Eq. (4) varies from 0 to $R(t', t)$, wherein, according to the model used, each act of the new center of crystallization forming in the critical zone is connected with one of the values of $l_i(t', t)$ from the current interval. For simplicity of choice procedure of possible critical distances $l_i(t', t)$ we assume that they change with time according to linear dependence in the form:

$$l_i(t', t) = R(t', t) \cdot (t' - t_m) / (t - t_m). \quad (11)$$

This means, that at the initial moments of crystallization ($t' \rightarrow t_m$) $l_i(t', t) \rightarrow 0$, i.e. nuclei arise at the film surface. With the course of time, the distance $l_i(t', t)$ increases from 0 to $R(t', t)$. It is equivalent to the shift of the layer, where the centers of crystallization arise from the surface to the boundary of the critical zone.

Specification of the dependence behavior $l_i(t', t)$ allows us to calculate the values $dV_1(t', t)$ and $dV_2(t', t)$ and by means of them the film volume fractions formed by the crystals of the central ($x_1(t)$) and adjacent to surfaces ($x_2(t)$) zones at any defined time moment $t_m \leq t \leq t_e$:

$$x_1(t) = \frac{4}{3} \pi \int_{t_m}^t \left(1 - 2 \frac{l_K(t', t)}{l_0}\right) (1 - x(t')) \cdot I(t') \cdot R^3(t', t) dt', \quad (12)$$

$$x_2(t) = \frac{2}{3} \pi \int_{t_m}^t \left(\frac{l_k(t',t)}{l_o} \right) \cdot A(t',t) \cdot (1-x(t')) \cdot I(t') \cdot R^3(t',t) dt' \quad (13)$$

$$\text{where} \quad A(t',t) = 2 + 3(t' - t_m)/(t - t_m) - ((t' - t_m)/(t - t_m))^3. \quad (14)$$

By summing the values $x_1(t)$ and $x_2(t)$ with taking into account Eq. (3) we obtain the total volume fraction of the crystalline phase:

$$x(t) = \frac{2}{3} \pi \int_{t_m}^t \left(2 + \frac{l_k(t',t)}{l_o} (A(t',t) - 4) \right) (1-x(t')) \cdot I(t') \cdot \left(R_k(t') + \int_{t'}^t (1-x(t'')) u(t'') dt'' \right)^3 dt' \quad (15)$$

The results of model calculations

Eq. (15) describes the kinetics of crystallization in the molten layers of small thickness l_o bounded by two lengthy parallel surfaces. In contrast to the well-known Kolmogorov equation [1] derived concerning the strictly volumetric scheme of the crystallization, Eq. (15) allows to take into account the contributions to the total crystallized volume fraction x of two parts made by crystals emerging away from the film surface (x_1) and in the crystal in the near-surface zones (x_2). As seen from Eqs. (12) and (13), the magnitude of these contributions depends on the ratio of the the critical bands width l_K and the layer thickness l_o .

In order to analyze these dependencies in more detail the equations (12), (13) and (15) were solved concordantly with the equations for heat conduction of the melt layers $\text{Fe}_{80}\text{B}_{20}$ of $l_o = 70 \mu\text{m}$ thickness subjected to the cooling on the copper quenching block. The calculations were performed by the numerical method of finite differences using explicit difference scheme [6]. Temperature rate dependences of the nucleation and crystal growth as well as the values used in the calculations of thermal variables were taken from the paper [7]. Parameter A was taken to be equal to its average value of 3. The width of the critical areas l_K was assumed to be independent of time. In different series of calculations we used fixed values l_K that belonged to the interval $0 - 0.5l_o$.

Fig. 2 shows the estimated dependences $x_1(t)$, $x_2(t)$ and $x(t)$, corresponding to the two values of the ratio l_K/l_o . As can be seen from the figure, the characteristic feature of the obtained kinetic curves is a sharp change in slope at some time t_s . The analysis of the full array of calculated data shows that during the passage of the inflection point the temperature of the crystallizing layer increases abruptly, verge towards the T_m ; the frequency of nucleation falls almost to zero, and the crystal growth rate value remains high enough ($u(t_s) \approx 1.4 \text{ m/s}$). This leads to the conclusion that the crystallization process is carried out in two stages. At the first stage (at $t < t_s$) the transformation arises at significant supercooling of the melt by the nucleation of new crystals and their further growth. At the point t_s an intensive release of the latent heat of crystallization occurs, the primary supercooling is removed, whereupon the formation of new nuclei is stopped and the further volume fraction increase of the crystalline phase arises only owing to the growth of previously nucleated crystals.

As follows from the comparison of Figs. 2a and 2b, the relative contributions to the value x of the two crystal types considered in the model depend on the value of ratio l_K/l_o . Thus, in the films with relatively small width of the critical zones ($l_K/l_o = 0.1$), crystals preserving the original spherical shape are mainly involved in the conversion (Fig. 2a).

For this example the final (at $t = t_e$) value x_1^e is 0.83. With the increase in the ratio l_K/l_o the growing contribution to the total volume fraction of the crystalline phase is made by crystals that at a certain stage of the process reach the surface of the melt film and, in accordance with the proposed model, take the form of truncated sphere. In particular, at $l_K/l_o = 0.4$ $x_2^e = 0.74$ (Fig. 2b).

In summary, the dependence of values x_1^e and x_2^e on the specific width of the critical areas l_K/l_o are shown in Fig. 3. It is evident, that in the range $l_K/l_o = 0-0.5$ the resulting truncated crystal volume fraction increases from 0 to 1, and the relative amount of full-sized spherical crystals is reduced accordingly. If $l_K/l_o = 0.285$, the equality of the values x_1^e and x_2^e is reached, i. e. both types of crystals make equal contributions to x^e .

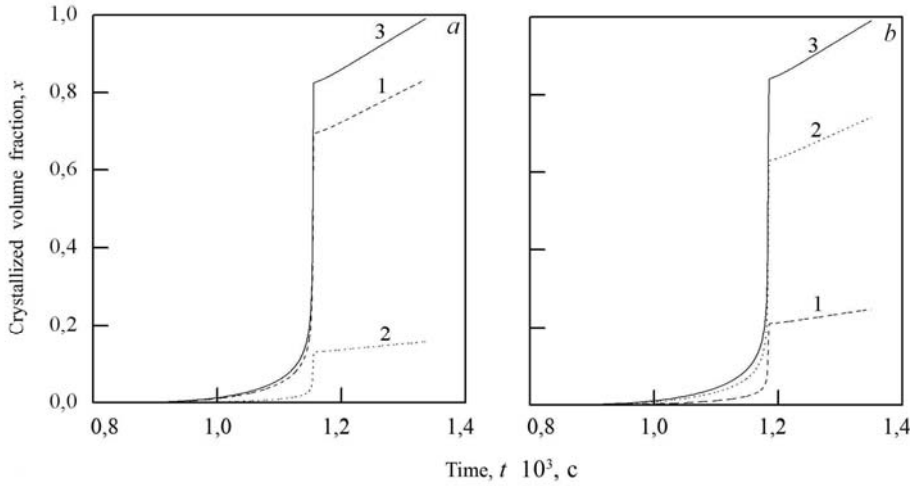


Fig. 2. Time dependences graphs of the crystalline phase amount for foils of $l_0 = 70 \mu\text{m}$ thickness at $l_K = 0,1l_o$ (a) and $l_K = 0,4l_o$ (b): 1 - fraction of the crystalline phase made by a spherical crystals x_1 ; 2 - fraction of the crystalline phase made by truncated crystals x_2 ; 3 - the total fraction of the crystalline phase x

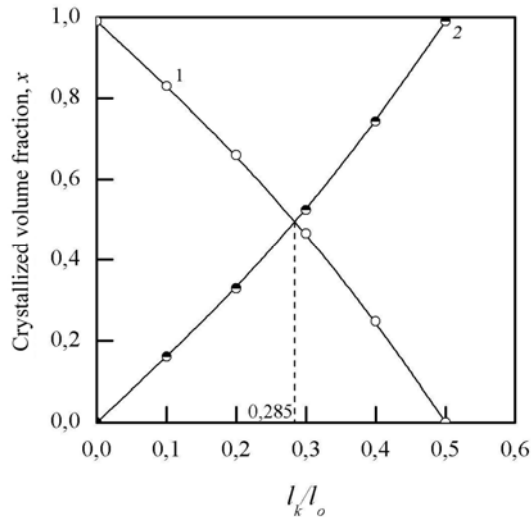


Fig. 3. The dependence of the crystalline phase fraction of the critical bands width l_K : 1 - the fraction of spherical crystals x_1 ; 2 - the volume fraction of crystals of a truncated form x_2

Conclusions

In the context of the approximation of effective rates of nucleation and crystal growth an improved model of mass crystallization of thin layers of melt, which takes into account the blocking effect of the growing crystals surfaces of the film has been created.

Kinetic equations for the processes of formation of spherical crystals nucleated away from the surface layer and crystals formed in the surface of the critical areas that undergo the blocking effect of surfaces and acquires the shape of truncated sphere have been derived.

The calculation analysis of crystallization kinetics of the Fe₈₀B₂₀ melt layers with thickness $l_0 = 70 \mu\text{m}$ cooled on a massive copper heat absorber has been made using the supposed model. It has been shown that with the increase in the width of the critical areas l_K the relative amount of truncated crystal grows and at $l_K/l_0 = 0.285$ their contribution to the overall fraction of the transformed volume becomes dominant.

References

1. Колмогоров А.Н. К статистической теории кристаллизации металлов / А.Н. Колмогоров // Известия АН СССР. Сер. математическая. – 1937. – № 3. – С.355–360.
2. Лысенко А.Б. Кинетическая модель массовой кристаллизации в приближении эффективных скоростей зарождения и роста кристаллов / А.Б. Лысенко // Вісник Дніпропетровського університету. Фізика. Радіоелектроніка. – 2011. – Т.19, № 2. – С.3–11.
3. Лысенко А.Б. Моделирование параметров микроструктуры быстрозакристаллизованных металлов / А.Б. Лысенко, О.Л. Кравец, Г.В. Борисова // Физика и техника высоких давлений. – 2007. – Т.17, №3. – С.52–62.
4. Лысенко А.Б. Влияние термического режима закалки из жидкого состояния на микроструктуру металлов / А.Б. Лысенко, О.Л. Кравец, А.А. Лысенко // Металлофизика и новейшие технологии. – 2008. – Т.30, №3. – С.415–427.
5. Лысенко А.Б. Расчет скорости охлаждения при закалке сплавов из жидкого состояния / А.Б. Лысенко, Г.В.Борисова, О.Л. Кравец // Физика и техника высоких давлений. – 2004. – Т.14, № 1. – С.44–53.
6. Самарский А.А. Введение в численные методы / А.А. Самарский. – М.: Наука, 1987. – 288 с.
7. Tkatch V.I. Computer simulation of Fe₈₀B₂₀ alloy solidification in the melt spinning process / V.I. Tkatch, S.N. Denisenko, B.I. Selyakov // Acta Metallurg. Mater. – 1995. – Vol.43, №6. – P.2485–2491.

Received 13.07.2013.

UDC 539.213: 548.51: 548.52

A. M. Ovrutsky, A. S. Prokhoda, O. I. Kushnerov

Oles Honchar Dnipropetrovsk National University

THE GROWTH KINETICS OF METALLIC CRYSTALS. RESULTS OF SIMULATIONS

The correct values of the surface kinetics coefficients were obtained for systems of Al, Cu, and Ni metals at sufficiently large sizes of nanocrystals in initial conditions. The simulation based on the molecular dynamics method was performed with applying our program for parallel computing and the LAMMPS program. We used the potentials of the embedded atom type. We applied NVT ensemble, but the volume of samples was not constant as they had free surfaces (they were smaller than the main cell). Our results showed that the classical Wilson-Frenkel model was not able to describe quantitatively the temperature dependence of the kinetics coefficients, and the Broughton, Gilmer and Jackson equation was valid at temperatures close to the melting point, not lower than 100 - 200 K. The temperature dependencies of the diffusion coefficients for these metals in the supercooled liquid state were analyzed. Discrepancies in the results of our simulation and the literature data were discussed.

Keywords: kinetics of crystallization, supercooled metals, diffusion, interfaces.

Получены корректные значения коэффициентов поверхностной кинетики для систем металлов Al, Cu, и Ni при задании сравнительно больших размеров нанокристаллов в начальных условиях. Моделирование по методу молекулярной динамики было выполнено с применением нашей программы для параллельных вычислений и программы LAMMPS. Были использованы потенциалы типа "погруженного" атома. Мы применяли NVT ансамбль, но объем образцов не был постоянным, поскольку они имели свободную поверхность (были меньше, чем основная ячейка). Наши результаты показали, что классическая теория Вильсона-Френкеля не в состоянии количественно описать температурную зависимость кинетических коэффициентов, а уравнение Броугхтона, Гилмера и Джексона справедливо при температурах, близких к температуре плавления, не ниже 100 - 200 К. Проанализированы температурные зависимости коэффициентов диффузии для указанных металлов в переохлажденном жидком состоянии. Обсуждены расхождения между результатами нашего моделирования и литературными данными.

Ключевые слова: кинетика кристаллизации, переохлажденные металлы, диффузия, межфазные поверхности.

Отримані коректні значення коефіцієнтів поверхневої кінетики для систем металів Al, Cu, Ni за порівняно великих розмірів нанокристалів в початкових умовах. Моделювання за методом молекулярної динаміки було виконано із застосуванням нашої програми для паралельних обчислень і програми LAMMPS. Були використані потенціали типу "зануреного" атома. Ми застосовували NVT ансамбль, однак об'єм зразків не був постійним, оскільки вони мали вільну поверхню (були меншими за основну комірку). Наші результати продемонстрували, що класична теорія Вільсона-Френкеля не в змозі кількісно описати температурну залежність кінетичних коефіцієнтів, а рівняння Броугхтона, Гілмера і Джексона є справедливим за температур, близьких до температури плавлення, не нижче 100 - 200 К. Проаналізовані температурні залежності коефіцієнтів дифузії для цих металів у переохолодженому рідкому стані. Обговорені розбіжності між результатами нашого моделювання та літературними даними.

Ключові слова: кінетика кристалізації, переохолоджені метали, дифузія, міжфазні поверхні.

Introduction

The kinetics of solidification controls the microstructure development of materials. It is therefore essential to have detailed understanding and knowledge of the kinetics during solidification of melts for improving production of metallic materials. To match the value of the surface kinetics coefficient, intensive convection was ensured by electromagnetic devices in some experimental works.

It is known long ago that the surface kinetic coefficient β_T in the ratio $\beta_T = v/\Delta T$ (v is the growth velocity, $\Delta T = T_m - T$, T_m - is the melting temperature) is the value of order 1 m/(s·K) for pure metal at the temperatures near the melting point T_m [1-3]. In the large temperature intervals it is better to consider the dependence of growth velocity on the surface supersaturation $v(\sigma)$ ($\sigma = \Delta\mu/kT$ is the relative supersaturation). In accordance with Wilson–Frenkel theory [4,5] this dependence for a pure material can be written as

$$v = \beta_s [1 - \exp(-\Delta\mu_T / kT)] \quad (1)$$

where β_s is the kinetics coefficient, $\Delta\mu_T$ is the difference of chemical potentials of two phases at the temperature T . Furthermore, the coefficient β_s can be expressed in terms of the diffusion coefficient D of the liquid [6]:

$$\beta_s \cong 6f_1 aD / \lambda^2 \quad (2)$$

where λ corresponds to an elementary diffusive jump distance of particles in the liquid, a is the interatomic distant, prefactor f_1 represents the fraction of collisions with the crystal that contributes to the growth of the crystal. It is assumed that the diffusion coefficient can be expressed by an Arrhenius law, $D = D_0 \exp(-Q/kT)$. However, some experimental data for pure metals (see Ref. [7]) allow arguing that their crystallization is not thermally activated.

Fedorov [3] had listed in his book some results of known experimental data concerning the kinetics coefficients for growth of metal crystal from pure melts and the coefficients of self-diffusion in these melts. After re-counting of β_T to β_s , we can see that these values are much greater than ones that can be evaluated according to Eq. (2) at $f_1 \cong 1$. But the sizes of growing crystals and surface supercoolings are not known exactly at measurements of experimental velocities. These quantities are known exactly at simulations.

In recent years, MD simulations have been applied extensively to study kinetics and thermodynamic properties of crystal-melt interfaces. It is important that nowadays simulations give values of many physic-chemical properties, including diffusivity that coincides well with the experimental values. The results of simulations for the Lennard-Jones liquid [7], for Cu and Ni [8] and for gold [9], did not confirm the dependence (1) for the surface kinetics. The kinetics coefficients calculated on the base of previous simulation results differed essentially from estimations on the basis of Wilson-Frenkel theory. For example, the authors of [9] have obtained the values $\beta_{T100} = 18.8 \pm 1.0 \text{ cm}\cdot\text{s}^{-1}\text{K}^{-1}$; $\beta_{T110} = 12.6 \pm 1.0 \text{ cm}\cdot\text{s}^{-1}\text{K}^{-1}$ and $\beta_{T111} = 7.0 \pm 1.0 \text{ cm}\cdot\text{s}^{-1}\text{K}^{-1}$ for different orientation of gold crystals. The authors of [10] have obtained for Ni-crystals significantly smaller anisotropy and somewhat higher values of β_T for low index $\{100\}$, $\{110\}$, and $\{111\}$ interfaces: $\beta_{T100} = 35.8 \pm 22$, $\beta_{T110} = 25.5 \pm 1.6$, and $\beta_{T111} = 24.1 \pm 4.0$ in units of cm/(s K).

The authors of [7] connected the kinetic coefficient with the average thermal velocity $(3kT/m)^{1/2}$ to explain the results of simulations of crystal growth in the LJ liquid:

$$v = f_2 (3kT / m)^{1/2} [1 - \exp(-\Delta\mu_T / kT)] \quad (3)$$

where f_2 is a constant of the first order.

Later, Mikheev and Chernov [11] have developed the density functional theory of freezing for the case of crystal-melt interface, which is rather diffuse on atomic scale. They proposed estimation, $v=(kT/m)^{1/2} \Delta T/T$, after simplifications of their results.

In this work, we present the simulation results concerning the growth of metal crystals from pure melts. The data are obtained in the large intervals of supercooling, including the growth from the amorphous state. In addition, we consider the size effect in crystal growth, i.e. the dependence of growth velocity on the crystal size. Our models have free surfaces and contain sufficiently many atoms.

Details of the simulation

The MD simulations were fulfilled using our program for parallel computing and the LAMMPS codes (large-scale atomic-molecular massively parallel simulator) [12]. In the case of LAMMPS, we included into the data file the tables of EAM potentials converted by C.A. Becker (see <http://www.ctcms.nist.gov/potentials/>) into the dynamo format (each table from 10000 points). In our program, the EAM tables from 5000 point each were used. Parallel calculations were fulfilled by means of Graph processors (NVIDIA graphics-cards) with the help of GPU software included in LAMMPS and CUDA software.

All simulations employed the Verlet algorithm [13] with a time step of 1.5 fs. The weak thermostating for isothermal annealing was chosen in all cases; in our program, a multiplier to velocity of atoms was $1 \pm 0.001 \sqrt{|T-T_t|/T}$ (T is a instantaneous temperature, T_t is the set temperature, sign “+” if $T < T_t$).

We applied NVT ensemble (constant number of atoms, volume of the main cell, and temperature), but the sample volume was not constant as they have free surfaces (were smaller than the main cell). The first step before simulations was preparing of samples for simulations. Initial form of models was created in the auxiliary program. All atom coordinates were passed in LAMMPS or in our program, and their melting was accomplished (fully or partly). Two forms of samples were prepared. Kinetics of growth of small crystallization centers (after nucleation) was studied in spherical samples with a free surface (nanodrops of 16384 atoms). They were formed in a result of fusion of an ideal crystal given in initial conditions at a temperature above the melting temperature in 100-200 K over a period of time >50 ps. Then they were quickly (1–2 ps) cooled to the chosen temperature of annealing (to obtain statistics for “one” temperature, the set temperatures for annealing were different slightly, 0.1 – 0.2 K). For analyzing the results of simulations, we use the program that enables viewing with the step in one angstrom all sections of the model with coordinates of atoms from saved files. The strong dependence of growth velocities on the size of crystallization centers was found in [14].

To study growth kinetics of nanocrystals, oblong samples (of 32768 atoms) in the form of cylinder with the structure of crystal phase were set in initial conditions (periodic boundary conditions along one axis were applied). Then their larger part was transformed into amorphous state by the way of many random displacements of atoms with further quick heating above melting point and then quick cooling to the chosen temperature. The nanocrystals of 5–7 nm in size (for them, the size effect is not as essential as for small crystallization centers) with initial interfaces of (100), (110) or (111) crystal type were able to grow at the constant temperature.

In addition, we can view many clusters of different kinds. Identification of clusters was fulfilled with the help of LAMMPS software or in results of procedure running, which determined the number of nearest neighbors and angles with nearest neighbors for every atom, and gives a color for atom visualization dependently on a cluster type (see Ref. [14]).

The values of the diffusion coefficients for Al and Ni and Cu at different temperatures were determined by measurements of mean-square displacements of atoms for the same potentials, which were used for studying of growth.

Results and the discussion

Relaxation processes occur in the supercooled melts after setting a certain temperature for annealing. The waiting time for appearance of crystallization center is larger than the time of relaxation. However, the measurements of growth velocities in oblong specimens should be fulfilled after the structure relaxation. The results of simulations for determination of diffusivity in melts of metals and growth velocities with using modern potentials are in a good agreement with experimental data. Therefore, a quantitative comparison of such data with predictions of theories is already opportune. The table 1 contains simulated and experimental data on kinetic coefficients β_T and β_S at the melting temperatures, the values of magnitudes D_0 and activation energy Q , which determine the temperature dependencies of the diffusion coefficients, and the values of the coefficients f_1 and f_2 that are chosen for best fitting of kinetic coefficients by Eqs. (1) and (3). It is necessary to note that the values of D_0 and activation energy Q are determined for not terrific supercoolings of liquid – roughly up to 200 K. Data of Ref. [19] give an evidence of the Arrhenius type dependence (constant Q) for copper in the large temperature period. It is unlikely as essential changes in a structure of materials take place near the glass-transition temperature.

Table 1

The simulated and experimental data on kinetic coefficients β_T and β_S at the melting temperatures, the values of magnitudes D_0 and activation energy Q

Material	$\beta_T, \text{m}/(\text{sK})$	$\beta_S, \text{m}/\text{s}$	$D_0 \cdot 10^8, (\text{m}^2/\text{s})$	Q, K	$\Delta H, \text{K}$	T_m, K	f_1	f_2
Al _{sim}	0.50±0.02 (our)	369	4.45	2617	1288	975	6	0.3
Ni _{sim}	0.30±0.02 (our)	366	7.5	5480	2075	1600	9	0.475
	0.39 [15]	549	8.6 [15]	5751	2098	1718 [15]	6.9	0.64
Ni _{exp}	0.2 [16]	284	7.7 [17]	5499	2098	1728	3.36	0.33
Cu _{sim}	0.65 (our)	592	4.5	3600	1301	1175	12	0.8
Cu _{exp}	1.58 [18]	2149	5.7 [19]	3883	1352	1356	29	2.96

It is clear that Eq. (3) approximates better the values of the kinetics coefficient near the melting temperature (the value of f_2 is closed to 1). Fig. 1 shows the temperature dependences of the growth velocities for Ni, Al and Cu obtained as results of simulation and also the curves calculated according to Eqs. (1) and (3) with prefactors that give the best fit at the melting point. We calculated the difference of chemical potential of two phases according to the equation $\Delta\mu = \Delta H (1 - (T/T_f)^2)/2$ which fits better such dependencies [14] than the Spaepen equation. The full lines in Fig. 1 give the temperature dependence of velocities calculated according to Eq. (1).

The dotted lines in Fig. 1 show the temperature dependence of velocities calculated according to Eq. (3). Those and other lines go close to the experimental dots near the melting point because the coefficients f_1 and f_2 are chosen from such condition. However, the coefficients f_1 is too large in comparison with (1). Analyzing the temperature dependences of growth velocities, we see that the Wilson-Frenkel theory with such great

coefficients, $f_1 \sim 10$, fits better the calculated data in wide temperature intervals. Thus, the simulated data concerning the growth velocities in the large temperature intervals give evidence of the thermo-activated growth.

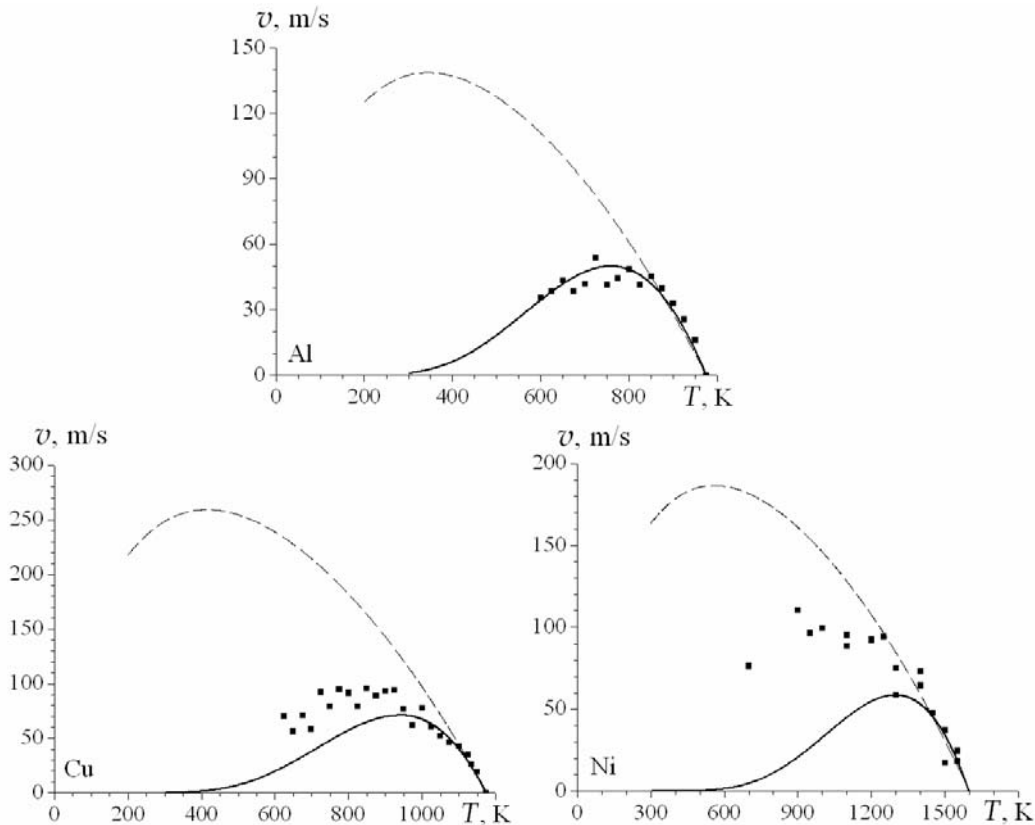


Fig. 1. The simulated growth velocities of single crystals and calculated data.

Full lines are calculated according to the Wilson-Frenkel theory; dotted lines are calculated according to the Broughton, Gilmer and Jackson equation.

Conclusions

The Broughton, Gilmer and Jackson equation for the evaluation of growth velocities is valid at the temperatures close to the melting points (not lower than 100-200 K from them). The simulated data concerning the growth velocities in the large temperature intervals give nevertheless an evidence of the thermo-activated growth. However, the values of the kinetics coefficient are much larger that is predicted by the Wilson-Frenkel theory for pure metals. For definitive conclusion about temperature periods, in which the first or second theory works better, it is necessary to carry out a careful study of diffusivity for these metals in the large temperature intervals and determine the temperature dependences of the activation energy Q .

References

1. Chernov A. A. Modern Crystallography, V. 3, Crystal Growth. / A. A. Chernov – Moscow, 1980. – 407 p. (in Russian).
2. Ovsienko D. E. Nucleation and growth of crystals from melts / D. E. Ovsienko –Kiev, 1994. – 238 p. (in Russian).

3. **Fedorov O. P.** Processes of crystal growth. Kinetics, Forms of Growth, Imperfections / O.P. Fedorov – Kiev, 2010. – 207 p. (in Russian).
4. **Wilson H. W.** On the velocity of solidification and viscosity of supercooled liquids / H.W. Wilson // Philosophical Magazine – 1900. – V. 50. – P. 238-250.
5. **Frenkel J. I.** Kinetic Theory of Liquids / J. I. Frenkel – Oxford, 1946. – 357 p.
6. **Jackson K. A.** The Interface Kinetics of Crystal Growth Processes / K.A. Jackson // Interface Science – 2002. – V. 10, № 2-3. – P. 159-169.
7. **Broughton J. Q.** Crystallization Rates of a Lennard-Jones Liquid / J. Q. Broughton, G. H. Gilmer, K. A. Jackson // Physical Review Letters – 1982. – V. 49. – P. 1496-1499.
8. **Hoyt J. J.** Kinetic phase field parameters for the Cu–Ni system derived from atomistic computations / J. J. Hoyt, B. Sadigh, M. Asta, S. M. Foiles // Acta Materialia – 1999. – V. 47, № 11. – P. 3181-3187.
9. **Celestini F.** Measuring kinetic coefficients by molecular dynamics simulation of zone melting / F. Celestini, J. M. Debierre // Physical Review E – 2002. – V. 65. – P. 041605-0416015.
10. **Sun D. Y.** Kinetic Coefficient in Ni Solid-Liquid Interfaces from Molecular Dynamics Simulation / D. Y. Sun, M. Asta, J. J. Hoyt // Physical Review B – 2004. – V. 69. – P. 024108-024115.
11. **Mikheev L. V.** Mobility of a diffuse simple crystal–melt interface / L. V. Mikheev, A. A. Chernov // Journal of Crystal Growth – 1991. – V. 112, № 2–3. – P. 591-596.
12. **Plimpton S.** Fast Parallel Algorithms for Short-Range Molecular Dynamics / S. Plimpton // Journal of Computational Physics – 1995. – V. 117, № 1. – P. 1–19.
13. **Verlet L.** Computer Experiments on Classical Fluids / L. Verlet // Physical Review – 1967. – V. 159 № 1. – P. 98-103.
14. **Ovrutsky A. M.** Peculiarities of crystallization at high undercooling: Analysis of the simulation data for aluminum / A.M. Ovrutsky, A.S. Prokhoda // Journal of Crystal Growth – 2011. – V. 314. – P. 258–263.
15. **Kerrache A.** Molecular-dynamics computer simulation of crystal growth and melting in $\text{Al}_{50}\text{Ni}_{50}$ / A. Kerrache, J. Horbach, K. Binder // EPL Europhysics Letters – 2008. – V. 81, № 5. – P. 58001-58007.
16. **Willnecker R.** Evidence of nonequilibrium processes in rapid solidification of undercooled metals / R. Willnecker, D. M. Herlach, B. Feuerbacher // Physical Review Letters – 1989. – V. 62. – P. 2707–2710.
17. **Meyer A.** Determination of self-diffusion coefficients by quasielastic neutron scattering measurements of levitated Ni droplets / A. Meyer, S. Stüber, D. Holland-Moritz, O. Heinen, T. Unruh // Physical Review B – 2008. – V. 77. – P. 092201-092204.
18. **Suzuki T.** Dendrite growth from the supercooled melt Original Research Article / T. Suzuki, S. Toyoda, T. Umeda, Y. Kimura // Journal of Crystal Growth – 1977. – V. 38, № 1. – P. 123-128.
19. **Meyer A.** Diffusion of Mass in Liquid Metals and Alloys Recent Experimental Developments and New Perspectives / A Meyer, F. Kargl // International Journal Microgravity Science Application – 2013. – V. 30, № 1. – P. 30–35.

Received 13.07.2013.

UDC 537.622 : 539 : 003.3

V. V. Kovalchuk

Odesa State Environmental University

QUANTITATIVE ANALYSIS OF NANOSTRUCTURES

The interest to surface disordered phases in modern nanoelectronics and recent progress in the combination of visualization and simulation techniques are discussed. The role of modeling and studying the properties of nanoclusters on Si surface is emphasized. The applications of the Model Molecular Graphics Package to such nanostructures are demonstrated, its interactivity possibilities are considered. Mathematical background and computation results are presented for the Modified IENT- α method, POTENTIAL package, and Graphic Package. The last one gives the 3D representation of the investigation of nanoclusters, processes of their formation through chemisorption and their final geometry. The results are important for nanotechnology.

Keywords: nanoclusters, model, quantum-dimensional system, visualization.

Обсуждаются причины интереса к поверхностно разупорядоченным состояниям в современной наноэлектронике и существующий прогресс среди методов визуализации и моделирования. Особое внимание уделяется роли моделирования при изучении свойств нанокластеров на поверхности кремния. Продемонстрировано применение пакета молекулярной графики Model Molecular Graphics Package к таким наноструктурам и рассмотрены его интерактивные возможности. Представлены математическое обоснование и результаты расчетов в программных пакетах Modified IENT- α method, POTENTIAL package, и Graphic Package. Последний пакет позволяет в трехмерном представлении проводить исследования нанокластеров, изучать процессы их образования в результате хемосорбции и получать окончательную геометрию. Полученные результаты представляют интерес для нанотехнологий.

Ключевые слова: нанокластеры, модель, квантово-размерные системы, визуализация.

Обговорюються причини інтересу до поверхнево розупорядкованих станів у сучасній наноелектроніці та прогрес у розробці методів візуалізації та моделювання. Особлива увага приділяється ролі моделювання при дослідженнях властивостей нанокластерів на поверхні кремнію. Продемонстровано застосування пакету молекулярної графіки Model Molecular Graphics Package до таких наноструктур та розглянуті його інтерактивні можливості. Представлено математичне обґрунтування та результати розрахунків у програмних пакетах Modified IENT- α method, POTENTIAL package та Graphic Package. Останній пакет дозволяє у тривимірному представленні проводити дослідження нанокластерів, вивчати процеси їх утворення в результаті хемосорбції та отримувати остаточну геометрію. Отримані результати є цікавими для нанотехнологій.

Ключові слова: нанокластери, модель, квантово-розмірні системи, візуалізація.

Introduction

Semiconductor surface forms a specific surface disordered phase (SDP) and the main peculiarities of modern nanoelectronic devices depend on the individual parameters of the surface phase. Furthermore, the reactions of atomic hydrogen (H), fluorine (F), chlorine (Cl) and bromine (Br) with Si surface are widely studied experimentally and many investigators observe the semiconductor SDP directly [1-3]. For the quantitative analysis of the creation of nanostructures like nanoclusters (NC) in Si and other solid materials the cluster distribution along the surface is necessary.

On the other hand, the recent progress in the combination of visualization and simulation techniques concurs in obtaining spectacular results in the investigation of chemical reaction mechanisms as well [4]. The traditional quantum chemical *ab initio* methods, based on the Hartree-Fock scheme became well-established in studies of the electronic and geometrical structure of solid NC's [1]. Therefore, the surface NC's as real objects and models of nanoelectronic materials for intellectual systems are of great interest.

Our Model Molecular Graphics Package (MMGP) is specially designed so as to allow us the high-level computerized visualization in molecular science. MMGP contains many interfaces with quantum chemical programs such as those of the semiempirical and molecular surface geometry generation that is based on an interatomic potential (for example, the modified Stillinger - Weber (MSW) potential).

In the paper the development and applications of the MMGP to the Si-NC structure is demonstrated. The MMGP generates detailed and easily interpretable and aesthetically attractive graphics representing models of molecular structures and related properties. The package offers a high level of interactivity through the use of the mouse and via a large set of menus and submenus organized in such a way that enables users to learn rapidly the basic operations leading to efficient visualization (see Fig. 1, 2).

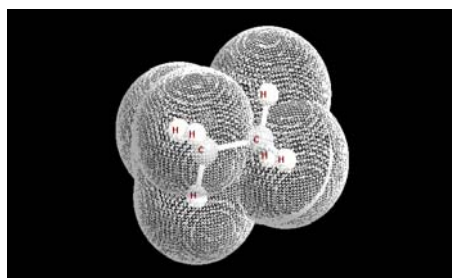


Fig 1. Map of the electron density distribution for the nanocluster.

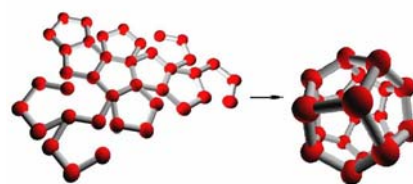


Fig.2. 3D - representation of the nanocluster formation.

For all the menu items, a help facility is implemented. Various representation options and attributes may be selected for adapting the visual output to personal needs and preferences: the molecular structures may be represented as discrete dots, and the global appearance may be modified via attributes such as background appearance, perspective or orthogonal projection, and others. The purpose of the MMGP is the interactive visual representation of three-dimensional (3D) models of molecular structures and properties for research. Due to the flexibility of the data- and program-structure, various chemical systems ranging from small compounds (clusters) to large macromolecules may be investigated; additional interfaces and tools can easily be implemented. The MMGP contains the tools that are necessary for the investigation and visualization of the results generated by the calculations with such an available program-package: Modified IEHT- α method, POTENTIAL package, Graphic Package.

Modified IEHT- α method

This is for semiempirical calculations of one-electron level energies, wave functions, and other parameters of electronic structure of NC. The estimation of the total energy of clusters that have different sizes follows

$$E_{tot} = \sum_{A \neq B} \frac{Q_A(\vec{r}_{AB}) - Q_A^*(\vec{r}_{AB})}{r_{AB}} + \sum_i g_i E_i - (E_{ee} + E_{exc}), \quad (1)$$

$$E_{exc} = \sum_{A \neq B} \sum_{\mu \neq \nu} \frac{1}{r_{AB}} v_{AB} S_{\mu\nu}^2 \quad (2)$$

where v_{AB} is a fitting parameter.

POTENTIAL package

This is a simulation program for calculations based on different types of interaction potentials. One of them is the modified Stillinger–Weber-type potential [2]. The Hamiltonian is

$$\begin{aligned} H(\vec{r}_1, \vec{r}_2 \dots \vec{r}_N, \vec{p}_1, \vec{p}_2 \dots \vec{p}_N) = \\ = \sum_{i=1}^N \frac{p_i^2}{2m} + \sum_{i < j} V_{int}^{(2)}(\vec{r}_{ij}) + \sum_{i < j < k} V_{int}^{(3)}(\vec{r}_{ij}, \vec{r}_{ik}, \vec{r}_{jk}) \end{aligned} \quad (3)$$

where $\vec{r}_1, \vec{r}_2 \dots \vec{r}_N$ are coordinates of the atoms, $V_{(2)int}$ is the twin potential (4); $V_{(3)int}$ is the tree-particle SW-potential

$$V_{int}^{(2)}(\vec{r}_{ij}) = \begin{cases} A \left(B \frac{1}{r_{ij}^p} - 1 \right) \exp \left(\frac{A}{r_{ij} - a} \right) \\ 0, \text{others} \end{cases}, \vec{r}_{ij} < 2.5 \sigma_{AB} \quad (4)$$

$$V_{int}^{(3)}(\vec{r}_{ij}, \vec{r}_{ik}, \vec{r}_{jk}) = \Pi_{ijk} + \Pi_{kij} + \Pi_{jki} \quad (5)$$

$$\Pi_{ijk} = A \left(\cos \theta_{jik} + \frac{1}{3} \right)^2 \exp \left(\frac{\delta_{ijk}}{r_{ij} - a} + \frac{\delta_{ijk}}{r_{ik} - a} \right)$$

where θ_{jik} is an angle, \vec{r}_{ij} and \vec{r}_{jk} , $\vec{r}_{ij} = |\vec{r}_i - \vec{r}_j|$ is a vector between i and j atoms in units of the equilibrium distance between the nearest atoms in the structure (\vec{r}_0). For Si $\vec{r}_0 = 2.351\text{\AA}$ (modified SW) and $\vec{r}_0 = 2.0951\text{\AA}$ (original SW). The energy unit equals to $E = 2.1675 \text{ eV}$, i.e. $E_{\text{Si-Si}}$ in the Si crystal. The parameters of the modified SW-potential are presented in [3].

Graphic Package

Graphic Package is a geometrical program based on 3D-representation of the investigation of NC.

We report the results of test calculations for adsorption processes and optical properties of the closely packed and ball-like Si NC. Real surface objects may be constructed by introducing stereochemistry, i.e., the 3D atomic positions, and it is important to visualize them as molecular models with the usual rendering techniques leading to 3D perception. MMGP visualization allows investigators to emphasize at length the different aspects of molecular structure of surface: chemical topology, conformational details, etc.

We applied the MMGP to the Si-SDP. With the appearance of semiempirical methods, the calculation of the equilibrium geometry and visualization of quite large model became possible (N=125 Atoms). The calculated bond lengths of some surface are given in Refs. [5-7].

As one can see from these data, the calculated interatomic distances are in a quite good agreement with the experimental ones. Especially, the changes of the Si-Si bond from a small Si-NC (2-10 atoms) to big ones are accurately described. We find the energies of NC, binding energy per atom, and interaction energy of the systems «NC-SDP» are obtained for more stable geometry. Furthermore, the energetic positions and equilibrium distances as well as of silicon are described rather well.

Another example of the adsorption process and chemical reactions on semiconductor surfaces is the interaction with halogen atoms [6]. When using the model to represent the SDP, a choice has to be made about the NC size, that is, the number of atoms that are treated explicitly in the calculations, and the level of precision of the required computation. Fortunately, the chemisorption of atoms on SDP seems to be of local character. This fact is greatly supported by ab initio model calculations, and particularly by the calculations for the chemisorption of F and Cl on Si-SDP.

In our calculation the single NC contains 10-100 Si atoms representing the first four layers of the Si-SDP. We regard this model as hypothetical molecules (quasimolecules) and do try to compare the computed results (for example, magic numbers) directly to experimental data of the corresponding impurities in the solids or chemisorbed systems [1]. The mass spectra of charged NC's, where magic numbers are observed, are given in [3].

Taking into account the internal structure of the ball-like Si NC's we investigate theoretically the adsorption and scattering of light by them. The theory for the interaction of electromagnetic fields with local charge-carriers near boundary of the small spherical semiconductor microcrystals was presented in [8]. In [5, 8] the dipole moments of NC (using MMGP) and transition dipole moments for local bulk states and local exterior surface states were calculated. It was shown that the dipole moments of the transitions for local states of the Si NC are large compared to the typical values of transition dipole moments for Si-NC.

Conclusions

It is shown that the calculated energy and geometrical characteristics obtained by MMGP are in satisfactory agreement with the experiment and others ab initio calculations [1-8]. The present calculations show that the MMGP can be used to obtain a detailed and reasonably accurate description of various aspects of the small halogen – Si- NC. In view of the interest of physicists to the visualization of such NC, one may foresee that the data banks representing the major types of stable systems will soon be available. Therefore, it is important for a physicist to have at hand the computer tools allowing visualization and

generation of computational information. The combination of MMGP with molecular dynamics in connection with the technique of simulated annealing makes it a very useful tool for the determination of geometries of large NC. Reconstruction processes at Si SDP or amorphous solids can be studied also in this way.

References

1. **Keghelian P.** Properties of silicon and silicon-carbon cluster assembled films / P. Keghelian, P. Melinon, A. Perez // Nanostructured materials. - 2009. - V. 12. - P. 277-280.
2. **Dresselhaus M.S.** Science of fullerenes and carbon nanotubes / M. S. Dresselhaus, G. Dresselhaus, P. Eklund // San Diego: Academic Press, 1996. - P. 24-229.
3. **Marsen B.** The energy gap of pristine silicon clusters / B. Marsen, M. Lonfat, P. Scheier, K. Sattler // J. Electr. Spectr. Rel. Phenom. - 2008. - V. 109. - P. 157-168.
4. **Blaudeck P.** Calculation of Molecules, Clusters and Solids with DFT-LDA Scheme / P. Blaudeck, Th. Freuenheim, G. Seifert and others // J. Phys.: Condensed Matter. - 2012. — V.4. — P. 6368-6371.
5. **Kovalchuk V.V.** Principles of research of the devices providing of nanomeasuring / V.V. Kovalchuk, L.V. Dolinska // Metrology and Devices. - 2010. - №4(24). - C. 49-59.
6. **Kovalchuk V.V.** Cluster morphology of silicon nanoparticles / V.V. Kovalchuk // Semiconductor Physics, Quantum Electronics & Optoelectronics. - 2007. - V. 10, № 4. - P. 81-86.
7. **Kovalchuk V.V.** Cluster modification semiconductor's heterostructures / V.V. Kovalchuk // Kiyv: HI-Tech, 2007. - 309 p.
8. **Kovalchuk V.V.** The Spectrum of an Exciton in Nano-Crystal Semiconductor Structures: Theory Book "Metal Clusters in Chemistry", Ed. by Prof. Braunstein, Oro and Raithby. WILEY-Press, 2009. - P. 1263-1267.

Received 13.07.2013.

UDC 621.372

I. V. Grymalyuk¹, O. O. Drobakhin²

¹*Institute for Technical Mechanics of NASU and SSAU*

²*Oles Honchar Dnipropetrovsk National University*

RESONANCE PHENOMENA IN A WAVEGUIDE-DIELECTRIC STRUCTURE

The physical processes occurring in the waveguide-dielectric structure that has the form of a section of rectangular cut-off waveguide with dielectric insertion filling completely the cross section of the waveguide are considered. There are travelling modes in the insertion.

The electromagnetic fields in the classic waveguide-dielectric resonator without devices for its excitation and with coupling elements are calculated. The expressions for the reflection and transmission coefficients of the structure under consideration are presented. The calculating results of the distribution of the modulus of the electric field along the longitudinal axis of the cut-off waveguide at the natural frequency and frequencies near to that are obtained. It is shown that the frequency deviation from the natural value greatly reduces the electric field inside the resonance volume. The positions of poles and zeros of the reflection coefficient are investigated with a fractional-rational approximation. The obtained results are useful for measuring the properties of dielectric materials using waveguide methods.

Keywords: waveguide-dielectric structure, resonance, fractional-rational approximation.

Рассматриваются физические процессы, имеющие место в волноводно-диэлектрической структуре в виде отрезка прямоугольного запердельного волновода с диэлектрической вставкой, полностью заполняющей поперечное сечение волновода. Во вставке существуют распространяющиеся волноводные моды.

Анализируется поведение электромагнитного поля в классическом волноводно-диэлектрическом резонаторе без учета устройств для его возбуждения, а также при использовании систем связи. Приводятся выражения для расчета коэффициентов отражения и прохождения исследуемой структуры. Приводятся результаты расчета распределения модуля напряженности электрического поля вдоль продольной оси запердельного волновода на резонансной частоте и на частотах, близких к ней. Демонстрируется, что отклонение частоты электромагнитного поля от резонансного значения приводит к значительному снижению напряженности электрического поля внутри резонансного объема. С помощью дробно-рациональной аппроксимации исследуется расположение полюсов и нулей функции коэффициента отражения. Полученные результаты являются полезными для проведения измерений свойств диэлектрических материалов волноводными методами.

Ключевые слова: волноводно-диэлектрическая структура, резонанс, дробно-рациональная аппроксимация.

Розглядаються фізичні процеси, які відбуваються в хвилеводно-діелектричній структурі у виді відрізка закритичного прямокутного хвилеводу з діелектричною вставкою, яка повністю заповнює поперечний переріз хвилеводу. У вставці існують хвилеводні моди, що поширюються.

Аналізується поведінка електромагнітного поля у класичному хвилеводно-діелектричному резонаторі без врахування пристроїв для його збудження, а також при використанні систем зв'язку. Наводяться вирази для розрахунку коефіцієнтів відбиття та проходження досліджуваної структури. Наводяться результати розрахунку розподілу модуля напруженості електричного поля вздовж повздожньої осі закритичного хвилеводу на резонансній частоті та на частотах, близьких до такої. Демонструється, що відхилення частоти електромагнітного поля від резонансного значення викликає значне зниження напруженості електричного поля всередині резонансного об'єму. За допомогою дробово-раціональної апроксимації досліджується розташування полюсів та нулів функції коефіцієнту відбиття. Отримані результати є корисними для проведення вимірів властивостей діелектричних матеріалів хвилеводними методами.

Ключові слова: діелектрично-хвилеводна структура, резонанс, дробово-раціональна апроксимація.

Introduction

In the present time, modern technologies and productions require the use of dielectric materials. It is necessary to obtain information about the properties of the dielectric material, such as its dielectric permittivity and its loss tangent. Various microwave methods are used to solve this problem. Among them an important place is occupied by devices using waveguide-dielectric structures.

Many papers [1-4] are devoted to the consideration of the devices on the basis of waveguide segments with dielectric inserts. According to the authors, the first attempt to produce a classification of the waveguide-dielectric systems was presented in [5]; there the basic physical ideas were realized. However, according our opinion, such analysis has only the proposition nature and, for example, the physical processes in a rectangular waveguide with a dielectric insert have not been completely analyzed.

The purpose of this paper is considering the resonance phenomena in such systems. The rectangular waveguide with a dielectric box completely filling the cross-section of the waveguide has been taken as an example. The choice of the proposed structure is determined by the fact that it has an analytic solution of the electromagnetic problem; the results of the analysis can be generalized for more complicated cases.

Main part

Let us consider the classic pattern of the waveguide-dielectric resonator excluding devices for its excitation. It is presented in the Fig. 1.



Fig.1. A waveguide-dielectric resonator model without its excitation device (a) and the variation of the cut-off waveguide excitation with dielectric filling inserts(b)

As known, the electromagnetic field components E_y , H_x and H_z of the main type of the mode H_{10} in a rectangular waveguide are not zeroes. If the origin of the longitudinal coordinate is situated in the middle of the dielectric insert, there are two cases in view of the axis of symmetry of the system under consideration: the first one is the situation when the magnetic wall is in the middle of the dielectric parallelepiped; and the second one – when the electric wall is in the middle of the dielectric parallelepiped. In the first case the electric field in the dielectric insert can be described by the expression

$$E_y = A \cos(\gamma z) \quad (1)$$

and the other case is

$$E_y = A \sin(\gamma z) . \quad (2)$$

The electric field outside the dielectric in both cases is described by the expression

$$E_y^0 = A_0 \exp(-\gamma_0 z) , \quad (3)$$

where A, A_0 are amplitude coefficients, $\gamma = \sqrt{\left(\frac{2\pi}{\lambda}\right)^2 \varepsilon - \left(\frac{\pi}{a}\right)^2}$, $\gamma_0 = \sqrt{\left(\frac{2\pi}{\lambda}\right)^2 - \left(\frac{\pi}{a}\right)^2}$ are propagation constants in a waveguide filled with a dielectric and in an empty one respectively, a is the size of the wide side of the waveguide, λ is the length of the electromagnetic wave in the waveguide, ε is dielectric permittivity.

The required tangential component H_x of the magnetic field is:

$$H_x = -A \frac{\gamma}{j\varpi\mu} \sin(\gamma \cdot z) \text{ in the first case and } H_x = A \frac{\gamma}{j\varpi\mu} \cos(\gamma \cdot z) \text{ in the second.}$$

Outside the dielectric it is $H_x^0 = -A_0 \frac{\gamma_0}{j\varpi\mu} \exp(-\gamma_0 z)$, where ϖ – cycle frequency, μ is the permeability of the medium. The boundary conditions for the tangential components E_y, H_x of the electromagnetic field can be satisfied only in the plane $z = \frac{L}{2}$ due to the symmetry of the system with the origin of z -coordinate in the center of dielectric slab, where L is the thickness of the dielectric insert. In the first case, the boundary conditions for E_y and H_x are

$$A \cos\left(\gamma \frac{L}{2}\right) = A_0 \exp\left(-\gamma_0 \frac{L}{2}\right) \text{ and } A\gamma \sin\left(\gamma \frac{L}{2}\right) = A_0\gamma_0 \exp\left(-\gamma_0 \frac{L}{2}\right), \text{ respectively.}$$

The condition for determining the natural frequencies is obtained via dividing the first expression by the second one

$$ctg\left(\gamma \frac{L}{2}\right) = \frac{\gamma}{\gamma_0}. \quad (4)$$

The similar expression for the second case is

$$tg\left(\gamma \frac{L}{2}\right) = -\frac{\gamma}{\gamma_0}. \quad (5)$$

Such approach of similar ideology was used by the authors of papers [6] with certain complications in satisfying the boundary conditions at the ends of waveguide systems with a dielectric filling.

A necessary condition for the initiation of resonance properties, as it is known, is the abrupt intensity changing of the electromagnetic field in a resonant volume with respective frequency changing. It should be noted that there are two radically different physical natures of the manifestation of resonant properties for the considered model. In the first case the resonance system is formed by a segment of a standard waveguide with traveling mode in the corresponding frequency band. In the other case, the waveguide segment is cut-off one without any traveling mode but a traveling mode exists in the dielectric insert. For the first case the equations for determining the natural frequencies have complex solutions, so natural frequencies also must be complex. This corresponds to the loss due to the electromagnetic energy radiation. It is a radical difference from the other case, in which the presence of the cut-off waveguide eliminates the radiation loss.

In our paper we consider the case with the cut-off waveguide as the simplest version for calculations. The size of the wide side of the waveguide $a = 12$ mm provides a dominant mode in the 3-cm wave-range. Let us suppose that hypothetical dielectric material has the dielectric permittivity $\varepsilon = 80$ and thickness $L = 10$ mm, under conditions

of absence dielectric losses ($\text{tg}\delta = 0$). In the case of the solution with magnetic wall (4), the chosen geometrical and electrical parameters of the system give the value of natural frequency $f = 10242$ MHz. At this frequency the distribution of the electric field strength modulus along the longitudinal axis from the point of symmetry in the dielectric insert and in the part of space outside is shown in Fig. 2a. The influence of the frequency changes on the distribution of the electric field strength modulus is illustrated in Fig. 2b.

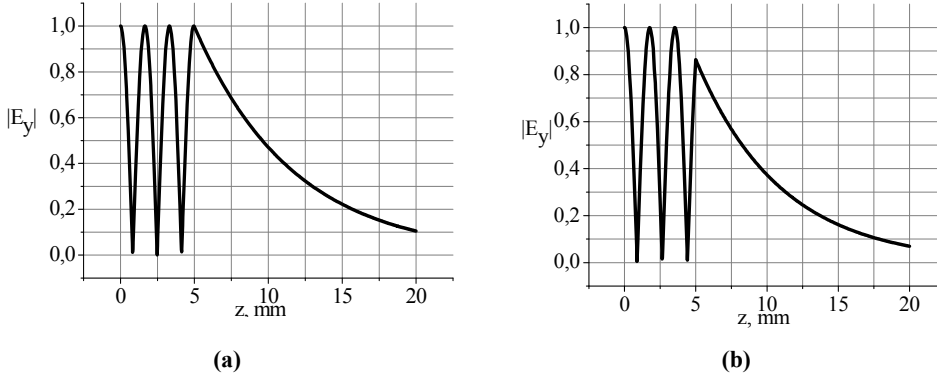


Fig. 2. The electric field strength modulus along the longitudinal axis of the cut-off waveguide at resonance frequency $f_R = 10242$ MHz (a) and near it $f = 9600$ MHz (b) for parameters of dielectric insert: $a = 12$ mm, $L/2 = 5$ mm, $\varepsilon = 80$

The view of the field with $L/2 = 5$ mm is considered in this figure due to the system symmetry. As we can see from Fig. 2b, the frequency deviation of the electromagnetic field from the natural one leads to a slight decrease of the strength only in the plane of the dielectric permittivity jump. Hence, it is clear that such simplified model of the waveguide-dielectric resonator can not give a full description of the physical processes occurring in this structure.

Obviously, for more complete description of processes in such structure it is necessary to take into account the devices for excitation of the cut-off waveguide inserts connected to the dielectric sample. There are several versions of the devices for excitation of cut-off waveguides. For example, in [8] a sharp change of sizes of the cross section in H -plane is used; according to [9] multilayer dielectric filling of the cut-off waveguide can be used; using coaxial transition is presented in [6]. For the succeeding analysis we shall use the model that has been shown in Fig. 1b, as the simplest one for the electromagnetic calculation.

Using the boundary conditions for the E_y , H_x components of the electromagnetic field in the planes of dielectric permittivity jumps, we can obtain the expressions for the

complex transmission $T = \frac{1+R}{1+r_1} \cdot \frac{e^{-\gamma_0 d} + r_1 e^{\gamma_0 d}}{1+r_2} \cdot \frac{e^{-\gamma L} + r_2 e^{\gamma L}}{1+r_3} (e^{-\gamma_0 d} + r_3 e^{\gamma_0 d}) \cdot e^{\gamma_1 d}$ and

reflection $R = \frac{q-1}{q+1}$ coefficients for this structure, where $q = \frac{\gamma_1}{\gamma_0} \cdot \frac{1+r_1}{1-r_1}$, $r_1 = \frac{q-1}{q+1} e^{-2\gamma_0 d}$,

$q_1 = \frac{\gamma_0}{\gamma} \cdot \frac{1+r_2}{1-r_2}$, $r_2 = \frac{q_2-1}{q_2+1} \cdot e^{-2\gamma L}$, $q_2 = \frac{\gamma}{\gamma_0} \cdot \frac{1+r_3}{1-r_3}$, $r_3 = \frac{q_3-1}{q_3+1} \cdot e^{-2\gamma_0 d}$, $q_3 = \frac{\gamma_0}{\gamma_1}$, and d is

the length of the unfilled part of the waveguide, L is the length of the central dielectric insert. The longitudinal distribution of the electric field strength along the cut-off waveguide with three dielectric parallelepipeds has been calculated.

Fig. 3 shows the corresponding results. Geometrical and electrical parameters are the size of the wide side of the waveguide $a = 12$ mm, the length of the external dielectric parallelepipeds $L_h = 20$ mm and permittivity $\varepsilon_1 = 10$, the length of the unfilled part of the waveguide $d = 10$ mm, the length of the central parallelepiped $L = 10$ mm and its dielectric permittivity $\varepsilon = 80$. The estimated resonance frequency is 10250 MHz for this configuration. The distribution for the resonance frequency is presented in Fig. 3a.

Fig. 3b shows a longitudinal distribution of the electric field strength for the same system, but the frequency of the electromagnetic field is 10000 MHz. The comparison of Fig. 3a and Fig. 3b shows that, as it follows from the theory of resonance phenomena, the deviation of the electromagnetic field frequency from the resonance value induces sharp reduction of the electric field strength inside the resonant volume in contrast to the results which have been obtained for the simple model.

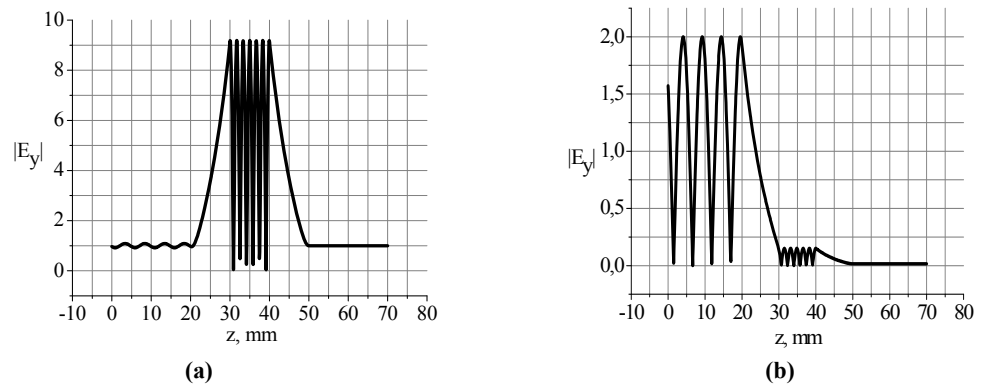


Fig. 3. The electric field strength modulus along the longitudinal axis of the cut-off waveguide structure that has been shown in Fig. 1b at resonance frequency $f_R = 10250$ MHz (a) and near it $f = 10000$ MHz (b) with structure parameters: $a = 12$ mm, $d = 10$ mm, $L = 10$ mm, $\varepsilon_1 = 10$, $\varepsilon = 80$

Some difference in frequencies for the first and the second models can be explained by the fact of coupling device effect on the resonance phenomena in the second model. The following example will show this effect. Let us consider the case where the dielectric insertion is a film of the thickness of 0.1 mm and all the other parameters remain unchanged. The results of calculation of the longitudinal distribution of the electric field strength for the length of the unfilled part of the waveguide $d = 10$ mm has been shown in Fig. 4a and corresponding ones for $d = 25$ mm are presented in Fig. 4b. Length $d = 10$ mm corresponds to the resonant frequency of 9943 MHz and $d = 25$ mm corresponds to 9752 MHz; it can be explained by changing the influence of the coupling constant of the exciting element on the resonance volume. For $d = 25$ mm the electric field strength increases by about an order of magnitude and oscillations of the electric field strength appear in the area of the first dielectric parallelepiped.

Moreover, the range between the minimum and maximum values of electric field strength has increased in tens times in comparison with the case of $L = 10$ mm. In the case of $d = 10$ mm, $L = 10$ mm the frequency deviation of the electromagnetic field from the resonance value leads to a sharp decrease of the electric field strength (Fig. 5).

For a comparison, the natural frequency for the first model (with the same geometrical sizes and electrical parameters of the central dielectric parallelepiped) determined from the equation (4) is 9750 MHz. It practically coincides with the

frequency (9752 MHz) for the second model with $d = 25$ mm. Thus, their natural frequencies determined from the simplest equation (4) coincide with the natural frequencies of the second model with sequential decreasing of coupling coefficients.

The values of the poles and zeros have been obtained by fractional-rational approximation [10] of the structure reflection coefficients as functions of frequency. It is well known that the positions of the poles coincide with resonance frequencies. The fact of convergence of the values of the poles and the calculated resonance frequencies confirms that the considered dielectric waveguide structure really manifests resonance phenomena.

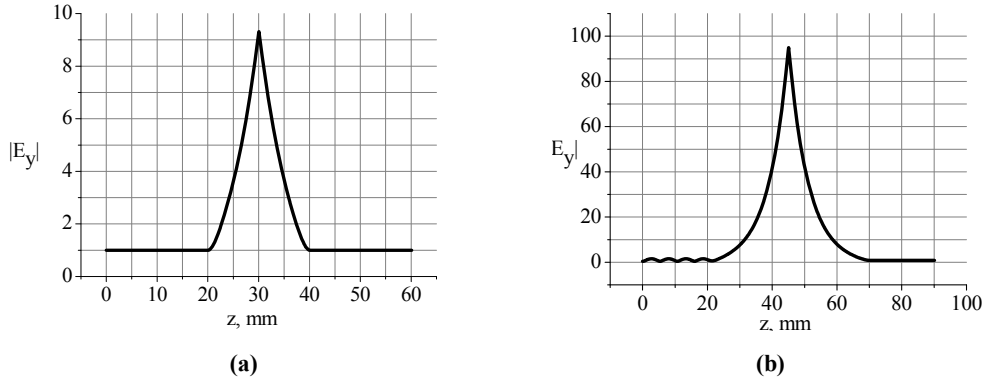


Fig. 4. The distribution of the electric field strength modulus along the longitudinal axis of the cut-off waveguide structure ($a = 12$ mm, $d = 10$ mm, $L = 0.1$ mm, $\varepsilon_1 = 10$, $\varepsilon = 80$) has been shown in Fig. 1b with various d : $d = 10$ mm, $f_R = 9943$ MHz (a), $d = 25$ mm, $f_R = 9752$ MHz (b)

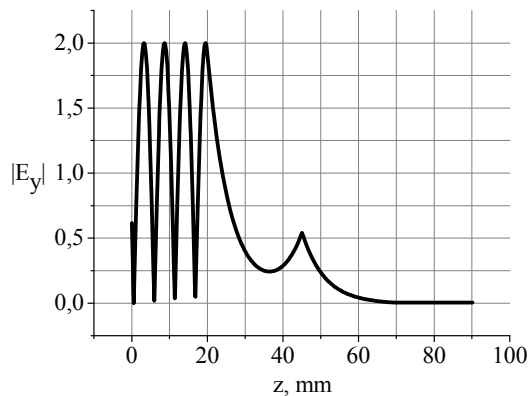


Fig. 5. The electric field strength modulus along the longitudinal axis of the cut-off waveguide structure ($a = 12$ mm, $d = 25$ mm, $L = 0.1$ mm, $\varepsilon_1 = 10$, $\varepsilon = 80$) at frequency $f = 9600$ MHz

Conclusions

As was shown, not every dielectric waveguide system, which has a resonance-like frequency dependence of the reflection or transmission coefficients, is actually a resonator system. The results have shown that the waveguide-dielectric system with a coupling element, which was presented by the completely filled dielectric parts of the cut-off waveguide, was the resonator. It was evidenced by the sharp reduction of the electric field strength modulus at the deviation of frequency from the natural one. The obtained results are useful for express measurements of dielectric material parameters with waveguide methods.

References

1. **Boria V. E.** Contributions to the Analysis and Design of All-Inductive Filters with Dielectric Resonators / V. E. Boria, M. Bozzi, D. Camilleri, A. Coves, H. Esteban, B. Gimeno, M. Guglielmi, L. Polini // Proc. 33-rd European Microwave Conference. – 2003. – P.1247 – 1250.
2. **Munir A.** Artificial Dielectric Rectangular Resonator with Novel Anisotropic Permittivity and Its $TE_{10\delta}$ Mode Waveguide Filter Application / A. Munir, N. Hamanaga, H. Kubo, I. Awai // IEICE Trans. Electron. – 2005. – V.E88-C, №.1. – P. 40 – 46.
3. **Popovic M. A.** Coupling-induced resonance frequency shifts in coupled dielectric multi-cavity filters / M. A. Popovic, C. Manolatu and M. R. Watts // Opt. Express. – 2006. – V. 14, №. 3. – P. 1208 – 1222.
4. **Shimizu T.** Measured results of some low-loss dielectric plates by cut-off circular waveguide method in millimeter wave region / T. Shimizu, Y. Kobayashi // 4th Topical Symposium on Millimeter Waves. – 2002. – Session: P-17. – P. 191 – 194.
5. **Yushchenco A. G.** Classification of waveguide-dielectric structures / A.G. Yushchenco // Proc. 8-th Int. Crimean Conference «Microwave and Telecommunication Technologies». – 1998. – P. 252 – 255.
6. **Bilous R. I.** Investigation of Magnetic Oscillations in a Waveguide-Coaxial Resonator / R. I. Bilous, S. P. Martyniuk, A. P. Motornenko, I. G. Skuratovskiy // Radiophysics and radioastronomy. – 2009. – V. 14, № 3. – P. 328 – 334.
7. **Poplavko Y. M.** Waveguide methods of microwave research of ferro-electrics / Y. M. Poplavko, V. I. Molchanov, V. M. Pashkov, Y. V. Procopenco, V. A. Kazmirencо, A. V. Yeremenco // Техника и приборы СВЧ. – 2010. – №1. – P. 39 – 51.
8. **Bladel J. V.** Dielectric Resonator in a Waveguide Below cutoff / J. V. Bladel // IEEE Transactions On Microwave Theory And Techniques. – 1981. – V. MTT-29, №. 4. – P. 314 – 322.
9. **Kapilevich B.** Application of the cut-off Resonator for microwave Monitoring of transformer oil / B. Kapilevich, A. Lipsky, B. Litvak // Microwave and Optical Technology Letters. – 2011. – V. 53, №. 1. – P. 66 – 68.
10. **Andreev M. V.** Determination of Parameters of Fractional-Rational Model Using Interpolation by Continued Fraction / M. V. Andreev, V. F. Borulko, O. O. Drobakhin, D. Yu. Saltykov // Conf. Proc. of the Int. Conf. on Mathematical Methods in Electromagnetic Theory. – 2006. – P. 264 – 266.

Received 13.07.2013.

TABLE OF CONTENTS

Theoretical physics

Gulov A. V., Moroz Ya. S. Amplification of Z' signal in $e^+e^- \rightarrow \mu^+\mu^-$ process.....5
Demchik V. I., Kolomojets N. V., Skalozub V. V. Spatial structure of the Polyakov loop in external chromomagnetic field in lattice SU(2) gluodynamics.....13
Antropov S. S. Fitting of Binder cumulants in SU(2) – gluodynamics.....18
Korkina M. P., Iegurnov O. O. Matching of Stephani and de Sitter solutions on the hypersurface of constant time.....25
Gorev V. N., Sokolovsky A. I. One-velocity and one-temperature hydrodynamics of plasma.....39
Lyagushyn S. F., Salyuk Yu. M., Sokolovsky A. I. Dynamics of electromagnetic field and its correlations in a medium consisting of two-level emitters.....47
Skalozub V. V., Tsygankov E. V. Real-time formalism for polarization operator of a charged scalar particle in external electromagnetic field.....56

Solid state physics

Moiseyenko V. N., Gorelik V. S., Dergachov M. P., Yevchik A. V., Shvets T. V., Beletsky A. A. Optical phenomena in matrix nanocomposites based on synthetic opals...64
Yevchik A. V., Moiseyenko V. N., Gorelik V. S., Dergachov M. P. Fabrication and optical characterization of thin synthetic opal films for designing coatings of solar cells...71
Sukhova O. V., Ustinova K. V., Syrovatko Yu. V. X-ray microanalysis of Fe(B, C)-based solid solutions.....76
Matysina Z. A., Elina E. V., Botsva N. P., Deviatkina M. Ye. Hydrogen absorption-desorption isotherms in magnesium intermetallic compounds.....82
Kushnerov O. I., Bashev V. F. Microstructure and mechanical properties of new multicomponent high-entropy alloys.....88
Gusevik P. S., Ryabtsev S. I., Dotsenko F. F. Structure and properties of pure Mn, Bi and MnBi films in metastable state.....94
Kutseva N. A., Bashev V. F., Derun A.Y., Larin V. S. Nanocrystallization processes in the “Finemet” type microwires under stress annealing.....100
Khandetsky V. S., Tonkoshkur Yu. A. Investigation of recharging processes for the volume localized states in polycrystalline semiconductors.....104
Antonova E. V., Tonkoshkur A. S., Kolbunov V. A. Dielectric properties of polymer composite material based on vanadium dioxide.....111
Lysenko A.B., Kosynska O.L., Borisova G.V., Kazantseva A.A. Crystallization kinetics under conditions of the quenching from a liquid state.....116
Ovrutsky A. M., Prokhoda A. S., Kushnerov O. I. The growth kinetics of metallic crystals. Results of simulations.....123
Kovalchuk V. V. Quantitative analysis of nanostructures.....129

Radiophysics

Grymalyuk I. V., Drobakhin O. O. Resonance phenomena in a waveguide-dielectric structure.....134

Наукове видання
ВІСНИК
ДНІПРОПЕТРОВСЬКОГО УНІВЕРСИТЕТУ
Серія: ФІЗИКА. РАДІОЕЛЕКТРОНІКА

Заснований у 1993 р.

Випуск 20

Англійською мовою

Свідоцтво про державну реєстрацію державного засобу масової інформації
Серія КВ № 7898 від 17.09.2003 р.

Мовний редактор С. Ф. Лягушин
Оригінал-макет М. П. Дергачов

Підписано до друку 08.11.2013. Формат 70x108¹/₁₆. Папір друкарський. Ум. друк. арк. 12,43.
Наклад 100 прим. Зам. №

Видавництво та друкарня “Ліра”.
49038, м. Дніпропетровськ, площа Десантників, 1
Свідоцтво про внесення до Держреєстру ДК № 188 від 19.09.2000 р.